Follow-up observations and characterisation of transiting hot Jupiter exoplanets

Benjamin Joseph Michael Clark

A thesis submitted to Keele University for the Degree of
Doctor of Philosophy

March 2019

Abstract

The discovery of the first hot Jupiter exoplanet more than twenty years ago raised many questions. Such large, hot planets were not predicted to exist so close to their host star. Since then, more than 125 hot Jupiters have been discovered (to date), with a total of 3726 exoplanets detected. With well-refined discovery methods and future detection surveys such as TESS and PLATO set to provide a wealth of ideal planets to study, we can now begin to move towards characterisation of these planets through follow-up observations.

Working towards this goal, the aim of this thesis was to undertake such observations to refine planetary parameters, search for additional planetary companions and variations within the light curves and to probe the atmospheric structure and composition of hot Jupiters. To achieve this, general purpose pipelines were created for the calibration of images, to perform aperture photometry and to explore the impact that choices of comparison star and aperture size had on values of eclipse depth and the light curve quality. A new method was introduced to allow apertures to be placed centrally over a de-focused PSF in a time efficient way, and a new de-trending method was used to improve the quality of transit light curves produced from short cadence data of the K2 mission.

Thermal emission from the hot Jupiter WASP-48b was detected in the $K_{\rm s}$-band using the 3.6 m *Canada-France Hawaii Telescope*. From the resulting occultation light curve a planet-to-star contrast ratio of $0.136 \pm 0.014\,\%$ was found which was in agreement with the value of $0.109 \pm 0.027\,\%$ that had been previously determined. From a global analysis, the system parameters were refined and a spectral energy distribution (SED) of the dayside atmosphere was constructed. Models with and without a thermal inversion were consistent with the data and the planet's orbit was found to be circular ($e < 0.072$ at 3σ).

Short-cadence K2 data of two previously known hot Jupiter exoplanets were also analysed. The WASP-55b and WASP-75b K2 light curves offered a high enough preci-

sion to allow the data to be searched for transit timing and duration variations, rotational modulation, starspots, phase-curve variations and additional transiting planets. Stellar variability was identified in the WASP-75 light curve, which may be a possible indication of rotational modulation, with an estimated period of 11.2 ± 1.5 days and a possible line of sight projected inclination angle of $i_* = 41 \pm 16°$. A global analysis of the K2 and previously published data was performed and the system parameters were refined.

Spectro-photomery observations of two hot Jupiters, WASP-77Ab and WASP-85Ab were analysed using the SINFONI instrument on the Very Large Telescope (VLT). The idea was to probe the day-side emission spectra of these planets by observing occultations at a higher resolution than broad-band photometry. However, observations were plagued with issues such as bad pixels and a lack of suitable comparison stars meaning poor quality light curves were produced. This combined with the stringent requirements needed for selected targets indicated that this particular instrument was not well-suited for these types of observation; an instrument with a wider field of view is necessary.

Overall, the work done in this thesis aimed to reduce the complexity and increase the reliability of these kinds of measurements. The routines created as part of this work are flexible enough to be applied to a broad range of data to provide high quality photometric measurements. The application of these to both space and ground based data produced light curves from which detailed analyses were obtained. They have the potential to be applied to a diverse number of observations, including large-scale surveys of occultation events which would allow a homogeneous analysis of exoplanet atmospheres.

Acknowledgements

I'd like to firstly thank my parents, they have always encouraged me to question the unknown things around me, raising me with a thirst for knowledge. Mum, you have always shown a true passion for astrophysics, and have inspired me from a young age to take interest in the subject. Dad, you have always worked hard and shown me that you only get out what you put in, you've motivated me to persevere, even when things were difficult. To the rest of my family, I apologise for not returning home as often as I should have done, but rest assured, I'll be back to boss you around as soon as possible.

To my friends both from Keele and from back home, thank you for keeping me sane by engaging me in other activities, whether it be hiking up mountains, playing video games or just visiting the pub, providing me with an outlet to relax has been more helpful than you realise. Oli, thank you for always being an ear to bounce ideas off and for always trying to keep them grounded in reality.

I would like to thank my primary supervisor Prof. Coel Hellier for his guidance throughout my Ph.D. as well as his patience and understanding with regards to my personal circumstances. I would also like to thank Dr. David Anderson for his advice, encouragement, the many tiring hours he spent imparting me with his wisdom and in particular the assistance with the WASP-48b paper.

Lastly, I would like to thank my incredible girlfriend Arica, without your love and support, I don't think I could have continued with this work over the past few years. Thank you for sticking by me when things were rough, you have brought happiness into my life in a time where I didn't think that was possible. Your kindness, sweetness and ability to make me laugh never fails to amaze me and you consistently inspire me to be a better person.

Contents

List of Figures

List of Tables

1 Introduction

1.1 Overview

An exoplanet is defined as a planet that exists beyond our Solar System and orbits a star other than our Sun. The idea that these type of planets exist is nothing new, it has captured the imagination of philosophers and scientists for centuries. Even as far back as 300 B.C., philosophers such as Epicurius realised that there was nothing to limit the possibility of other planets existing, he quoted "*Moreover, there is an infinite number of worlds, some like this world, others unlike it ... For the atoms out of which a world might arise, or by which a world might be formed, have not all been expended on one world or a finite number of worlds, whether like or unlike this one. Hence there will be nothing to hinder an infinity of worlds.*" He even speculated about the possibility of life on other planets, " *For nobody can prove that in one sort of world there might not be contained ... the seeds out of which animals and plants arise ...* " (Konstan 2016). Epicurius wasn't alone in these thoughts, again circa 300 BC. Metrodorus of Chios who, believing the Universe to be infinite, alluded to the possibility of other planets existing "A single ear of corn in a large field is as strange as a single world in infinite space" (Kitchin 2012). These ideas however, were against the popular opinion of the time.

It wasn't until the 16^{th} century that things began to change. What is now referred to as the Copernican revolution occurred in 1543, when Nicolaus Copernicus devised a model of heliocentric planetary motion which was published as part of his *De revolutionibus orbium coelestium*. The theory, which described the orbit of the planets in our Solar System around the Sun, was controversial at the time as it went against the idea that the Earth was located at the centre of the Universe and unique in its existence. Giordano Bruno, an Italian philosopher, built upon the theory and postulated that the Copernican model of our Solar System could apply to every star in the sky. He stated that "*This space we declare to be infinite... In it are an infinity of*

worlds of the same kind as our own" (Munitz 1951). He is today considered a martyr for science and free-thought after he was burned at the stake for his views in 1600. A decade later, in 1610, Johannes Kepler discovered that planetary motion could be described by three laws which helped to establish the Copernican model as one that was scientifically plausible. At the same time Galileo Galilei was able to provide further evidence in support of this theory after observing the moons of Jupiter through his invention of the telescope.

Just over two centuries later came the first claimed potential discovery of an exoplanet, this would be the start of an era of false detections. In 1855, captain William S. Jacob of the East India Trading company detected anomalies in the binary star 70 Ophiuchi and cautiously determined that they could be caused by an orbiting exoplanet (Jacob 1855). See (1896) made a stronger claim for an "unseen body" in the system, however these claims were dismissed shortly thereafter by Moulton (1899) due to the dynamic instability that the system would have. The original claim was eventually shown to be erroneous by Heintz (1988) due to large systematic errors in the original data. Despite the erroneous claim, it is still impressive to think that astronomers were attempting to measure anomalies of such a small magnitude at a time where data was recorded by hand and there were no computers to process data.

The first evidence of an exoplanet comes from an observation in 1917. Unbeknownst to the astronomers at the time, they had discovered indirect evidence of the existence of a planet, around what we now know to be a white dwarf. van Maanen (1917) recorded the stellar spectra of what they referred to as "two faint stars with large proper motions". In 2016, it was discovered that the photographic plates containing these spectra showed evidence of heavy elements. Heavy elements cannot exist on the surface of a star for long, they quickly fall towards the stellar core due to their weight. Today, we explain this by the deposition of material onto the stellar surface by the left over remnants of planets that would have been partially or fully destroyed after the event that created the white dwarf (Vanderburg et al. 2015). Obtaining polluted white dwarf spectra enables us to retrieve information on the interior composition of

the orbiting planets.

The mid twentieth-century saw a large number of mistakenly claimed exoplanet detections or possible detections. Publications such as those from Kaj Strand (Strand 1942; Strand 1957), Peter Van de Kamp (van de Kamp & Lippincott 1951; van de Kamp 1963), Oliver Jensen (Jensen & Ulrych 1973), Alexander Deich (Deich & Orlova 1977) and Marek Demianski (Demianski & Proszynski 1979) all hinted at the first detection of an exoplanet, but none provided robust evidence.

Even as recently as three decades ago, the existence of planets orbiting stars other than our Sun could be described with nothing more than speculation. People were certain that exoplanets existed but there was a lack of concrete evidence. There is still some ambiguity today with regards to which detection can be claimed as the first discovered exoplanet. The first observational evidence of exoplanets, came from a team that was led by A.M. Lagrange in 1983; they observed the star Beta Pictoris in the infrared and found the first planetary disk ever to be observed. Whilst not a detection of an exoplanet, it showed that material existed in a disk around another star. This was thought to be the way in which the planets in our own Solar System were created and therefore could be behind the creation of planetary systems around other stars.

In 1988, the first tentative report of a detected exoplanet was made around γ Cephei A (Campbell, Walker & Yang 1988) using the radial velocity (RV) method (section 1.2.1). However, shortly after publication, the system was studied by Walker et al. (1992) who observed stellar activity with a very similar period to that of the proposed companion planet. They concluded that the previous signal was due to the activity of the star, not a companion planet. It was only in 2003, where Hatzes et al. (2003) used 21 years of RV data to confirm that a planet did, in fact, exist around γ Cephei A.

The most widely accepted detection of the first exoplanets to be discovered was made by Wolszczan & Frail (1992). They discovered two rocky planets that orbited the pulsar PSR B1257+12 by looking at the differences in arrival times of radio pulses from

the host star. Whilst this was the first solid detection of a planet outside of our Solar System, the environment around a neutron star is very different to the one around our Sun. It is likely that these planets were not originally orbiting the star in their current form before its neutron star phase. It is thought that they are the stripped cores of larger gas giants that have survived the supernova which created the neutron star or perhaps secondary planets formed from the material remnants.

The first detection of an exoplanet around a Sun-like star came from Mayor & Queloz (1995). They discovered a planetary companion to the star 51 Pegasi using the RV method (section 1.2.1). However, what was unexpected was that the mass of the discovered body was around the same as that of Jupiter but the planet was only around eight million kilometres from the star, far inside the orbit of Mercury around our Sun. A planet of this size on such an orbit was unexpected. Planetary formation theories at the time, and even those of today, do not explain how a planet like this can form in situ; there is not enough mass so close to the star and temperatures are far too high to allow rocky planetesimals to form. The explanation that Mayor & Queloz (1995) put forward was the the planet has migrated to its location by orbital evolution. However, this raised questions about how a mechanism such as this can occur. We now know this newly discovered class of planets as hot Jupiters. They are defined as having a mass that is similar to that of Jupiter, but too low to start deuterium burning ($\lesssim 13\ M_{\rm Jup}$; Spiegel, Burrows & Milsom 2011) and an orbit with a time period less than 10 days. They appear to be relatively commonplace and we have found approximately 170 to date [1]. The confirmation of the existence of a planet outside of our Solar System was a significant milestone in the history of exoplanet detection and it helped pave the way for future detections.

The next major development was the first detection of a planet using the transit method (Section 1.2.2) by Charbonneau et al. (2000). They observed a transit of HD 209458b, which was already known from radial velocity observations, across its host star. Transit events are able to provide us with a wealth of information (again,

[1] Data taken from https://exoplanetarchive.ipac.caltech.edu on 22 May 2018

please see Section 1.2.2 for the full details) but the main parameters they are able to provide is the inclination angle of the orbit with our line of sight and the radius of the planet. Therefore, if it is also possible to observe radial velocity measurements for a transiting system, then we are able to determine both the mass and radius of the exoplanet. This allows us to infer its bulk density and place constraints on its internal composition. This was followed shortly by the first detection an exoplanet's atmosphere. Charbonneau et al. (2002) observed the transmission of light from the host star through the atmosphere of HD 209458b and as a result were able to detect sodium. In a space of a few decades we went from speculating about the existence of exoplanets to being able to measure their physical properties and compositions.

Despite being theorised about for centuries the field is still in its infancy, exoplanets are very much still in the public interest today. Whether it is the Solar System analogue, TRAPPIST-1, that harbours potentially habitable planets (Gillon et al. 2016; de Wit et al. 2018; Grimm et al. 2018) or the Earth-sized planet, Proxima b, that exists within the habitable zone of the star nearest to the Sun (Anglada-Escudé et al. 2016; Ribas et al. 2016) exoplanets frequently make international headlines. There have been a vast amount of discoveries over the past two decades thanks in part to dedicated missions such as the Wide Angle Search for Planets (WASP - Pollacco et al. 2006) and Kepler (Koch et al. 2010b). It has been revealed that not only do exoplanets appear to be common, but they are also very diverse, spanning a wide range of masses, radii and orbits. With 3726 planets discovered to date[2] we are within the golden age of exoplanet astronomy. The field is perhaps spurred onward by the vision of finding an Earth-like analogue with the potential to support life.

Over the past twenty years there have been some major and even surprising discoveries, such as the first multi-planet system around a star other than our Sun (Paul Butler et al. 1999), a direct image taken of an exoplanet (Kalas et al. 2008), an exoplanet with a density that implies it is rocky (Charpinet et al. 2011), an Earth-size planet withing the habitable zone of another star (Quintana et al. 2014), an Earth-like

[2]https://exoplanetarchive.ipac.caltech.edu/ - 22 May 2018

planet with a 1.6 $R_{\oplus}$ on a 385 day orbit around a G2 type star (Jenkins et al. 2015 - although a study from Mullally et al. 2018 may cast doubt on the validity of the confirmation of the signal as a planet) and more recently the detection of extragalactic planets outside of our own galaxy (Dai & Guerras 2018).

With all of the progress that has been made so far, there are still many questions that we do not have answers for. It appears that the formation of planets is common, but we currently lack the understanding of how the process works. To improve our understanding of how these systems are created and change over time it is necessary to not only increase our sample size through the discovery of new exoplanets, but also to fully characterise and understand the systems that have already been discovered. Observations like these are not easy and often push telescopes to the limit of what is currently observable. They can sometimes be hampered by systematic noise. This thesis looks at these kinds of observations. It focuses on follow-up observations and the characterisation of exoplanets that have already been discovered. It is also important to ensure that the underlying work behind these observations is reliable enough to ensure that inferences made about these systems are correct. The remainder of this chapter will cover the methods by which we detect and analyse these planets as well as the properties of a giant class of planet known as hot Jupiters.

1.2 Detection Methods

Exoplanets are usually small and faint in comparison to their host stars, which makes them challenging to detect through direct observation. Instead, indirect methods are often used to discover and analyse planets outside of our Solar System. There are a number of methods by which this can be done. The remainder of this section will discuss the main methods.

Radial velocity (RV) and Astrometry work by using the gravitational effects that a planet has on its host star, which causes it to wobble. This wobble is detectable through the shift of its spectroscopic lines (RV) or by its physical motion in the sky

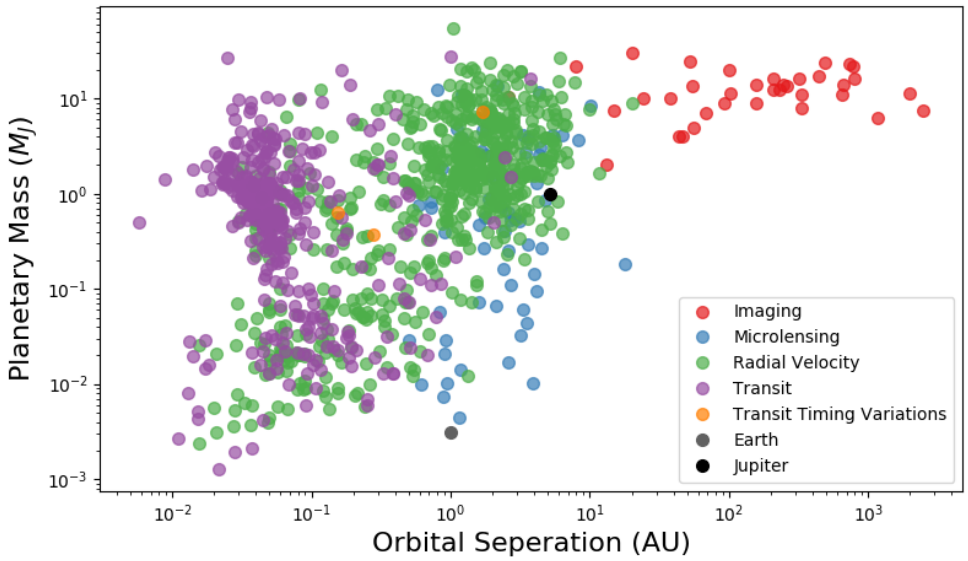

Figure 1.1: A Plot of mass against orbital separation for discovered planets to date, where only planets that have had both parameters calculated are shown. The purple points represent planets discovered by the transit method, green points indicate those discovered by the radial velocity technique, red points show those discovered by direct imaging, blue show micro-lensing discoveries and yellow points represent planets found using timing techniques. Earth and Jupiter are represented by the grey and black points respectively. Data from `https://exoplanetarchive.ipac.caltech.edu` - 21/05/18

(astrometry). Transits occur when a planet passes between us and its host star from our perspective. The amount of light that it blocks is measurable and allows us to calculate a range of parameters. Planets detected via the transit timing method are discovered based upon the varying timing of these eclipses, which vary due to gravitational interactions of unseen planets. Microlensing discoveries occur when a star with a planet passes over a background source which amplifies the amount of light we receive by acting as a lens due to general relativity. Finally, direct imaging involves taking images that directly show the existence of a planet.

These different detection methods are sensitive to certain populations of exoplanets meaning that each method has certain biases towards types of planets. Figure

1.1 shows an example of this effect. Radial velocity measurements favour very large planets with close orbits. This is because these factors cause the gravitational perturbation of the host star to be largest and therefore easier to detect. Direct imaging methods are biased toward large planets that orbit at large distances. Large planets are brighter and therefore easier to detect and a high orbital separation allows the two objects to be spatially resolved more easily. The transit method is sensitive to planets with larger radii on smaller orbits. Larger radii cause more of the host star's light to be blocked, resulting in a more prominent transit depth. For a planet to be discovered, multiple transits have to be detected. For planets that orbit closely to their star, this can happen in a matter of days; whereas for planets such as Earth it would take years to confirm more than one transit.

It is therefore important to note that the population statistics that are revealed as more planets are detected, may reveal more about the detection method itself, rather than the true distribution of exoplanets. Any conclusions drawn in general should cautiously take this into account. The rest of this section will now describe the main detection methods in more detail.

1.2.1 Radial Velocity

Radial velocity (RV) measurements are possible due to the gravitational effect an orbiting exoplanet has on its host star. For an example system with a single planet such as the one presented in figure 1.2, both the star and the planet will orbit a common centre of mass, or barycentre. Through spectroscopic observations of the star, a Doppler shift will be seen in stellar spectral lines due to the periodic red and blue shifting of light as the star orbits this point. This Doppler shift can then be measured using equation 1.1, to create a radial velocity curve like the one shown in figure 1.3.

$$V_r = c\frac{\lambda - \lambda_0}{\lambda} \tag{1.1}$$

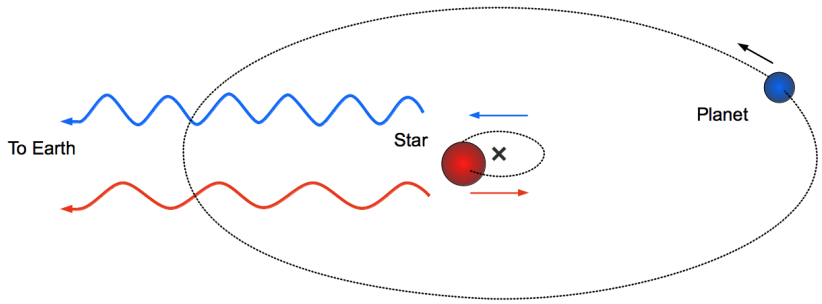

Figure 1.2: A representation of the basic principles behind the radial velocity method. Both the star and planet orbit a barycentre (x). As the star orbits this point, the light that is received by Earth is periodically blue and red shifted. Source: `https://commons.wikimedia.org/wiki/File:Radial_Velocity_Exoplanet_Detection.png`

Where V_r is the radial velocity, λ is the measured wavelength, λ_0 is the rest wavelength and c is the speed of light. The radial velocity curve allows us to measure parameters of the system directly. The shape of the curve provides information on the eccentricity of the system. A circular orbit will produce a purely sinusoidal curve and an eccentric orbit producing a more sawtooth-like curve due to the varying orbital speed of the star induced by the planet. An example of a circular and an eccentric curve are shown in figure 1.3. The period P_{orb} of the planets orbit can be directly obtained from the period of the curve.

An estimate of the minimum mass of the planet can also be calculated, assuming that the stellar mass has been measured separately, for instance estimated from its spectral type and luminosity through evolutionary models (Delfosse et al. 2000) or measured more accurately if the star is part of a binary system where the orbits can be fully resolved (Karttunen et al. 1987). The radial velocity semi amplitude (K_*) is directly measurable from the semi amplitude of the radial velocity curve. We can obtain an expression for K_* from the geometry of the system by using Kepler's second and third laws as well as the laws of conservation of momentum (Perryman 2011). The expression is shown in equation 1.2 (Cumming, Marcy & Butler 1999, Equation 1).

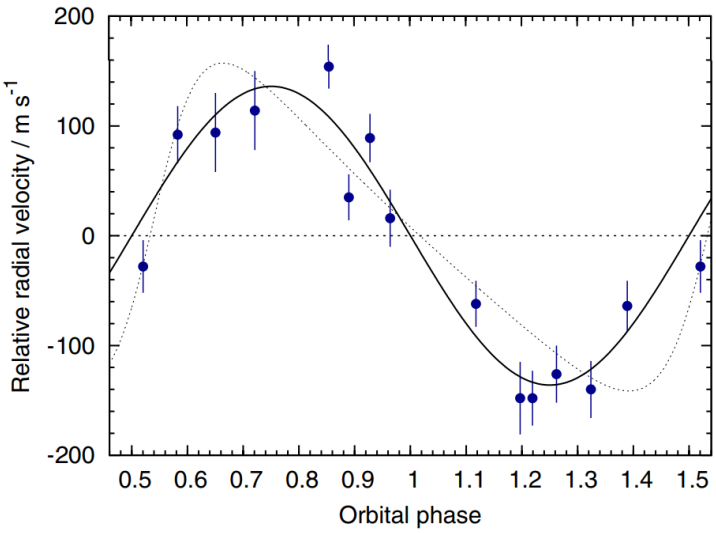

Figure 1.3: An example of a radial velocity curve for WASP-48b (Enoch et al. 2011). Radial velocity is plotted as a function of orbital phase. The blue points represent the measured radial velocities, the black solid line is the best-fitting circular radial velocity model and the dotted line shows a model with an eccentric solution.

$$K_* = \left(\frac{2\pi G}{P_{orb}}\right)^{\frac{1}{3}} \frac{M_p \sin i}{(M_p + M_*)^{\frac{2}{3}}} \left(1 - e^2\right)^{-\frac{1}{2}} \tag{1.2}$$

Where G is the gravitational constant M_p is the mass of the planet and M_* is the stellar mass, e is the eccentricity of the orbit and i is the angle of inclination between the orbital plane and our line of sight. Under the assumption that the stellar mass is significantly greater than the mass of the planet (i.e. $(M_p + M_*)^{\frac{2}{3}} \approx M_*^{\frac{2}{3}}$) we can re-arrange equation 1.2 to get an expression for the mass of the planet:

$$M_p \sin i \approx \left(\frac{P_{orb}}{2\pi G}\right)^{\frac{1}{3}} K_* M_*^{\frac{2}{3}} \left(1 - e^2\right)^{\frac{1}{2}} \tag{1.3}$$

The equations that we can derive have a dependence on the inclination angle i. It is therefore not possible to calculate the mass of the orbiting exoplanet using standard radial velocity measurements alone. However, the inclination angle to the orbital plane can be calculated using the transit method (section 1.2.2), meaning that the mass of

planet can be determined if both methods are used for a given system. In some cases, where absorption or emission lines are detectable from the atmosphere of the orbiting planet, it is possible to measure the radial velocity of the planet itself (Snellen et al. 2010; Brogi et al. 2012). This allows the masses of the two objects to be calculated directly using Newton's law of gravity.

From equation 1.2 we can see that radial velocity signal is heavily dependent on the planet-to-star mass ratio. A system where the planetary mass is large compared to the stellar mass will produce a larger signal. It also has a dependence on the orbital period of the planet. Although this is to a lesser extent due to the cubic root in the expression, the dependence is slightly more significant than it would appear. A planet with a short orbital period means that the full orbit can be measured more often in the same given length of time than a planet with a large period. This means that the overall signal-to-noise ratio will increase and the orbit can be constrained with a higher precision. The radial velocity method is most sensitive to large planets on short orbits around their host stars making it an ideal method of detecting hot Jupiters.

Echelle spectrographs, such as the one used on the High Accuracy Radial velocity Planet Searcher (HARPS), are commonly used for radial velocity measurements and are able to achieve precisions of approximately 0.3 ms^{-1}. The size of radial velocity semi amplitudes of planets detected to date vary from around 0.35 ms^{-1} for Super-Earths (Feng et al. 2017) up to approximately 1813 ms^{-1} for brown dwarfs (Udry et al. 2002). To put that in perspective, an Earth-like planet, in an Earth-like orbit, around a Sun-like star will produce a radial velocity signal of 0.1 ms^{-1} (Seager & Deming 2010a). Whilst our current instruments and methods cannot quite reach that limit, it is feasible that we could detect an Earth-sized planet in the habitable zone around another star. For example, a 0.1 $M_{\odot}$ M-Dwarf with an Earth mass planet orbiting within 0.1 AU will produce a radial velocity of 0.9 ms^{-1} (Seager & Deming 2010a). However, getting the signal-to-noise ratio high enough for such an observation is difficult due to the low brightness of the example host star.

There are a number of limitations to the radial velocity method. It is only

sensitive to stars that host planets with the orbital plane aligned well with our line-of-sight. Systems with a higher inclination angle may not be detected at all, although systems that are perpendicular to our line-of-sight can be well studied by astrometric methods (section 1.2.3). RV measurements also require many, well-defined spectral lines as the signal strength of each is fairly low. This becomes an issue when trying to observe massive stars from the ground, due to the lack of these lines in wavelengths associated with observable windows of our atmosphere. Early main sequence stars are also not well suited to RV measurements as they rotate at a faster speed and again have few well-defined spectral lines (Ortiz et al. 2016). It is difficult to measure the radial velocities of any rapidly rotating star as the high speeds will cause broadening of spectral lines, increasing the uncertainty in their position beyond the precision that is required. As well as this, the changing spectra of variable stars can dwarf the signal produced by an orbiting planet, making measurements almost impossible. It is also possible that astrophysical noise may be a limiting factor in detecting an Earth-size exoplanet due to effects such as granulation, stellar oscillations as well as short and long term variability due to magnetic interactions (Dumusque 2016).

One advantage of this method however, is that it doesn't rely on the low transit probability (section 1.2.2); rather than having to wait for a transit event, radial velocities can be recorded at any point in the star's orbit. Radial velocity surveys also have the advantage of being in operation for two decades, meaning that they are able to discover exoplanets with much greater periods, for example HD 24040b, a 4 M_{Jup} planet with a 10 year orbit around its host star (Boisse et al. 2012).

There have been 672 planets discovered by the radial velocity method to date[3] (statistics gathered on 22 May 2018). It is responsible for a large majority of the exoplanets discovered, second only to the transit method. As well as being used to discover the first exoplanet around a Sun-like star (Mayor & Queloz 1995) this method has been used to identify planets around multiple star systems (Patience et al. 2002), planets with eccentric orbits (Cochran et al. 1997) and more recently surveys have

[3]Nasa Exoplanet Archive - https://exoplanetarchive.ipac.caltech.edu/index.html

been finding Earth-sized exoplanets around M-dwarf stars, such as Ross 128b (Bonfils et al. 2017). The future also looks promising, with the TESS (Ricker et al. 2014) and PLATO (Rauer et al. 2014) space missions set to provide a wealth of exoplanet candidates bright enough for follow-up study with the radial velocity method.

1.2.1.1 The Rossiter McLaughlin Effect

The Rossiter-McLaughlin (RM) effect occurs during a transit (section 1.2.2), where an exoplanet passes in front of its host star from our perspective. As the planet transits the star it partially blocks the blue or red shifted light which is produced by the rotating star (figure 1.4). This causes an apparent shift in the stellar radial velocity measurements and produce an anomaly that can be seen in the RV curve (e.g. figure 1.5). The shape of the resulting anomaly allows the projected stellar rotation velocity ($v \sin i_*$) to be measured, as well as the projected angle between the star's equatorial plane and the orbital plane of the planet which is known as the spin-orbit angle or obliquity (λ). The orbital obliquity of a system may give us insight into its history. Particularly in the case of hot Jupiters, where the formation and possible migration of these planets is poorly understood. For example, the young age and well-aligned orbit

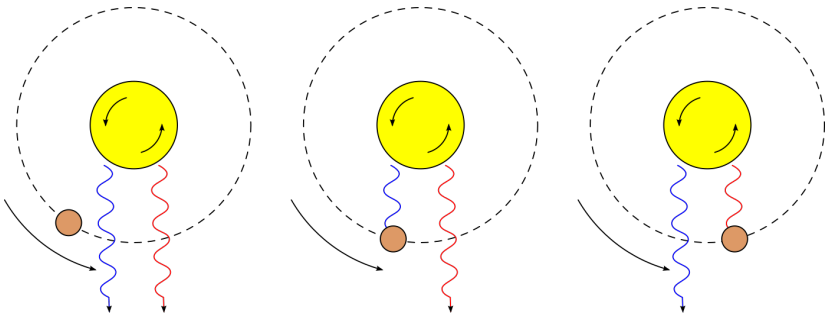

Figure 1.4: A simplified example of how the Rossiter McLaughlin effect works. As the planet (brown) passes in front of its host star (yellow) from the perspective of the observer (the bottom of the image) it will partially block either blue or red shifted light depending on its orbital position. Source: `https://commons.wikimedia.org/wiki/File:Rossiter-McLaughlin_effect.png`

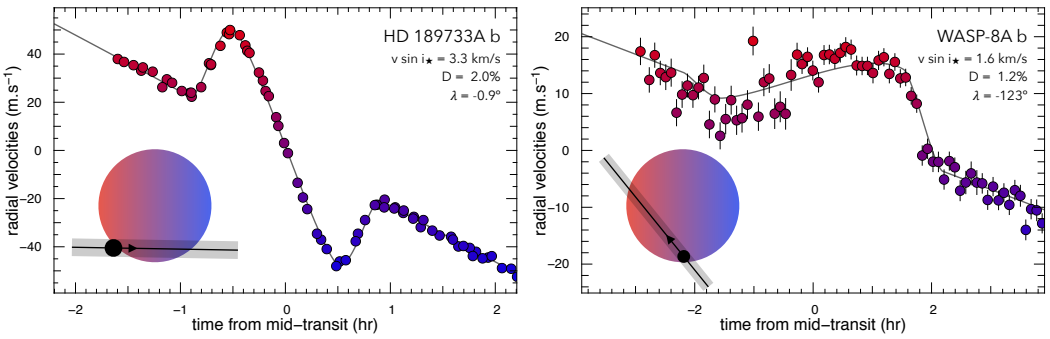

Figure 1.5: An example of radial velocity anomalies (as described in the text) caused by the Rossiter-McLaughlin effect for two stars, HD 189733A b (left) and WASP-8A b (right) using data from the HARPS spectrograph. The data points are coloured with respect to whether light being blocked from the star is blue or red shifted and the best fitting model is represented by the black line. A representation of the orbits is shown in the lower left hand corner of each figure. For HD 189733A b the orbit is well aligned, so both the red and blue shifted parts of the RM effect are seen. For WASP-8A b however, the orbit is misaligned and so only the red shifted part of the effect is clearly visible in the data. The figure was taken from Triaud (2017b)

.

of the WASP-84b system implies that it migrated to its current position through the disk as opposed to high-eccentricity migration (Anderson et al. 2015c).

The RM effect was first measured for HD 209458b (Queloz et al. 2000) which was based upon the methods of Rossiter (1924) and McLaughlin (1924) which was previously used for binary stars. Since then, measuring the RM effect has become commonplace, at least for hot Jupiters, with 125 systems being measured to date[4]. One surprising result from these measurements is that there appears to be a wide range of obliquity angles. In fact, almost a third of hot Jupiters appear to have misaligned orbits (Triaud 2017b) and there have been a few planets with retrograde orbits (Anderson et al. 2010; Esposito et al. 2014). Such diversity could indicate that there is more than one migration pathway behind the existence of hot Jupiters. Future instruments such as ESPRESSO, the successor to HARPS (Pepe et al. 2014) will be able to measure

[4]TEPCAT- http://www.astro.keele.ac.uk/jkt/tepcat/obliquity.html - 08/05/18

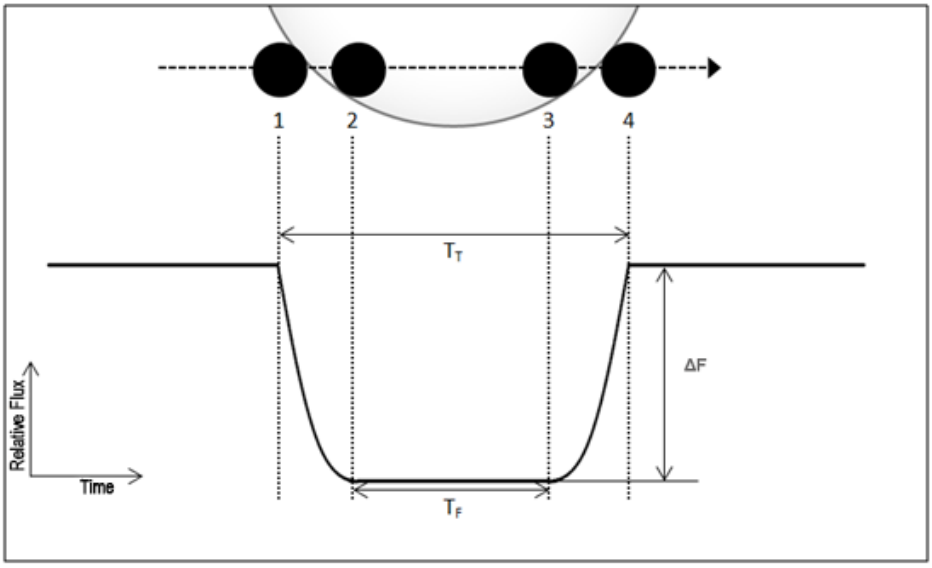

Figure 1.6: A diagram of a planetary transit. The solid black line represents the dip in light received from the star as the planet (solid black) passes in front of its host star (black outline). Points 1-4 represent the start and end of ingress and then egress, respectively. T_T represents the total transit duration, T_F is the time between the end of ingress and the start of egress, ΔF is the ratio between the received flux inside and outside of transit.

this effect for super-Earths and provide even more insight into the properties of these systems.

1.2.2 Transit Method

A transit occurs when a planet passes between its host star and our line of sight. It will partially block the light we receive from the star causing a temporary, apparent decrease in its brightness, as shown in figures 1.6 and 1.7. The amount of flux blocked is usually very small in comparison to the total light received from the star, for example, an Earth-like planet around a Sun-like star causes a 0.01 % decrease in brightness (Ollivier et al. 2009). That said, some planets can produce transit depths on the order of a few percent, such as the 3.23% dip of HATS-6 b (Hartman et al. 2015).

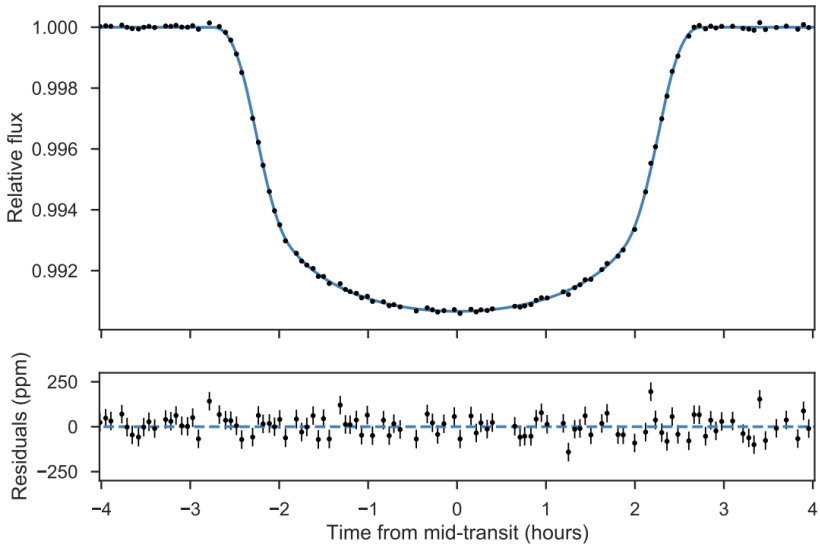

Figure 1.7: An example of a transit lightcurve for EPIC247098361b where relative flux is plotted as a function of time (top). The bottom panel shows the residuals around the best fitting model which is shown in blue. Figure taken from Brahm et al. (2018)

.

Thanks to missions such as WASP (Street et al. 2003), Kepler (Borucki et al. 2010) and its successor K2 (Howell et al. 2014), there have been 2926[5] planets discovered by the transit method since the initial detection of HD 209458b by Charbonneau et al. (2000).

Ingress and egress, shown by points 1-2 and 3-4 respectively in figure 1.6, describe the parts of the transit where the planet has not yet fully moved onto the stellar disk from our perspective. The amount of light blocked in these regions depends on how much of the planet covers the stellar disk. However, we tend to see a curve rather than a linear dip, as stars do not have a constant luminosity across their surface. Instead, the edges of a star will appear darker due to an effect known as limb darkening (Espinoza & Jordán 2015). Limb darkening occurs mainly due to changes in optical depth. Light

[5]https://exoplanetarchive.ipac.caltech.edu - accessed on 22 May 2018

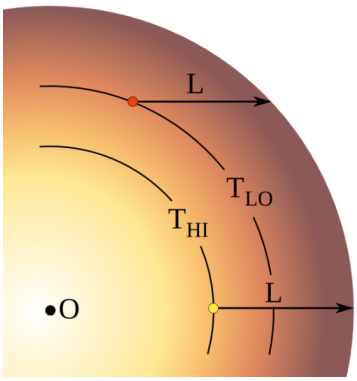

Figure 1.8: Limb darkening of a star where L is equal to an optical depth of one. Towards the centre of the star (O) from our perspective, which is to the right of the figure, an optical depth of one means that we see light from a higher temperature region (T_{HI}). Towards the edge of the star, the same optical depth allows light that is produced nearer to the surface, and hence cooler and fainter (T_{LO}), to be produced. This causes the edges or limbs of the star to appear darker than the centre. Source: `https://www.paulanthonywilson.com`

escapes from the stellar surface when the density is sufficiently low enough to have an optical depth equal to one. Near the centre of a star, an optical depth of one corresponds to a region deep in the photosphere, compared to a much shallower region when we view the edges of a star (see figure 1.8). This means that we can see light escaping from a region that is much hotter near the centre of the star, so it appears brighter.

Transits are very useful, the lightcurve alone is able to provide us with a wealth of information about the system. There are four observables that can be obtained directly from the transit lightcurve: The period of the system (P) can be obtained if two or more (consecutive) transits are observed as it is simply the time difference between every transit event. The total transit duration T_T and the time between the end of ingress and the start of egress T_F as well as the transit depth ΔF can all be obtained from the shape of the lightcurve (figure 1.6). Equations 1.4 to 1.7 show four useful parameters that can be derived directly from these observables. For the full derivation of these, please see Seager & Mallén-Ornelas (2003). These expressions rely on four

main assumptions: the stellar mass (M_*) is much greater than the planetary mass (M_p), the orbit of the exoplanet follows a circular path, the mass-radius relationship (Demircan & Kahraman 1991) of the star is known and the planet must orbit a single star only.

$$\frac{R_p}{R_*} = \sqrt{\Delta F} \tag{1.4}$$

$$b \equiv \frac{a}{R_*}\cos i = \left[\frac{(1-\sqrt{\Delta F})^2 - \frac{\sin^2(t_F\pi/P)}{\sin^2(t_T\pi\ /P)}(1+\sqrt{\Delta F})^2}{1-\frac{\sin^2(t_F\pi/P)}{\sin^2\left(\frac{t_T\pi}{P}\right)}}\right]^{1/2} \tag{1.5}$$

$$\frac{a}{R_*} = \left[\frac{(1+\sqrt{\Delta F})^2 - b^2\left[1-\sin^2(\frac{t_T\pi}{P})\right]}{\sin^2(\frac{t_T\pi}{P})}\right]^{1/2}; \tag{1.6}$$

$$\rho_* \equiv \frac{M_*}{R_*^3} = \left[\frac{4\pi^2}{P^2G}\right]\left[\frac{(1+\sqrt{\Delta F})^2 - b^2(1-\sin^2[\frac{t_T\pi}{P}])}{\sin^2(\frac{t_T\pi}{P})}\right]^{3/2}. \tag{1.7}$$

The transit depth gives us the planet-star radius ratio through the use of equation 1.4, where R_p is the radius of the planet and R_* is the stellar radius. Using this relation with information from the transit shape, we are then able to derive the impact parameter in equation 1.5, which describes the projected distance between the planetary and stellar disk centres when they are aligned. Another useful parameter is the ratio a/R_* given in equation 1.6, where a is the semi-major axis of the planet's orbit and R_* is the stellar radius. More interestingly however, the stellar density ρ_* can be obtained directly from equation 1.6, where G is the gravitational constant, with the use of Kepler's third law (equation 1.10) and under assumptions listed above.

From these derived parameters, it is possible to obtain five physical parameters: the stellar mass, the stellar radius, the orbital inclination angle (i), the semi-major axis (a) and the radius of the planet (R_p). Again, see Seager & Mallén-Ornelas (2003) for the full derivation, but using the above equations, we are able to obtain equations 1.8 to 1.11. Firstly, the stellar mass can be determined from equation 1.7 with the stellar mass-radius relation to obtain equation 1.8, where $M_\odot$ is the solar mass, $\rho_\odot$ is

the average solar density and k and x are coefficients based on the type of star (see Ryden, Peterson & Demianski 2010).

$$\frac{M_*}{M_\odot} = \left[k^3 \frac{\rho_*}{\rho_\odot}\right]^{\frac{1}{1-3x}}. \tag{1.8}$$

Once the stellar mass has been determined, it can be introduced into equation 1.9 to obtain a value for the stellar radius:

$$\frac{R_*}{R_\odot} = k\left(\frac{M_*}{M_\odot}\right)^x = \left[k^{1/x}\frac{\rho_*}{\rho_\odot}\right]^{\frac{x}{(1-3x)}}; \tag{1.9}$$

where $R_\odot$ is the solar radius. The stellar radius can then be used with the transit depth in equation 1.4 to calculate the radius of the planet. The stellar mass can also be used with Kepler's third law and the period of the orbiting planet to calculate the semi-major axis through equation 1.10.

$$a = \left(\frac{P^2 G M_*}{4\pi^2}\right)^{1/3} \tag{1.10}$$

Once the stellar radius and the semi-major axis have been found, it is possible to use the equivalence in equation 1.5 along with the value of the impact parameter to calculate the orbital inclination angle:

$$i = cos^{-1}\left(\frac{bR_*}{a}\right) \tag{1.11}$$

One important consequence of now being able to calculate the inclination angle is that, if it is also possible to obtain radial velocity measurements for the system (section 1.2.1), then the degeneracy mentioned with regards to equation 1.3 can now be broken. This means that it is also possible to measure the mass of the planet. Knowing both the mass and the radius of an orbiting exoplanet allows us to estimate its bulk density. The bulk density of a planet is able to inform us of its interior composition, for example the dense, possibly carbon-rich super-Earth 55 Cancri e (Madhusudhan, Lee & Mousis 2012). Using this density, we can classify the planet in terms of whether it is gaseous or rocky in nature and determine if it is likely to have a significant atmosphere.

The issue with the transit method is that there is a low probability of a transit event occurring. To observe a transit from Earth, the orbital plane of the system has to be almost identically aligned with that of our line of sight. A small deviation from this and we may not be able to observe a transit at all. This is especially an issue for planets orbiting at a large distance or those that have a small radius. This can be seen through equation 1.12, which shows the probability of observing a transit (p_T).

$$p_T = \frac{R_*}{P^{2/3}} \left(\frac{4\pi^2}{GM_*} \right)^{1/3} \tag{1.12}$$

An additional problem is that a transit is an event that lasts for a short amount of time, sometimes just a few hours, such as the 3.59 hour transit of Kepler-18c (Holczer et al. 2016). They also only occur periodically, which for Earth-like planets means that a transit will occur once over the order of years. Preferably, multiple transits should be observed to help confirm the planetary nature of the object. These two factors mean that ideally, constant observation of a star is required for a long period of time, in order to detect a transit.

1.2.2.1 Transit Surveys

Continuous observations can be challenging, especially from the ground due to the rotational period of the Earth. Space missions are more plausible but are very costly. Despite these drawbacks, the last two decades have seen a wealth of successful transiting planet surveys. WASP and the Hungarian-made Automated Telescope Network (HATNet) have been the two most arguably successful ground based surveys to date, with 134[6] and 61[7] discoveries respectively.

The WASP survey comprises of two robotic telescopes; one at Roque de los Muchachos Observatory in La Palma which searches the Northern hemisphere and one at the South African Astronomical Observatory located in Sutherland, South Africa

[6]https://exoplanetarchive.ipac.caltech.edu/ - 22 May 2018
[7]https://hatnet.org/ - 22 May 2018

which searches the Southern Hemisphere. Each site consists of eight wide-angle cameras that give each telescope a 480 square degree field of view. Photometric measurements of stars are recorded with a cadence of one minute. Since its initial discovery of WASP-1b and WASP-2b (Collier Cameron et al. 2007a), it has made an abundance of discoveries, which it still consistently provides (e.g. Hellier et al. 2018).

HATNet (Bakos et al. 2004) is comprised of seven small 200mm lens telescopes, with five located in the Fred Lawrence Whipple observatory in Arizona and two located at the Mauna Kea observatory in Hawaii, both in the United States of America. The large distance between each of the telescopes means that they can monitor the sky for almost twenty four hours a day. It has been in operation since 2003 with its latest discovery being the low density, hot-Saturn HAT-P-67b (Zhou et al. 2017).

The Hungarian-made Automated Telescope Network-South (HATSouth) is the southern equivalent of the HATNet project (Bakos et al. 2013). It consists of six 180mm lens telescopes located across Africa, Australia and South America. Again, the large longitudinal separation of the telescope allows near 24 hour monitoring. The survey has discovered 48 planets to date[8].

The Kilodegree Extremely Little Telescope (KELT) is another ground-based transiting exoplanet survey (Pepper et al. 2007). Its goal is to search for transiting planets around stars with apparent V magnitudes of 8 to 10. There are two telescopes; KELT-North located in Arizona, USA and KELT-South located in Sutherland, South Africa. Similar to other transit surveys, KELT has a wide, 676 square degree field of view and uses lenses with a 4.2cm aperture. KELT has made 20 discoveries to date[9].

The MEarth project is a survey that aims to detect planets in the habitable zone of nearby M-dwarf stars (Irwin et al. 2009). Due to the small radii of M-dwarf stars, the transit depth can be quite large, meaning the survey has the potential to find ideal candidates for follow-up observations. The project consists of two 0.4m telescopes, one in the Northern hemisphere located in Arizona, USA and one in Cerro Tololo in La

[8]https://hatsouth.org/ - 22 May 2018
[9]Data taken from https://exoplanetarchive.ipac.caltech.edu on 22 May 2018

Serena, Chile that covers the Southern hemisphere. MEarth was responsible for the discovery of the nearby rocky super-Earth LHS 1140b (Dittmann et al. 2017).

Also probing bright stars in the sky for planets is the The Multi-site All-Sky CAmeRA (MASCARA), with the ability to observe stars down to a V magnitude of 8.4 (Talens et al. 2017b). Similar to other surveys, it consists of a northern and southern counterpart with two stations located in La Palma in Spain and La Silla observatory in Chile. It has only been in operation since July 2017, and has made one detection so far: MASCARA-1b, which is a hot Jupiter orbiting a bright 8.3 V-magnitude star (Talens et al. 2017a).

Another relatively new transit survey is the Next-Generation Transit Survey (NGTS) (Wheatley et al. 2018). It is another wide-field survey that aims to discover transiting planets around bright stars. Specifically, NGTS aims to find Neptune-size and smaller exoplanets. NGTS is located at the Paranal Observatory in Chile and consists of twelve 200mm telescopes. It has two published discoveries to date; NGTS-1b, a hot Jupiter around an M-dwarf star (Bayliss et al. 2018) and NGTS-3Ab, a hot Jupiter around a binary star system (Günther et al. 2018).

The Kepler spacecraft has been prolific in the discovery of transiting exoplanets. It was launched in March 2009 with the goal of detecting Earth-like exoplanets (Koch et al. 2010a). To do this, it continuously observed around 100,000 stars in a region near to the Cygnus and Lyra constellations, which resulted in astounding success with a total of 2304 transiting planets discovered[10]. However, the original mission ended in May 2014, when two out of the four reaction wheels used to stabilise the pointing of the spacecraft failed. Since then, the K2 mission has been in operation, which uses the radiation pressure from the Sun, its thrusters and the two remaining reaction wheels to monitor stars along the ecliptic plane. The K2 mission has been just as successful, with 292 confirmed planets discovered to date with a further 480 candidate planets awaiting confirmation[11].

[10]Data taken from https://exoplanetarchive.ipac.caltech.edu on 22 May 2018
[11]https://www.nasa.gov/kepler/discoveries - 22 May 2018

1.2.2.2 Transit Timing Variations

If a single planet orbits a star it will usually do so with a fixed, predictable period, meaning the timings of the transit can be accurately predicted. However, if there are unseen companion planets also orbiting the star, then their gravitational interactions with the observed planet will cause its orbit to be perturbed. This will cause the timings of the transit to vary such as the ones shown in figure 1.9. Measuring these transit-timing variations (TTVs) allows us to detect additional planets in the system, even if they themselves do not transit the host star (Agol & Fabrycky 2017). The size of these TTVs depends on the mass of the secondary planet as well as the period and orbital separation of the two planets. The approximate timing offset for a two-planet

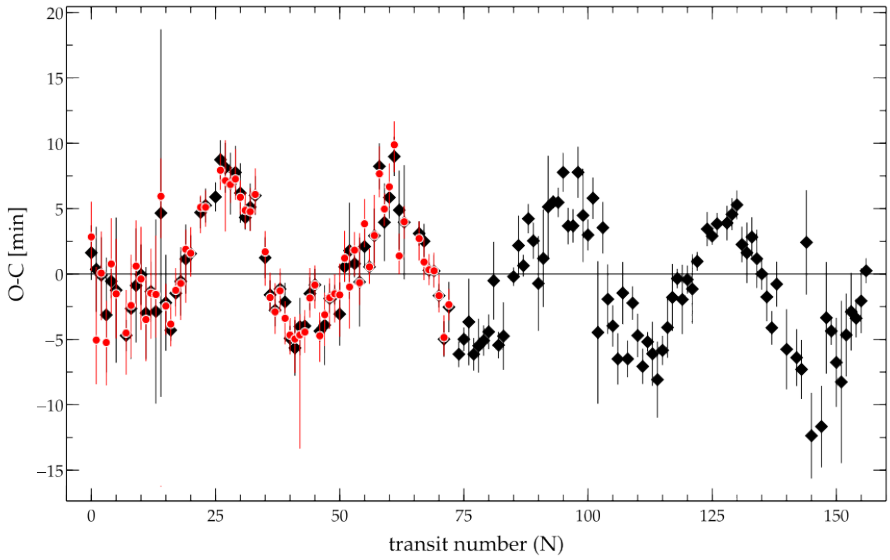

Figure 1.9: Transit timing variations observed in Kepler-19b, indicating the presence of two unseen planets, Kepler-19c and Kepler-19d. The plot shows the difference between the observed transit times and those that were expected if there were no companion planets in the system. The Y axis shows the observed transit time minus the calculated transit time (O-C). The black points are data from Malavolta et al. (2017) and the red points were taken from the original discovery of the TTVs (Ballard et al. 2011) The figure was adapted from Malavolta et al. (2017).

system is give by equation 1.13 (Holman & Murray 2005).

$$\Delta t \sim \frac{45\pi}{16}\left(\frac{M_2}{M_*}\right) P_1 \left[\frac{a_1}{a_2\left(1-e_2\right)}\right]^3 \left(1-\sqrt{2}\left[\frac{a_1}{a_2\left(1-e_2\right)}\right]^{3/2}\right)^{-2} \tag{1.13}$$

Where Δt is the timing offset, M_2 is the mass of the secondary planet, M_* is the stellar mass, a_1 and a_2 represent the semi-major axis of the transiting and secondary planet respectively and e_2 is the eccentricity of the second planet. If the second planet is also transiting then the masses of the planets can be estimated using both analytical methods and through N-body simulations (Hadden & Lithwick 2016). For example, the masses of the planets in the WASP-47 system were measured through TTVs (Becker et al. 2015).

1.2.3 Astrometry

Astrometry works using the same principles as the radial velocity technique (section 1.2.1). The star and planet will orbit a common centre of mass or barycentre. As the star orbits around this point, its position will appear to periodically shift in the night sky or 'wobble' compared to other stars. The extent of this shift can be represented by the angular semi-major axis of an ellipse that is projected on the plane of the sky (α) in equation 1.14 (Perryman 2011).

$$\alpha = \frac{M_p}{M_* + M_p} a \tag{1.14}$$

Where M_p is the planetary mass, M_* is the stellar mass and a is the semi-major axis of the planet-star orbit. Astrometry is therefore particularly sensitive to high mass planets on long orbits around their host star.

Detecting a planet using this method requires precise measurements of a stars position in the sky over time. These observations can be especially difficult from the ground due to noise introduced by the terrestrial atmosphere and as a result, no confirmed planets have been detected using this method to date. With the recent

launch of the Gaia spacecraft in 2013, it is expected that approximately 21,000 planets will be discovered using astrometry (Perryman et al. 2014).

1.2.4 Microlensing

Microlensing is a method that is capable of detecting exoplanets at great distances from Earth. It occurs as a consequence of general relativity, first proposed by Einstein (1936), where the distortion of spacetime around a massive object can act like a lens

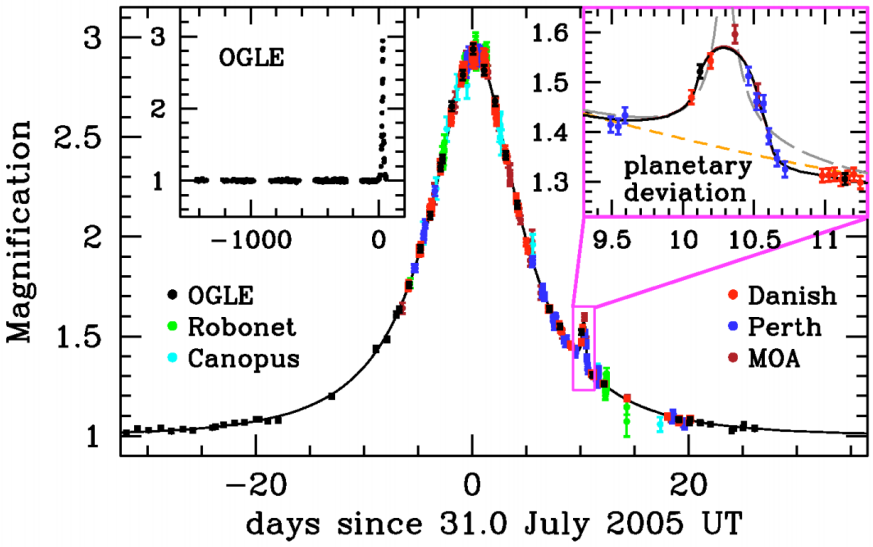

Figure 1.10: The gravitational microlensing event lightcurve for OGLE-2005-BLG-390 (Beaulieu et al. 2006). The magnification of the background source is plotted as a function of time. The best fit model is plotted as the black line and the multi-coloured points represent data taken with different instruments as indicated in the figure. The left inset shows the same lightcurve over a long period of time. Whereas the right inset shows a zoomed section of the lightcurve around the deviation caused by the presence of a planet in the system, with a single lens model shown by the orange dashed line and the best two-lens model, which provides a poor fit to the data, is shown by the grey dashed line. The figure was taken from Beaulieu et al. (2006).

and drastically magnify any background light sources (Mao & Paczynski 1991). If a star is in the foreground and it aligns with a background star from the perspective of Earth, this magnification causes a drastic increase in light received from the background star. Events like these typically occur over durations of a few days to a few weeks. However, if the star has an orbiting companion such as a planet, then it will also temporarily act like a lens and magnify the same light from the background star. This causes a further increase in the light received from the system, except this event will be much shorter, typically of the order of a few hours. An example of a lightcurve in this situation is shown in figure 1.10, where the detection of a planet is shown by the deviation a few days after peak brightness.

This method is advantageous as, in complement to the transiting and radial velocity measurements, it is more sensitive to planets that orbit at moderate-to-large distances away from their host stars. It is also capable of detecting low mass planets, even down to near-Earth mass, such as OGLE-2013-BLG-0341L B b, which has a mass just over twice that of Earth and orbits a set of binary stars at approximately 1 AU (Gould et al. 2014). Microlensing surveys such as the Optical Gravitational Lense Experiment (OGLE - Udalski et al. 1992) or the Microlensing Observations in Astrophysics (MOA - Hearnshaw et al. 2006) also have the benefit of being able to target tens of thousands of stars at much greater distances than those of other methods. There have been 60 planets discovered using this method to date [12] and there have been some major discoveries, like the detection of extragalactic planets (Dai & Guerras 2018).

The drawback of this method however, is that micro-lensing events occur rarely. It also only occurs a single time for a system, with the likelihood of an event occurring again being very low. The systems observed are also usually very faint, these two factors make any follow-up studies almost impossible. Without follow-up study, it is not possible to further constrain the parameters of the system.

[12]Data taken from https://exoplanetarchive.ipac.caltech.edu on 22 May 2018

1.2.5 Direct Imaging

Direct imaging involves imaging the planet and star system directly. The drawbacks of this method are obvious; stars are significantly brighter than their planetary companions. For most exoplanets that we are interested in, the planet-to-star flux ratio is between 10^{-5} to 10^{-10} in optical wavelengths, with the Earth around the Sun having a flux ratio of 10^{-10} (Perryman 2011). Exoplanets can be detected directly from either reflected light from their host star in the optical, or from their own thermal emission at infra-red wavelengths. Young, giant planets that are still cooling down after recently forming are favourable targets in the infra-red, as the flux ratio between them and their host star is not as small, with typical values of the order of 1-3 % (e.g. Qatar-4b - Alsubai et al. 2017). Any telescope used must have the resolution to observe both the star and planet as separate point sources, so the orbital distance between the two should be large. For this method to work, we need the ideal conditions of a bright planet, orbiting at great distance from a nearby star.

Despite the unfavourable requirements, there have been many technological advancements that have allowed direct imaging of a planet to happen. One such advancement is the use of adaptive optics. Adaptive optics work to mitigate the effects of astronomic seeing caused by turbulence in the terrestrial atmosphere. They work by either using a guide star or an artificial guide star, where a laser beam generates a source of light in the atmosphere. The motion of this guide star is recorded and a secondary, deformable mirror inside of the optical path of the telescope is controlled in such a way to counteract these effects (Males et al. 2014). Adaptive optics can be used alongside a coronagraph, which is placed over a target star so that the detector can be sensitive enough to observe any surrounding planets without becoming saturated with light from the star.

There have been 44 objects discovered by direct imaging to date, with 18 of those having a planetary mass estimated below 12 times the mass of Jupiter [13]. Imaging can

[13]Data taken from https://exoplanetarchive.ipac.caltech.edu on 22 May 2018

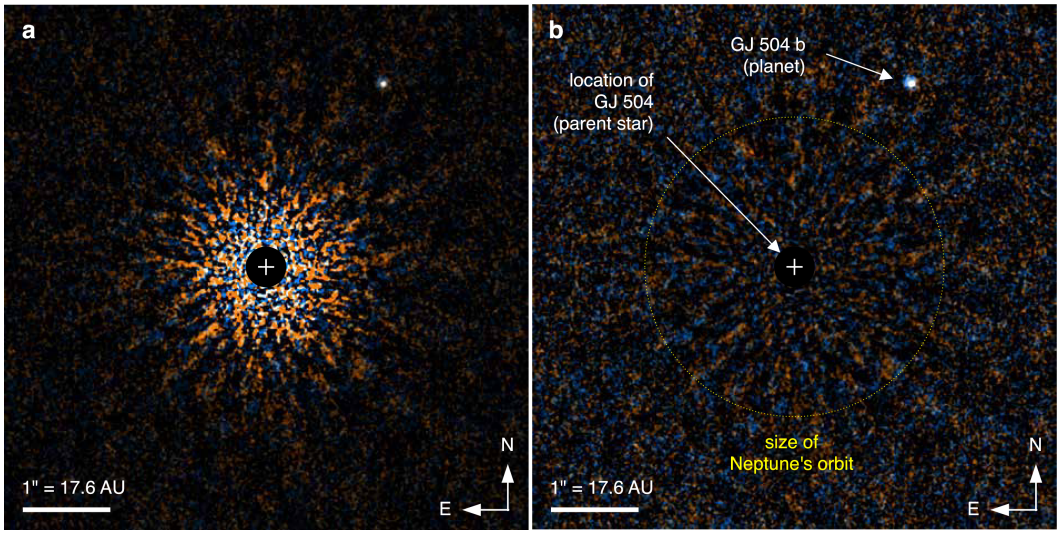

Figure 1.11: An example of direct imaging taken for the discovery of GJ 504 b. Both figures show composite images where orange represents H-band observations and blue represents J-band observations. The left panel shows the intensity of light with flux from the star being suppressed and the right panel shows the signal-to-noise ratio for the same image. The orbiting planet can clearly be seen as a white dot in the top right hand corner of each image and it is labelled in the right panel. The orbit of Neptune around our Sun is shown to give a sense of scale to the image. The figure was taken from Kuzuhara et al. (2013).

produce striking results such as those for GJ 504b, a cold Jupiter orbiting a Sun-like star, shown in figure 1.11. This method of discovery holds enormous potential. As well as confirming the planetary nature of objects discovered through indirect methods, proposed missions such as the Exo-Planet Imaging Camera and Spectrograph (EPICS) on the upcoming European Extremely Large Telescope (E-ELT) could have the ability to perform spectroscopy directly on gas giant exoplanets allowing an extremely detailed insight into their composition (Markus E. Kasper 2008).

1.3 Hot Jupiters

1.3.1 General Properties

The discovery of the first hot Jupiter was somewhat of a surprise, formation theories could not explain the existence of a planet with such a large mass, so close to its host star (Mayor & Queloz 1995). These giant, short-period planets are very different to anything found in our own Solar System. A hot Jupiter is defined as having a mass that is comparable or greater than the mass of Jupiter ($M_{\rm Jup}$) but less than $\sim 13\ M_{\rm Jup}$, the approximate limit at which deuterium burning begins (Spiegel, Burrows & Milsom 2011).

They also orbit close to their host stars, with a majority of hot Jupiters having semi-major axes within 0.1 astronomical units (AU), as shown in the top left panel of figure 1.12, which is well inside the orbit of Mercury in our own Solar System with a semi-major axis of 0.387 AU. These planets can even have extremely close orbits; one example is HATS-18b that orbits at 0.018 AU and has actually spun-up its host star (Penev et al. 2016).

These planets are dubbed 'hot' due to high temperatures that have been recorded for their atmospheres. As figure 1.12 shows, they regularly reach temperatures of around 2000 K (e.g. Talens et al. 2017a; Hellier et al. 2011b) and in extreme cases can get much hotter, such as KELT-9b that undergoes a substantial amount of ultraviolet

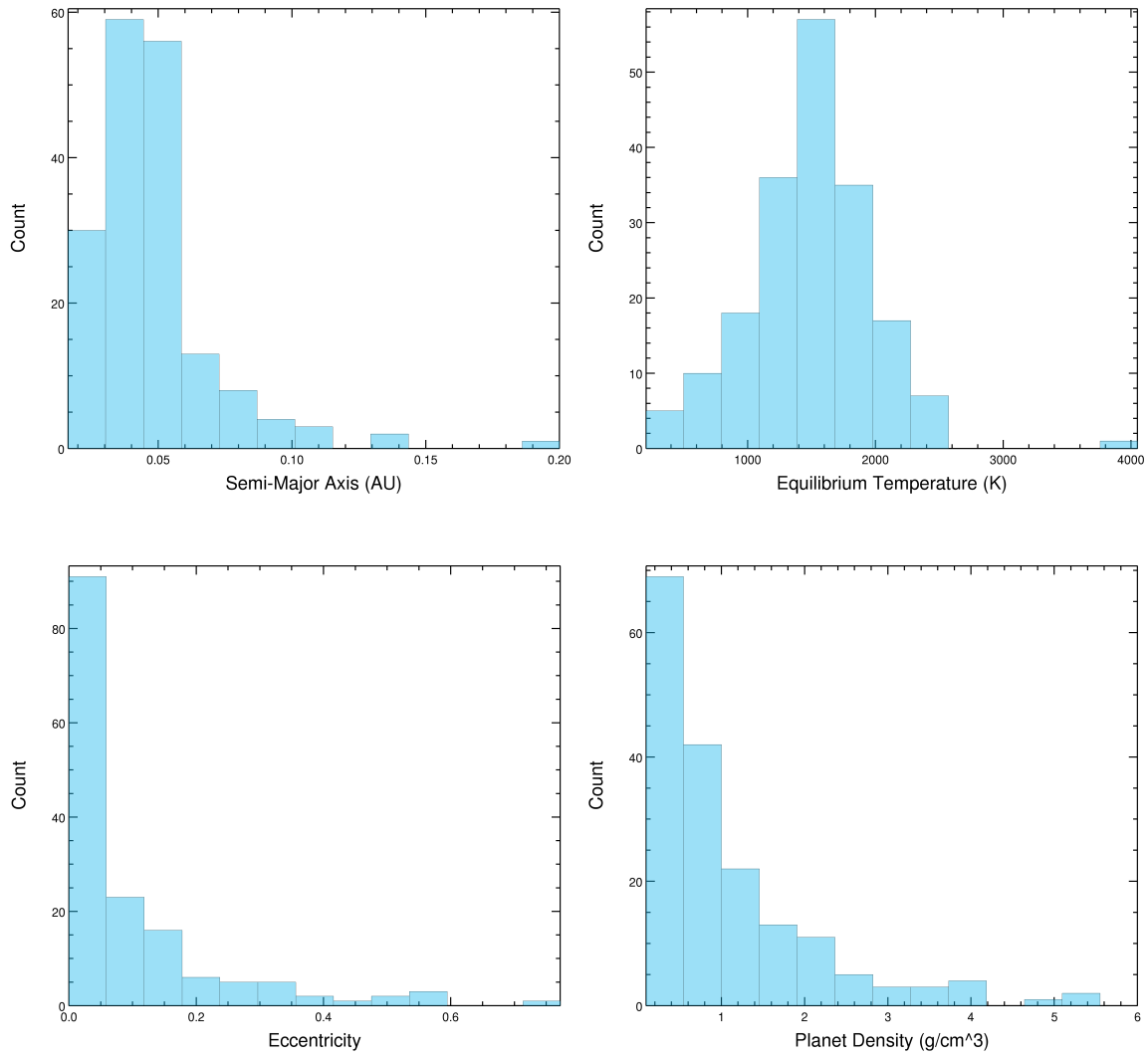

Figure 1.12: Histograms of the properties of the current known population of hot Jupiters. The top row shows how the semi-major axis (left) and equilibrium temperature (right) values are distributed and the bottom row shows the eccentricity of discovered hot Jupiters in the left plot and the density of these planets to the right. These plots show the basic properties of this class of planets. Hot Jupiters orbit close to their host stars, have high equilibrium temperatures and tend to have circular orbits and low densities. Data from `https://exoplanetarchive.ipac.caltech.edu` - 21/05/18

irradiation and reaches a temperature of 4600 K (Gaudi et al. 2017).

Most hot Jupiters appear to have low-eccentricity or circular orbits (e.g. WASP-6 b, WASP-13 b and WASP-49 b in Stassun, Collins & Gaudi 2017). Although, a non-negligible amount of hot Jupiters with large eccentricities have been found to exist (e.g. Hellier et al. 2015). It appears that their orbits become circularised over relatively short time-scales through tidal dissipation (Fabrycky & Tremaine 2007; Rodríguez & Ferraz-Mello 2010). It is also expected that these interactions will tidally lock hot Jupiters to their stars, where the planet's rotation rate synchronises to that of its orbit, meaning that the same side of the planet constantly faces the star it orbits (Perryman 2011). Having a constant day and night side can lead to large temperature differentials within the atmosphere of the planet (Showman et al. 2009) with high-speed winds predicated to circulate this heat around the planet (Miller-Ricci Kempton & Rauscher 2012).

Hot Jupiters also have relatively low densities, a majority of those seen in figure 1.12 are much less dense than the gas giant Jupiter in our Solar System, with a density of 1.326 g cm^{-3} (Gudkova & Zharkov 1999). As an extreme case, HAT-P-65b has a density of just 0.096 g cm^{-3} (Hartman et al. 2016). There appears to be some mechanism that causes these planets to have inflated radii; they are much larger than theory predicts (Burrows et al. 2000; Fortney & Hubbard 2004; Laughlin et al. 2005). Hot Jupiters should cool and contract over time, as they produce no internal source of heat. There are a number of proposed ways as to why this is not the case. Tidal forces, as described above, could be transferred as thermal energy throughout the planet (Leconte et al. 2010). The high-speed winds, mentioned above, could drive heat from stellar radiation deep down into the atmosphere (Showman & Guillot 2002). It could occur through ohmic dissipation, where energy is transferred to the planetary interior as its magnetic field interacts with atmospheric winds (Batygin & Stevenson 2010) or it could be that the composition of the planetary atmosphere is such that it allows the planet to retain its heat (Burrows et al. 2007a).

Hot Jupiter planets appear to be most common around F and G type stars, with a few examples discovered around K type stars. The occurrence rate of these planets

around these stars however, has been found to be on the order of ~ 1 % (Marcy et al. 2005; Mayor et al. 2011; Wright et al. 2012) making them a rare class of planet. For comparison, Earth-size planets have a calculated occurrence rate of ~ 20 % (Fressin et al. 2013; Petigura, Marcy & Howard 2013). There have also been a small number of discoveries around A type stars (e.g. Collier Cameron et al. 2010) and there have been three planets detected around M-dwarf stars, including the recent discovery of NGTS-1b (Bayliss et al. 2018). Despite these planets being rare, they are discovered frequently due to biases of the detection methods used, as was noted in section 1.2.2.1. Because of their properties, hot Jupiters are ideal for in-depth follow-up studies and characterisation.

1.3.2 Formation and Migration

As noted in section 1.3.1, hot Jupiters are somewhat of a problem when it comes to planetary formation theories. They are not expected to form in their current position as the temperatures would be far too high for planetesimals to form (Lin, Bodenheimer & Richardson 1996).

The core-accretion model (Perri & Cameron 1974) has been well-studied and is widely accepted for the formation of planets in our Solar System (Mordasini et al. 2008; Militzer et al. 2008; Guillot 2005). The basic principles of the model state that a newly created system will contain a protostar and a protoplanetary disk. This disk contains gas and dust from the remnants of the interstellar cloud that collapsed after the protostar was formed. Beyond the snow line, small, solid ice particles can condense from compounds such as water and methane. These small particles within this disk then collide and form small clumps from around 1 cm to 1 m in size, although the process by which they do so is poorly understood (Ward 1996). These clumps will then stick together to form larger objects until they are pf the order of a few hundred kilometres in size; these are known as planetesimals. Gravitational attraction between these planetesimals and surrounding material creates planetary embryos. Once these embryos reach a critical mass, which is approximately 10 $M_{\oplus}$ (Pollack et al. 1996),

runaway gas accretion occurs, which sweeps up nearby material from the disc. This occurs rapidly, forming a massive gas envelope. It is only halted when all of the local material surrounding the planet in the disc has been accreted. This produces planets with a solid core and a large gaseous atmosphere.

This theory is able to explain the existence of gas giant planets in our Solar System, which are comprised of large hydrogen and helium atmospheres (Guillot 1999). However, it cannot describe the formation of giant planets interior to the snow line, where hot Jupiters are found. The high temperatures and radiation pressure from the protostar causes gases to dissipate far too quickly for this model of core accretion to work.

Another theory of in-situ formation is the gravitational instability model. Here, a part of the disk that is susceptible to a gravitational instability fragments producing clumps that eventually form a planet. However, this method is not plausible so close to the protostar; the fast rotation speed and hot temperatures will support the surrounding disk against any gravitational collapse of this type.

Planetary migration appears to be a more likely candidate to explain the formation of hot Jupiters. Under this scenario the planet forms far enough away from the protostar to allow core accretion to occur and then migrates inwards. Two major types of migration have been proposed that occur by either interacting with the disk or through gravitational scattering caused by other large bodies in the system.

In the first scenario, disk migration, the planet interacts with material in the surrounding disk of gas. There are three potential ways that a planet can migrate through the disk. The first, type I migration, occurs when a low mass planet that is still part of the disk excites spiral density waves at Lindblad resonances in the surrounding material (Ward 1997). The regions where this occurs will in turn exert a torque on the planet, the outer region causes a negative torque and is usually stronger, causing the planet to migrate towards the star (Tanaka & Ward 2004). Type II migration occurs when the planet becomes massive enough to clear a gap in the region of the disk in which it orbits (Lin & Papaloizou 1986). The planet exerts a force on the disk

to maintain this gap and by doing so also ties its orbital migration to it, causing the planet to move inward with the disk's accretion onto the star. Type III migration works on a similar principle but where there is only a partial gap in the region around the orbit of a Saturn mass planet. Co-orbital torques in the surrounding trapped gas can create a positive feedback loop, causing very swift or "runaway" migration to occur (Masset & Papaloizou 2003).

The second scenario requires interactions with another large body in the system. Planet-planet scattering is one such example, where strong gravitational interactions occur between two or more closely orbiting planets or planetesimals (Rasio & Ford 1996). These kinds of dynamic interactions can move planets onto orbits with high eccentricities and inclination angles (Raymond, Armitage & Gorelick 2009) and even eject planets from the system (Beaugé & Nesvorný 2012). This method can explain well the eccentricity distribution seen in hot Jupiters (Chatterjee et al. 2008). It also provides an explanation of hot Jupiters in circular orbits, as a planet thrown into a short, eccentric orbit is expected to circularise over time through tidal interactions with its host star (see section 1.3.1).

Kozai-Lidov cycles are another proposed way that a hot Jupiter can migrate to its current position (Kozai 1962; Lidov 1962). They occur when a planet orbits a binary system or if the system contains an additional massive planetary companion; the eccentricity and inclination angle between the two bodies undergo periodic oscillations. They can force a planet with an initially circular orbit into one with a large eccentricity and a short orbital distance and can even flip a largely inclined orbit so that the planet orbits in a retrograde motion (Fabrycky & Tremaine 2007). As with planet-planet scattering, tidal interactions will then circularise the orbit, whilst possibly leaving a hot Jupiter with a high orbital inclination angle.

No theory is able to perfectly explain the existence of hot Jupiters. The large range of obliquities and non-zero eccentricities found in the population of known hot Jupiters point to more of a chaotic, gravitational scattering event as a means of formation. There are systems however, that support the theory that migration occurs

through the disk (e.g. Anderson et al. 2015c).

1.4 Exoplanet Atmospheres

1.4.1 Overview

Most exoplanets have been discovered via the radial velocity or transit methods. While, as noted, these methods do provide us with a wealth of information about the discovered planets such as their bulk composition and orbital parameters, they do not reveal much about the interior structure or composition of these planets. Atmospheric study, on the other hand, is able to provide a much more detailed insight into both factors. There are currently two main ways to analyse the atmospheres of these planets; the first, known as transmission spectroscopy, uses the absorption of star light by a planet's atmosphere during a transit event. The other is known as an occultation or secondary eclipse, where the planet passes behind its star causing the thermal emission it produces to be blocked. By measuring the amount of thermal emission that decreases during an occultation at a particular wavelength, we are able to build up a spectrum of the day-side atmosphere of the planet.

One of the main driving factors behind the atmospheric study of extrasolar planets is that it is key to answering one of the major questions in science: is it possible for life to exist elsewhere in the Universe? To answer this, we need to learn about the atmospheric compositions of the planets we discover, to determine whether or not they contain life-supporting molecules such as oxygen, water and carbon dioxide. The eventual goal of being able to study such a planet may be some time away, but by studying hot Jupiters we can refine the observational techniques, models and theories of planetary atmospheres. The characteristics of smaller and more Earth-like planetary atmospheres can be obtained as the technology of our observational instruments improves. By studying hot Jupiters now, we can get an insight into how atmospheric physics works in planets outside of our own Solar System.

The detection and characterisation of exoplanet atmospheres is a significant challenge. There are a number of questions that need to be answered when it comes to the study of an exoplanet's atmosphere. For instance, what is the molecular composition of the atmosphere? What are the temperatures and pressures and do they change with height? Does the atmosphere have any internal structures such as clouds or winds? How does the host star influence the atmosphere? These are difficult questions to answer, but it is becoming possible to tackle them with advancements in observational techniques and modelling.

1.4.1.1 Transmission Spectroscopy

Transmission spectroscopy is responsible for a number of atmospheric discoveries (Sing et al. 2011; Deming et al. 2013). As discussed in section 1.2.2 when a planet passes in front of its host star it is possible to determine the radius of the planet with respect to that of the star. Furthermore, if the exoplanet has an atmosphere, molecules contained within it will absorb light from the host star at particular wavelengths depending on their composition. This means that the depth ratio has an extra dependence on the planet's atmosphere. This can be seen in equation 1.15 where ΔF represents the depth of the transit, R_p is the radius of the planet (excluding the atmosphere), R_* is the stellar radius and $\Delta z(\lambda)$ is the depth of the atmosphere dependent on wavelength.

$$\Delta F = \left(\frac{R_p + \Delta z(\lambda)}{R_*} \right)^2 \tag{1.15}$$

In other words the apparent radius of the planet will change with respect to wavelength. Plotting radius as a function of wavelength is known as a transmission spectrum. An example of a transmission spectrum can be seen in figure 1.13. Features in this spectrum allow the elements or molecules in the atmosphere to be determined. By defining an atmospheric scale height H (equation 1.16) the transit depth increase caused by the atmosphere (Δz) can be defined as in equation 1.17 (Seager 2010).

$$H = \frac{k_B T}{\mu_m g} \tag{1.16}$$

Where k_B is Boltzmann's constant, T is the temperature of the atmosphere, μ_m is mean molecular mass and g is the local gravitational constant.

$$\Delta z = \frac{\pi(R_p + N_H H)^2}{\pi R_*^2} - \frac{\pi R_p^2}{\pi R_*^2} = 2N_H \Delta F \left(\frac{H}{R_p}\right) \tag{1.17}$$

Where N_H, the number of scale heights, which usually has a value of around 1. This method is only sensitive to the atmosphere along the day-night boundary (as this is the atmospheric region viewed during a transit). Also, factors such as clouds and hazes in the upper atmosphere can mask some absorption features (Pont et al. 2008).

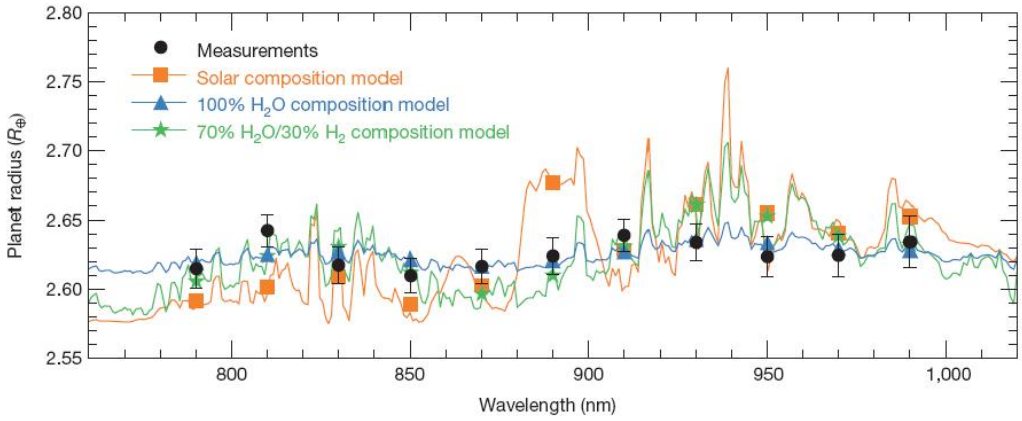

Figure 1.13: An example of a transmission spectrum. The planet radius is plotted as a function of wavelength. This particular spectrum is for the super-Earth exoplanet GJ1214b taken from Bean, Miller-Ricci Kempton & Homeier (2010). Possible models (coloured lines) are plotted against the measured values (black points). This lack of strong features in this particular observation indicates that the atmosphere may be dominated by heavy molecules such as water vapour.

1.4.2 Secondary Eclipses

For a star-planet system where the orbital plane is approximately aligned with our line of sight; as well as a decrease in light seen due to a planetary transit, there will also be a dip in light due to a secondary eclipse, or occultation. This is where the planet

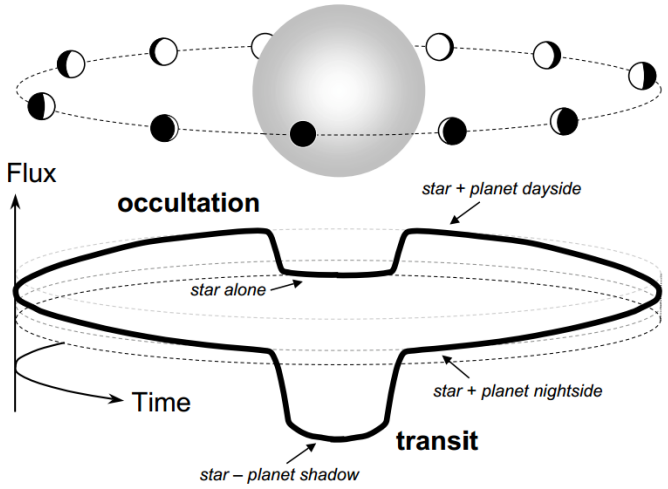

Figure 1.14: A diagram of the orbit of a planet around its host star. The solid black line represents the amount of flux we receive from the system as a function of its orbit. As can be seen there are two key events; a transit and an occultation. The dashed black lines help to represent the variation in flux between these two events (section 1.4.3). This figure was taken from Winn (2010)

.

passes behind its host star. This happens usually at half of an orbital phase (for a circular orbit) and is caused by the light we received from the planet being blocked. An example of this can be seen in figure 1.14. The occultation is usually observed in the infra-red where this event is most prominent due to the cooler temperature of the planet. By observing in the infra-red it is assumed that any reflected star light is negligible and only the day-side thermal emission from the planet is being measured. In the same way as for transmission spectroscopy, this event can be viewed in many wavelengths. This means we can build up a picture of the spectral energy distribution (SED) of the day-side atmosphere. An example of this can be seen in figure 1.15.

When the planet is completely blocked from our point of view by its host star, the amount of light received will decrease by an amount δ_{occ} as can be seen in equation 1.18.

$$\delta_{\text{occ}} = \left(\frac{R_p}{R_*}\right)^2 \frac{I_p}{I_*} \tag{1.18}$$

Where I_p and I_* are the intensities of the planet and star respectively. A value for $\frac{R_p}{R_*}$ can simply be found from transit measurements. This means that we can directly calculate the relative brightness of the planetary disk.

By assuming that the occultation is viewed in such a wavelength that only thermal emission was being received from the planet and by considering both the planet and star as discs with uniform brightness we can approximate the star and planet as blackbodies (equation 1.19).

$$\delta_{occ}(\lambda) = \left(\frac{R_p}{R_*}\right)^2 \frac{B_\lambda(T_p)}{B_\lambda(T_*)} \tag{1.19}$$

Where $B_\lambda(T)$ is the Planck function (equation 1.20).

$$B_\lambda(T) = \frac{2hc^2}{\lambda^5} \frac{1}{e^{\frac{hc}{\lambda k_B T}} - 1} \rightarrow \frac{2k_B T}{\lambda^2} \tag{1.20}$$

Where h is Planck's constant, c is the speed of light, λ is the measured wavelength, k_B is the Boltzmann constant and T is the temperature. Under the Raleigh-Jeans limit ($hc/\lambda k_B \ll 1$) the Planck function can be approximated by the final term in equation 1.20. Using this in conjunction with equation 1.19 allows us to directly relate the decrease in light to the temperature of the two bodies (equation 1.21).

$$\delta_{occ}(\lambda) = \left(\frac{R_p}{R_*}\right)^2 \frac{T_p}{T_*} \tag{1.21}$$

We can calculate the temperature of the star from spectral studies and therefore, with equation 1.21, the temperature of the planet. This method measures the average emission over the entire day-side of the exoplanet; in comparison to the transmission spectroscopy method that measures the atmosphere at the day-night terminator. As both of these methods measure the atmosphere of the planet at different points, they can be used alongside each other to provide complementary information.

As well as infra-red observations, we can also measure an occultation at shorter wavelengths to obtain the reflectance spectrum from the planet's day-side (e.g. Rowe et al. 2008). While this is hard to do in practise due to occultation depths being as low as 10^{-9}, the depth due to only reflected light can be represented by equation 1.22.

$$\delta_{occ}(\lambda) = A_\lambda \left(\frac{R_p}{a}\right)^2 \tag{1.22}$$

This equation allows us to measure the geometric albedo A_λ. The geometric albedo is the amount of flux actually received compared to the amount of flux a perfectly reflecting sphere with the same radius would produce. This albedo can give us an insight into structures such as clouds and hazes within the atmosphere. Both of these factors can cause large variations in the albedo so can be calculated via reflectance.

As well as the occultation depth, another useful parameter than can be calculated from a secondary eclipse is the eclipse midpoint. If the exact timing of a transit and occultation are known, very tight constraints can be placed upon the eccentricity of the system and a value for $e\cos(\omega)$ can be calculated (Charbonneau et al. 2005). This is shown in equation 1.23.

$$e\cos(\omega) \simeq \frac{\pi}{2P}\left(t_1 - t_2 - \frac{P}{2}\right) \tag{1.23}$$

Where e is the eccentricity of the system, ω is the argument of the periastron, P is orbital period, t_1 is time of the transit and t_2 is the timing of the secondary eclipse. We can therefore obtain an estimate for the eccentricity of the system if an independent value of ω has been measured.

As well as the timing of eclipses, eccentricity also affects the duration of transits (T_1) and occultations (T_2) which can be seen in equation 1.24.

$$e\sin(\omega) \simeq \frac{T_1 - T_2}{T_1 + T_2} \tag{1.24}$$

Therefore, through the use of equations 1.23 and 1.24 we can directly evaluate the eccentricity without a need for ω. By using this estimate along with those obtained through radial velocity measurements we can place tight constraints on the eccentricity of the system.

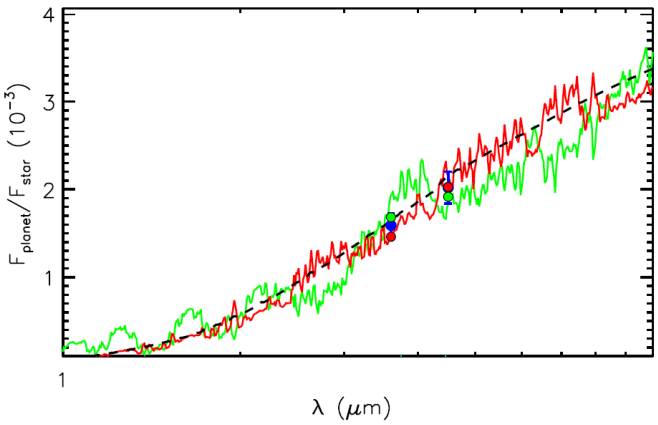

Figure 1.15: Taken from Smith et al. (2012) for the atmosphere of the exoplanet WASP-24b. It shows the planet-to-star flux ratio plotted against wavelength. The blue circles and error bars represent the occultation depths that had been determined. There are two atmospheric models shown, the green assumes no thermal inversion whereas the red line represents a model that has a thermal inversion. The black dashed line shows the nearest fitting black body model.

1.4.3 Phase Curves

Most hot Jupiter's that have been discovered to date have short orbital periods and orbit close to their host star. As noted in section 1.3.1 it is believed that this orbit causes synchronisation between the orbital motion and the rotation of the planet causing it to become tidally-locked (similar to the Earth-Moon system). This means that the planet will have a permanent day side, which constantly receives flux from the star while the opposite hemisphere remains in darkness. What happens with the large amounts of heat received by the day-side of the planet is currently unknown. It has been theorised that instead of one side of the planet being hot and the other remaining cold, that processes such as strong winds redistribute the heat around the entire planet. Measuring the day-night temperature gradients of these planets can help us gain insight into where there are any extreme thermal or chemical differences between the two sides of the planet.

By observing the changes in the planet's thermal emission as a function of orbital phase, we can determine the day-night temperature difference for these hot Jupiter's (Cowan & Agol 2008). This is known as a phase curve, an example of which can be seen in figure 1.16. Constant observation of the system is required in order to obtain the full phase curve, as a result, such observations are usually made from space based telescopes.

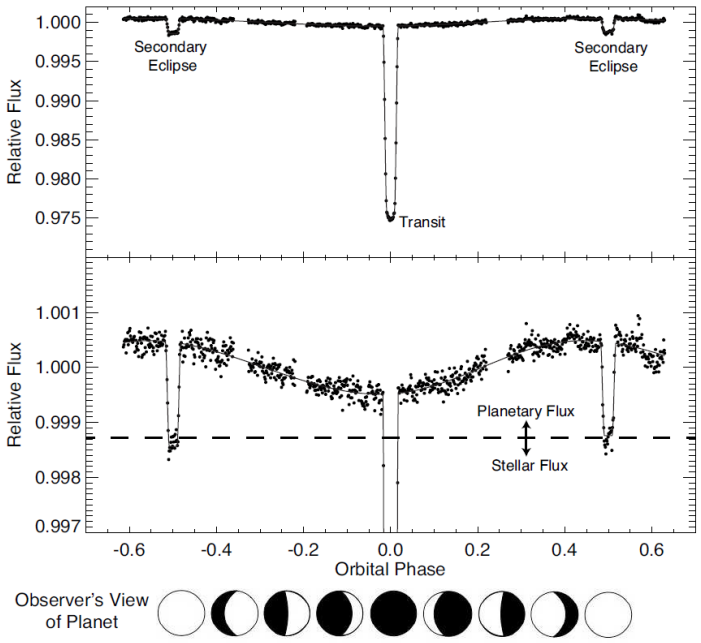

Figure 1.16: An example of a phase curve from the hot Jupiter HD 189733b measured in the 4.5 μm band by Spitzer. The plots show how the flux we receive from the system varies with orbital phase. The top plot highlights both transits and secondary eclipses. Both plots show the same system with the bottom plot having a slightly modified scale to highlight the variations in flux between these events. The horizontal dashed line in the bottom plot represents the level of the secondary eclipse depth. The flux from the planet alone is simply the variations in flux above this line. Image taken from Madhusudhan et al. (2014).

By measuring the variations in the amplitude of the flux between the maxima and minima values with respect to the secondary eclipse depth, we can calculate the

size of the day-night temperature gradient. The orbital phase at which the minima and maxima occur tell us the locations of the hottest or coldest parts of the atmosphere, for example, we would expect a hot Jupiter to be warmest towards the centre of its day-side atmosphere and therefore would expect the flux to be maximum just before the occultation.

1.4.4 Thermal Inversions

Thermal inversions are features seen in the pressure-temperature profiles of a planet's atmosphere. They refer to when the temperature of an atmosphere begins to increase with height instead of decreasing as expected. An example of a thermal inversion is represented by the red line in figure 1.17. Thermal inversions are present in all Solar System planets where it is thought they are caused by ozone or methane in the upper stratosphere of the atmospheres.

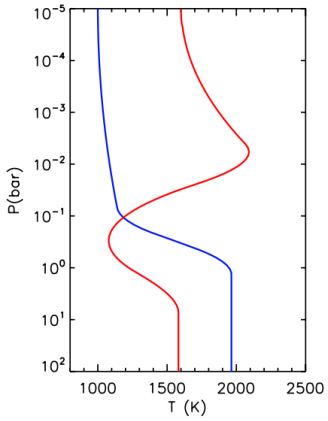

Figure 1.17: This figure shows an example of a pressure-temperature profile for the atmosphere of a hot Jupiter where temperature is plotted against pressure. The figure is oriented such that the Y-axis represents the "height" of the atmosphere. The red line represents an atmosphere that has a thermal inversion whereas the blue line represents one without. Image taken from Madhusudhan & Seager (2010).

A clear indication of thermal inversions is where emission is produced from molec-

ular features across a large wavelength range as opposed to absorption. However, evidence for thermal inversions is currently heavily reliant upon theoretical models. This is because the current photometry methods do not allow for a detailed enough analysis of the molecular structure of an atmosphere. Data from recent hot Jupiters have suggested that several planets show thermal inversions (Christiansen et al. 2010; Knutson et al. 2008). However, in many cases the observations are not robust enough to make a definite claim of thermal inversion (Madhusudhan & Seager 2010).

The cause of these inversions is likely due to some form of strong absorber located in the upper-atmosphere of these planets that thermally absorb the external stellar irradiation from the nearby host star. Two molecules that have been put forward as possible candidates for this absorption are Titanium Oxide (TiO) and Vanadium Oxide (VO) (Hubeny, Burrows & Sudarsky 2003; Fortney et al. 2006). These are strong absorbers of optical and near ultraviolet light and could exist in the temperatures of a Hot Jupiter atmosphere. Recently, TiO has been directly detected in the hot Jupiter WASP-19b giving a very strong case for this theory (Sedaghati et al. 2017).

Fortney et al. (2008) put forward the possibility that there were two classes of hot Jupiters; those that showed thermal inversions and those that did not. The paper theorised that these planets could be classed upon the activities of their host stars. While this classification system worked well for most planets, there were too many exceptions for this theory to hold true. Built upon this system, a more accurate classification system was proposed by Madhusudhan (2012) whereby a two dimensional classification system was used with the atmosphere's carbon-oxygen ratio as the second dimension. This is the most state of the art model for the theory of temperature structures of hot Jupiter atmospheres. It is still not perfect but fits well with most observations to date. These models will be further refined as more detailed molecular analysis of exoplanet atmospheres becomes possible.

1.4.5 Habitable Zone and biosignatures

The habitable zone refers to the region around a star where temperatures are sufficient enough for H_2O to exist in a liquid form (Huang 1959; Kopparapu et al. 2013). Liquid water is one of the main requirements of familiar forms of life and as such its detection could hint at the possibility of alien life. The habitable zone is determined by stellar temperature and orbital distance. Essentially, regions where temperatures are between 273 K and 373 K are considered to be habitable. In reality, the habitable zone can be extended beyond this temperature region since other mechanisms such as tidal heating (Jackson, Barnes & Greenberg 2008) or the greenhouse gas effect (Pierrehumbert & Gaidos 2011) can heat up a planet or allow it to retain heat. An Earth-sized planet within the habitable zone that shows signs of biomarkers would be a key candidate for determining the possibility of life outside of our planet.

A biosignature gas is one that can only be produced by the presence of life. Gases produced as a by-product of life can be expelled into the atmosphere where they accumulate. Detections of these gases would be a key indicator of alien life. The idea behind biosignature detection is to locate an atmosphere that is severely out of thermochemical redox equilibrium (Lederberg 1965). Redox chemistry is used by all life on earth (Seager & Deming 2010b), the idea is that gases from these reactions create a thermochemical redox disequilibrium that can be detected. For example, the Earth's atmosphere has oxygen and methane levels that are several orders away from this equilibrium state. A single gas that is completely outside of chemical equilibrium can also be a key indicator of life, again, using Earth as an example, oxygen or ozone are many magnitudes higher than those predicted by chemical equilibrium. Care must be taken to ensure that detection of these gases are not false positives. For example, a planet with a run-away greenhouse gas effect could cause the wide-scale evaporation of any water on the planet surface. Water vapour could then build up in the atmosphere where photo-dissociation could cause the loss of hydrogen molecules into space causing a temporary build up of oxygen in the atmosphere of the planet. Biosignature detection is still in the early days of theory and will be refined as technological improvements

are made to allow the detection and characterisation of Earth-size planets and their atmospheres

2 Data Calibration and Reduction

This section describes the methods and processes that were used to translate the raw data into parameters from which conclusions can be drawn. This process involves two main stages: data calibration, where the raw data are manipulated to remove factors such as instrumental systematics, and data reduction, where lightcurves are extracted from fully-calibrated images and fitted with models.

2.1 Data Calibration

Unfortunately, most charged-couple devices (CCDs) are not ideal detectors; they suffer from a number of issues that means incident light is not measured with perfect accuracy. Figure 2.1 shows an example of a raw, uncorrected image taken with the Canada-France Hawaii Telescope (CFHT). For any observations, these effects must be mitigated so that images are useful for scientific purposes. In order to undertake these calibration steps, the programming language Python[1] was utilised along with with two main astronomy libraries; PyFITS (Barrett & Bridgman 1999) and AstroPy (The Astropy Collaboration et al. 2013). PyFITS provides an interface to allow Flexible Image Transport System (FITS) files to be directly analysed or manipulated with Python. AstroPy provides a range of astronomy tools including multiple classes and functions that were used throughout this work. The Python code is provided in Appendix A.1 and is summarized briefly below.

2.1.1 Extracting Images

Most of the raw data obtained came in the form of FITS cubes, which are files that contain multiple exposures compressed into a single FITS file. The first calibration

[1] https://python.org

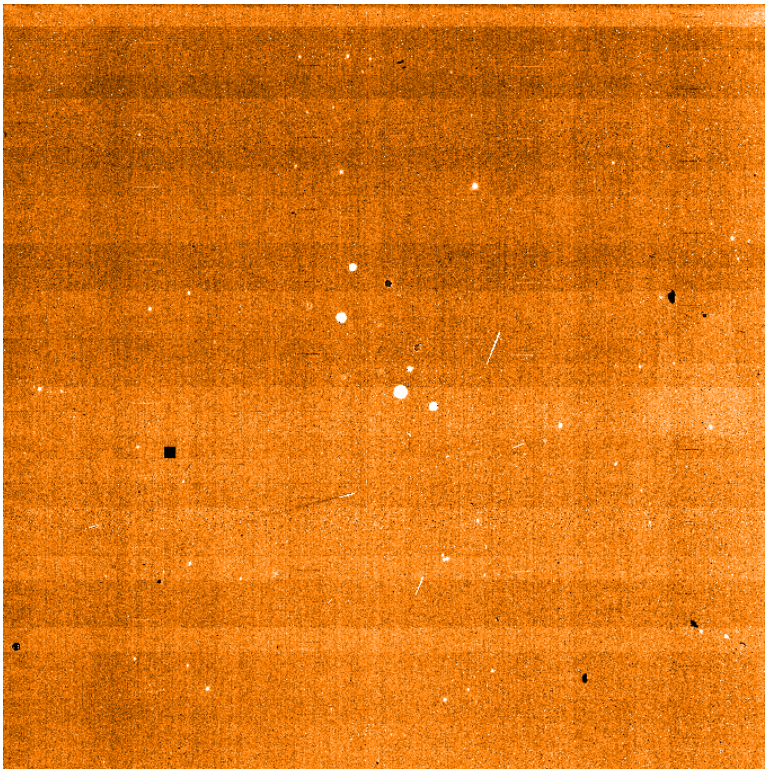

Figure 2.1: An example of a raw image retrieved from the CFHT Wide Infra-Red CAMera (WIRCAM) observation of WASP-24b. The detector has a number of defects that must be corrected before scientific analysis can be carried out.

step was to normalise the structure of any initial FITS images. A script was created using PYFITS that split the image along its third axis producing separate FITS files for each individual exposure from within the cube. Some instruments had more than one detector, which produced FITS files with exposures containing multiple detector images. Where this was the case, these were also individually extracted. Care was taken to ensure that each individual image was given a header with the correct information. For example, in the CFHT reduction noted in chapter 4, the original cube header included separate keywords that stated the individual observation times of each image. A routine was created that allowed the reading of these individual times before performing a barycentric time correction and writing the new values to the individual FITS headers. The output of this step was a folder for each detector, containing all of the individual images from an observation.

2.1.2 Calibration Pipeline

In chapter 4 it was found that manually calibrating images, rather than using pre-processed data from pipelines such as I'Iwi on the CFHT (Thanjavur, Teeple & Yan 2011), allowed for an optimised calibration method that produced a higher quality lightcurve. Raw science images were acquired along with dark and flat calibration images and the calibration steps listed below were written into an automated Python pipeline. The pipeline was designed to be flexible, accepting data inputs from both the CFHT and the High Acuity Wide-field K-band Imager (HAWK-I). This section shall describe why these calibration techniques are necessary and how they were applied.

2.1.2.1 Bias and Dark

Bias frames are images that are taken with the lowest possible exposure time where no light is incident on the detector. As a result, the image produced should map the readout noise and digital interference noise with the readout computer. Not all pixels will necessarily return a value of zero when read out; instead they give a value within

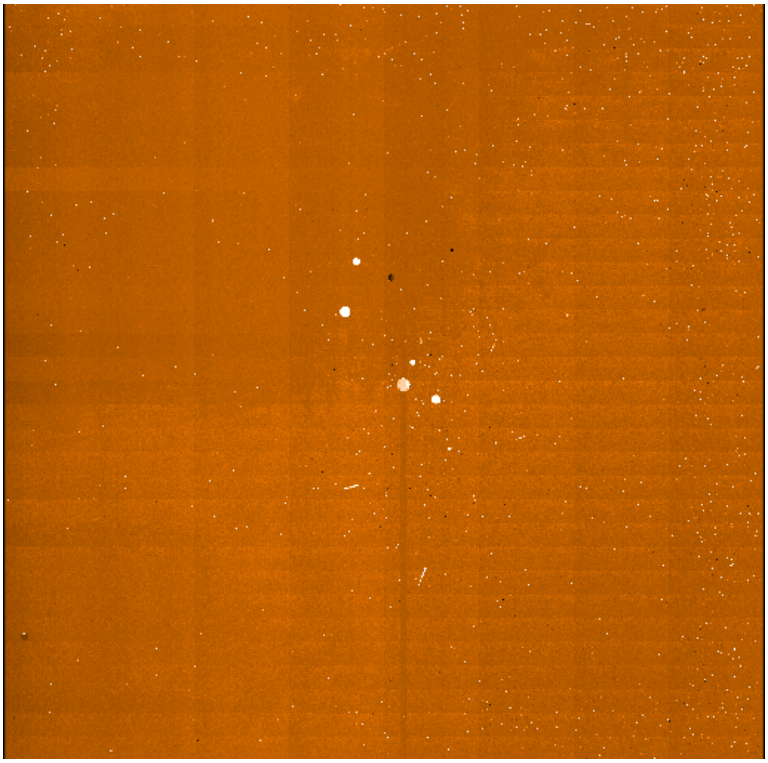

Figure 2.2: An example of a "master" dark image, produced by combining dark images taken with the CFHT, as described in the text. It shows thermal noise and interference produced by the detector and other nearby equipment when there is no incident light.

a small distribution around zero. In order to stop negative values being read, a bias value is introduced that causes all pixel values to become positive. A bias frame can be subtracted from any science images used to help remove these effects. However, in modern CCDs that are in good condition, bias frames usually contain little signal. Instead, dark frames that contain some bias information are used.

There is a certain amount of dark current produced by the detector even when there is no light incident upon it (see section 2.2.2). In order to reduce this noise from the science images, dark images can be used. These are taken when there is no light incident upon the detector. This way, only the thermal noise produced from the detector is recorded. Since the thermal noise will increase with exposure time, it

is important to not to over or underestimate the amount of noise. Care is taken to ensure that the dark images obtained have the same exposure times as the science and flat images. Taking many of these images allows a much more accurate picture of the noise to be built up, especially if they are taken at certain points during the observation. These images are then combined by taking the median value of every pixel (so that anomalous pixel values due to factors such as cosmic rays do not have a major influence). This median combined image is known as a "Master Dark", an example of which is shown in figure 2.2. This is then subtracted from both the raw and flat images.

2.1.2.2 Flat Fielding

Flat-field images can be used to remove the effect of irregularities in the optical path as well as variations in pixel sensitivity. It helps to reduce the effects of things such as reflections, dust on optical surfaces, misaligned optics and vignetting. Flat images are taken when the detector is lit uniformly across all pixels. There are two main types of flats; "sky flats" and "dome flats". Sky flats are taken during twilight where the sky is an approximately uniform colour. Dome flats are images taken of an illuminated, closed dome. Before applying the flats to any raw images they had to be manipulated. Firstly, the master dark mentioned above was subtracted from each image. The resulting images were then combined by taking the median values of each pixel. However, in this case it is possible that the illuminating light may have varied over time (e.g. a flickering dome light). To avoid this largely affecting the values in the median combined image, each image was scaled by a certain factor such that the mode (most frequent pixel value) of all images was the same before any combining took place. The image was then normalized to stop the science image from having large values. An example of the master flat is shown in figure 2.3. The dark-corrected raw images were divided by this normalized flat to remove any flat-field variations.

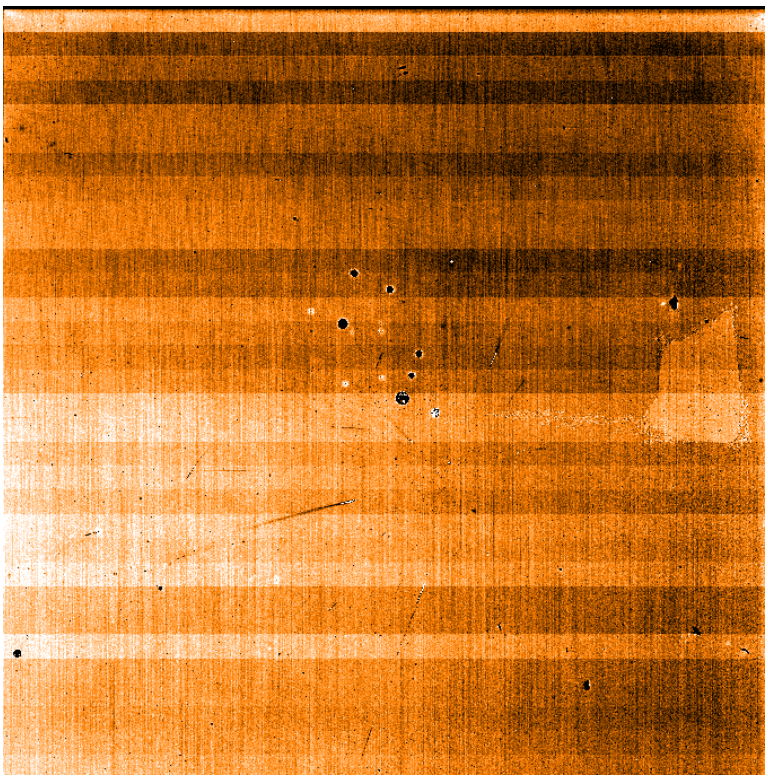

Figure 2.3: An example of a "master" flat-field image, produced by median-combining flat images taken with the CFHT at twilight. It shows irregularities in the telescope optics and systematic pixel variations.

2.1.2.3 Bad Pixel Mask

Hot or dead pixels can also be an issue when analysing raw images. Hot pixels are singular pixels that have a persistent and high dark current value. They are located at fixed positions on the detector. Dead pixels are essentially the opposite where little or no signal is recorded. These pixels were identified by examining individual pixels within the master flat image. The positions of pixels with values five times outside of the median absolute deviation around the median pixel value were flagged as bad. These were then set to a value of "not-a-number" (NaN) to make them easy to detect and distinguishable from good pixels within the image.

2.1.2.4 Saturated Pixels

When a pixel receives its maximum limit of light before being read, it will no longer count any incoming photons. This is known as the saturation limit. This limit varies between each detector, for CFHT the saturation limit is 36,000 Analogue-to-Digital Units (ADU). Any pixels that were found to be above this limit were flagged as bad.

2.1.2.5 Bad Pixel Handling

Bad pixels that were not located near any bright objects (i.e. the stellar point spread functions or PSFs) were simple to correct. The median value of a surrounding 5×5 pixel window was a good estimate of the missing pixel value and was therefore used to replace the bad pixel value. The replacement of bad pixel values that lie within stellar PSFs however is much more complex. Rather than conventionally trying to interpolate across pixel values, such as in the work of Croll et al. (2015) an attempt was made to use PSF fitting routines to determine an estimated pixel value. This involved re-sampling a good background-subtracted PSF and positioning it as centrally as possible on the background-subtracted PSF containing bad pixels. The PSF was then scaled so that subtracting the two images produced a value as close to zero as possible. The pixel value that was missing was then taken from the fitted PSF. This method saw marginal success and was able to reproduce known pixel values with $\sim$ 20 % accuracy. This however, was too high an uncertainty for the sensitivity of occultation measurements, so for the purposes of the CFHT reduction, these values were simply flagged as bad and excluded from further photometry in section 2.2.

2.1.2.6 Non-linearity Corrections

Most detectors will only respond in a linear way up until a certain limit, the count rate produced by the detector will no longer be proportional to the incident amount of photons once this limit has been exceeded. To correct for this, it is possible to rescale

these measurements based upon a polynomial fit to the response curve of the detector. In the case of the CFHT measurements, the coefficients for this polynomial fit were obtained from the instrument web page[2].

2.1.2.7 Corrected Images

All of the above steps were applied to the raw data containing the target star. An example of a fully calibrated image is shown in figure 2.4.

2.2 Aperture Photometry

Aperture photometry is one of the crucial aspects of this work. It is the process of converting raw pixel count-rates to a value that represents the amount of light received from, in the case of this work, a PSF within an image representing a star. To perform photometry an aperture with a certain size is usually placed centrally around a star. The apertures used in this work were circular, with its size determined by its radius. The values of all pixels in this area are then summed, with pixels on the boundary given certain weights depending upon how much of that pixel lies within the aperture. However, this is the sum of the count from the star as well as the sky background. We're interested in the former, so the latter must be calculated and subtracted from this value. To do this, an annulus is place around the aperture with an inner radius usually a few pixels larger than the aperture radius (see figure 2.7). A value of the sky background per pixel in the aperture is calculated as the median of all pixels within the background annulus. This is multiplied by the number of partial pixels within the aperture to get an estimate for the total background count within this region. This value is then subtracted from the original aperture sum to produce a count from the source alone.

[2] `http://www.cfht.hawaii.edu/Instruments/Imaging/WIRCam/pics.WIRCam/transfercurve_20080405_plot_nonlincorr_vs_fluxmeasured.jpg`

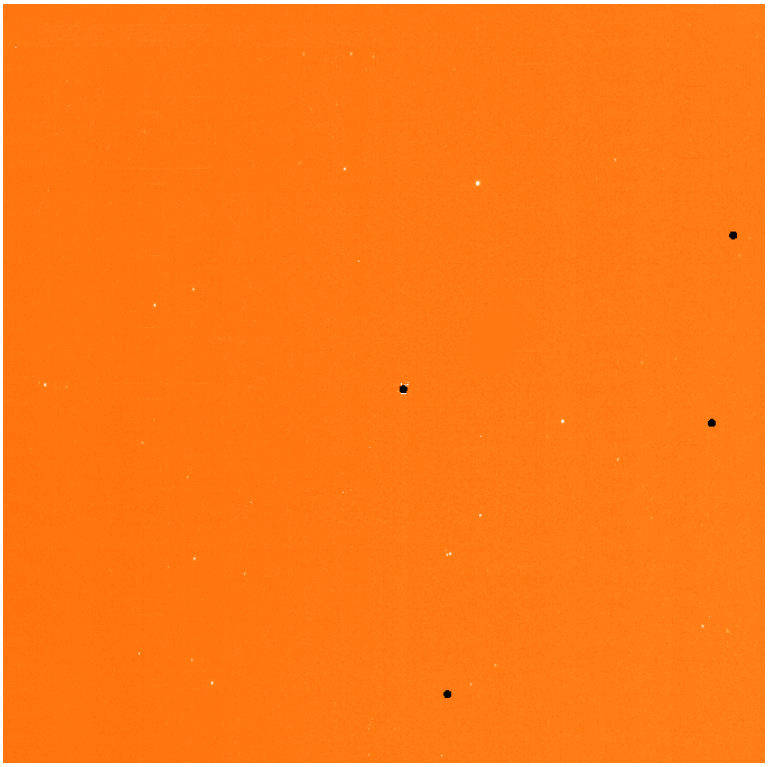

Figure 2.4: The same image as in figure 2.1 but all of the corrective steps listed in the text have been applied. This type of image is now ready for analysis. The black regions indicate masked stellar PSFs that contained one or more bad pixels. The brighter (white) regions are the PSFs of the target and comparison stars.

2.2.1 Centering Algorithm

In order to perform photometry, apertures must be placed centrally over the PSF. It is important that the apertures are well-centered; small inaccuracies in this can mean that flux from the star is only partially measured, particularly when smaller apertures are used. Centering the aperture is not as trivial as it first sounds; de-focusing the telescope, which is common practise for ground-based transit and occultation observations (Southworth et al. 2009), can produce asymmetric doughnut-like PSFs (figure 2.5). Not only can these PSFs drift during the course of an observation due to slight inaccuracies in this system as well as scintillation, but the distribution of flux within

them can vary. A centering algorithm is therefore required to ensure that the aperture is well placed throughout the entirety of the observation. Failing to do so would mean that correlated noise, on the same scale as some occultation depths could be introduced into the final time series lightcurves. For the work performed in this thesis, a centering routine was built into the photometry method (section 2.2.3). As well as centering the aperture, the PSF positions on the detector were also recorded to check whether they showed any correlation with the output light curve.

There were a number of centering methods that could have been used. In the case of observations that are in-focus, such as those from the K2 mission in chapter 3, the point-spread functions (PSFs) are approximately Gaussian. As a result, a simple Gaussian-centroid method could be used, where a Gaussian function is fitted to the X and Y dependent flux profiles around a star and the central position is returned. However, in the case of some observations, such as those of WASP-48b in chapter 4, the telescope can be defocused. Defocusing was done as it offers a number of advantages; firstly it spreads the stellar PSF over a larger number of pixels to reduce any intra-pixel variations. It also helps to minimise any flat-field inaccuracies and keeps the count rate below the non-linearity range of the detector. However, as mentioned, the PSF is no longer Gaussian-like so an alternative centering method must be used.

Nikolov et al. (2013) uses a Gaussian convolution method. This essentially involves extracting a sub-image of a small window around a star and convolving it with a Gaussian kernel. This produces a smooth PSF with a well defined peak. The standard Gaussian centroid method can then be applied and the coordinates of the central peak can be calculated in reference to the sub-image and eventually the detector. This method was tested as part of the CFHT analysis. While this method appears to mostly track the centres of the defocused PSFs well, it is a time consuming process. For example, tracking the position of 15 stars in one image takes over 30 times longer than simply Gaussian centering; this can become an issue when dealing with large data sets containing many stars. Care must also be taken when choosing the window size to create the sub-image. It must be large enough to contain all of the flux from the PSF

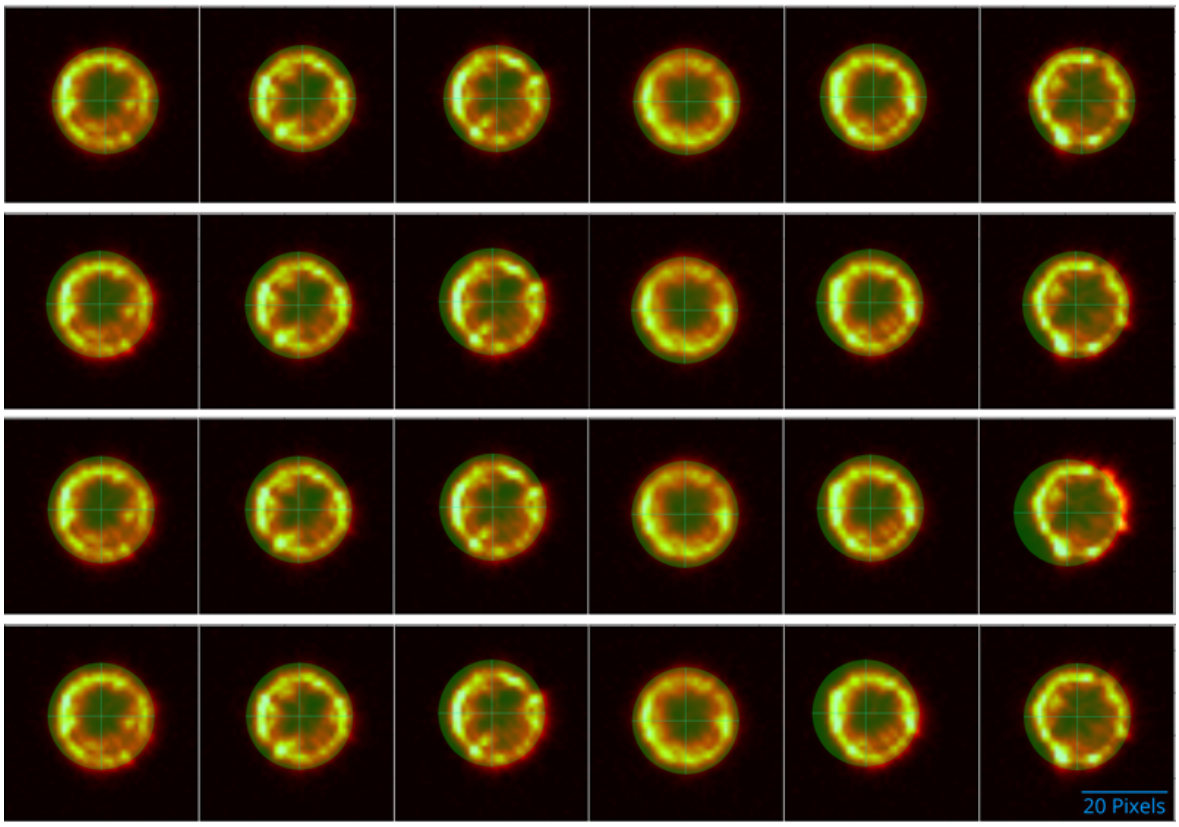

Figure 2.5: An example of the accuracy of different centroid methods. The stars are represented by the yellow and red "ring" shape whereas the apertures are shown by the light blue cross-hairs. The top row represents the new MPF algorithm written during this project, the second row shows the flux-weighted centroid aperture positions, the third shows the Gaussian convolution method and the last row shows the apertures centered with the PSF fitting method. Here a small aperture size has been used to exaggerate any offsets.

but no so large as to include other stars. The central peak can also be heavily affected by the full-width half-maximum (FWHM) and ellipticity of the Gaussian kernel that is convolved with the image. In the case of this work, both values were measured using the PSFMEASURE package in PYRAF[3] for all bright stars.

[3] `http://www.stsci.edu/institute/software_hardware/pyraf`

Another method that was tested during the course of this work was using comparative PSF fitting to centre the aperture (Kuijken & Rich 2002). Initially the central coordinates of all bright, isolated stars in a single reference image were obtained visually. Using PYRAF a model PSF was created with the chosen stars. This model was then fitted to all stars in all images and the best central coordinates were returned. However, this method appeared to be poor with the central coordinates deviating quite far from the apparent centre of the star (figure 2.6). This was perhaps due to the varying distribution of flux over the course of the observation producing different PSFs from those created from the reference image.

The flux-weighted centroid method is commonly used for observations of this type (Knutson et al. 2012). The X and Y flux profiles of a small region around a star (selected using a predefined value) are measured. An integral is then performed to give a value for the total flux within the profile. Integrals are then performed from the edge of the region to each pixel position. The pixel position that returns 50 % of the original flux is taken as the centre. This method was developed again using PYRAF and was one of the quickest methods tested. It also returns fairly accurate centroid positions although there is a slight tendency for the centroid positions to be offset towards a bright peak in the PSF (figure 2.5).

As none of the above methods are particularly ideal, a new algorithm was created to quickly identify the centre of a defocused PSF to a high degree of accuracy. This new mean-profile fitting (MPF) method worked by considering the mean X and Y profile of the stellar PSFs, rather than the whole PSF in two dimensions to allow for a much more time efficient analysis. The best-fitting model was a hybrid solution that made use of two Voigt profiles (V) (McLean, Mitchell & Swanston 1994) with a central linear region. A least square fit was performed to the PSF profile $f_p(x)$, with the free parameters being: the amplitude of the left Voigt profile A_1, the amplitude of the right Voigt profile A_2, the width of the gap between the two W, the central coordinate of the profile C, the Gaussian full-width half maximum F_g and the Lorentzian full-width

half maximum F_l. The equations used to fit the profile were given by:

$$\begin{aligned} f_p(x) &= V(x; A_1, F_g, F_l, C) && \text{for} \quad x < C - \tfrac{W}{2} \\ f_p(x) &= \tfrac{2A_1C + A_1W - 2A_2C + A_2W}{2W} + \tfrac{x(A_2 - A_1)}{W} && \text{for} \quad C - \tfrac{W}{2} \leq x \leq C + \tfrac{W}{2} \\ f_p(x) &= V(x; A_2, F_g, F_l, C) && \text{for} \quad x > C + \tfrac{W}{2} \end{aligned} \tag{2.1}$$

where x represents the pixel coordinate of either the X or Y mean profile. As figure 2.5 shows, this method was able to detect the central position of the PSFs with a greater degree of accuracy than all of the other methods studied. The drawback however, is that it will not work well for blended PSFs or in crowded fields with other PSFs nearby. For the purposes of the photometry in this thesis however, this method works well (see chapter 4).

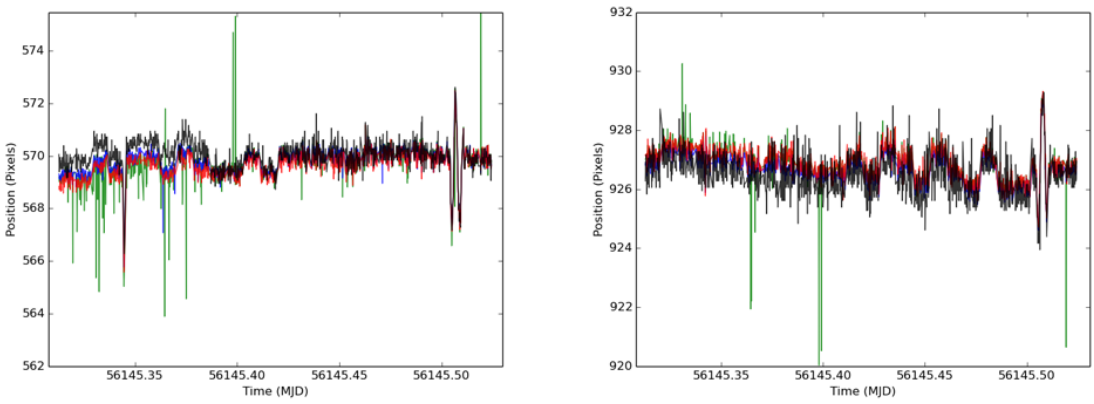

Figure 2.6: The central pixel positions returned by each different centroid method against observation time. The first figure (left) shows the X coordinate against time and the second (right) shows the Y coordinate against time. The black line shows the positions returned by the new MPF algorithm. The red line represents the flux-weighted centroid method, the green shows the PSF fitting method and the blue represents the Gaussian convolution method. The star moves no more than two pixels from its mean location, so large deviations in position represent inaccuracies in the method used.

Figures 2.5 and 2.6 show comparisons between each centroid method. PSF fitting appears to be especially poor for centroid applications on de-focused CFHT data. The

other two methods work fairly well, but differ as they are offset slightly towards the brightest peak in the donut-shaped PSF. The MPF method works well, which was confirmed by visually inspecting the placement of apertures and from the quality of lightcurve that was produced.

2.2.2 Noise Sources

There are a number of sources of noise that can cause a non-negligible amount of uncertainty in any measurements taken, the main sources are discussed briefly below.

Photon Noise

Stars do not produce a constant stream of photons; instead they are emitted at random times. This means that the probability of arrival of consecutive photons at a detector in one interval is independent of any other interval. As a result, the arrival of photons will follow a Poisson distribution. This means that the photon noise can be represented by the square root of the number of arrival counts (Howell 1989).

Read Noise

Read noise is caused by the uncertainty when retrieving the electronic signal from a detector and the small uncertainty in the current or voltage of the signal produced by the incoming photons. However, for modern instruments, this noise is equivalent to only a few electrons. For observations carried out in this work the values of read noise were typically tens of electrons.

Dark Current

Depending on its temperature, the detector has a certain amount of thermal noise. This can cause electrons to be freed from the material itself and can contaminate the signal being measured. This noise can be significantly reduced by subtracting 'dark images' (or images that are taken with no incident light on the detector) from the science images (See section 2.1.2). The detector can also be cooled to reduce this effect.

Using the above two methods, the dark current noise can ideally be reduced to a point where it is negligible for short exposure times.

Seeing

Seeing in the atmosphere of our planet can cause the blurring of images and essentially degrade the overall quality of ground-based observations. It is caused by turbulence in our atmosphere which can cause variations in its refractive index and means that light rays passing through it are perturbed. This variation can change over time and is made worse in the case of small patches of turbulent atmosphere. These variations can be responsible for features in light curves such as a stellar full-width half max (FWHM) that varies over time and can become an issue if there is a large difference in the response of different pixels on the detector. To reduce these effects, it is possible to defocus images. This causes the light to be spread out over a larger number of pixels and hence reduces the problems caused due to intra-pixel sensitivity differences (see section 2.2.1).

Other Noise Sources

As well as the noise sources listed above there are a number of other factors that can affect observations. For example there can be changes in observational conditions such as cloud cover or increased sky background light due to moonlight, twilight or artificial light pollution. There are also a number of instrumental effects that can influence the amount of light recorded such as fluctuations in the temperature of the detector, non-linearity of pixels or small changes in the location of the star on the detector (Sing & López-Morales 2009). These sources of noise are hard to avoid and must therefore be dealt with during the data analysis phase that will be described in section 2.4.

Estimating the Noise

Calculating a value for the noise is useful in error analysis. Equation 2.2 shows how the Signal-to-Noise (S/N) ratio is calculated for each star (Howell 1989) assuming that the dark current noise is negligible.

$$\frac{S}{N} = \frac{N_*}{\sqrt{N_* + n_{pix}\left(N_s + N_r^2\right)}} \tag{2.2}$$

Where N_* is the count from the star, n_{pix} is the number of pixels in the stellar aperture, N_s is the mean sky background value per pixel and N_r is the read noise.

2.2.3 Photometry Routine

A photometry routine was created using PYTHON, its purpose was to convert the fully calibrated images from section 2.1.2 into time series lightcurves for a given number of stars. The code can be seen in appendix A.2. To do this, the target star was initially identified within the image and its position was visually confirmed through the use of Aladin[4].

Once the target star had been identified, companion stars were located. Companion stars are necessary in order to remove sky variation from the flux of the target star. As the observations were taken from the ground, sky variations due to factors such as light pollution can cause the amount of light measured from that target star to vary over time. Nearby companion stars with a similar brightness will also show this same variation. By observing many comparison stars and averaging those that do not show intrinsic variation, a super-companion star can be created. This can then be used along with the target star to produce a differential light curve.

To enable the automated detection of comparison stars, the image was first convolved with a reference kernel to produce an image with approximately Gaussian PSFs. This was then used with SEP (Barbary 2016; Bertin & Arnouts 1996), a PYTHON source extractor package, to provide approximate reference pixel coordinates of all stars within the image. Every star was ranked in terms of the absolute value of the difference in total count between it and the target star. A limited number of the stars most similar in magnitude to the target star were selected to be measured with those

[4]Aladin Sky Atlas http://aladin.u-strasbg.fr/

located nearer the target being favoured (See section 2.3). For simplicity's sake, we considered only a single detector when choosing comparison stars in the cases where multiple detectors were available. There are also possible disadvantages of using companion stars located on different detectors; they could respond quite differently to incident light and could have different values of read-out noise or slightly different alignments with the focal plane.

Once a list of stellar coordinates had been obtained, the centering algorithm from section 2.2.1 was used to detect the central position of every PSF that was to be measured in each image. Circular aperture photometry was then performed over a range of sensible aperture sizes using the PhotUtils package of Astropy (Bradley et al. 2017). A sky annulus was used to estimate the sky background level within each of the apertures and the photometric uncertainty was calculated using equation 2.2.

The photometry routine output values of time, flux, flux error, sky background level, X and Y pixel positions, FWHM size, airmass, exposure time and aperture size. It also output separate files containing the time series data for each star and aperture size. The routine was created to be flexible, to allow it to work on any transit or occultation data set with the aim of making the analysis of photometric images of this type more efficient.

2.3 The effect of aperture size and reference stars on eclipse depth and timing

Two factors have the potential to introduce systematics into the differential lightcurves needed for transit or occultation photometry; the choice of companion stars and the selected aperture size. As stated in section 2.2, companion stars are needed to remove sky variation. However, the choice of these stars must be made carefully. Stars that show intrinsic variation can introduce unwanted noise or trends into the final lightcurve and can even affect the value of eclipse depth that is measured. Using companion stars that are too dim can also introduce unwanted white noise into the lightcurve. The

choice of aperture size also affected the final lightcurve. An aperture size that was too small would mean that not all of the flux within the PSF would be measured. The whole PSF needs to be counted due to the small signals that occultation events produce. If too large an aperture were selected however, the sky background could begin to contribute to the summed flux. This has the potential to increase the scatter of the final lightcurve to the extent where an eclipse cannot be detected. Therefore, both the chosen comparison stars an aperture sizes needed to be selected with care.

Initially, in order to select aperture size, an optimal aperture selection method was used as suggested by Howell (1989). This essentially involved performing a signal-to-noise calculation (equation 2.2) as a function of aperture radius. While this method helped to reduce the overall white noise of the lightcurve produced, most of the aperture sizes returned were small enough to cause some of the source flux to lie outside of the aperture (figure 2.7). This is not ideal, given that it is important to measure as much of the signal as possible, so this method was deemed unsuitable and an alternate had to be found.

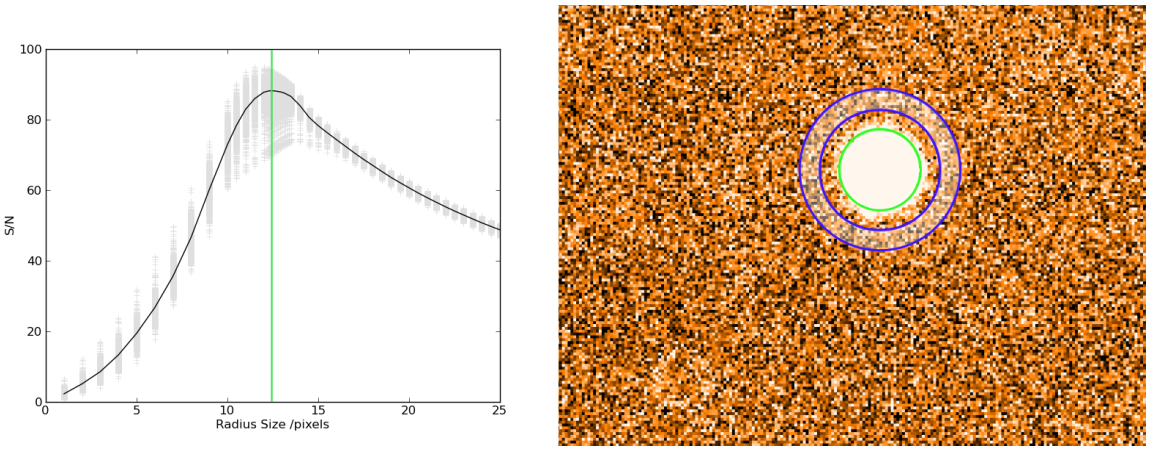

Figure 2.7: The left plot shows signal-to-noise ratio against aperture radius size for a selected PSF. The blue line represents the calculated peak value. The right plot shows an example of aperture photometry using the radius size corresponding to the peak value in the left plot. The green circle represents the aperture and the blue circles represent the sky background annulus. As can be seen, some of the source flux lies outside of the aperture.

A method that involves using weighted companion stars was initially investigated (Burton et al. 2012). This is where each companion star is normalised and then multiplied by a certain coefficient before being combined into a super-companion star using equation 2.3.

$$L(t) = \frac{F_{\mathrm{targ}}(t)}{\sum_{n=0}^{N} C_n F_n(t)} \tag{2.3}$$

Where $L(t)$ is the differential light curve, F_{targ} is the flux of the target star, F_n is the flux of the n^{th} companion star and C_n is the weighting factor for that companion. The weighting factors were determined by modifying the Markov Chain Monte Carlo (MCMC) routine described in section 2.5. However, this method produced lightcurves heavily plagued with systematics and was unable to reproduce robust weighting factors over repeat runs of the same observation.

A common method appears to be to create differential lightcurves for the target and each companion star for every aperture size (Croll et al. 2010a; Sing & López-Morales 2009). The companion stars and apertures that produce the lightcurve with the lowest out-of-eclipse root mean square (RMS) scatter are used as calibration stars. This method however is limited, it ignores the amount of correlated noise that is introduced into the lightcurves and fails to account for the improvements that can be made by combining the time-series lightcurves of companion stars.

Croll et al. (2015) put forward a method in which the effect these parameters have on the final lightcurves can be investigated with more detail. It builds upon the methods of (Croll et al. 2010a). Instead of considering just the RMS of the output lightcurves, the value of RMS $\times\beta^2$ was used to determine the quality of lightcurve produced, where β is a parameter defined in Winn et al. (2008) to estimate correlated noise. The methods used in this work, build slightly upon those of Croll et al. (2015) and the steps of the analysis are detailed below. Again, this method was written using Python, and was created so that it could be applied to any occultation or transit

data set. The code for this routine can be found in appendix A.3.

The first step was to create initial differential lightcurves; one for every target star and every aperture size. These lightcurves were then input into a global MCMC (see section 2.5) where an occultation or transit model was fitted to the data. The residuals of this fit were used to calculate the RMS $\times\beta^2$ factor. The comparison stars were then ranked in order of their lowest, more favourable, RMS; those that produced the best lightcurves were selected as candidates for a super-companion star as described above. Another set of lightcurves were then created using a combination of the selected comparison stars. A single star was added each time starting with the best comparison star until a combination lightcurve consisting of all stars was created. This was again done for every aperture size. All of these lightcurves were then again run through individual MCMCs. The outputs of these MCMCs could then be used to explore fully what the impact of the choice of companion star and aperture size made on both the eclipse depth and lightcurve quality. The posterior distributions of the MCMCs that showed the lowest RMS $\times\beta^2$ were combined to produce system parameters that took into account these effects.

2.4 Time-Varying Effects

There are a large number of time varying atmospheric and instrumental effects that can introduce correlated noise into ground-based time series observations. During the data analysis, a number of different parameters were recorded so that they could be checked for correlation with any output lightcurves. The following parameters were recorded for all observations; airmass, exposure time, changes in sky background, the X and Y positions of the stars on the detector and the changes in the full-width half maximum of stellar PSFs. Figure 2.8 shows an example of these trends measured for the WASP-48b data-set (chapter 4). It is important to remove this correlated noise as it can have significant effects on the measured light curve parameters. Unlike uncorrelated (white) noise, these trends could artificially alter the apparent occultation depth and

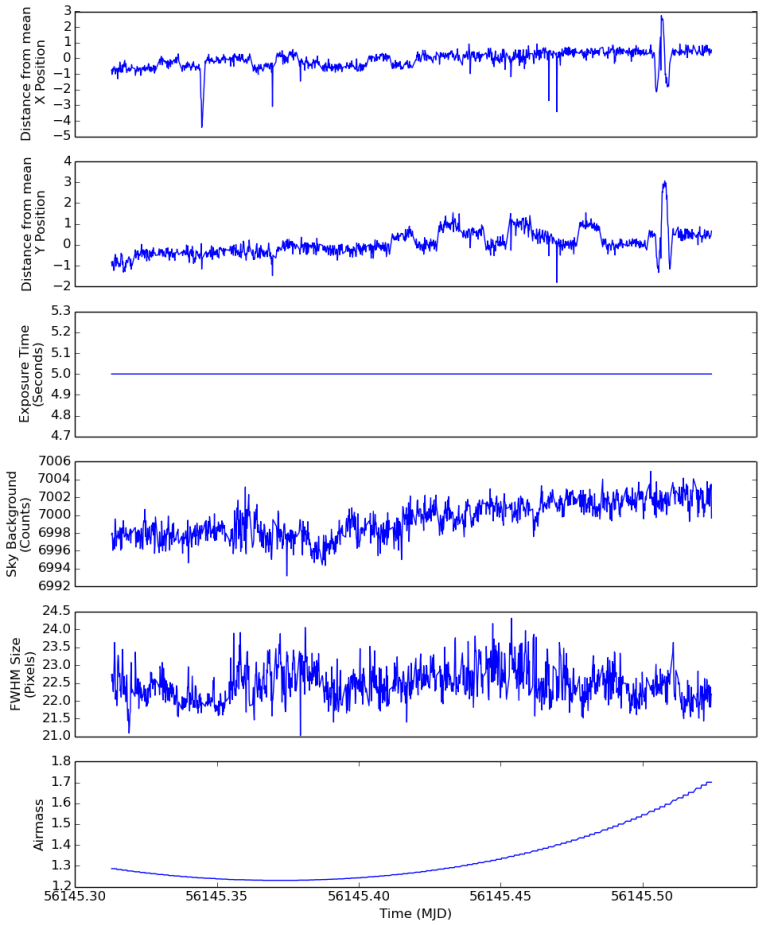

Figure 2.8: An example of the possible correlated parameters measured for the WASP-48b data set. The top two plots show deviations from mean X and Y position respectively. The third plot shows the exposure time (constant during this observation). The fourth is the mean sky background count local to the measured stars. The fifth shows the changes in FWHM size with respect to time. The bottom plot shows how airmass varies throughout the observation.

even factors such as eclipse duration.

Any correlations due to changes in exposure time should be fairly obvious. The

longer a detector is exposed for, the more light it is able to collect. Therefore the raw flux levels tend to differ substantially for different exposure times (unless the change in exposure time is very small). Values of exposure time were recorded during the original observations and are retrieved from the FITS header during analysis (section 2.2).

Correlations can be less obvious for changes in airmass. At higher airmass, the incident light has to travel through more and more atmosphere. This causes an increase in the atmospheric dispersion which causes light from a source to be refracted. Consequently, the flux from a star will decrease at higher airmass (Smart 1933). Again, the airmass was recorded during observation and was retrieved in the same way as exposure time.

As the sky background is not uniform across the entire field-of-view, systematic effects can remain even after the use of companion stars. The sky background local to each star is recorded during aperture photometry, so these values are also used to check for correlations.

Seeing, caused by turbulence in the Earth's atmosphere can be responsible for varying FWHM size over time. Small patches of especially turbulent atmosphere can effectively spread the incident light over more pixels on the detector causing an increase in FWHM. This varying FWHM can cause two issues; firstly, due to intra-pixel sensitivities, where pixels will respond differently to the same incident light. Spreading the light into other pixels during certain parts of the observation but not others can cause slight discrepancies in the amount of flux measured. Secondly, it can mean that in some cases, the light from the star is spread outside of the aperture causing further flux to be lost.

As stated in section 2.2.1, the position of stars on the detector does not remain constant. Both the X and Y coordinates of all stars are recorded as described in section 2.2.1. Again, due to the pixel sensitivity issues listed above, this introduce correlated noise into the lightcurve.

To determine if any correlation existed between any of the above trends and the output light curves the Pearson correlation coefficient was computed. This is a measure

of linear correlation between two different data sets. It returns a value between 1 and -1, where 1 represents perfect correlation, -1 shows perfect anti-correlation and 0 shows no correlation. Positive correlation values imply that as one variable increases, so does the other. A p-value is also returned which has a value of between 0 and 1. This is the probability that the data would have been produced in its current form if the null hypothesis (i.e. there is no correlation between the two data sets) was true. As the data includes white noise (uncorrelated random noise), it is very unlikely that a 0 correlation coefficient will ever be returned. Correlation coefficients and p-values were obtained by comparing each of the above trends with the lightcurve residuals.

2.5 Markov Chain Monte Carlo Analysis

In order to model the secondary eclipse and transit light curves a Markov Chain Monte Carlo (MCMC) method was used. MCMC analysis is a popular Bayesian method of solving multiple parameter-fitting problems in exoplanetary analysis as well as many other areas of science (Anderson et al. 2013; Lendl et al. 2013; Christiansen et al. 2010). It offers a way of optimizing the fit of an occultation model to the lightcurve data points in a relatively quick way. A more comprehensive grid search, where all of the parameter space is explored would produce a better model, but the time requirements of such an analysis make it impractical. The MCMC method used for this work was based on the one used by Collier Cameron et al. (2007b), Pollacco et al. (2008) and Enoch et al. (2010a). It allows a global, simultaneous analysis of multiple sets of data for an exoplanetary system. It is able to compute models for transit, occultation, radial velocity and Rossiter McLaughlin data. The routine is described in great detail in the literature, but the basics principles of the method are the following:

1. The MCMC starts at a certain point in parameter space, usually with approximately accurate initial parameters, and an initial likelihood is calculated.

2. The parameters are then randomly modified by drawing from a uniform dis-

tribution which runs from -1 to 1. This is multiplied by the parameter uncertainties and added to the previously accepted value before the likelihood is calculated again.

3. If the likelihood is higher than the previous value then the new parameters are accepted. If not, the new parameters are accepted with a probability that is proportional to $\exp\left(-\frac{\Delta\chi^2}{2}\right)$ (Collier Cameron et al. 2007b), where χ^2 represents the chi-square statistic.

Repeating these steps a large number of times will converge towards a parameter space that fits the data well. An initial burn-in period occurs for an initial number of steps, where data are discarded to allow the MCMC to settle towards a good starting point; this is particularly useful if it started with bad input parameters. Following this, the values of all parameters in an accepted step are recorded. There are two different types of parameters used in the MCMC: proposal parameters, which are controlled by the methods described above and derived parameters, which are calculated physically using the proposal parameters. These proposal and derived parameters are listed in table 4.2. Once the MCMC is complete, the values of each parameter are obtained from the median of their posterior distributions, with the uncertainties estimated from the lower (15.85 %) and upper (84.15 %) percentiles.

2.5.1 Transit and Occultation Models

The transit model is described in detail in Mandel & Agol (2002) but it shall be described here briefly. The transit is modelled as an eclipse of a spherical star by an opaque spherical planet. The separation of the centres of the two objects from our point of view is defined as d (which varies over time). A value z is then defined so that it obeys equation 2.4

$$z = \frac{d}{r_*} \tag{2.4}$$

The value p is also defined such that it is equal to the ratio of the radii of the two objects (equation 2.5)

$$p = \frac{r_p}{r_*} \tag{2.5}$$

The following function is then used to model the lightcurve, assuming that the planet is small in comparison to its host star (usually a reasonable assumption).

$$F = 1 - \frac{I^*(z)}{4\Omega}\left[p^2\cos^{-1}\left(\frac{z-1}{p}\right) - (z-1)\sqrt{p^2-(z-1)^2}\right], \tag{2.6}$$

where $I^*(z) = (1-a)^{-1}\int_{z-p}^{1} I(r)2rdr$, $I(r) = 1 - \sum_{n=1}^{4} c_n(1-\mu^{n/2})$, $\mu = \cos\theta = \sqrt{1-r^2}$, $0 \leq r \leq 1$, $\Omega = \sum_{n=0}^{4} c_n(n+4)^{-1}$ and c_n represents the quadratic limb darkening coefficients.

The model used for occultations is also based upon this method but with no limb darkening coefficients, since it is the planet that is being eclipsed. The only free parameters in this case are therefore eclipse depth, duration and midpoint.

2.5.2 Detrending

Once any correlations described in section 2.4 have been clearly identified, it is necessary to de-trend the input light curve. This is where correlated noise is removed from the lightcurve by dividing it by a function similar to the one in equation 2.7.

$$Trend = a_0 + \sum_{n=1}^{N} a_n Z_n + b_n {Z_n}^2 \tag{2.7}$$

Where a_n and b_n are the de-trending coefficients, where b_n can be set to 0 depending on whether linear or quadratic de-trending is required. Z_n represents each of the parameters found to contain a correlation. The MCMC was modified so that it was able to perform this type of de-trending for any input parameter through singular value decomposition (Press et al. 1992; Anderson et al. 2011).

2.6 Residual Permutations

A residual permutations method, also known as a "Prayer-Bead" analysis, was used to determine the effect of any correlated noise upon the parameters mentioned in section 2.5 (Gillon et al. 2007). The advantage of this method over bootstrapping for example, is that it keeps the original time structure of any red noise in tact. In order to perform this analysis, the output model, trend and residuals were used from the MCMC (section 2.5). The residuals were then shifted by one point (i.e. the point that was first in the observation is now last). The new residuals are then multiplied back by the model and the trend from the original output. This is repeated until every data point within the light curve has been shifted; resulting in as many light curves as there were points. Each of these light curves was then run through the MCMC as described in section 2.5. The outputs from all MCMCs were recorded. The occultation depth was taken to be the median value of the resulting depths and the uncertainty limits were taken as the 1σ level. This could then be compared to the depths produced by the MCMC. Large discrepancies between the two values would indicate that the red noise has had a large effect on the output parameters and further action would have to be taken in order to reduce the effects.

3 Follow-up observations with K2

3.1 Overview

This section presents the analysis of K2 short-cadence data of two previously known hot Jupiter exoplanets: WASP-55b and WASP-75b. The contents are based upon a paper published in the Publications of the Astronomical Society of the Pacific, volume 130, issue 985. As well as writing the paper, I was responsible for the reduction, analysis and interpretation of the data. Dr David Anderson and Professor Coel Hellier provided guidance and support on the Starspot and stellar rotation section as well as how to handle the potential transit timing and duration variations noted in section 3.4. Dr Oliver Turner assisted with the transit timing and duration variation analysis and Teo Mocnik provided a routine for fitting the phase-curve variations.

The K2 mission has been in operation since May 2014 following the failure of two reaction wheels of the Kepler satellite (Howell et al. 2014). It now monitors fields along the ecliptic plane. The spacecraft uses the radiation pressure of the Sun along with its two remaining reaction wheels and thrusters to stabilize pointing (Van Cleve et al. 2016). However, resultant observations suffer from an increased level of pointing jitter compared to the original Kepler mission. The roll of the spacecraft introduces systematics in the photometric lightcurves on a time-scale of approximately 6 hours, meaning that the quality of the photometry can be degraded by up to a factor of 4 (Howell et al. 2014). Despite this, methods such as self flat-fielding (Vanderburg & Johnson 2014), K2SC (Aigrain, Parviainen & Pope 2016) and routines that have been personally developed (Močnik et al. 2016) can reduce this effect to the extent that the quality of the produced data is near that of the original mission. The K2 spacecraft offers observations of unprecedented quality when compared to most observational tools currently available for this purpose.

Following the initial discovery of an exoplanet, subsequent observations are common if a planet possesses unique characteristics. One example of this is the high-mass,

short period hot Jupiter WASP-18b (Hellier et al. 2009). They are also frequent if the system is readily observable from Earth; for example, those with a bright host star such as WASP-33b (Christian et al. 2006) or planets with a large transit depth such as WASP-43b (Hellier et al. 2011a). For the planets that appear to be ordinary or more difficult to observe, follow-up observations can range from infrequent to absent. The lack of follow-up can mean we subsequently miss crucial discoveries about these systems. For example, WASP-47b was initially believed to be a standard, non-unique hot Jupiter. However, observations as part of the K2 campaign revealed that it was part of a multi-planet system, with the discovery of two additional transiting planets: WASP-47e, a super-Earth sized inner planet and WASP-47d, a Neptune sized outer companion (Becker et al. 2015). A more distant planet, WASP-47c, was also detected as part of an RV survey in a more eccentric orbit (Neveu-VanMalle et al. 2016). WASP-55b and particularly WASP-75b are examples of two planets that have had little follow-up since their initial discoveries.

WASP-55b was found to be a moderately inflated hot Jupiter with a mass of $0.57 \pm 0.04\ M_{\rm Jup}$ and a radius of $1.30 \pm 0.05\ R_{\rm Jup}$ (Hellier et al. 2012). It orbits WASP-55 (EPIC 212300977), a G1, 1.01 $M_{\odot}$, 1.01 $R_{\odot}$star, with a period of 4.47 days. WASP-75b was discovered by Gómez Maqueo Chew et al. (2013) as a hot Jupiter with a mass of $1.07 \pm 0.05\ M_{\rm Jup}$ and a radius of $1.27 \pm 0.05\ R_{\rm Jup}$. It orbits WASP-75 (EPIC 206154641), a 1.26 $M_{\odot}$, 1.14 $R_{\odot}$, F9 star with an orbital period of 2.484 days.

The rest of this chapter will present a refined set of system parameters for WASP-55b and WASP-75b. The K2 lightcurves were also searched for transit timing and duration variations, stellar rotational modulation, starspot occultations, phase-curve variations and the residual lightcurves were searched for additional transiting companions.

3.2 K2 Data Reduction

3.2.1 Data Extraction

WASP-55b was observed during campaign 6 of the K2 mission, which ran from 2015 July 14 until 2015 September 30. It produced a total of 112,672 short-cadence images. WASP-75b was observed during campaign 3, it produced 101,370 short-cadence images between 2014 November 14 and 2015 February 3. The target pixel files were retrieved for each system using the Barbara A. Mikulski Archive for Space Telescopes (MAST[1]).

The large motion of the point spread function (PSF) on the detector in campaign 3 was cause for concern when reducing the raw images. A traditional fixed-mask method used by a majority of the K2 data reduction to date (e.g. Močnik et al. 2016) appeared to degrade the precision of the output lightcurves. To resolve this issue, the aperture photometry routine described in section 2.2 was used, with aperture sizes ranging from 0.5 to 8.5 pixels in steps of 0.25 pixels that used a flux-weighted centroid method to re-position the aperture based upon the PSF position in each frame. The advantages of this method were that the aperture could travel with the moving PSF while still taking into account fractional pixel values. Other methods were attempted, such as a mask that moved with the PSF, this method lowered the RMS but also ended up introducing more systematic noise that could not be corrected by any de-trending processes. For the WASP-75b dataset an aperture size of 6.5 pixels was the best aperture size. It led to a reduction in the RMS from 368 PPM to 325 PPM and for WASP-55b, a 5.5 pixel aperture reduced the scatter from 568 PPM to 530 PPM.

3.2.2 De-trending

As noted in Section 3.1, K2 lightcurves contain systematics that correlate with position of stellar flux on the detector. This is visibly seen as a sawtooth-like pattern in the

[1]https://archive.stsci.edu/k2/

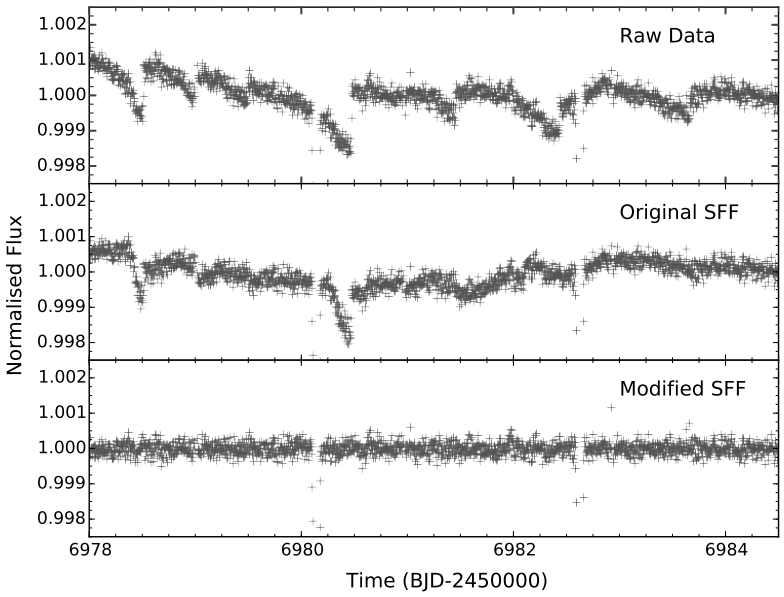

Figure 3.1: The top panel shows a section of the raw WASP-75b lightcurve that contains strong systematics that correlate with PSF position, binned to 5 minute intervals. The middle panel shows the same section of the de-trended lightcurve produced by the original self-flat fielding method and the bottom panel shows the de-trended lightcurve produced by the modified method used in this paper.

lightcurve, which can be observed in Figure 3.1. The self-flat fielding method (Still & Barclay 2012) was able to remove most of the systematics from the lightcurve. However, it was noted that the polynomial fit to the flux versus arclength data was sometimes quite poor. Testing of different methods found that convolving the data with a Gaussian kernel produced a much better fit, which was able to account for small deviations in the trend of the data. For WASP-75b there were still areas of strong systematics caused by a high spacecraft jitter, that were not corrected well by either method. The systematics correlated heavily with the X and Y position of the PSF on the detector, with large jumps in position and flux at every thruster event. A moving gradient was used to detect the areas with jumps and it used these dates as boundaries between windows over which to correct the systematics, rather than a fixed window size. With this method, a third order polynomial fit to the flux versus arclength trend was enough to successfully remove the visible trends (Figure 3.1).

To model the low-frequency variability from the lightcurve of WASP-75b a Gaussian convolution method was used, similar to that of Močnik et al. (2016) but with a kernel size larger than the time-scales of systematic noise and transit events. This was then removed from the lightcurve before further analysis. A running median filter was also performed, with a kernel size of 21 points, to clip all data that were greater than 8-σ from the median-filtered residuals. In total, 2409 and 4905 points were clipped from the WASP-55b and WASP-75b lightcurves respectively. The de-trended lightcurves are shown in figures 3.2 and 3.3.

3.3 System Parameters

To determine the parameters of the system, an adaptive Markov chain Monte Carlo (MCMC) routine (chapter 2.5; Collier Cameron et al. 2007b; Pollacco et al. 2008; Anderson et al. 2015a) was used to simultaneously analyse the K2 lightcurves with their respective, previously published radial velocity (RV) data.

For WASP-55b and WASP-75b, the normalised K2 lightcurves were analysed

with the CORALIE RVs from Hellier et al. (2012) and Gómez Maqueo Chew et al. (2013), respectively. The orbit was assumed to be circular for the main MCMC runs, but eccentricity was set as a free parameter on subsequent runs to place a constraint on its upper limit for both systems. An additional run was performed using the ground-based transit lightcurves from Hellier et al. (2012) for WASP-55b and Gómez Maqueo Chew et al. (2013) for WASP-75b to refine the ephemeris of both planets by extending the baseline. The updated system parameters are shown in Tables 3.1 and 3.2 and the phase-folded lightcurves and models in Figures 3.4 and 3.5.

A four-parameter law was used to determine the limb darkening coefficients with values interpolated from those of Sing (2010) and based upon stellar temperature. For both systems, the stellar effective temperatures produced limb darkening coefficients that were in good agreement with the shape of the lightcurve. There were no visible anomalies in the residuals (see the middle panel in Figures 3.4 and 3.5) as has been the case for some planets that have been studied to date (e.g. Močnik, Southworth &

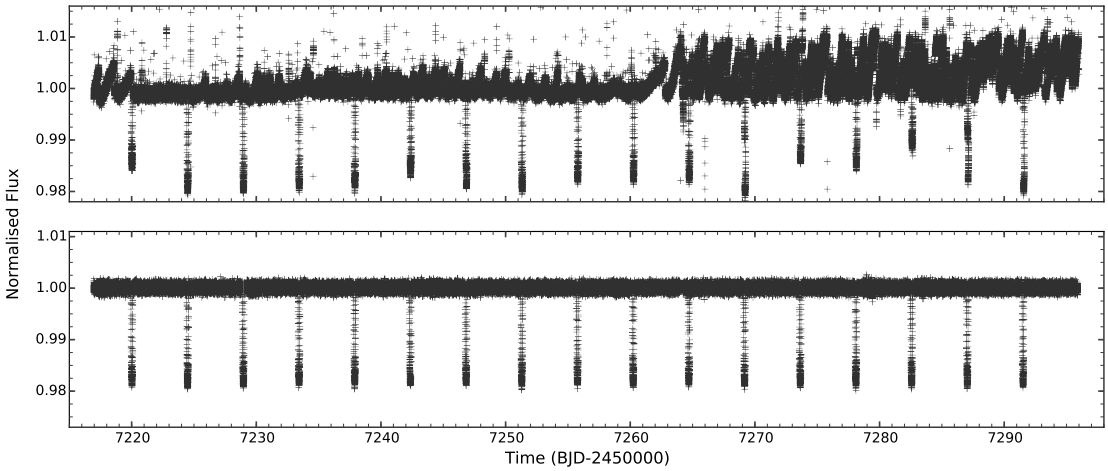

Figure 3.2: The top plot shows the raw lightcurve of WASP-55b and the bottom plot shows the lightcurve obtained by de-trending and clipping the raw lightcurve as described in Section 3.2.2; normalised flux is plotted against time for each. The de-trending algorithm is successful in removing all large scale systematic variations within the lightcurve.

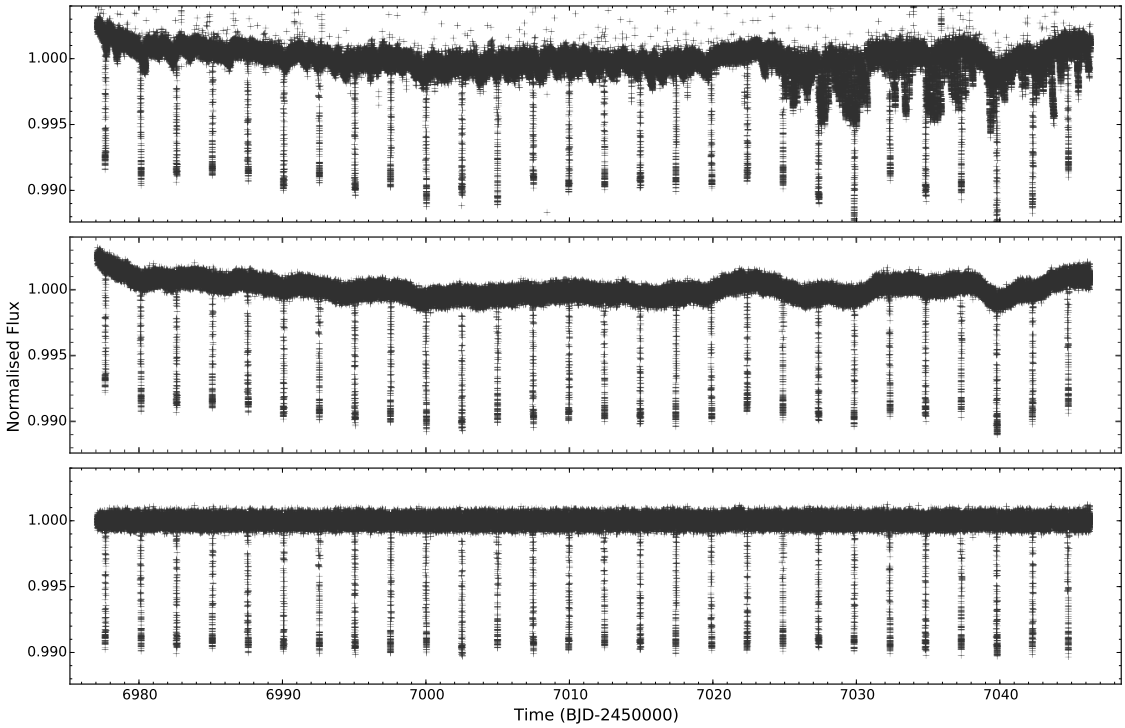

Figure 3.3: Similar to figure 3.2 expect the lightcurve for WASP-75b is plotted. The top plot shows the raw lightcurve from the K2 photometry, the middle panel shows the SFF de-trended and clipped lightcurve and the bottom panel shows the lightcurve with the removal of any detected low-frequency stellar variation.

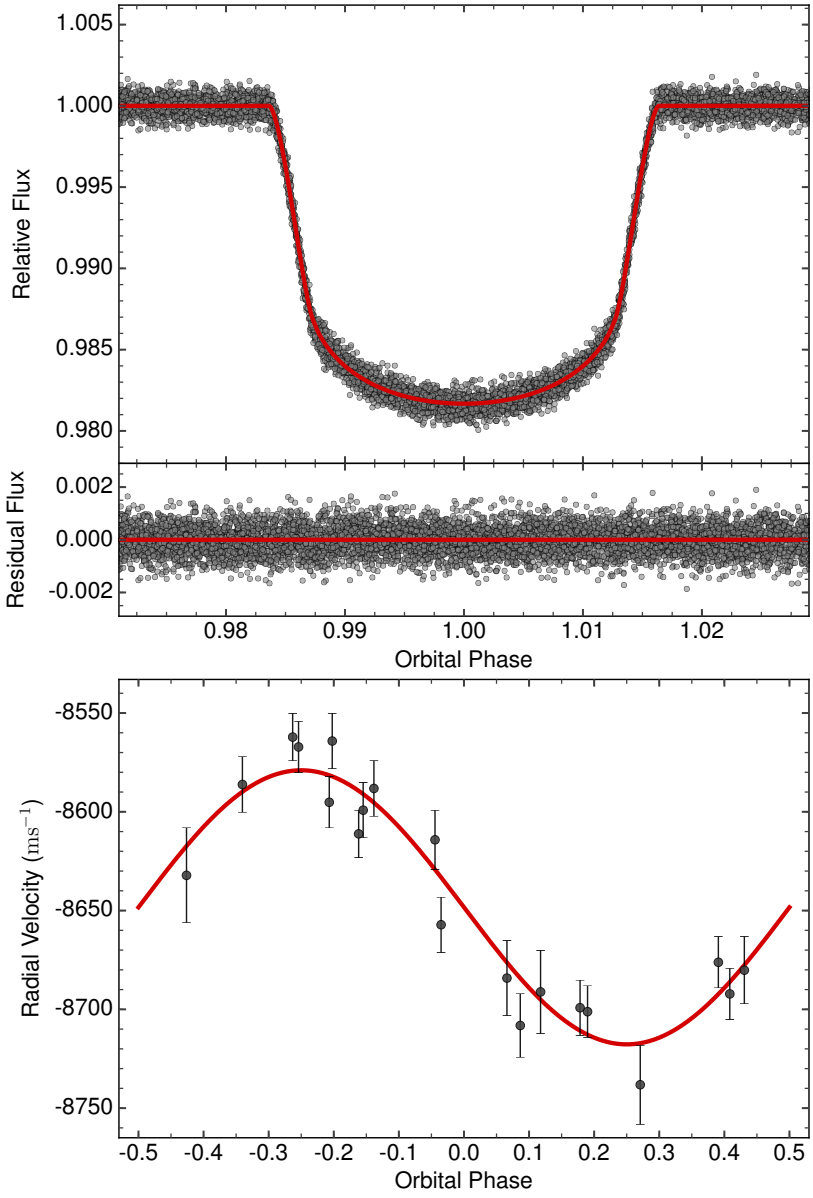

Figure 3.4: The top plot shows the fully de-trended, phase-folded K2 lightcurve for WASP-55b. The model produced by the global MCMC run is shown by the red line. The middle panel shows the residuals of the fit and the bottom panel shows the radial velocity measurements with the best-fitting orbital model in red.

Table 3.1: Orbital, stellar and planetary parameters from the MCMC analysis of WASP-55b (EPIC 212300977). Each of the proposal parameters, derived parameters, and parameters controlled by priors are listed separately. The results of this work and those provided by the literature are both tabulated.

Symbol (unit)	This Work	Hellier et al. (2012)	Southworth et al. (2016)
MCMC proposal parameters			
P (days)	4.465630 ± 0.000001	4.465633 ± 0.000004	4.4656291 ± 0.0000011
$T_{\rm c}$ (days)	7256.25436 ± 0.00003	5737.9396 ± 0.0003	6416.71565 ± 0.00013
T_{14} (days)	0.1459 ± 0.0002	0.147 ± 0.001	0.147 ± 0.003^{a}
$R_{\rm P}^2/{\rm R}_*^2$	0.01551 ± 0.00005	0.0158 ± 0.0003	0.0155 ± 0.0002
b	0.18 ± 0.03	0.15 ± 0.12	0.03 ± 0.23^{a}
K_1 (m s^{-1})	69 ± 4	70 ± 4	70 ± 4
γ (m s^{-1})	-4324 ± 3	-4324.4 ± 0.9	-
MCMC proposal parameters constrained by priors			
M_* ($M_\odot$)	1.16 ± 0.03	1.01 ± 0.04	$1.162^{+0.029}_{-0.033}$
$T_{\rm eff}$ (K)	6070^{+51}_{-46}	5960 ± 100	6070 ± 53
Fe/H	0.09 ± 0.05	-0.20 ± 0.08	0.09 ± 0.05
MCMC derived parameters			
i ($^\circ$)	89.0 ± 0.2	89.2 ± 0.6	$89.83^{+0.57}_{-1.20}$
e	0 (fixed) ($<$0.22 at 3σ)	0 (fixed) ($<$0.20 at 3σ)	-
a (au)	0.0558 ± 0.0006	0.0533 ± 0.0007	0.0558 ± 0.0005
R_* ($R_\odot$)	1.11 ± 0.01	$1.06^{+0.03}_{-0.02}$	$1.102^{+0.020}_{-0.015}$
$\log g_*$ (cgs)	4.413 ± 0.006	$4.39^{+0.01}_{-0.02}$	$4.419^{+0.009}_{-0.015}$
ρ_* ($\rho_\odot$)	0.85 ± 0.01	$0.85^{+0.03}_{-0.07}$	$0.869^{+0.026}_{-0.041}$
$M_{\rm P}$ ($M_{\rm Jup}$)	0.62 ± 0.04	0.57 ± 0.04	$0.627^{+0.037}_{-0.038}$
$R_{\rm P}$ ($R_{\rm Jup}$)	1.34 ± 0.01	$1.30^{+0.05}_{-0.03}$	$1.335^{+0.031}_{-0.020}$
$\log g_{\rm P}$ (cgs)	2.9 ± 0.03	2.89 ± 0.04	2.94 ± 0.03
$\rho_{\rm P}$ ($\rho_{\rm J}$)	0.26 ± 0.02	$0.26^{+0.02}_{-0.03}$	$0.247^{+0.017}_{-0.021}$
T_P (K)	1305 ± 12^{b}	1290 ± 25	1300^{+15}_{-13}

[a] Calculated using the parameters from Southworth et al. (2016) using the equations of Seager & Mallén-Ornelas (2003)

[b] Assuming a zero bond albedo and efficient day–night redistribution of heat.

Table 3.2: Similarly to Table 3.1 the orbital, stellar and planetary parameters from the MCMC analysis of WASP-75b (EPIC 206154641) are shown. Each of the proposal, derived and parameters controlled by priors, are listed separately. Again the results of this work and those provided by the literature are listed.

Symbol (unit)	This Work	Gómez Maqueo Chew et al. (2013)
MCMC proposal parameters		
P (days)	2.4842014 ± 0.0000004	2.484193 ± 0.000003
$T_{\rm c}$ (days)	7009.94594 ± 0.00002	6016.2669 ± 0.0003
T_{14} (days)	0.08097 ± 0.00008	0.0822 ± 0.0011
$R_{\rm P}^2/{\rm R}_*^2$	0.01133 ± 0.00005	0.0107 ± 0.0003
b	0.8926 ± 0.0007	$0.882^{+0.006}_{-0.008}$
K_1 (m s^{-1})	145 ± 4	146 ± 4
γ (m s^{-1})	2264 ± 3	2264.29 ± 0.06
MCMC proposal parameters constrained by priors		
M_* ($M_\odot$)	1.16 ± 0.03	1.14 ± 0.07
$T_{\rm eff}$ (K)	6035^{+88}_{-93}	6100 ± 100
Fe/H	0.07 ± 0.09	0.07 ± 0.09
MCMC derived parameters		
i ($^\circ$)	81.96 ± 0.02	$82.0^{+0.3}_{-0.2}$
e	0 (fixed) (<0.10 at 3σ)	0 (fixed)
a (au)	0.0377 ± 0.0006	$0.0375^{+0.0007}_{-0.0008}$
R_* ($R_\odot$)	1.27 ± 0.02	1.26 ± 0.04
$\log g_*$ (cgs)	4.294 ± 0.008	4.29 ± 0.02
ρ_* ($\rho_\odot$)	0.566 ± 0.003	0.56 ± 0.04
$M_{\rm P}$ ($M_{\rm Jup}$)	1.08 ± 0.05	1.07 ± 0.05
$R_{\rm P}$ ($R_{\rm Jup}$)	1.31 ± 0.02	1.270 ± 0.048
$\log g_{\rm P}$ (cgs)	3.16 ± 0.01	$3.179^{+0.033}_{-0.028}$
$\rho_{\rm P}$ ($\rho_{\rm J}$)	0.48 ± 0.02	$0.52^{+0.06}_{-0.05}$
T_P (K)	$1688^{+25}_{-26}{}^a$	1710 ± 20

[a]Assuming a zero bond albedo and efficient day–night redistribution of heat.

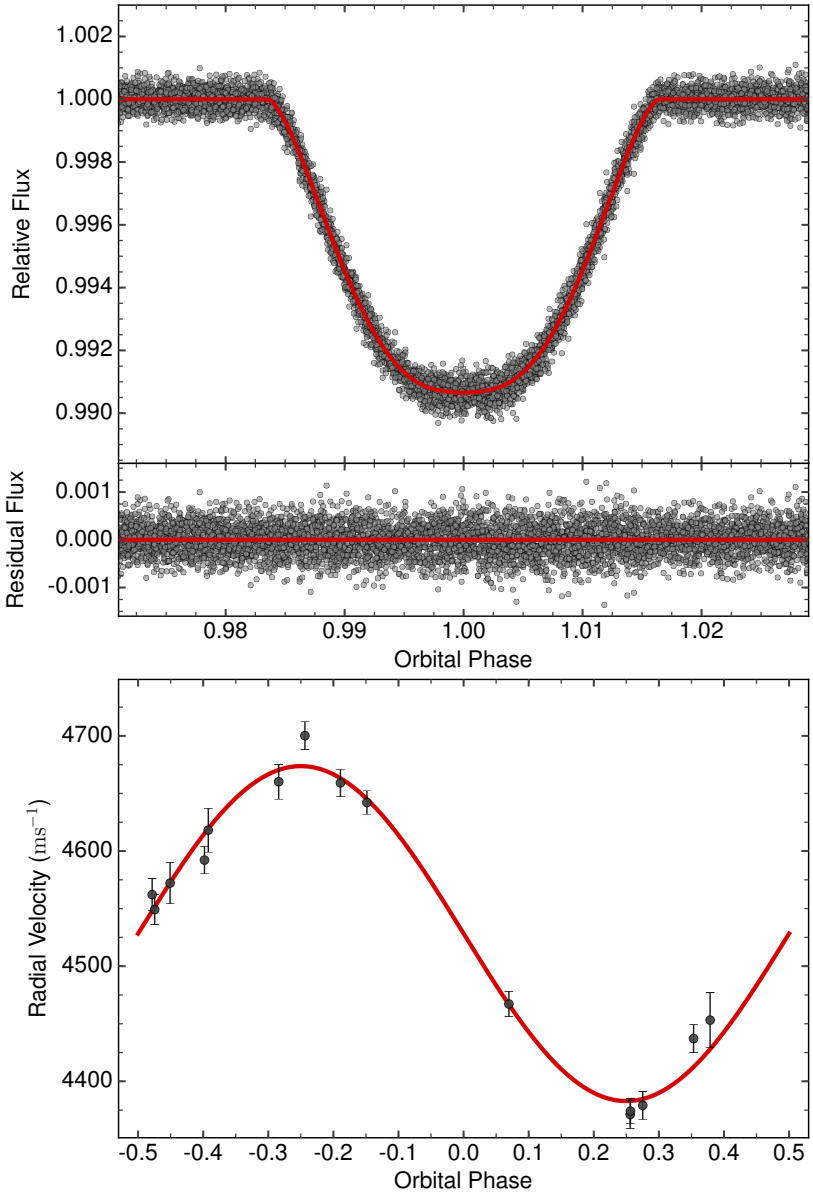

Figure 3.5: The same as Figure 3.4 except for WASP-75b. The top panel shows the fully de-trended, phase-folded K2 lightcurve and model in red. The middle panel shows the residuals of the fit and the bottom panel shows the radial velocity measurements with the best-fitting model in red.

Hellier 2017).

Values of the stellar mass were obtained from a comparison with stellar models by using the BAGEMASS code of Maxted, Serenelli & Southworth (2015a). This took as inputs, the spectroscopic values of stellar effective temperature and metallicity ($[\frac{\mathrm{Fe}}{\mathrm{H}}]$) as well as stellar density from initial MCMC runs. The calculated values were used as a prior constraint in the global MCMC.

Evans et al. (2016) discovered a faint, nearby companion to WASP-55b. They determined that it had a magnitude difference of 5.210 ± 0.018 in the r_{TCI} band[2] at a distance of $4''345 \pm 0''010$, placing it within the aperture that was used. Using Equation 3 of Daemgen et al. (2009), the lightcurve was corrected for the additional flux measured from the companion star. The result was a minor difference in the calculated eclipse depth, with a new value of 0.01551 ± 0.00005 compared to 0.01550 ± 0.00004 before the correction.

3.4 Transit duration and timing variations

Additional planetary companions can cause variations in the timing of transit events due to the gravitational perturbations that they cause (Agol et al. 2005; Holman & Murray 2005). These transit timing variations (TTVs) can range from the order of minutes up to hours for longer period orbits (Holczer et al. 2016) or those near mean-motional resonances. Transit duration variations (TDVs) are also expected to be produced by planetary companions and can also be caused by orbiting bodies such as Exomoons (Kipping 2009). The K2 data were searched for transit timing variations (TTVs) and Transit duration variations (TDVs) by splitting the lightcurves at mid-points between each transit. A single MCMC was then performed for each transit, with no other input data. The parameters from the global MCMC run were used as prior constraints, with transit epoch and duration set as free parameters.

[2]The Two Colour Instrument (TCI) on the 1.54 m Danish telescope in La Silla, Chile, which is approximately equivalent to a wide-passband Cousins I filter.

Against the null hypothesis of equally spaced and equal duration transit events, for WASP-55b χ^2 values of 28.7 and 6.3 were found for the TTVs and TDVs, respectively, with 17 degrees of freedom. Upper limits were placed on the TTVs of 25s and 100s for the TDVs. For WASP-75b, the measured TTVs and TDVs had a χ^2 of 24.8 and 36.3, with 28 degrees of freedom. The upper limits for the TTVs and TDVs were 35 s and 120 s respectively. There was a visual hint of a sinusoidal trend in both the TTVs and TDVs for WASP-75b, which could imply the existence of an additional body in the extrasolar system, as noted above. A sinusoidal curve was fit to the data using a non-linear least squares method (dashed line in figure 3.7). However, this only provided a marginal improvement in the fit, with the model-subtracted residuals having a χ^2 of 24.5 for the TTVs and 35.8 for the TDVs. The fit is not significant enough to claim the existence of any signal, but the slight improvement in fit warrants further study with future, high-quality observations. Given the lack of significant TTVs and TDVs, the existence of large, close-in companion planets can be ruled out for both systems.

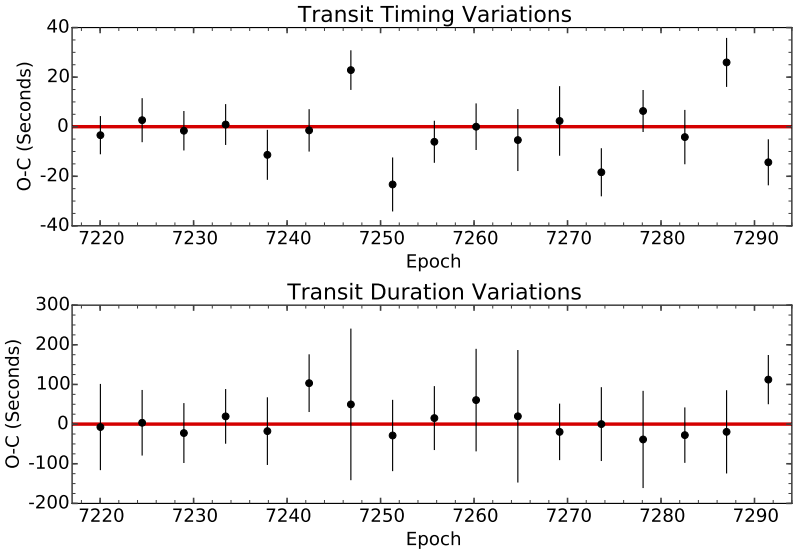

Figure 3.6: The plots shows the difference between the observed and calculated times (top) and durations (bottom) of the WASP-55b transits. The red lines represent the expected Observed-Calculated values should there be no timing deviations.

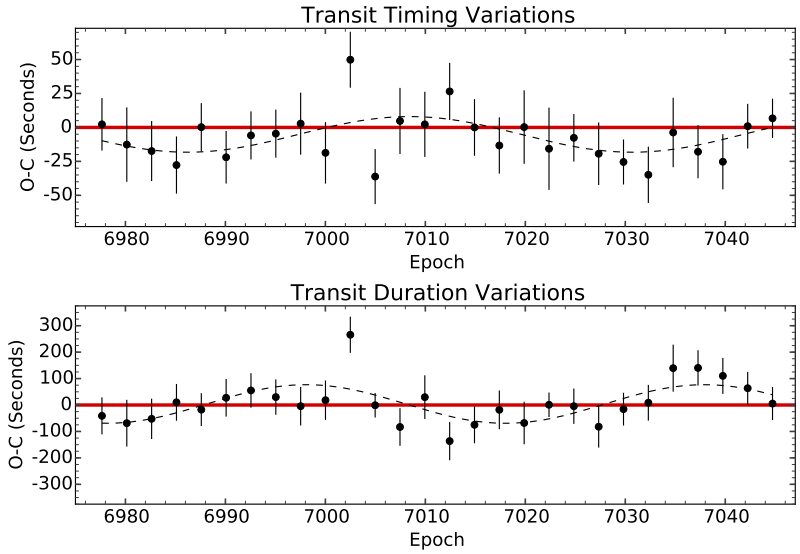

Figure 3.7: Similarly to Figure 3.6 this plots show the observed-calculated times for the transit timing (top) and the transit duration (bottom) for WASP-75b. An additional dashed line shows a sinusoidal fit as described in the text.

The TTVs and TDVs for WASP-55b and WASP-75b are shown in figures 3.6 and 3.7 respectively.

3.5 Starspots and Stellar Variation

A transiting planet that crosses a starspot will cause an apparent, temporary brightening of the light received from the system (Pont et al. 2007; Rabus et al. 2009) usually visible as an upward 'bump' in a transit lightcurve. Starspots have been detected from the ground (Tregloan-Reed, Southworth & Tappert 2013) as well as in K2 data (Močnik, Southworth & Hellier 2017). A thorough visual inspection was performed, searching for starspots in both the de-trended lightcurves and model-subtracted residuals but no evidence of any starspot occultations was discovered in either the WASP-55b or WASP-75b data.

No variations were found in the WASP-55b lightcurve but low-frequency variations were detected in the WASP-75b lightcurve. To investigate these, K2SC (Aigrain, Parviainen & Pope 2016) was used to obtain a systematic-corrected lightcurve from the pre-search conditioned K2 data, which included low-frequency variations but excluded transit events (Figure 3.8). This was used as the initial low-frequency variation lightcurve included a long-term trend that was removed well by the pre-search data conditioning module. The autocorrelation function (ACF) of McQuillan, Aigrain & Mazeh (2013) was used alongside a Lomb–Scargle (LS) periodogram to search the lightcurve for rotational modulation. From the ACF, a period of 11.7 ± 0.5 days was determined from the first three peaks, that is possibly indicative of rotational modulation. This is in agreement with the value of 11.2 ± 1.5 produced by the LS-periodogram (figure 3.8).

For WASP-75b, an updated value for macroturbulence ($v_{\rm mac}$) of 4.05 ± 0.41 km s^{-1} was calculated using the calibrations of Doyle et al. (2014). It produced a new value of $v \sin(i_*) = 3.8 \pm 1.0$ km s^{-1}assuming spin-orbit alignment. This implies a stellar rotation period of 16.9 ± 4.5 days. The marginal agreement between the predicted and measured values of stellar rotation could hint at the possibility of a non-aligned stellar inclination angle. The new $v \sin(i_*)$ was used with the more conservative LS-periodogram measurement of the rotation period of the star to determine that WASP-75b has a possible rotation speed of $v = 5.7 \pm 0.8$ km s^{-1} and a stellar line-of-sight inclination angle of $i_* = 41 \pm 16\,^{\circ}$. Assuming Sun-like starspot latitudes and differential rotation, the stellar line-of-sight inclination angle would be $i_* = 39 \pm 14^{\circ}$.

It is possible to use the value of i_* with the obliquity angle, that can be measured using the Rossiter–McLaughlin (RM) effect (Rossiter 1924; McLaughlin 1924; Triaud 2017a), to calculate the true angle (Ψ) between the stellar rotation and orbital axes. Ψ is important in theories of the formation and evolution of planetary systems (Campante et al. 2016). A RM measurement of WASP-75b would therefore be beneficial in this case. The estimated amplitude of the RM effect is 13 ± 3 m s^{-1} for WASP-75b. This should be measurable with high-resolution spectrographs and a typical RV precision of ~ 4 m s^{-1} is predicted from a 900 s HARPS spectrum of WASP-75.

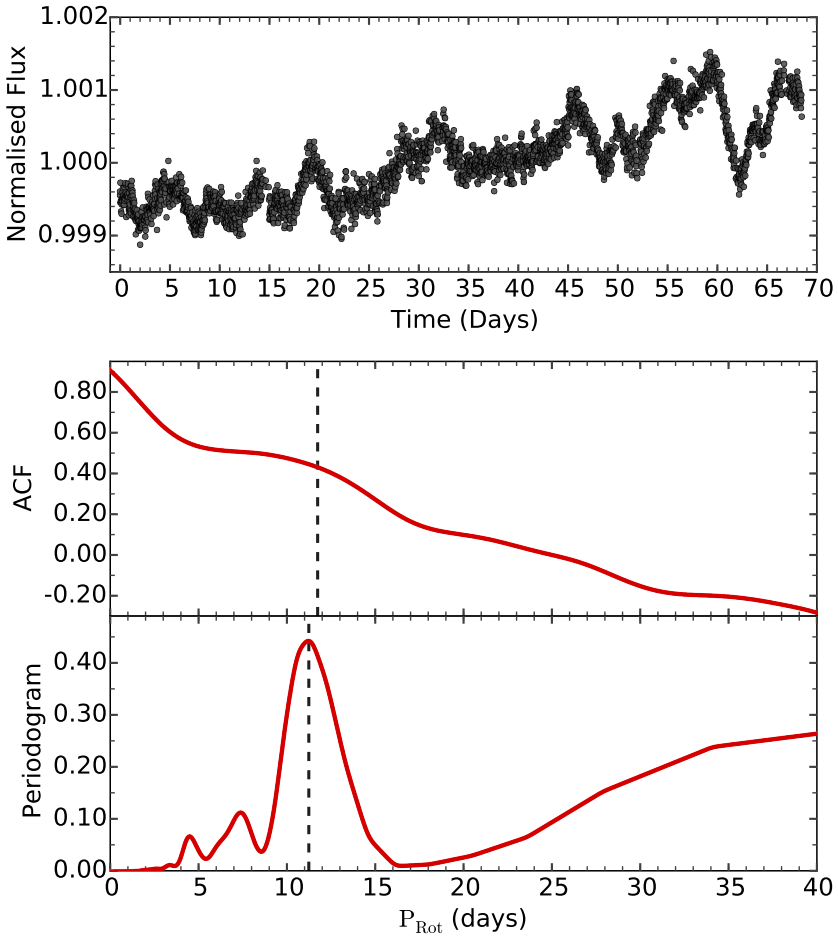

Figure 3.8: The top plot shows the transit-subtracted, SFF de-trended, sigma-clipped WASP-75b lightcurve, binned to 10 minute intervals. The middle plot shows the ACF profile in red, with the centre of the detected peak represented by a black dashed line. The bottom plot displays the LS periodogram of the system, again with the strongest peak shown by the black vertical line.

3.6 Phase-curve variations

At optical wavelengths, phase-curve variations are expected to comprise four main constituents. The first is ellipsoidal variations, a primarily geometrical effect which causes modulation at half the orbital period due to the non-circular shape of the

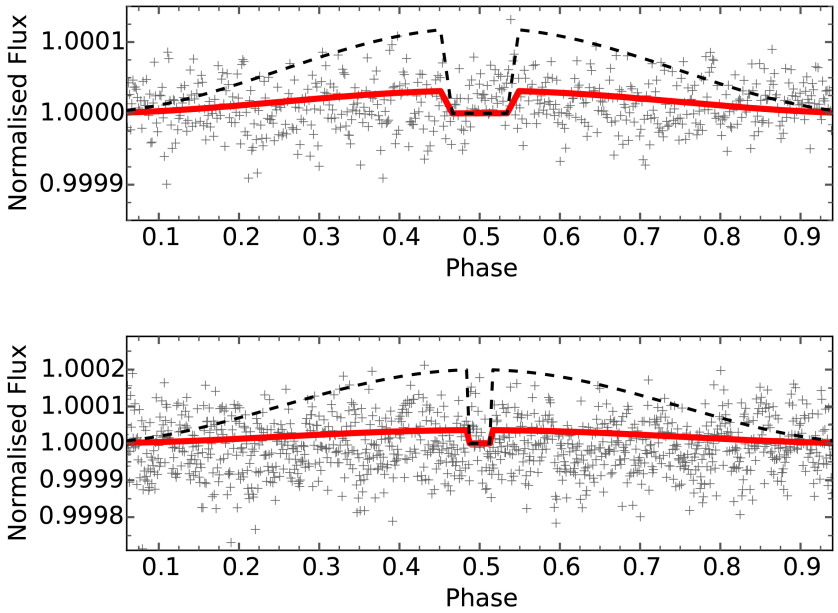

Figure 3.9: The phase-folded residuals for the WASP-75b (top) and WASP-55b (bottom) lightcurves, binned to 5 minute intervals. The red lines show the models for the predicted phase variations described in Section 3.6 and the predicted secondary eclipses at an orbital phase of 0.5. The black dashed lines show the model for an estimated upper limit for phase variations in each system.

star (Jackson et al. 2012; Welsh et al. 2010). The second is Doppler beaming, where the orbiting planet causes variations in the density of photons towards the observer depending on its orbital position (Groot 2012). Thirdly a component of the light from the star is expected to be reflected from the planetary surface, which varies depending on the albedo of the planet and again, its orbital position (Madhusudhan & Burrows 2012). Finally, it is also possible to observe a secondary eclipse, where the planet is occulted by the host star, providing the orbital plane is aligned well with our line-of-sight (Esteves, De Mooij & Jayawardhana 2013). Using equations from Mazeh & Faigler (2010) and the system parameters in Tables 3.1 and 3.2 the predicted amplitudes of these effects were calculated and a phase-curve model was created for each of the two systems. Predicted amplitudes of ellipsoidal variations, Doppler beaming and reflection

(as well as secondary eclipse depth[3]) were 0.4, 0.9 and 13 PPM for WASP-55b and 3.4, 1.9 and 26 PPM for WASP-75b.

A Levenberg–Marquardt algorithm was used to attempt to fit the above model to the phase-folded residual lightcurve of each system. However, in both cases, a negligible amplitude provided the best fit, which was also confirmed visually. Therefore no phase variations were detected in either system. The predicted values were also lower than the precision of the lightcurves; even if variation of this magnitude were to exist, it would not be detectable with the current data. It is possible that the de-trending methods used could have removed phase variations from the original data, but signal injection tests performed by Močnik, Southworth & Hellier (2017) have shown that the SFF method should preserve periodic variations. Therefore conservative estimates were made on the upper limits of the phase curve variations and secondary eclipse depths of 100 PPM for WASP-55b and 60 PPM for WASP-75b. As a result, upper limits can be placed on the geometric albedos of 0.8 and 0.2 for WASP-55b and WASP-75b, respectively. The geometric albedo of a planet is the ratio of its reflected light compared to that of a ideal, flat, fully reflective surface, as observed from the light source. The higher the value of geometric albedo, the more reflective the planet is. The upper limit for WASP-75b is comparable to that of Mars in our own solar system, while the upper limit for WASP-55b is around 20% higher than that of Venus (Mallama, Krobusek & Pavlov 2017). The phase-folded, binned residual lightcurves are shown in figure 3.9 along with the predicted and lower-limit phase-curve models.

3.7 Additional Transiting Planets

To search for signals of additional transiting planets the box-least-squares method of Collier Cameron et al. (2006) was used on the model-subtracted residuals for each

[3]During secondary eclipse, the light received from the planet is blocked. At optical wavelengths, such as this observation, thermal emission is negligible so the eclipse depth is approximately equal to the amplitude of the reflected light.

planet. No significant signals were found in the residuals of WASP-55b dataset but there were significant peaks in the periodogram of WASP-75. However, further inspection revealed that this was due to the presence of residual correlated noise. Therefore no signals were found from additional transiting planets with periods between 0.5 and 35 days in either the WASP-55b or WASP-75b data and upper limits were placed on the eclipse depths of additional planets to 280 and 190 PPM at a period of 0.5 days. As a sanity check, this method was verified on the known additional transiting planets in the WASP-47b system. Using the same method, two additional companions with periods of 0.79 days and 9.03 days were discovered, in good agreement with the literature (Becker et al. 2015).

3.8 Conclusions

In this section the K2 data taken during campaigns 3 and 6 were used to produce and analyse lightcurves for the WASP-75b and WASP-55b systems respectively. The orbital parameters of both systems were refined, as the high quality lightcurves allowed the transit to be modelled with a much greater precision than is possible from ground-based observations. In some cases, the measured parameter precision was improved by a factor of over 6-σ compared to the original measurements (e.g. Planet-to-star area ratio in Table 3.2). As well as updating the system parameters, the lightcurves were also searched for transit timing and duration variations, rotational modulation, starspots, phase curve variations and additional transiting planets; discovering rotational modulation in WASP-75b.

Generally, the refined parameters agreed well with the previously published results and there were no major discrepancies between the different sets of data for each planet. For WASP-55b the parameters produced by this work, shown in Table 3.1, agreed very well with those of Southworth et al. (2016). Generally, similar values were found but to a higher precision, as expected. Minor differences were found between the results produced here and those of Hellier et al. (2012) which have arisen as the

stellar metallicity from Mortier et al. (2013) was used, rather than CORALIE spectra. BAGEMASS (Maxted, Serenelli & Southworth 2015a) was also used to estimate the stellar mass instead of the empirical mass-calibration used by Enoch et al. (2010b); The method has been tested on eclipsing binary stars and validated against other models (Maxted, Serenelli & Southworth 2015a). The different method, combined with a different stellar metallicity are responsible for the divergent values. The estimate of the mass of WASP-55 agrees well with the value from Southworth et al. (2016), which was also produced by interpolating stellar evolutionary models. The orbital separation was calculated using Kepler's third law (equation 1.10) which depends on the stellar mass and period of the system. The larger stellar mass found here produced a larger semi-major axis, which in turn gave a greater value for the stellar radius. Therefore, the different metallicity value, and method used to determine the stellar mass, are responsible for all of the large deviations between the two sets of parameters.

For the WASP-75b dataset there were minor differences between the derived values of orbital period, transit depth, transit duration and the impact parameter and those of Gómez Maqueo Chew et al. (2013). The orbital period, transit depth and transit duration were direct measurements from the transit lightcurves and the impact parameter is calculated using only these parameters (see section 1.2.2). The differences arose as the higher quality data was able to allow a better constraint of the transit shape. The result of this is that similar physical parameters were derived, but to a higher precision.

Due to the results being slightly different to previously published value, there has been only a minor shift in the parameter space of the physical properties of the systems. There is a marked improvement in the precision of the planetary radius due to the high-quality lightcurves. The results also provide confirmation that WASP-55b is more inflated than predicted by the models of (Baraffe, Chabrier & Barman 2008) and, as stated in Southworth et al. (2016), the planet would make a good candidate for atmospheric analysis with transmission spectroscopy.

There were no strong TTVs or TDVs for either WASP-55b or WASP-75b. For

WASP-55b there were a small number of outliers in both the TTVs and TDVs. Residual systematics that were not fully removed by the de-trending process appear to have minor effects, to the order of seconds, on the calculated transit times and durations when each transit was studied individually. For WASP-75b there was a single outlier ($>$ 2-σ from the expected value) in the TTVs at an epoch of 7002.49 which corresponded to the largest uncertainty in the TDV measurements. This measurement is from a transit where data have been clipped due to a thruster event that occurred during the egress portion of the eclipse. As part of the egress is missing, it is difficult to constrain the transit timings when fitting a single lightcurve. The lack of significant signals ruled out the presence of any large, nearby companion planets for both systems and upper limits of 25 s and 35 s were placed on the TTVs and 100 s and 120 s on the TDVs for WASP-55b and WASP-75b respectively.

There was no evidence of starspot occultations in either system, but there did appear to be low-frequency variation in WASP-75b. This gave a tentative estimate of its rotation period as 11.7 ± 0.5 days and an estimate of the stellar line-of-sight inclination angle of $i_* = 41 \pm 16$ °. The stellar rotation period for WASP-75b indicated a gyrochronological age of 0.86 ± 0.32 Gyr using Barnes (2007), 1.0 ± 0.4 Gyr using Mamajek & Hillenbrand (2008) and 2^{+4}_{-2} Gyr using Meibom, Mathieu & Stassun (2009). While consistent with each other, the gyrochronological ages are slightly lower than the 3.9 ± 0.8 Gyr age estimated by BAGEMASS. This could be an indicator that the planet has spun-up the rotation rate of its host star through tidal interactions as the orbit has decayed (Brown et al. 2011). There was no evidence of phase curve variations or additional transiting planets in either system.

This work has shown a close agreement between the parameters produced by data from space-based and ground-based instruments. K2 observations allow a much more precise retrieval of exoplanetary parameters over ground-based observations but repeated, good-quality observations from ground-based instruments, such as those of Southworth et al. (2016), are good enough to accurately constrain the system parameters. The advantage of K2 observations is that they offer periods of continuous

observation which aid in the detection of properties such as the possible stellar modulation in the lightcurve. Such continuous observation is difficult from the ground and requires the use of multiple observatories (see section 1.2.2). In this case, the high-quality nature of the K2 lightcurves enables the detection of transit timing and duration variations on the order of seconds, phase-curve variations on the scale of 60-100 PPM and can detect additional transiting planets with depths as low as 190 PPM.

4 Occultations from Ground-based Observatories

4.1 Overview

In this chapter, the results of ground based observations of occultations of WASP-48b are presented. This section is based upon a paper originally published to Astronomy and Astrophysics, volume 615. I was the lead author and I was primarily responsible for the calibration and reduction of the data as well as the analysis, interpretation of results and writing the paper. I was also solely responsible for the creation of the software pipelines listed in the Appendix section of this thesis. Dr D.R. Anderson was responsible for carrying out the observation as well as guidance on how to carry out the analysis. Dr N. Madhusudhan was responsible for the atmospheric modelling of the planet's day-side atmosphere. Prof. Coel Hellier provided guidance throughout a majority of the work and assisted in writing the paper. Dr A.M.S. Smith helped plan the observations and offered guidance on the initial data reduction. Finally, Prof. A.C. Cameron provided the MCMC routine used in section 4.3.3.

As noted in section 1.4.2, the thermal emission of a transiting planet can be measured by observing the system during an occultation of the planet by its host star (e.g. Charbonneau et al. 2005; Deming et al. 2005; Anderson et al. 2013; Bean et al. 2013; Shporer et al. 2014a; Stevenson et al. 2014; Delrez et al. 2016). By measuring the amount of light blocked over a range of wavelengths it is possible to construct the spectral energy distribution (SED) of the planet's day-side atmosphere. The aim of this chapter was to measure these SEDs so that they could be fit with a theoretical model allowing the internal composition and temperature profile of the atmosphere to be determined (e.g. Line et al. 2014; Madhusudhan et al. 2014).

A thermal inversion is an increase in temperature towards lower pressures in upper planetary atmospheres. Inversions have been claimed for a few hot Jupiters (e.g. Machalek et al. 2008; Wheatley et al. 2010; Haynes et al. 2015). The archetype

of a planet with an inversion was HD 209458 b (Knutson et al. 2008), but a repeat observation cast doubt on the inversion's existence (Diamond-Lowe et al. 2014; Schwarz et al. 2015; Line et al. 2016). Repeat observations are useful as they can help to refine the precision to which the eclipse depth is measured (Agol et al. 2010), can highlight inconsistencies in reduction methods (Zellem et al. 2014) and can give us insight into the stability or weather variations of exoplanet atmospheres (Rauscher et al. 2007; Armstrong et al. 2016).

WASP-48b is a hot Jupiter ($0.98 \pm 0.09\,M_{\rm Jup}$, $1.67 \pm 0.08\,R_{\rm Jup}$) in a 2.1-day orbit around an evolved F-type star ($1.19 \pm 0.05\,M_{\odot}$, $1.75\,R_{\odot}$; Enoch et al. 2011; hereafter E11). O'Rourke et al. (2014) detected the planet's thermal emission in the H, $K_{\rm s}$, and *Spitzer* 3.6-μm and 4.5-μm bands, and found the SED to rule out the presence of a strong atmospheric thermal inversion.

This chapter reports the detection of the thermal emission of WASP-48b from new observations in the $K_{\rm s}$-band (2.1 μm). The data obtained is analysed together with existing occultation lightcurves, radial-velocity data, and transit lightcurves to also update the system parameters. The atmospheric properties of the planet are investigated by comparing the derived SED with model spectra.

4.2 Observations and Data Reduction

The occultation of WASP-48b was observed on 06 Aug 2012 through the $K_{\rm s}$ (8302) filter with the Wide-field Infrared Camera (WIRCam) on the 3.6-m Canada-France Hawaii Telescope (CFHT). WIRCam consists of four 2048 × 2048 pixel, near-infrared (0.9–2.4 μm) detectors, with a total field of view of $20\farcs5 \times 20\farcs5$ (Puget et al. 2004). WASP-48 and nearby stars were observed for 5 hours, with 1236 images being obtained each with exposure times of 5 s. Four images were discarded post-egress, with MJDs between 56145.5119 and 56145.5124, as star trails indicated telescope motion. The telescope was defocused by 2 mm to minimise the effects of flat-fielding errors and to increase the duty cycle. The airmass of the target varied between 1.28–1.23–1.76 during

the sequence. Barycentric corrections were performed for each image accounting for the light travel time of the system.

The data were calibrated using methods similar to that of Croll et al. (2015), rather than using the pre-calibrated data produced from the I'iwi 2.1.1 pipeline. They found that the pipeline introduced additional systematics that degraded the overall quality of lightcurves produced. An automated pipeline was created in PYTHON[1] in order to optimise the data reduction for occultation photometry. The main differences between the I'iwi pipeline and that of Croll et al. (2015) are that they do not use a reference pixel subtraction, a cross-talk correction or a sky frame subtraction. They also have a more lenient bad pixel masking process and they elect to throw away frames if a bad pixel is found within any apertures. The data calibration routine followed the following steps:

1. *Dark correction*

   For the WASP-48b dataset, the dark images consisted of 30 images. These images were median combined to produce a master dark image. This was then subtracted from the master flat field and science images in the usual way (section 2.1.2).

2. *Sky flat correction*

   To create the master flat field image, the 17 raw dithered twilight flat images that were taken for the observation were median combined. The science images were then corrected by dividing by the normalised master flat image.

3. *Saturated pixels*

   As with the I'iwi pipeline, all pixels with values $> 36,000$ Analog-to-digital units (ADU) were considered to be above the saturation threshold and flagged as bad.

[1] http://www.python.org

4. *Bad pixel masks*

   In a similar way to Croll et al. (2015) the master sky flat was used to detect bad pixels. Those that deviated away from the median value by more than 5 times the median absolute deviation (MAD) were flagged as bad.

5. *Bias and non-linear corrections*

   A simple bias subtraction and non-linear corrections were applied to the data, using the WIRCam non-linearity coefficients [2] that were taken in April 2008. Due to the telescope being defocused and the short exposure time, the maximum pixel values are $\sim$15,000 ADU. This is far from the non-linear regime of the detector and the calculated eclipse depths appear to be relatively independent of the non-linear correction.

6. *Sky subtraction*

   A full sky frame subtraction was not used. Instead, the local sky background level around each of the stellar point spread functions (PSF) was estimated when performing aperture photometry (see Section 4.3.1).

7. *Bad pixel corrections*

   In an attempt to correct the bad pixels in the science images, they were separated into two catagories: those near to, or within, the stellar PSFs and those that were located in the sky background. Sky background pixels were replaced using the median value of a 5×5 window around the pixel. For both the target and reference stellar PSFs, any PSFs that contained bad pixels were discarded. Prior to this, an attempt was made to improve on previous interpolation methods by replacing bad pixels using a comparison with good PSFs in the same image (see section 2.1.2.5). Firstly, each PSF was isolated in a small, background-subtracted window. The brightest PSF that did not contain bad

[2] http://www.cfht.hawaii.edu/Instruments/Imaging/WIRCam/WIRCa mNonlinearity.html

pixels was used as a reference kernel. This reference kernel was then fitted to each PSF that had a bad pixel, using a least squares method and the SCIPY NDIMAGE SHIFT package. Pixel values from the fit of the kernel were then used to replace any bad pixel values in the stellar PSF. Testing this method with known pixel values showed that the matched pixel value had a 3-σ accuracy of $\sim$20 %. Whilst this was an improvement over linear interpolation, it still had the possibility to introduce a non-marginal error in the final flux values and therefore, any PSFs with bad pixels were simply rejected.

4.3 Data Analysis

4.3.1 CFHT occultation

Standard circular aperture photometry was used to measure the flux of each star (section 2.2). Circular annular radii were used to estimate the mean background level for every star that was measured. For simplicity, the analysis was limited to include only stars on the same detector as WASP-48.

As the telescope was defocused, common practise is to use the flux-weighted centroid (FWC) method (Knutson et al. 2012; Kammer et al. 2015; Vida et al. 2017) to find the centre of stellar PSFs. However, slight inaccuracies in this method appeared to produce correlated noise in the final lightcurves, especially when using smaller apertures. By investigating further, it was discovered that the detected position would often not be central to the PSF, but instead would be offset by 1-2 pixels. This can be seen in the top mean X-Y profiles in figure 4.1. The detected position relative to the PSF would also vary between images. This appears to be due to the time-varying, non-radially symmetric distribution of flux within the PSF.

To solve this issue, a new mean-profile fitting (MPF) method was used to find the central positions of the stellar PSFs. The method is described in section 2.2.1. It works by fitting a hybrid Voigt profile to the mean X and Y profiles of a small window

around each stellar PSF. Figure 4.1 shows that this method provided a more precise method of detecting the central co-ordinates of the defocused PSFs, which produced a lightcurve containing less correlated noise. This method also produced an estimate for the full-width half-maximum (FWHM) of the defocused PSF using Equation 4.1, an adaptation of the FWHM approximation of Olivero (1977).

$$F_v = W + 0.5346F_l + \sqrt{0.2166F_l^2 + F_g^2} \tag{4.1}$$

Where F_v is the FWHM of the hybrid Voigt profile, F_l is the FWHM of the Lorentzian component of the Voigt profile and F_g is the FWHM of the Gaussian component of the Voigt profile.

Both instrumental effects and the terrestrial atmosphere are sources of noise for ground-based observations. Changes in airmass, sky background, the pixel position of the stars on the detector and the FWHM of the PSF were investigated. Correlations between each of these parameters and the residuals of a model fit to our preliminary differential lightcurve were examined. Having employed the profile fitting method, no significant correlations were found.

The photometric uncertainties were calculated taking into account dark current, read-out noise and Poisson noise of both the star and the sky (see section 2.2.2).

4.3.2 Optimising aperture radii and reference star choices

Differences between the results of repeat analyses is an issue in exoplanet occultation studies (e.g. Evans et al. 2015). The main problem is that the relationship between eclipse depth and the choice of aperture radii and reference stars is often not thoroughly investigated. These two factors can occasionally have a large effect on the resulting eclipse depth and can therefore directly influence inferences that are made about exoplanetary atmospheres. Croll et al. (2015) put forward a method that allows the extent to which these parameters influence the eclipse depth to be explored. A very similar method is used to fully explore this relationship for the WASP-48b $K_{\rm s}$–band reduction.

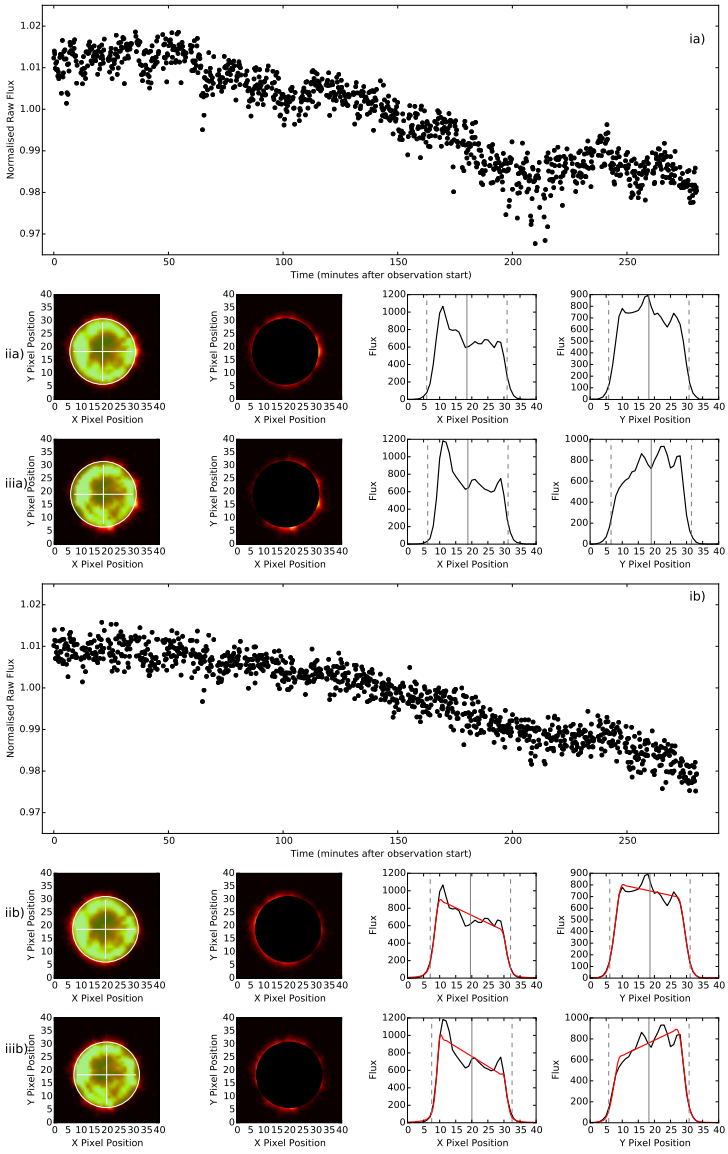

Figure 4.1: A comparison between the commonly used flux-weighted centroid (FWC) method (labelled *a*) and the mean profile-fitting (MPF) method used in this work (labelled *b*). A particularly small aperture is used in this figure to highlight the differences between the two. Panels *i* show the raw lightcurves obtained from each method. The panels *ii* and *iii* show two example PSFs with overlaid apertures. The panels show, from left to right: an image of the PSF overlaid with the chosen aperture (white), the aperture subtracted from the PSF, the mean profile of the PSF window in the X direction and the mean profile of the PSF window in the Y direction. The gray vertical lines represent the detected centre of the PSF for each different profile, while the dashed lines show the placement of the aperture. The red lines in Figures *iib* and *iiib* show the profile that was detected using the MPF method.

The steps of the routine are outlined below.

1. *Source detection*

   SEP, a python Source Extractor Package (Barbary 2016; Bertin & Arnouts 1996), was used to detect all reference stars within the image. The location of the target star was input manually. As the telescope had been defocused, the non-Gaussian PSFs caused the source detection algorithm to fail. As a solution, the background was first calculated and subtracted from the image using SEP. The remaining image was convolved with a PSF kernel, which was pre-selected from the WASP-48b CFHT images, with the requirements of having a high total flux and an absence of bad pixels. This resulted in an image containing Gaussian-like PSFs that was then used with the SEP package to return the coordinates of all stellar PSFs within the image.

2. *Aperture photometry*

   The aperture photometry method from section 4.3.1 was used to perform photometry with a wide range of apertures for the target star and the detected reference stars. For WASP-48b, aperture radii of sizes between 15 and 25 pixels were used in steps of 0.25 and recorded the flux of 40 reference stars.

3. *Initial reference star ranking*

   Initial differential lightcurves were created that consisted of the target star, divided by each reference star, for every aperture size. Each of these lightcurves were analysed individually in a global Markov Chain Monte Carlo analysis (MCMC - see sections 2.5 and 4.3.3), with all transit and radial velocity data from Section 4.3.3, to produce an occultation model. The $RMS \times \beta^2$ was then calculated for the residual scatter of each lightcurve, where β is a parameter

that provided an estimate of the correlated noise within the time-series data (Winn et al. 2008). All reference stars were then ranked in order of the lowest $RMS \times \beta^2$ and the best seven were selected for further analysis.

4. *Combined reference star lightcurves*

   These selected reference stars were then combined to produce further differential lightcurves with potentially lower residual scatter. They consisted of the median-combined lightcurves for every possible combination of the best reference stars and aperture sizes. Once again a full, global MCMC was performed to produce an occultation model and used the residual $RMS \times \beta^2$ to rank the lightcurves.

5. *Eclipse depth dependencies*

   Figure 4.2a shows the determined $RMS \times \beta^2$ as a function of aperture size and number of reference stars. Similar to Croll et al. (2015), best aperture radii and reference star ensemble were chosen by selecting all output lightcurves that produce an $RMS \times \beta^2$ less than 15% above the minimum $RMS \times \beta^2$. This was an arbitrary number, used by Croll et al. (2015), it was also found to give a reasonable representation of the lowest region of $RMS \times \beta^2$ in Figure 4.2a. Figure 4.2b shows how the eclipse depth varies for the same aperture radii and reference star ensembles. For WASP-48b, there was little correlation between the $RMS \times \beta^2$ and the eclipse depth for sensible aperture choices. This indicated that the determined eclipse depth is relatively independent of the choice of these two factors.

6. *Combining outputs*

   As a final step, the output posterior distributions from the MCMCs of the lightcurves that showed the lowest $RMS \times \beta^2$ were combined. For these initial MCMCs, excluding occultation lightcurves from other sources, the calculated eclipse depth was 0.138 ± 0.014 % at a phase of 0.4998 ± 0.0010 in the K_s-band. The lightcurves and models for these are shown in Figure 4.3.

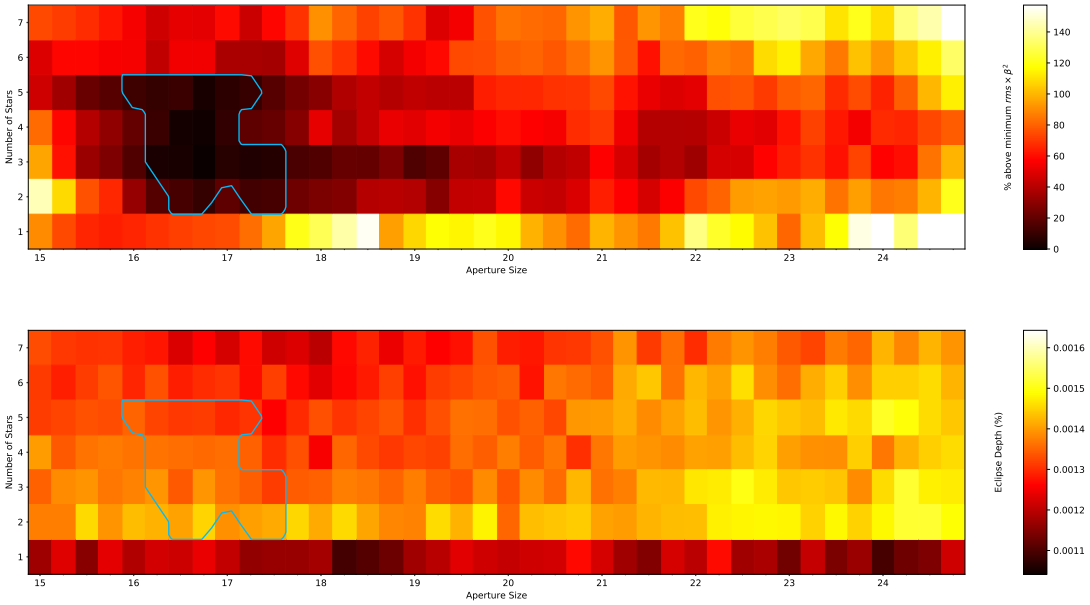

Figure 4.2: *Top:* The percentage of $RMS \times \beta^2$ above the minimum value (0.00201) shown as a function of aperture size and the number of included reference stars. *Bottom:* the percentage eclipse depth as a function of aperture size and number of reference stars. In both cases, the blue contours indicate the region that contains all values less than 15 % above the minimum $RMS \times \beta^2$.

4.3.3 Modelling the transit, occultation and orbit

To determine the parameters of the system, an adaptive MCMC code was used (Collier Cameron et al. 2007b; Pollacco et al. 2008; Anderson et al. 2015b). As well as the initial MCMCs mentioned in section 4.3.1, a final global MCMC was also performed for each of the lightcurves that produced the lowest $RMS \times \beta^2$ in section 4.3.2. These final MCMCs used an additional 4 occultation lightcurves as well as 5 transit lightcurves and 14 radial velocities from SOPHIE (E11) as inputs. The posteriors of every MCMC were then combined and the median and median absolute deviation of the distributions were taken as the parameter values and uncertainties.

The transit lightcurves available for WASP-48b included the LT/RISE and WASP

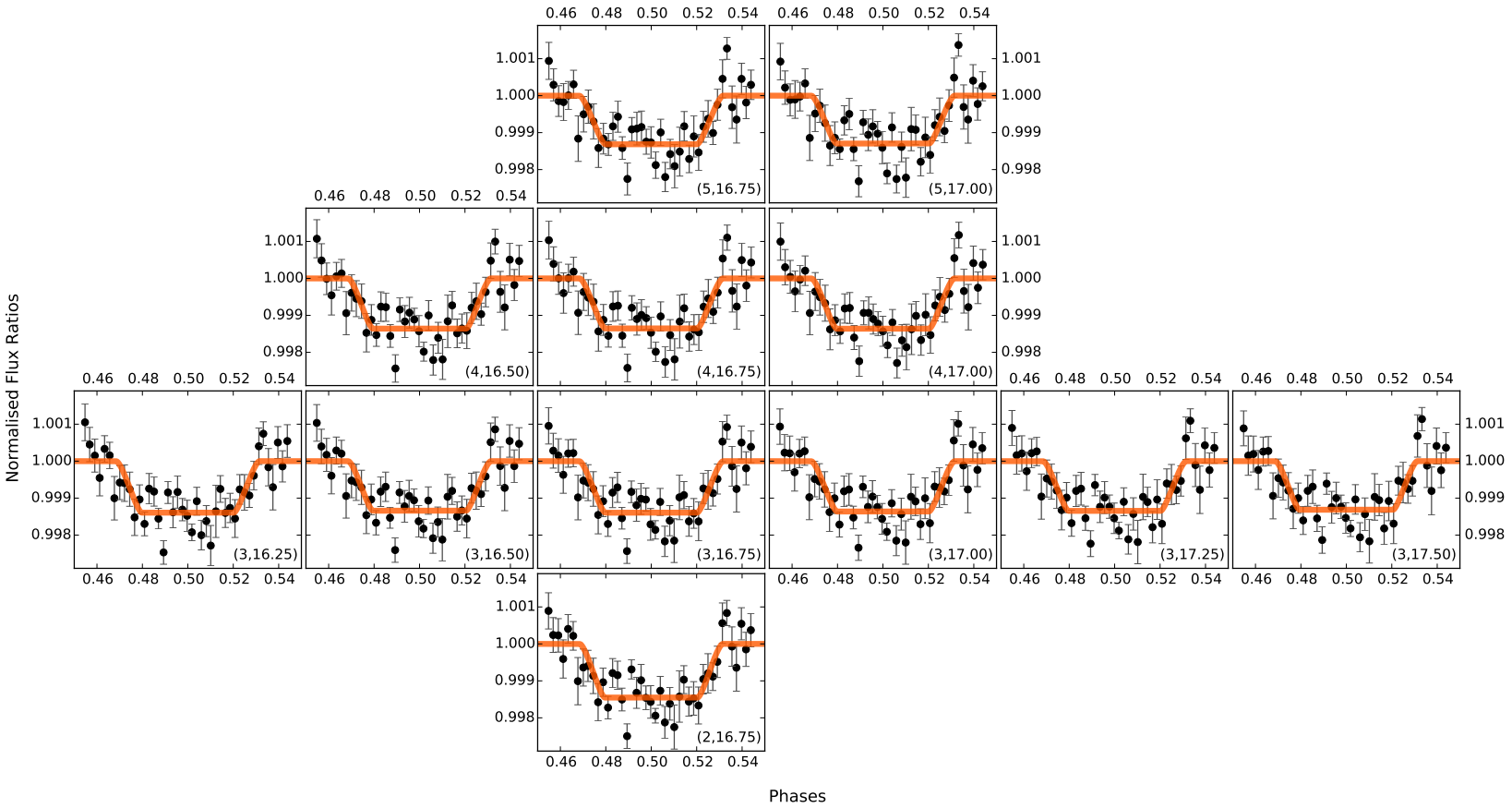

Figure 4.3: The twelve WASP-48b K_s-band occultation lightcurves that show the lowest $RMS \times \beta^2$, created by different combinations of reference stars and aperture sizes. The data are binned in intervals of 10 minutes, with the orange model indicating the MCMC fitted solution for that particular aperture and reference star combination. The caption within the figure lists the number of reference stars and aperture size respectively.

Table 4.1: The transit lightcurves used in our MCMC analysis. The key corresponds to the panels in Figure 4.4. The final column gives source of the lightcurve.

Ref.	Date	Filter	Cadence (s)	Facility	Source
LC1	2010-07-01	$V+R$	71	LT/RISE 2.0m	E11
LC2	2011-05-25	Gunn r	50–90	Cassini 1.52 m	C15
LC3	2011-08-23	Gunn r	50–80	Calar Alto 2.2 m	C15
LC4	2013-07-24	Cousins I	110–120	Calar Alto 1.23 m	C15
LC5	2014-06-02	Cousins R	115–134	Calar Alto 1.23 m	C15

lightcurves from the discovery paper (E11), an ingress observed with the Faulkes Telescope North (hitherto unpublished), the single transit of Sada et al. (2012), 34 transits from the Exoplanet Transit Database[3] (Poddaný, Brát & Pejcha 2010) and all 10 transits from Ciceri et al. (2015), hereafter C15. An initial MCMC fit was performed for each lightcurve using the model of Mandel & Agol (2002) and the four-parameter, non-linear limb darkening law of Claret (2000) and Claret (2004). Transits with high scatter or with significant gaps in the data during the observation were rejected. Transits were then selected based upon their residual RMS, which resulted in 5 transits (the LT/RISE transit from E11, and four transits from C15) being used in the final MCMC runs (Table 4.1; Figure 4.4).

The occultation data consisted of the CFHT K_s-band lightcurves and the H-band, K_s-band, 3.6–μm and 4.5–μm lightcurves from O'Rourke et al. (2014). The H-band and K_s-band observations of O'Rourke et al. (2014) were obtained using the Palomar 200 inch Hale telescope. These observations may have suffered from the reference star and aperture size degeneracies noted in section 4.3.2, but given that the raw data was not publicly available, the processed data from O'Rourke et al. (2014) was used in the final MCMCs. The 3.6–μm and 4.5–μm observations were made using the *Spitzer* space telescope. For each MCMC, both of the specific CFHT K_s-band

[3]http://var2.astro.cz/ETD/archive.php

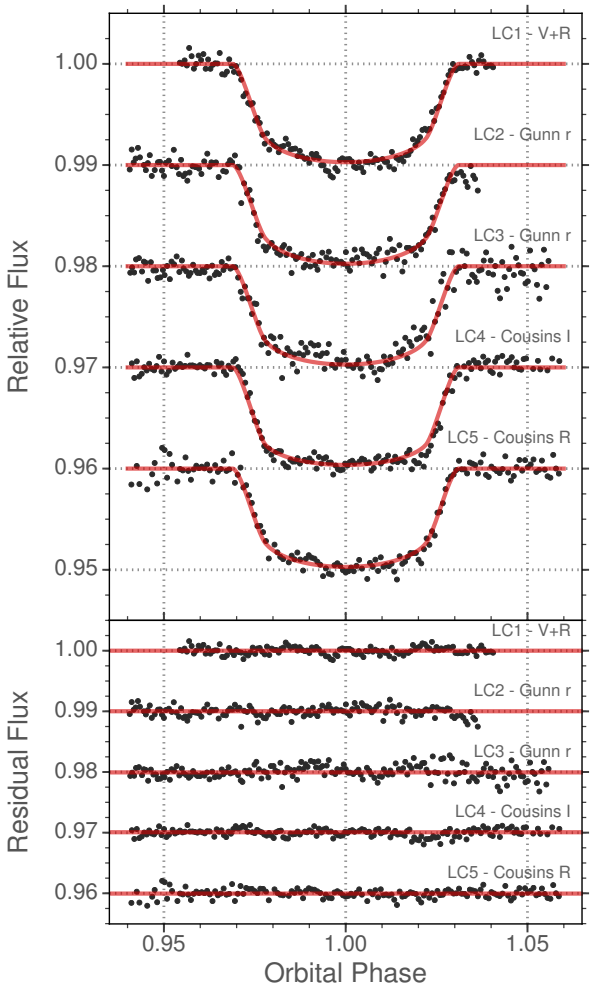

Figure 4.4: *Upper panel*: The transit lightcurves, de-trended as described in the text, and the best-fitting transit model from the MCMC analysis. See Table 4.1 for a further description of each observation. The lightcurves are binned to 2 minute intervals for comparison. Each lightcurve is shifted downwards on the Y axis by 0.01 to allow all lightcurves to be displayed on the same plot. *Lower panel*: The residuals about the fits.

lightcurve and the Palomar K_s-band lightcurve were fit with a single model.

The MCMC code allows the de-trending of both transit and occultation lightcurves against multiple parameters. All transit lightcurves were de-trended with a quadratic

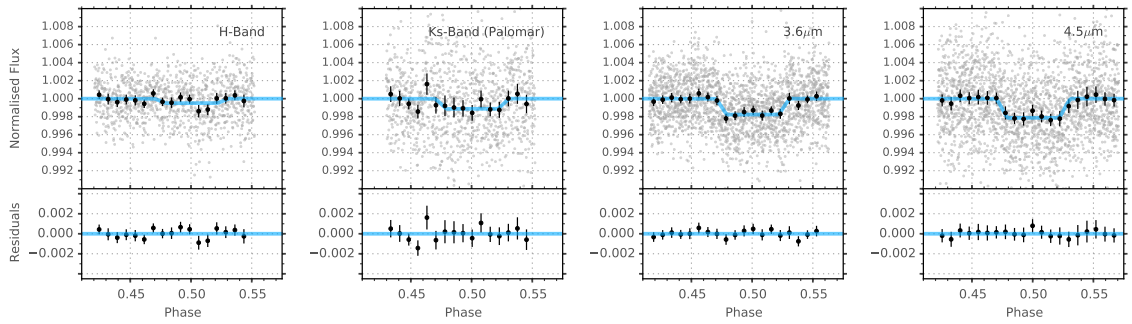

Figure 4.5: The occultation lightcurves from O'Rourke et al. (2014), de-trended as described in Section 4.3.3. The best-fitting occultation models from the global MCMC analysis are plotted in blue. The black points with error bars show the data binned in 20 minute intervals. The bottom row shows the binned residuals about the fits.

function of time as it led to a decrease in the residual RMS scatter over linear de-trending or not de-trending. The *Spitzer* lightcurves were de-trended for the PSF position and the *Palomar* data was de-trended against linear time. The model with which to de-trend the K_s-band CFHT lightcurve was chosen using the Bayesian information criterion (Schwarz 1978), which penalises model complexity. Possible dependencies on time, airmass, detector position, sky background and FWHM were investigated in various combinations, but a linear function of time alone resulted in a significant improvement in the final $RMS \times \beta^2$.

The free parameters used in the MCMC code are listed in Table 4.2 as 'proposal' parameters. Values of stellar mass ($1.113 \pm 0.084\,M_\odot$) and age (6.5 ± 1.7 Gyr) were obtained from a comparison with stellar models using the BAGEMASS code of Maxted, Serenelli & Southworth (2015b). Inputs of $T_{\rm eff} = 6000 \pm 150$ K and [Fe/H] $= 0.12 \pm 0.12$ from the spectral analysis of E11 and $\rho_* = 0.276 \pm 0.018\ \rho_\odot$ were used from an initial MCMC run. At each step in the MCMC analysis, a value of M_* was drawn from a normal distribution with mean and standard deviation equal to the BAGEMASS-derived values.

The median values and the 1σ limits of the final MCMC parameters combined posterior distributions are presented in Table 4.2. The corresponding models along with the transit lightcurves are plotted in Figure 4.4 and the de-trended occultation lightcurves in Figure 4.5.

The system parameters were updated by analysing the five highest quality tran-

Table 4.2: Orbital, stellar and planetary parameters from the MCMC analysis. Each of the proposal parameters, derived parameters, and parameters controlled by priors is listed separately.

Parameter	Symbol (unit)	Value
MCMC proposal parameters		
H-band occultation depth	δ_H (%)	0.050 ± 0.015
Ks-band occultation depth	δ_{Ks} (%)	0.136 ± 0.014
3.6μm occultation depth	$\delta_{3.6}$ (%)	0.176 ± 0.013
4.5μm occultation depth	$\delta_{4.5}$ (%)	0.213 ± 0.020
Orbital period	P (d)	$2.14363400 \pm 0.00000002$
Epoch of mid-transit (BJD-2 450 000, TDB)	T_c (d)	$5\,876.88019 \pm 0.00015$
Transit duration (from first to fourth contact)	T_{14} (d)	0.130 ± 0.001
Planet-to-star area ratio	$R_{\rm P}^2/{\rm R}_*^2$	0.00917 ± 0.00010
Impact parameter	b	0.66 ± 0.02
Semi-amplitude of the stellar reflex velocity	K_1 (m s^{-1})	134 ± 10
Centre-of-mass velocity	γ (m s^{-1})	$-19\,684 \pm 7$
	$e\cos\omega^\dagger$	$0.00046^{+0.00091}_{-0.00074}$
	$e\sin\omega^\dagger$	$0.00040^{+0.01325}_{-0.00417}$
Stellar mass‡	M_* ($M_\odot$)	1.113 ± 0.084
MCMC Derived parameters		
Orbital inclination	i (°)	81.59 ± 0.40
Orbital eccentricity	e	<0.008 at 1σ
		<0.072 at 3σ
Semi-major axis	a (AU)	0.034 ± 0.001
Phase of mid-occultation	$\phi_{\rm mid-occultation}$	0.5003 ± 0.0006
Occultation duration	T_{58} (d)	0.131 ± 0.001
Duration of occultation ingress ($\approx$ egress)	$T_{56} \approx T_{78}$ (d)	0.0194 ± 0.0011
Stellar radius	R_* ($R_\odot$)	1.594 ± 0.051
Stellar surface gravity	$\log g_*$ (cgs)	4.079 ± 0.021
Stellar density	ρ_* ($\rho_\odot$)	0.275 ± 0.017
Planetary mass	$M_{\rm P}$ ($M_{\rm Jup}$)	0.920 ± 0.080
Planetary radius	$R_{\rm P}$ ($R_{\rm Jup}$)	1.485 ± 0.052
Planetary surface gravity	$\log g_{\rm P}$ (cgs)	2.980 ± 0.038
Planetary density	$\rho_{\rm P}$ ($\rho_{\rm J}$)	0.28 ± 0.03
Planetary equilibrium temperature *	T_P (K)	1980 ± 54

*Assuming a zero bond albedo and efficient day–night redistribution of heat.
† $\sqrt{e}\cos\omega$ and $\sqrt{e}\sin\omega$ were used as proposal parameters but $e\cos\omega$ and $e\sin\omega$ are reported here for convenience.
‡Constrained by a Gaussian prior.

Table 4.3: A comparison between the calculated solution and the literature.

Parameter	E11	C15	This Work
b	0.73 ± 0.03	0.66 ± 0.03^a	0.66 ± 0.02
ρ_*	0.21 ± 0.04	0.303 ± 0.022	0.275 ± 0.017
M_*	1.19 ± 0.05	1.062 ± 0.074	1.113 ± 0.084
R_*	1.75 ± 0.09	1.519 ± 0.051	1.594 ± 0.051
$M_{\rm P}$	0.98 ± 0.09	0.907 ± 0.085	0.920 ± 0.080
$R_{\rm P}$	1.67 ± 0.01	1.396 ± 0.051	1.485 ± 0.052

[a]The angle was calculated using: $b = a \cos i / R_*$.

sits together with all the available radial velocities and occultation lightcurves. In Table 4.3 some key system parameters from the calculated solution are compared with those of E11 and C15. A stellar density that is $1\,\sigma$ lower than C15 was obtained. This resulted in a stellar mass, via evolutionary models, $\sim 0.4\,\sigma$ larger than found by C15. In turn, the stellar radius found is $1\,\sigma$ larger than that of C15. As both transit depths are similar, the planetary radius is also larger by $1\,\sigma$. The radius derived for WASP-48b is consistent with that predicted by the empirical relation of Enoch, Collier Cameron & Horne (2012) based on the planet's mass, irradiation and host-star metallicity ($1.51 \pm 0.04\ R_{\rm P}$).

It was then checked to see whether any single lightcurve could have biased the time of mid-occultation, and therefore the occultation depths of the other bands, in the global solution. The occultation mid-points and depths, from MCMCs in which only one occultation lightcurve was fit, are consistent with those obtained from the final MCMCs (Table 4.4).

The $K_{\rm s}$-band occultation depth (0.109 ± 0.027 %) of O'Rourke et al. (2014) is consistent with the fit to their data (0.108 ± 0.026 %) and with the depth from the fit to the $K_{\rm s}$-band data alone (0.138 ± 0.014 %) as well as the global solution (0.136 ± 0.014 %). The timing offset of the eclipse for the global solution (0.9 ± 1.9 mins) was consistent with the timing offset produced from the MCMCs in section 4.3.2, using the CFHT occultation alone (-0.3 ± 2.2 mins). The values of $e \cos \omega$ are also in good agreement, with values of 0.00046 ± 0.00091 and 0.00000 ± 0.00103 for the global and CFHT $K_{\rm s}$-band MCMCs respectively. This demonstrates that the $K_{\rm s}$-band CFHT data is able to solely constrain the timing of the occultation.

From an analysis of the radial-velocity data and limited transit data, E11 found the eccentricity of the orbit to be small and consistent with zero: $e = 0.058^{+0.058}_{-0.035}$.

The addition of the CFHT occultation lightcurve results in a far tighter constraint on eccentricity (Figure 4.6), and more so with the addition of the four occultation lightcurves of O'Rourke et al. (2014). Thus the eccentricity was found to have a value of $e < 0.008$ at the 1-σ level and $e < 0.072$ at the 3-σ level.

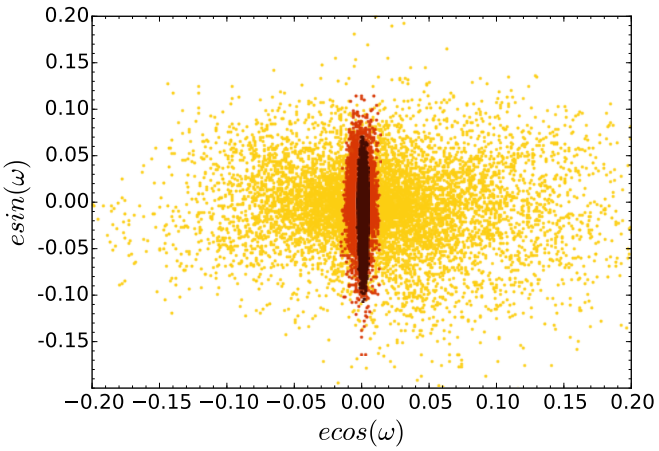

Figure 4.6: The posterior distributions of $e \sin \omega$ and $e \cos \omega$ for different subsets of data (represented by different colours). The results are plotted from analysing transit lightcurves and radial velocities alone (yellow), when including the K_s-band CFTH occultation lightcurve (red) and when the four occultation lightcurves of O'Rourke et al. (2014) were also included (black).

4.3.4 Checking the effects of time-correlated noise

Time-correlated noise can produce variations in lightcurves with similar amplitudes to occultations meaning the measurements of the latter could be affected. The levels and timescales of red noise in the occultation lightcurves was estimated by comparing the residual scatter with the white-noise expectation for a range of temporal bin sizes (Figure 4.7). This suggested that red noise could be significant in both of the Palomar lightcurves and in the *Spitzer* 3.6-μm lightcurve.

The effect of red noise on the measurements of the occultation depth and mid-point was investigated using the residual permutations or "Prayer-Bead" method (Gillon et al. 2009b; Winn et al. 2009). The residuals were sequentially shifted from each of the de-trended occultation lightcurves before adding back the model and trend

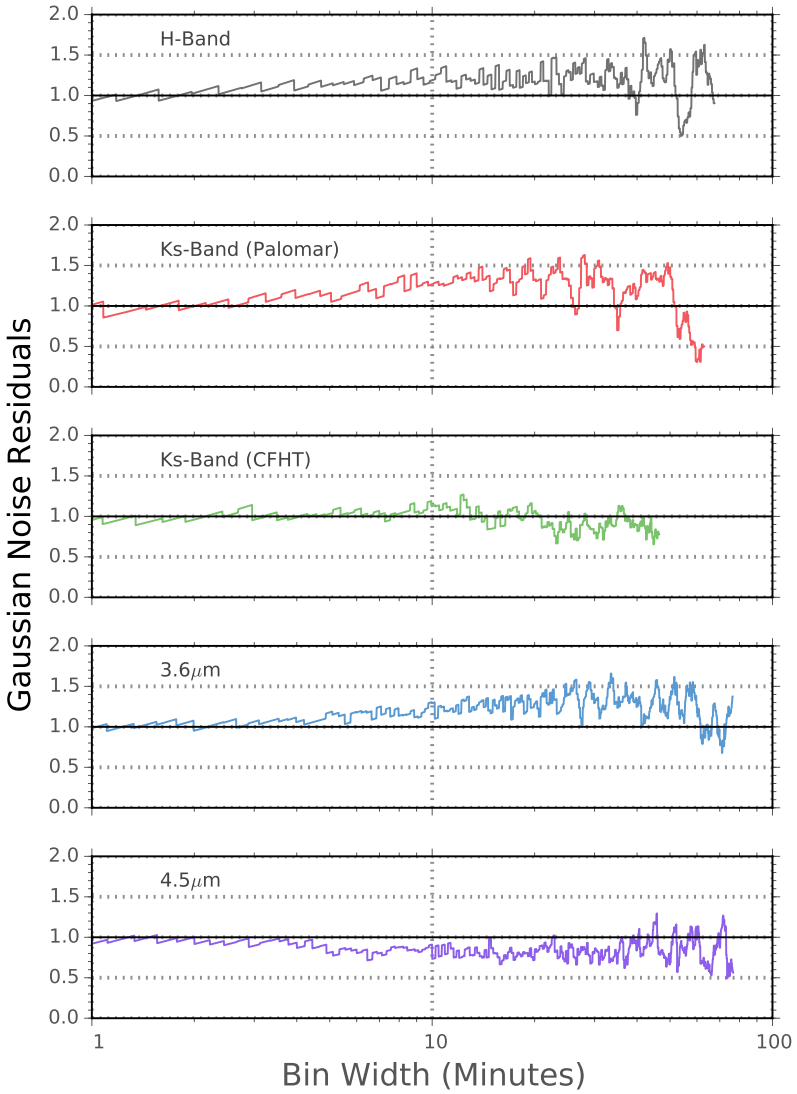

Figure 4.7: Residual RMS versus bin width as compared to the white-noise expectation. This is similar to the common RMS vs. bin-width plot (e.g. Figure 6 of Hardy et al. 2017), except the white-noise prediction has been divided out so that deviations from this level are clearer.

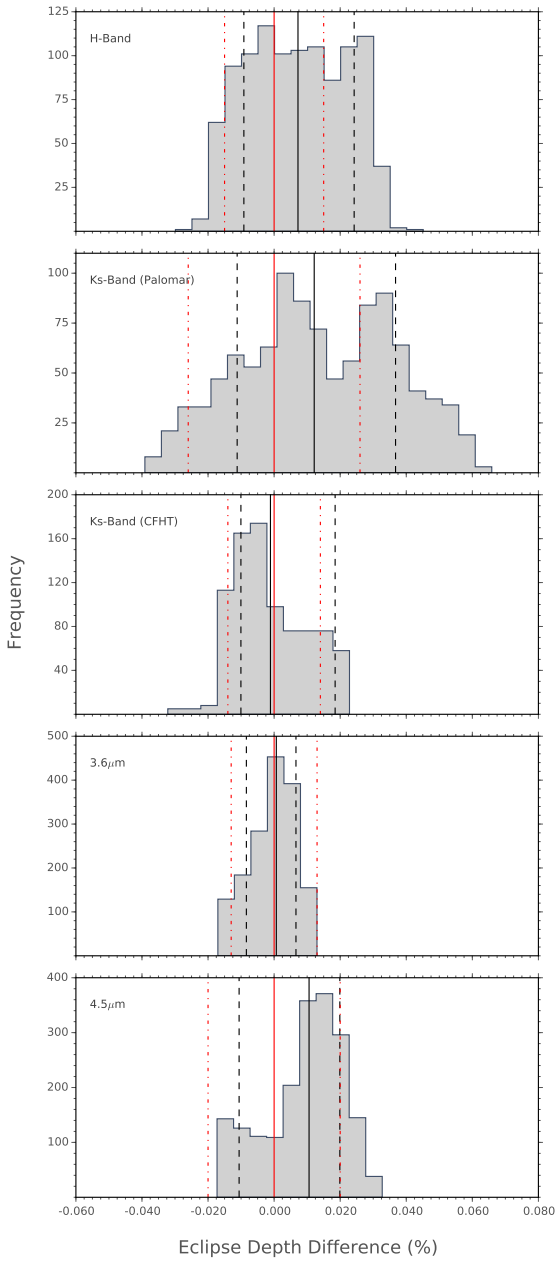

Figure 4.8: The distributions of occultation depth produced by the residual permutations method. In each case, the value from the final MCMCs (solid red line) has been subtracted; the dashed red lines are the MCMC 1-σ limits. The solid and the dashed black lines are the medians and the 1-σ confidence intervals of the residual-permutations distributions.

function, such that there are as many lightcurves produced as there are data points. Thus the temporal structure of any red noise was preserved. Then the MCMC code was applied to each of these lightcurves. The distributions of the occultation depths is plotted in Figure 4.8 and the median and 1-σ limits of the distributions of occultation depth and mid-point are given in the final two columns of Table 4.4. From the close agreement with the values of the final MCMCs, it appears that red noise does not significantly affect the results, therefore the final MCMC solution was adopted. (Table 4.2).

4.4 Atmospheric analysis

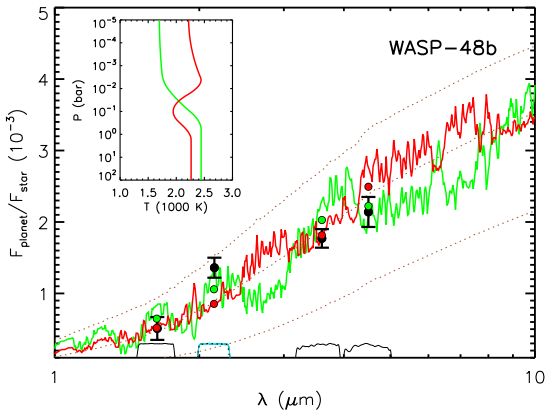

Figure 4.9: A comparison of the planet-to-star contrast ratios of WASP-48b with model spectra. The red line depicts a model with a thermal inversion and the green line is for a model without an inversion. The black points show the contrast ratios from the analysis (Table 4.2) and the coloured points show the band-integrated values of the two models. The transmission curves of each filter are plotted in black, though the CFHT K_s-band is plotted in blue and the black dotted line is the Palomar K_s-band. The similarity between the two allows them to be analysed together. The inset plot shows the the pressure-temperature profiles of the two models. The three dashed lines are black bodies with temperatures of 1500, 2100 and 2500 K.

Possible constraints on the thermal structure and chemical composition of the day-side atmosphere of WASP-48b were investigated by comparing the planet-to-star flux ratios of Table 4.2 with atmospheric models. The H-band and K_s-band, due to

their lack of strong spectral features, are spectral windows that probe the temperature profile in the deep atmosphere of the planet, which is expected to be isothermal for pressures above $\sim$ 1 bar (Madhusudhan 2012). On the other hand, the *Spitzer* 3.6 and 4.5 μm bands span spectral features due to several molecules and hence probe temperatures at different altitudes in the atmosphere. Importantly, these two bandpasses are particularly useful for constraining thermal inversions in hot Jupiters as, for solar composition atmospheres, the presence of a strong thermal inversion is expected to result in significantly higher thermal emission at 4.5 μm than at 3.6 μm due to strong CO emission (Burrows et al. 2007b; Burrows, Budaj & Hubeny 2008; Fortney et al. 2008; Madhusudhan & Seager 2010).

The day-side emergent spectrum of WASP-48b was modelled using the atmospheric modelling and retrieval method of Madhusudhan & Seager (2009) and Madhusudhan (2012). The model computes line-by-line radiative transfer in a plane-parallel (1-D) atmosphere assuming hydrostatic equilibrium, local thermodynamic equilibrium (LTE), and global energy balance. A Kurucz model was assumed for the stellar spectrum (Castelli & Kurucz 2004) appropriate for the stellar parameters. The pressure-temperature (P–T) profile and molecular volume mixing ratios were free parameters in the model. The P–T profile comprised of six free parameters and the volume mixing ratio of each molecular species, assumed to be uniformly mixed in the atmosphere, constituted an additional free parameter. The dominant sources of opacity expected in hot Jupiter atmospheres were included, namely, molecular line absorption due to H_2O, CO, CO_2, CH_4, C_2H_2, HCN, TiO, and VO (see e.g. Madhusudhan 2012; Moses et al. 2013) and H_2-H_2 collision-induced absorption (Borysow 2002). The generality of the parametric P–T profile and the range of molecules included allowed an exhaustive exploration of the model parameter space, including models with and without thermal inversions and those with oxygen–rich versus carbon-rich compositions. However, given the limited number of observations available, the goal of the present work was not to find a unique model fit to the data, but instead to constrain the regions of atmospheric parameter space that are allowed or ruled out by the data.

It was found that current data provide only marginal constraints on the presence of a thermal inversion in the day-side atmosphere of WASP-48b. The observations and two model spectra are shown in Figure 4.9. Both models have a solar abundance composition in chemical equilibrium (Burrows & Sharp 1999; Madhusudhan 2012) but with very different temperature profiles, one with a thermal inversion and the other without. Both profiles produce a model that is consistent with the data, but the model without a thermal inversion provides a marginally better fit. In the non-inverted model, the spectral features are caused by molecular absorption due to the temperature decreasing with altitude above the planetary photosphere at $\sim$1 bar. The peaks in the H and K_s bands and in part of the 3.6-μm band show continuum emission from the photosphere due to the lack of significant molecular features at those wavelengths.

The molecular features in the 3.6-μm and 4.5-μm bands are caused predominantly by H_2O and CO. In contrast, in the inversion model, the peaks in the spectra are caused by molecular emission features due to the same molecules, H_2O and CO, whereas the troughs represent the continuum emission from the photosphere. The H-band and K_s-band points very well constrain the isothermal temperature profile in the lower atmosphere to be ∼2300 K, regardless of the presence/absence of an inversion in the upper atmosphere. The error bar on the 4.5-μm measurement, which is crucial to constrain the thermal inversion, makes it hard to distinguish between the two models. Moreover, a featureless blackbody spectrum of ∼2100 K, as shown by the central dotted curve, also provides a reasonable match to the data, further confirming the inability of the data to constrain the temperature profile in the upper atmosphere. Finally, while solar composition models as shown here provide a good match to the current data the actual composition is largely unconstrained due to degeneracy with the inconclusive temperature profile.

4.5 Discussion

The thermal emission of WASP-48b was detected in the K_s-band, finding a planet-to-star contrast ratio of 0.136 ± 0.014 %. By optimising the selection of aperture radii and reference star choices, using a calibration pipeline that is optimised for ground-based occultation photometry and using a new centering method, a significant improvement in the quailty of lightcurve was obtained. Compared to traditional methods, the RMS scatter of the final lightcurves were reduced by ∼30 %.

The results were combined with existing infrared measurements to investigate the planet's atmosphere. It was found that the current data marginally favour an atmosphere without a thermal inversion, but are also compatible with its presence. There are a number of similar cases, where the data are unable to strongly constrain the presence of a temperature inversion (Knutson et al. 2008; Désert et al. 2011; Smith et al. 2012; Todorov et al. 2013; Line et al. 2016; Hardy et al. 2017). In fact, even for well studied atmospheres, the detection of a thermal inversion can be ambiguous. The first temperature inversion in the atmosphere of a hot Jupiter was claimed for HD 209458 b, which became the archetype (Knutson et al. 2008). However, recent studies based on new data and a reanalysis of existing data have found no evidence for a strong temperature inversion (Diamond-Lowe et al. 2014; Schwarz et al. 2015; Line et al. 2016). Confirming the presence of a thermal inversion can be difficult because there is often a degeneracy caused by the limited number of SED data points and the degrees of freedom allowed by the molecular abundances in model spectra (Madhusudhan & Seager 2009). The precision of the contrast ratios is also a factor in distinguishing between models. Specifically, a higher precision measurement at 4.5-μm would help to

discriminate between the two scenarios in figure 4.9. Also, as photometric bandpasses can average over multiple molecular features, small inversions can often be masked. High-precision spectroscopic observations, such as those in Deming et al. (2013), will ultimately be required to place stringent constraints on the temperature profile as well as chemical composition of the atmosphere of WASP-48b. Murgas et al. (2017) performed such observations of WASP-48b with the ground-based OSIRIS spectrograph on the 10.4 m Gran Telescopio Canarias (telescope). They obtained a flat, featureless optical transmission spectrum of WASP-48b that agreed with a cloud-free atmosphere including the presence of titanium oxide and vanadium oxide. However, the result was not statistically significant enough to claim a detection of either molecule.

A $K_{\rm s}$-band eclipse depth similar to that of O'Rourke et al. (2014) was determined. The CFHT $K_{\rm s}$-band depth is 0.029 % larger than the value that they report, which in comparison to their 0.027 % reported uncertainty indicates that there is little variation between the two measurements. This rules out large temperature variations or violent storms on short time-scales in the atmosphere of WASP-48b at the deep regions that the $K_{\rm s}$-band is able to examine. The result also helps to place a limit on the systematics of these types of ground-based observations; despite using a different telescope and detector, as well as a different reduction method, a $K_{\rm s}$-band eclipse depth was measured that agrees with O'Rourke et al. (2014) to the 1-σ level. However, this is not the case for all repeat occultation analysis that have been performed from ground-based instruments. For example the Ks-band measurements of TRES-3b preformed by de Mooij & Snellen (2009) and Croll et al. (2010b) were discrepant by $\gtrsim$2-σ, which Croll et al. (2010b) note, is best explained by the impact of systematic uncertainties in the observations of de Mooij & Snellen (2009).

It is important to ensure that transit and occultation analyses are robust and produce repeatable eclipse depths. It is believed that the method put forward by Croll et al. (2015), and used in this work, sufficiently explores the effects that choices in aperture size and companion stars have on the final result. As well as this, the presence of correlated noise was determined to have little effect on the resulting eclipse depth. By ruling out factors such as these, the eclipse depths produced should be reliable and enable us to make accurate deductions about exoplanets and their atmospheres.

Table 4.4: The occultation depths and mid-occultation phases of WASP-48. We adopt the values in bold.

Waveband (μm)	From O'Rourke et al. (2014)		**Final MCMCs**		Individual MCMCs		Residual permutation	
	Occult. depth (%)	Phase of mid-occult.	**Occult. depth (%)**	**Phase of mid-occult.**[b]	Occult. depth (%)	Phase of mid-occult.	Occult. depth (%)	Phase of mid-occult.
1.6 (H)	0.047±0.016	0.5010±0.0013	**0.050±0.016**	**0.5003±0.0006**	0.050±0.015	0.5030±0.0069	0.057±0.017	0.5009±0.0063
2.1 (Ks)(Palomar)	0.109±0.027	0.5010±0.0013	**0.136±0.014**[a]	**0.5003±0.0006**	0.108±0.026	0.5003±0.0024	0.120±0.024	0.5005±0.0022
2.1 (Ks)(CFHT)	-	-	**0.136±0.014**[a]	**0.5003±0.0006**	0.138±0.014[c]	0.4998±0.0010[c]	0.135±0.014	0.5002±0.0009
3.6	0.176±0.013	0.5001±0.0026	**0.176±0.013**	**0.5003±0.0006**	0.177±0.013	0.5001±0.0007	0.180±0.011	0.5004±0.0010
4.5	0.214±0.020	0.5013±0.0015	**0.213±0.021**	**0.5003±0.0006**	0.213±0.020	0.5023±0.0012	0.224±0.013	0.5005±0.0006

[a] We fit a single model to both K_s-band data sets in each MCMC.

[b] In the global MCMCs the occultation mid-phase and duration were common to each lightcurve.

[c] Values were obtained from the combined posteriors of the individual MCMCs as discussed in 4.3.2.

5 Ground-based Spectrophotometry of Exoplanet Atmospheres

5.1 Overview

The thermal emission of an exoplanet is measurable from the ground by viewing an occultation of the planet by its host star (e.g. Anderson et al. 2013). As noted in section 1.4.2, by measuring this at several wavelengths we can populate the spectral energy distribution (SED) of a planet's dayside atmosphere. By comparing the SED to detailed model spectra we can infer properties of the atmosphere, such as its composition and temperature structure (Madhusudhan et al. 2011). To date this has mostly been accomplished using broad-band photometric measurements such as those of Gillon et al. (2009a) and those in chapter 4. Though useful, the information content of broad-band measurements is limited and often proves insufficient to distinguish between disparate atmospheric models (Madhusudhan & Seager 2010).

A major advancement in the study of exoplanet atmospheres will be made by progressing from broad-band photometry to spectroscopy. With spectroscopy the dayside SED of an exoplanet can be measured with a significantly higher resolution than is obtainable through photometry and, further, it is possible with a only single observation. This is a challenging concept but Bean et al. (2013) have shown, using MMIRS on the 6.5m Magellan II telescope, that this technique is feasible from ground-based instruments. Detailed SEDs will allow a much more precise retrieval of the thermal structure of planet's dayside atmospheres, it can identify molecular bands and, with repeat observations, even possibly search for variations in the spectrum caused by the exoplanet's weather. An exciting prospect is the diagnostic potential of planets carbon-to-oxygen (C/O) ratios. It has been suggested that C/O ratios may be indicative of the migration pathways of hot Jupiters (Madhusudhan, Amin & Kennedy 2014). With current technology, such investigations are only possible for the most favourable targets. This section details an attempt at making such observations for two planets: WASP-77Ab and WASP-85Ab.

5.2 Observations and Data Reduction

WASP-77Ab and WASP-85Ab were observed using using the Spectrograph for INtegral Field Observations in the Near Infrared (SINFONI) instrument on the VLT. SINFONI is an integral field unit that observes in the near-infrared at wavelengths between 1.1 to

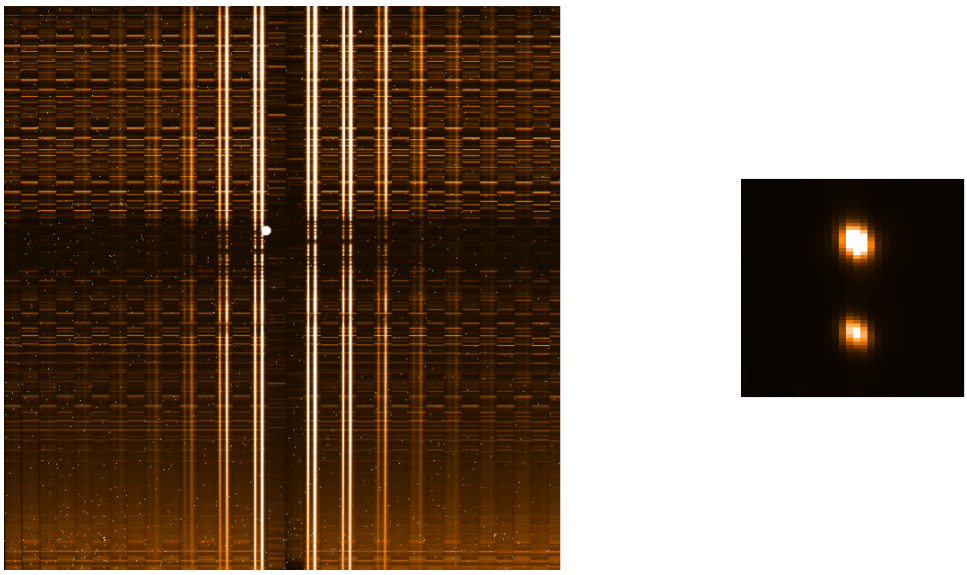

Figure 5.1: The left plot shows a raw image obtained from SINFONI, where the vertical axis represents wavelength and the horizontal axis contains the spatial pixels. After correcting for a number of effects as described in the text, these images are reconstructed into the fully calibrated images shown on the right. With a single image created for each of the discrete wavelengths recorded.

2.45 μm. An integral-field unit (IFU) was more suitable than a long-slit spectrograph because it makes easier to obtain un-blended spectra of both a target and reference star, and should have negligible losses of stellar light out of the fibers. IFUs work by splitting up a two dimensional image into slices which are dispersed across a detector. This results in an image with a number of columns or slit-lets that can be reconstructed using software back into a two-dimensional image. All observations used the H+K grating with the largest spatial pixel scale providing a $8''\times\ 8''$ field-of-view. This was the maximum field of view available for the instrument. This small viewing area places tight constraints on the possible exoplanet host star targets that can be viewed using this instrument; they must be located close to another star of similar brightness. The advantage of an integral field is that it is able to provide spectral measurements with a much finer resolution than is possible through broad band photometry. SINFONI provides a resolution of 1500 with H+K gratings and with such a large telescope aperture it was estimated that occultation depths errors of $\sim$30 ppm would be achieved per spectral bin of $\sim$50 nm.

WASP-77Ab was observed on 09 Oct 2013 and again on 23 Nov 2013. The initial observation had a per-image exposure time of 15 seconds, this was lowered to 4 seconds

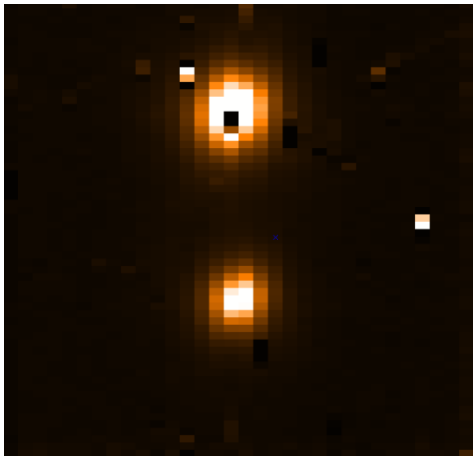

Figure 5.2: An example of bad pixel artefacts that were produced from the ESO calibration pipeline. These anomalies, if summed by aperture photometry, could provide false values which will nullify the detection of any occultation event.

for the second observation as it was noted that the count rates were approaching the non-linear regime of the detector. It also increased the time resolution of the data. A total of 94 images were obtained for the first observation of WASP-77Ab and a total of 198 images were recorded for the second. WASP-85Ab was observed on 06 May 2014 with a 15 second exposure time obtaining 194 images.

As noted in section 2.1.2, having manual control over the calibration routines can lead to a higher quality lightcurve. There were also issues with the automated pipeline from the European Southern Observatory (ESO) returning pixel artefacts in the final images, an example of which can be seen in figure 5.2. In order to solve this issue and attempt to achieve the highest precision possible, a data calibration routine was written in Python, making use of the SINFONI reduction routines through the Python Common Pipeline (Python-CPL) package (Streicher 2016). However, due to the type of instrument, the calibration routine was a little more complex than the one noted as part of the CFHT observations in section 4. Figure 5.1 shows the differences between the raw and fully-calibrated SINFONI images, in which spectra are converted into images corresponding to an individual wavelength bin. The basic steps that were followed are outlined below.

1. *Fixing Bad Lines*
   The first step was to remove all "bad lines" from every raw image, including the calibration images. These lines are introduced at the detector level, where four outer pixels along either side of each row are used to estimate the bias level

within the entire row. This bias level is then subtracted from the pixel values in the row. If a hot or dead pixel happens to lie within the outer region, the bias correction that has been performed will be incorrect, meaning the entire row of pixels will have incorrect values. To correct for this, bad pixels within this outer region were detected by searching for pixels that were more than 18 times the median absolute deviation away from the median edge value. Once these had been identified, the bias correction that had originally been applied was calculated and added back to the row of pixel values. The true bias correction, calculated ignoring any bad pixels in the outer regions was then subtracted from the data.

2. *Dark and Flat Correction*
   The master darks and flats were then created in the same way as described in section 2.1.2; dark images of the same exposure time were median combined to produce a master dark which was then subtracted from each flat image before they were combined in the same way. The "distortion", "object" and "wavelamp" images were then corrected by subtracting the master dark and dividing by the normalised flat that had the corresponding exposure time.

3. *Bad pixel Detection*
   One of the main motivations for producing this pipeline was the large number of hot or dead pixels that were still present after being processed with the SINFONI reduction pipeline from ESO (see figure 5.2). It appeared that bad pixel positions in the science image did not correspond well with those produced from the generated bad pixel map. To correct this, a bad pixel detection routine was created which worked along similar lines as the one provided by Abuter et al. (2006) but with slightly more stringent selection criteria. Linearity images, that show how pixel responses vary with intensity, were used as an initial step to detect bad pixels. A polynomial model was fit to each pixel variation and those that deviated by more than 7 times the median absolute deviation away from the median fit were flagged as bad. The master flat and dark images, noted above, were also used to detect bad pixels. This was done in the same way as noted in section 4.2, where values with large deviations away from the median were flagged. All of these bad pixel maps were then combined to produce a bad pixel mask.

4. *Bad pixel Correction*
   To correct for a majority of the bad pixels detected, a bilinear interpolation was used. A small, 3×3 window of pixels was isolated around the bad pixel and the bilinear interpolation method of SciPy (Jones et al. 2001) was used to determine the missing pixel value. Having spatial information from the horizontal axis and spectral information from the vertical axis provided estimated

pixel values in good agreement with known pixel values. This method proved much more successful than the bad pixel correction attempt made in section 4.2. The only time this method failed was when two or more bad pixels were located next to each other. In this case, no correction was applied and the pixel values were set to "NaN"

5. *Computing Distortions*
   Distortions within the SINFONI instrument depend on wavelength and can vary over time. The CPL "sinfo_rec_distortion" routine[1] was used along with the distortion frames taken nearest to each specific observation to produce a distortion map and a table of slitlet distances.

6. *Wavelength Calibrations*
   Each slitlet in the raw images had a wavelength offset. To determine this offset, the CPL "sinfo_rec_wavecal"[1] recipe was used, which produced a wavelength calibration map.

7. *Spectra to Image Conversion*
   The CPL routine "sinfo_rec_jitter"[1] was then used along with the distortion map, slitlet distances and wavelength calibration to reconstruct two dimensional images from the dark and flat corrected science images. These data were stored in a cube containing two dimensional images as a function of wavelength. An example of once of these calibrated images is shown in figure 5.1.

The fully calibrated images from this routine were much cleaner and contained few pixel artefacts; only those pixels that were not corrected as described item 4 above remained which were handled during data analysis (section 5.3).

5.3 Data Analysis and Results

Before measuring the flux, the cube that was produced in section 5.2 was split into spectral bins. Each set of images inside the cube, that spanned a certain wavelength range, were co-added in order to increase the signal-to-noise ratio to a level high enough for an occultation measurement to be performed. This was initially done using 50 nm bins, in order to try to maximise the spectral resolution of the potential dayside SED.

Circular aperture photometry was then performed using the routine described in section 2.2 with some minor changes. Apertures with radii from 3 pixels to 13 pixels

[1] `http://www.eso.org/sci/facilities/paranal/instruments/sinfoni/doc/VLT-MAN-ESO-14700-3517_v93.pdf`

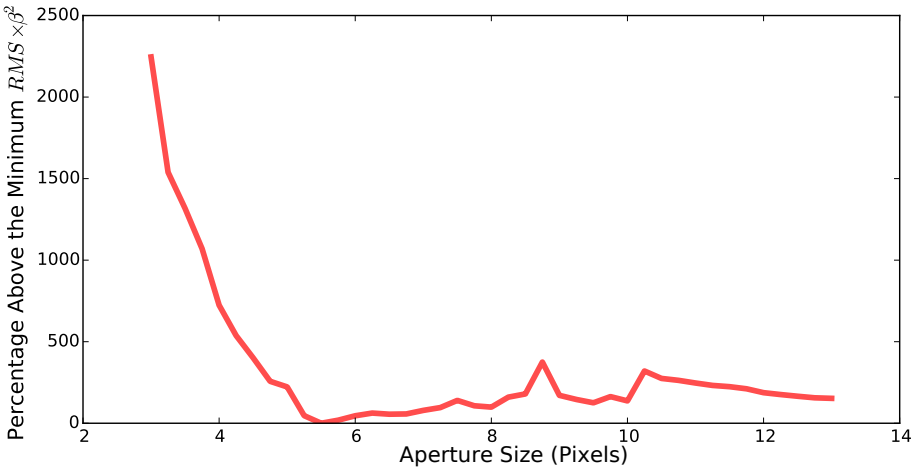

Figure 5.3: The effects of aperture size on the $RMS \times \beta^2$ of the occultation residuals for WASP-85Ab. In this case, a best aperture of 5.5 pixels was found.

were used, in steps of 0.25 pixels. The first minor change was that the source detection algorithm was not used as it wasn't necessary due to the limited number of stars on the detector, instead, stellar PSF locations were input manually. As well as this, any image that contained a "NaN" pixel within the circular aperture was completely rejected and the measurements of both stars were discarded. Finally, instead of a circular annulus, the median value of the entire frame was used as the sky background level, due to the small size of the image.

As with section 4.3.2, the effect of aperture size on the output lightcurve was studied. However, due to the existence of only a single comparison star, the process was greatly simplified. Differential lightcurves were created for each aperture size using the target and comparison star. A global MCMC was then performed and the residuals of the lightcurves were ranked according to their $RMS \times \beta^2$ (Winn et al. 2008). An example of the effect of aperture size on $RMS \times \beta^2$ is shown in figure 5.3. The aperture radii sizes that showed the lowest $RMS \times \beta^2$ residuals were 5.5 pixels for the WASP-85Ab data, 8 pixels for the WASP-77Ab 23 Nov 2013 data 9.5 pixels for the 09 Oct 2013 WASP-77Ab observation.

Unfortunately, no reasonable eclipse depths were produced by the measurements. It seems that the observations were plagued with large amounts of correlated noise, of an order of magnitude larger than a planetary transit. In an attempt to improve this, the spectral binning width described earlier was increased to improve the signal-to-noise ratio. Instead of 50 nm bins, two images were created corresponding to the

H and Ks bands, in a similar way to regular photometry. Despite this lower spectral resolution, the lightcurves obtained were still of very poor quality. Figure 5.4 shows the best lightcurves obtained for each of the observations.

An attempt was made to search for correlations between the occultation lightcurves and the parameters mentioned in section 2.4. Taking the WASP-77Ab November data set as an example, the parameters studied are shown in figure 5.5. There was a large correlation between the lightcurve and the X and Y position of the PSF in every set of data. De-trending was attempted between these parameters and the lightcurve using the MCMC of section 2.5 in various ways, including using a polynomial function similar to those used for Spitzer occultation data (e.g. Shporer et al. 2014b). Figure 5.6 shows the best fitting trend model, which for WASP-77Ab consisted of quadratic X and Y position. The de-trended lightcurve is still of very poor quality, with large systematics masking any occultation.

5.4 Conclusions

The attempt at measuring the day-side emission spectra of WASP-77Ab and WASP-85Ab using SINFONI was unsuccessful. The observations were plagued by large amounts of correlated noise, that masked any occultation signal. There were two main possible causes for this source of noise: intra-pixel sensitivity variations, which have already been shown to produce correlated noise in time-series observations (e.g. Knutson et al. 2012) and the comparison star being too dim to account for variations in systematic and astrophysical noise.

It is possible however, that the data calibration routine described in section 5.2 may have modified the pixel values in an incorrect way. Extensive testing was done to test whether this was the case. Steps such as the dark and flat corrections were skipped to see if it would result in the improvement of the final lightcurve as well as using only good frames where bad pixels were rejected entirely instead of being estimated. None of these changes resulted in a higher precision lightcurve.

It appears that SINFONI is not well suited to these kinds of measurements. The small field-of-view significantly lowers the population of transiting exoplanets that can be examined. Visual binary stars are the only systems that are observable with the $8'' \times 8''$ field-of-view, of which there are few. it is unable to account for the correlated noise produced by scintillation within the Earth's atmosphere. The large systematics apparent in the lightcurves are also cause for concern; given their scale, it seems that measuring an occultation event with SINFONI is quite unlikely. Multi-Object Spectrographs, that utilise multiple IFUs to operate over a much larger field-of-view may be more suited to this type of observation.

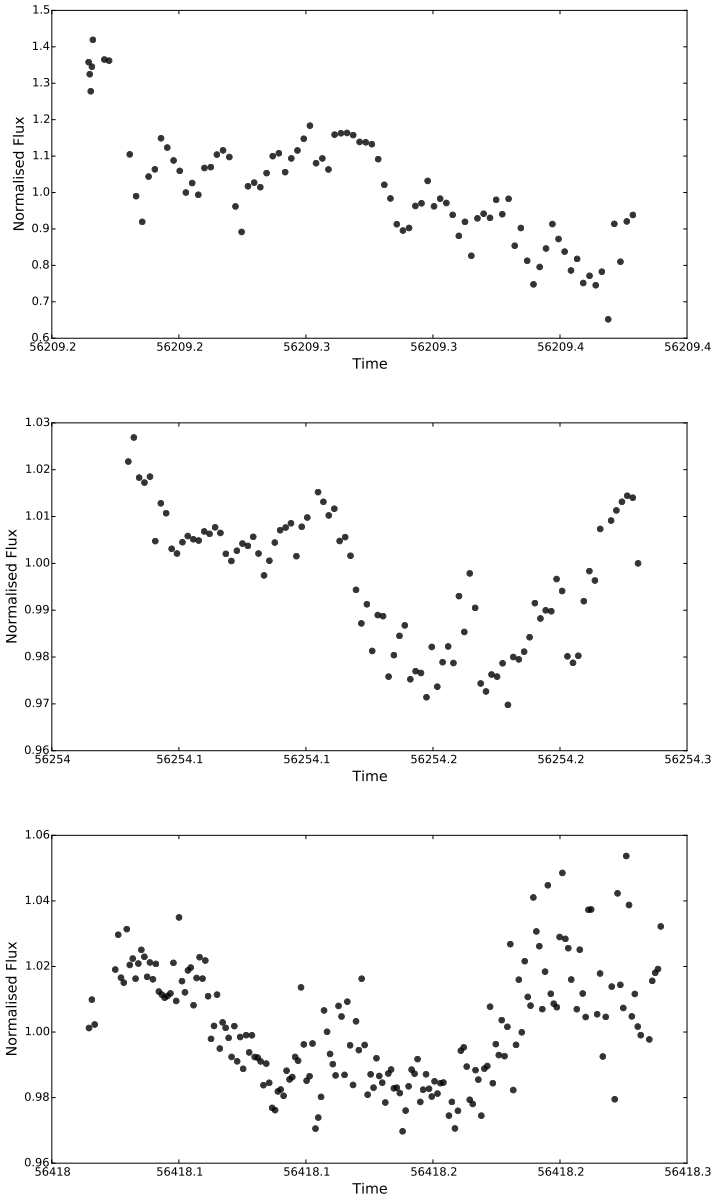

Figure 5.4: The differential lightcurve produced from spectrophotometry as described in the text for combined spectral images spanning the Ks band. The top plot shows the best lightcurve for WASP-77Ab taken on 09 Oct 2013, the middle plot displays the lightcurve for WASP-77Ab taken on 23 Nov 2013 and the bottom plot represents the best lightcurve for WASP-85Ab The lightcurves show strong systematic noise which dominates any occultation signal.

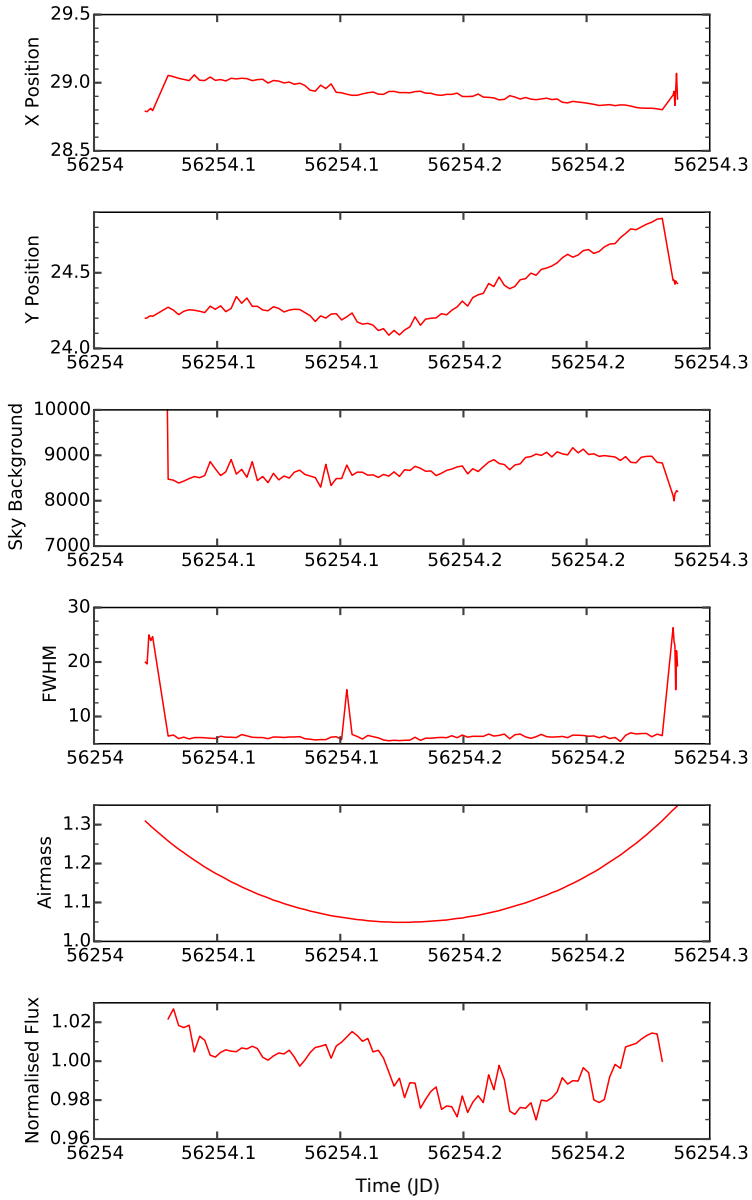

Figure 5.5: The various parameters measured in order to check for correlation with the noise in the occultation lightcurve. The plots show, from top to bottom: X position, Y position, the sky background level, FWHM, Airmass and the normalised flux. All of these parameters are plotted against time.

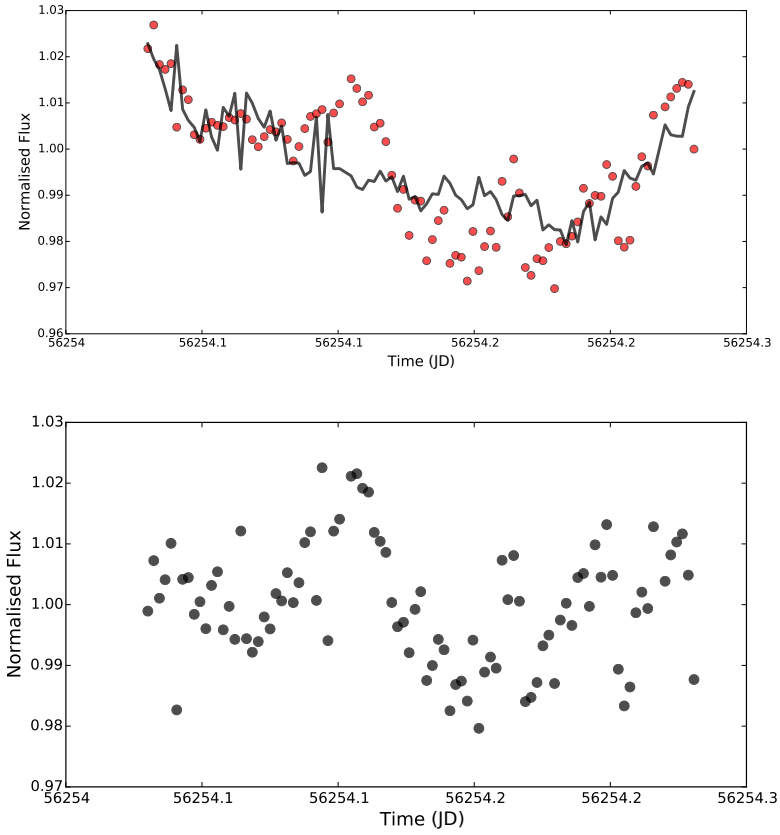

Figure 5.6: The top plot shows the lightcurve obtained for the WASP-77Ab November observation. The best-fitting trend model, produced by the MCMC as described in the text, is plotted in black. The bottom panel shows the de-trended lightcurve; large systematics are still present meaning that no occultation is detected.

6 Conclusions and Future Work

6.1 Summary

In this thesis I have presented new results from the K2 spacecraft as well as the CFHT instrument, produced from both the transit and occultation methods respectively. I have also created pipelines for the calibration and reduction of such data, which was undertaken in an automated way to improve the time efficiency as well as the robustness of the photometry procedure. I have thoroughly investigated the effects on aperture size and comparison star choice on sensitive secondary eclipse measurements, as well as investigating the depth to which correlated noise affected the measurements. The system parameters for three planets, WASP-55b, WASP-75b and WASP-48b have been updated and thermal emission from WASP-48b was also presented.

The photometry and data calibration pipelines, presented in section 2, were a beneficial outcome of the work done in this thesis. Rather than using the pre-processed data, usually available as an end product from observatories, it was found that having more control over the exact data calibration steps allowed them to be fine-tuned to produce higher quality lightcurves. I created the automated calibration routine described in section 2.1 to allow this level of control, whilst being flexible enough to be compatible with images from different instruments. This routine was used on the WASP-48b CFHT data and contributed to a 30 % improvement in the quality of the lightcurve. The method of photometry I was previously able to use involved IRAF[1]. Multiple input files with many parameters had to be manually input every time a data set was reduced. Not only was this time consuming but it also allowed the input of human error, with little verification once the input files had been edited. Once the routine was run on a data set, it produced a large photometry output file that had to be manually edited to extract and organise the relevant data. The routine written as part of this thesis allows time-series lightcurves to be extracted from photometric data in an automated fashion. It requires a single, more simplified input file and produces lightcurves as outputs, which are useful for the MCMC analysis mentioned in section 2.5 as well as the aperture and comparison star measurement routines of section 2.3. It allows a greater number of comparison stars to be measured more easily through source detection and does not place a limit on the number of aperture radii that can be measured simultaneously. The routine also produces a number of useful parameters that can be used for de-trending the lightcurves as described in section 2.4. Both of these routines can be used on any photometry images and they have been tested on

[1]Image Reduction and Analysis Facility - http://iraf.noao.edu/

data from observatories such as the Liverpool Telescope, Spitzer and Keele Observatory as well as those mentioned in this thesis.

Chapter 3 presents updated system parameters for WASP-55b and WASP-75b with up to a 6σ improvement over previous results in some cases. Ensuring system parameters are correct is important; it makes certain that the inferences that we make about these systems are based on robust values. The K2 data offered much greater precision photometry over ground-based observations. To achieve a high precision lightcurve, the commonly used self-flat fielding de-trending method was improved by using Gaussian convolution over polynomial fitting, and a variable window size was used over which to determine the flux versus arc-length correlation. The high quality data revealed possible stellar variation in WASP-75 which allowed an estimate of the stellar inclination angle to be made. The data also showed that repeated ground-based measurements of a transiting planet are enough to accurately constrain the basic system parameters to a reasonable degree.

Chapter 4 reported the detection of the thermal emission of WASP-48b from CFHT observations in the $K_{\rm s}$-band (2.1 μm). The data marginally supported an atmosphere with a thermal inversion. The analysis highlighted the importance of taking into account the effects of correlated noise, as well as the choice of comparison stars and aperture sizes used. Without factoring these into the analysis, the final eclipse depth could be unreliable, which in turn would make the deductions made about its atmosphere fallible. This is important for all ground-based time series photometry, including transits, but is more important for occultations where a higher sensitivity was required. Without a thorough understanding of how these factors affect the final outputs, the eclipse depth and timing values, and therefore inferences made from them, may not be entirely robust. It was also noticed as part of the analysis that there was an apparent correlation between the lightcurves that were being produced and the FWHM of the PSF. This appeared to be down to small inaccuracies in the flux-weighted centroid method due to the shape of the de-focused PSFs. A new method was created to accurately centre de-focused sources in a time efficient manner. The use of this effectively removed the correlation without the need for any de-trending. Due to the eclipse depth measurement being similar to a previously published value, the results of these observations were also able to rule out large, short time-scale storms deep within the atmosphere of WASP-48b. Ideally, continuous monitoring of these systems would be able to reveal more about their possible long term variability.

The reduction of SINFONI data in chapter 5 showed that the instrument's IFU was not suited to secondary eclipse measurements. The main issue was determined to be the small field of view of the instrument, allowing only close visual binary stars to be observed with this method and intra-pixel sensitivity variations. The requirement of needing two stars in close proximity lead to the only available targets having a fainter companion. The magnitude difference between the target star and the only available

comparison star was too large and the effects of the telluric atmosphere were not fully removed by dividing out its flux. This produced lightcurves with systematics that were significantly larger than the expected eclipse depths. Even combining all of the images corresponding to wavelengths with a high signal-to-noise did not present a detection. While this method holds merit in terms of its ability to provide a more detailed SED for the atmosphere, it is currently not feasible to do with SINFONI. Methods such as using a multi object spectrograph such as KMOS on the VLT hold more potential as they allow more targets to be selected over a wider field of view.

6.1.1 Additional Achievements

As well as the work detailed in this thesis, I have worked on a number of other projects that have not yet been noted. I instead list these below.

The first of these was the reduction and analysis of a number of occultation measurements taken with the High Acuity Wide-field K-band Imager (HAWK-I) instrument on the VLT. Data for WASP-18b, WASP-50b and WASP-51b were analysed. The same reduction steps as those performed for the CFHT data were undertaken, but no eclipses were detected. This seems to be due to a lack of suitable comparison stars in each of the data sets. The instrument was configured to run in windowed mode; this significantly reduces the overhead times between every read of the detector. However, it does this by sacrificing a large part of the instruments field of view, reducing the ability to measure the photometry of a number of surrounding stars. WASP-18b and WASP-51b both had only a single, much fainter companion star within the images and WASP-50b had three companion stars, one had a similar magnitude but did not remove the telluric systematic noise from the target lightcurve to a large enough extent to retrieve any eclipse. Future observations on this instrument will use the full frame if the inclusion of multiple, good quality companion stars cannot be included in the windowed mode observations.

Secondly, two more CFHT data sets have been reduced: occultations of WASP-24b and WASP-36b in the Ks and K-continuum bands, respectively. The method presented in chapter 4 was largely followed and an occultation was detected for each planet. Preliminary results show an eclipse depth of 0.11 ± 0.04 % for WASP-24b and 0.12 ± 0.05 % for WASP-36b. WASP-24b had a single useful companion star, that was similar in magnitude and on the same detector as the target star. This was shown by the output $RMS \times \beta^2$ values, with the addition of other stars producing a significantly poorer quality lightcurve than the single comparison alone. WASP-36b produced the best $RMS \times \beta^2$ with a combination of 2 nearby comparison stars. The WASP-36b measurement is similar to that of Zhou et al. (2015) and WASP-24b is yet to have its thermal emission in the Ks-Band published. Further testing, that includes other

comparison stars from different detectors is currently under way and a publication showing the results is in preparation.

A version of the photometry routine, presented in chapter 2 was modified so that it was specifically compatible with Spitzer measurements. The main aim of this was to reduce unpublished WASP-36 b data from the spacecraft so that it could be used in conjunction with the CFHT measurements noted above. Both the photometry routine and the MCMC listed in section 2 were modified to use the pixel level decorrelation method of Deming et al. (2015). The routines were verified by analysing the WASP-24b data from Smith et al. (2012) with similar results being achieved. Due to the automated nature of the pipelines and the similarity between Spitzer observations, around 66 unpublished data sets were reduced with this method. These analyses are awaiting the inclusion of follow-up data in global MCMCs, so that updated parameters can also be provided, before these results are published.

In November to December 2016, the 60 cm reflector telescope was partially operational at the Keele Observatory. Follow-up transit observations of recently discovered planetary candidates were undertaken. However, most observations were plagued by issues with the telescope, its tracking or bad weather. A new algorithm was written for the obtained data, that could cope with large tracking anomalies and the misalignment of the World Coordinate System (WCS) coordinates. The transformation between bright sources in every image was calculated to provide accurate tracking of the target and comparison stars. Any cloudy images were also automatically rejected. These methods lead to a successful observation of a transit of WASP-155b on 28 Nov 2016.

6.2 Extension of Current Work

A natural progression from the work that has been done during this thesis would be to analyse further sets of occultation photometry from the CFHT. As noted above in section 6.1.1, data taken for WASP-24b and WASP-36b have already being reduced, and the analysis techniques produce a lightcurve that sufficiently shows the thermal emission of each planet being blocked by its host star. A number of additional previously unpublished occultation data sets also exist. These include data on occultations yet to be detected for WASP-33b and WASP-80b, as well as WASP-43b which has already had a Ks-Band measurement taken at the Anglo-Australian telescope (Zhou et al. 2014). The methods used in chapter 4 could be easily applied to such data in order to swiftly produce occultation lightcurves for each system. These kinds of measurements not only help to constrain the atmospheric properties of the planet, but also provide measurements of brightness temperature and help to refine the eccentricity of the system (see section 4.5). Currently, only a handful of the hot Jupiters discovered

have had their thermal emission observed; once the previously obtained data has been analysed and published, more data could be obtained to build up the sample size of hot Jupiters with secondary eclipse measurements, providing ground work for comparative studies on the discovered properties of these planets. Further to this, the lessons learnt from CFHT can be applied to other ground based instruments, such as HAWK-I on the VLT, to allow a broader range of planets to be observed with the larger aperture size.

As well as photometric methods, spectrophotometry is an alternative technique that holds a large amount of potential in regards to probing exoplanetary atmospheres. While photometry is useful, the information retrievable from these broad-band measurements is limited and often proves insufficient in distinguishing between disparate atmospheric models (Madhusudhan & Seager 2010). With spectrophotometry the dayside SED of an exoplanet can potentially be measured with a significantly higher resolution than is achievable through photometry. Furthermore, it is obtainable from a single observation, rather than the multiple observations required with standard photometry. Rather than using the single IFU on SINFONI as has been described previously in this thesis, I have obtained measurements of WASP-121 b on 03 February 2016 in the H and K bands using the K-band multi object spectrometer (KMOS) on the 8 m VLT. Measurements have been attempted with this instrument before, such as those of Parviainen et al. (2015) and the observational technique that was used has built upon these previous studies. Lessons were learned such as ensuring the target stars were very well centred in each individual IFU and keeping tight control of the detector integration time to ensure that the count limit was well within the linear response region of the detector. WASP-121 b is a very inflated planet ($1.01 \pm 0.14\ M_{\rm Jup}$; $1.75 \pm 0.06\ R_{\rm Jup}$) in a short orbit (1.27 days) around a bright ($K = 9.4$) F6V star (Kataria et al. 2018). The planet's large size and extreme irradiation ($\sim 7 \times 10^9$ erg s^{-1} cm^{-2}) translate into exceedingly favourable theoretical expectations for the planet's thermal emission. This, as well as six nearby stars of similar brightness within the field of view of KMOS, make it an ideal target. Once the data have been reduced, and should they show an occultation of the planet by its host star, the methodology used can be repeated for other systems. KMOS should allow the retrieval of a detailed SED of the dayside atmospheres of hot Jupiters. It should also produce a much more precise insight into the thermal structure of these planets' atmospheres, help identify molecular bands and potentially constrain their carbon-to-oxygen (C/O) ratios; a potential diagnostic into the migration pathways of hot Jupiters (Madhusudhan, Amin & Kennedy 2014).

6.3 Upcoming instrumentation

The future of exoplanet discovery and characterisation is promising; there are a number of planned ground and space based instruments that will allow the detection as well as the characterisation of smaller, even Earth-sized planets. This section will briefly list the upcoming missions for the detection and follow-up observation of exoplanets.

6.3.1 TESS

The Transiting Exoplanet Survey Satellite (TESS) launched successfully on 18 April 2018. It is the first ever space-based all-sky transiting survey, with a planned two year mission to study the brightest stars in the vicinity of our Solar System (Ricker et al. 2014). TESS will use four, wide-field $24^\circ \times 24^\circ$ cameras to observe 26 sections of the sky per year. Each of these sections will have some overlap, which grows towards almost continuous observation near the ecliptic poles, where ideal targets for the future James-Web Space Telescope (JWST) will be found. TESS will observe at least 200,000 main sequence stars, with each star being observed continuously for a period of at least a month. The brightest 100,000 stars will have a short one minute cadence, with the whole sky having a cadence of thirty minutes. TESS aims to detect a large sample of Neptune-sized planets, but should also detect those down to the size of Earth. However, it is most likely Earth-sized planets will be discovered around M-dwarf stars due to the short period limitations of TESS, which is approximately 10 days in general (Ricker et al. 2014). TESS will focus on stars that are brighter than an apparent magnitude of 12, finding targets that are anywhere up to 100 times brighter than those detected by the current transiting space survey K2 (section 1.2.2). The much brighter host stars allow follow-up observations to be much easier, meaning TESS should provide a wealth of targets ideal for detailed characterisation and suitable for both ground and space-based follow-up observations.

6.3.2 PLATO

PLAnetary Transits and Oscillations of stars (PLATO) is another large-scale exoplanet detection survey (Catala 2009). Its goal is to detect earth-sized planets around the habitable zone of Sun-like stars (Rauer & Catala 2010). Like TESS, it will target the brightest stars in the sky (4-11 m_v) to provide targets well-suited for follow-up observations. PLATO will consist of 24 cameras, providing a cadence of 25 seconds and two faster operating cameras with read-out times of about 2.5 seconds. All of the cameras combined will provide a total 2250 deg^2 field of view per pointing. The

current plan is to observe two fields over at least a two year period covering the missions four year time line (Rauer et al. 2014). Unlike TESS however, as well as the transit method, PLATO will also perform asteroseismology on the host stars of any detected planets, producing accurate values of age and mass. With these values, PLATO will be able to provide measurements of planetary masses, radii and age with a high degree of accuracy. Over one million stars are expected to be observed with 50 % total coverage of the sky. PLATO should be able to detect planets with moderately large orbits, making its mission goal of detecting Earth-sized planets within the habitable zone a very real possibility. The mission should return a vast amount of confirmed exoplanets and will even have the precision to detect objects such as exomoons and planetary rings.

6.3.3 JWST

The James Webb Space Telescope (JWST) is a space telescope set to be launched in May 2020 (Gardner et al. 2006). It will house a large 6.5 meter primary mirror, with four instruments that provide both imaging and spectroscopy in the near and mid infra-red. The atmospheric study of exoplanets is one of the mission goals of the JWST. It will be able to perform spectroscopy of star-planet systems during both transit and occultation events. JWST will be able to measure the dayside emission spectra of hot Jupiters with unprecedented detail and even allow the characterisation of Earth-sized exoplanets. The targets that can be viewed will be restricted by host star brightness and position, but by the time JWST launches, it is expected that many prime candidates will be produced from surveys such as NGTS, TESS and PLATO as well as those already detected from surveys such as WASP.

6.3.4 E-ELT

The European Extremely Large telescope (E-ELT) will be the largest optical/infra-red telescope ever created. It will be situated in Cerro Armazones in northern Chile and will have a segmented primary mirror that is 39 meters in diameter, with a 4.2 meter secondary mirror (Gilmozzi & Spyromilio 2007). The extreme spatial resolution offered by such a large primary mirror will allow the direct imaging of giant exoplanets. Its instrumentation will also allow precise radial velocity measurements, down to the order of 1 cm s^{-1} (Pasquini et al. 2010). With such precision, the detection of Earth-like planets within the habitable zone of stars through the radial velocity method is a likely possibility. The high resolution spectrograph, EELT-HIRES, will have the potential to characterise the high-profile targets detected from missions mentioned

above, such as PLATO. It will have the resolution to detect individual molecules such as oxygen, carbon dioxide and even water vapour by studying exoplanetary emission and transmission spectra (Udry et al. 2014). The E-ELT will offer an unprecedented ability for the characterisation of hot Jupiters as well as much smaller exoplanets discovered in the coming decades.

6.4 Final Word

The long term aim of this work is to begin to understand the properties of extra-solar planets, to determine their composition, interior structures and methods of formation. The work done as part of this thesis is a long way from the true realisation of this goal, but it is a small step in the right direction. Understanding hot Jupiters and exoplanets in general will require a monumental effort from humanity; significant advances must be made in both observational techniques and theoretical modelling. The rewards however are numerous and the potential of discovering life outside of our planet is very real.

Publications

Refereed

- **Thermal emission of WASP-48b in the Ks-band**
  Clark, B.J.M., Anderson, D.R., Madhusudhan, N., Hellier, C., Smith, A.M.S. and Cameron, A.C., 2018. Astronomy & Astrophysics, 615, A86

- **An Analysis of Transiting Hot Jupiters Observed with K2: WASP-55b and WASP-75b**
  Clark, B.J.M., Anderson, D.R., Hellier, C., Turner, O.D. and Močnik, T., 2018. Publications of the Astronomical Society of the Pacific, 130(985), p.034401.

- **The well-aligned orbit of Wasp-84b: evidence for disk migration of a hot Jupiter**
  Anderson, D.R., Triaud, A.H.M.J., Turner, O.D., Brown, D.J.A., Clark, B.J.M., Smalley, B., Cameron, A.C., Doyle, A.P., Gillon, M., Hellier, C. and Lovis, C., 2015. The Astrophysical Journal Letters, 800(1), p.L9.

- **Starspots on WASP-85**
  Mocnik, T., Clark, B. J. M., Anderson, D. R., Hellier, C., & Brown, D. J. A. (2016). The Astronomical Journal, 151(6), 150.

- **Starspots on WASP-107 and pulsations of WASP-118**
  Mocnik, T., Hellier, C., Anderson, D.R., Clark, B.J.M. and Southworth, J., 2017. Monthly Notices of the Royal Astronomical Society, 469(2), pp.1622-1629.

In proceedings

- **Ground-based occultations of WASP-24b and WASP-36b**
  Clark, B.J.M., Anderson, D.R., Madhusudhan, N., Hellier, C., Smith, A.M.S. and Cameron, A.C., 2018.

- **New data and Updated parameters of 7 WASP planets**
  O.D. Turner, D.R. Anderson, B.J.M Clark, D.J.A. Brown, A. Collier-Cameron, L. Delrez, M. Gillon, and P. Rojo, 2018.

A Python Code

I was the sole author of all code that is included below, which was created for the purpose of the work included in this thesis.

A.1 Data Calibration Pipeline

```
#------------------------------------ Data Calibration Pipeline ------------------------------------#
#b.j.clark@keele.ac.uk - v1.06 (02/11/2017)
#----------------------------------------

############ USER VARIABLES ############
direc = "/data/1_imaging/cfht/w36/1.raw/" #directory containin all raw data (including calibration images)
output_dir="w36_cal" #name of output directory
newdir = False #create a new directory for outputs
master_table = "datamaster.cfht" #output data log name
nstars = 20 #maximum number of stars for detection algorithm
row_correction=False#Correct Bad row values (darker streaks)
debug_short_test=False #only reduce 10 science images if True
sci_ob="WASP-36"#the  target object keywork
skipimcor=False#skip science image correction if already performed
ap_size_lim=200 #minimum npix for valid aperture
ap_mult=2#amount to multiply mean aperture radius for "aperture" pixels
sigma_psf = 4#amount bg pix clip from median
show_sources=False
remove_bad = True#removes psfs that contain nans

############ LIBRARIES ############
from standard import *
import pandas
from astropy.time import Time
import pyfits

############ GLOBAL VARIABLES ############
global dataset #pandas dataframe for file logging
global index_master #index in pandas table

prihdr("Data Calibration Pipeline")

############ CLASSES ############
class cfht_img:
    #class to handle reading and writing while preserving CFHT data structure
    def __init__(self,fl):
        self.fl = fl
        self.fits = pyfits.open(fl)
        self.extensions = len(self.fits)
        self.imgs, self.hdrs = [], []
        for ext in range(0,self.extensions):
            Ext = self.fits[ext]
```

```
43              Hdr = Ext.header
44              Data = numpy.asarray(Ext.data,dtype="float")
45              structure = Data.shape
46              if len(structure) == 3:
47                  self.frames = structure[0]
48                  sub_imgs,sub_hdrs = [],[]
49                  for frm in range(0,self.frames):
50                      sub_imgs.append(numpy.asarray(Ext.
                        data[frm],dtype="float"))
51                      sub_hdr = Hdr.copy()
52                      sub_hdr["MJD-OBS"] = float(
                        sldate_mjd(Hdr,frm))
53                      sub_hdrs.append(sub_hdr)
54                  self.imgs.append(numpy.asarray(sub_imgs))
55                  self.hdrs.append(sub_hdrs)
56              else:
57                  self.frames = 1
58                  self.imgs.append(Data)
59                  self.hdrs.append(Hdr)
60
61      def write(self,fname,clobber=False):
62          hdu = pyfits.PrimaryHDU()
63          hdu.header = self.hdrs[0]
64          hdus = [hdu]
65          for i in range(1,self.extensions):
66              hdu = pyfits.ImageHDU()
67              hdu.data = self.imgs[i]
68              try:
69                  self.hdrs[i]["BITPIX"]
70              except TypeError:
71                  hdu.header = self.hdrs[i][0].copy()
72              else:
73                  hdu.header = self.hdrs[i].copy()
74              hdu.header["BZERO"] = 1
75              hdus.append(hdu)
76          img_out = pyfits.HDUList(hdus)
77          img_out.writeto(fname,clobber=clobber)
78
79      def write_frames(self,fname,frame="all",clobber=
        False):
80          fbase = fname.split(".fits")[0]
81          for f in range(self.frames):
82              if f != frame and frame != "all":
83                  continue
84              hdu = pyfits.PrimaryHDU()
85              hdu.header = self.hdrs[0]
86              f=int(f)
87              try:
88                  if int(self.frames) == 1:
89                      hdu.header['MJD-OBS'] = self.hdrs[1
```

```
                        ]['MJD-OBS']
                    else:
                        hdu.header['MJD-OBS'] = self.hdrs[1
                        ][f]['MJD-OBS']
                except TypeError:
                    print "FRAME:",f
                    print fname
                    print self.fl
                    print "\n\nMJD:,", hdu.header['MJD-OBS']
                    print "\n\n"
                    print len(self.hdrs[1])
                    raise
                    sys.exit()
                hdus = [hdu]
                for i in range(1,self.extensions):
                    hdu = pyfits.ImageHDU()
                    if int(self.frames) == 1:
                        hdu.data = self.imgs[i]
                        hdu.header = self.hdrs[i].copy()
                    else:
                        hdu.data = self.imgs[i][f]
                        hdu.header = self.hdrs[i][f].copy()
                    hdu.header["BZERO"] = 1
                    hdus.append(hdu)
                img_out = pyfits.HDUList(hdus)
                if not os.path.exists(fbase+"_%02d"%f+
                ".fits"):
                    img_out.writeto(fbase+"_%02d"%f+".fits",
                    clobber=clobber)

############ FUNCTIONS ############
def norml(array):
    return array/median(array)

def sldate_mjd(header, frame,mjd=True):
    utc = Time(header["SLDATE"+"%02d"%(frame+1)])
    if mjd==True:
        return utc.mjd
    else:
        return utc.jd


def find_closest_exp(tablobj, exp):
    exps = numpy.asarray(tablobj.exp.unique())
    return exps[zip(*sorted(zip(numpy.abs(exp-exps),
    range(0,len(exps),))))[1][0]]


def darkcombine(images,output,combine="median",clobber=
False):
```

```
134         to_combine = {}
135         for ext in range(1,5):
136             to_combine[ext] = []
137         for IM in images:
138             for ext in range(1,len(IM.imgs)):
139                 for frame in range(0,len(IM.imgs[ext])):
140                     to_combine[ext]
141                     IM.imgs[ext][frame]
142                     to_combine[ext].append(IM.imgs[ext][
                        frame])
143         out = []
144         for ext in to_combine:
145             if combine == "median":
146                 out.append(numpy.nanmedian(to_combine[ext],
                    axis=0))
147             if combine == "mean":
148                 out.append(numpy.nanmean(to_combine[ext],
                    axis=0))
149         hdu = pyfits.PrimaryHDU()
150         hdu.header = IM.hdrs[0]
151         hdu.header["OBSTYPE"] = "MASTERDARK"
152         hdus = [hdu]
153         for i in range(1,5):
154             hdu = pyfits.ImageHDU()
155             hdu.data = out[i-1]
156             hdu.header = IM.hdrs[i][0]
157             hdu.header["BZERO"] = 0
158             hdu.header["OBSTYPE"] = "MASTERDARK"
159             hdus.append(hdu)
160         img_out = pyfits.HDUList(hdus)
161         img_out.writeto(output,clobber=clobber)
162 
163     def flatcombine(images,masterdark,output,combine=
    "median",scale="median",clobber=False):
164         to_combine = {}
165         for ext in range(1,5):
166             to_combine[ext] = []
167         for IM in images:
168             for ext in range(1,5):
169                     to_combine[ext].append(IM.imgs[ext])
170         out = []
171         for ext in to_combine:
172             img_set = numpy.asarray(to_combine[ext],dtype=
                "float") - masterdark.imgs[ext]
173             if scale == "median":
174                 img_med = numpy.nanmedian(img_set)
175                 img_set = [x*(img_med/numpy.nanmedian(x))
                    for x in img_set]
176             elif scale == "mean":
177                 img_med = numpy.nanmean(img_set)
```

```
178                 img_set = [x*(img_med/numpy.nanmean(x)) for
                    x in img_set]
179             if combine == "median":
180                 out.append(norml(numpy.nanmedian(img_set,
                    axis=0)))
181             elif combine == "mean":
182                 out.append(norml(numpy.nanmean(img_set,axis=
                    0)))
183             else:
184                 raise ValueError("Need a method to combine
                    images..")
185         hdu = pyfits.PrimaryHDU()
186         hdu.header = IM.hdrs[0]
187         hdu.header["OBSTYPE"] = "MASTERFLAT"
188         hdus = [hdu]
189         for i in range(1,5):
190             hdu = pyfits.ImageHDU()
191             hdu.data = out[i-1]
192             hdu.header = IM.hdrs[i]
193             hdu.header["BZERO"] = 0
194             hdu.header["OBSTYPE"] = "MASTERFLAT"
195             hdus.append(hdu)
196         img_out = pyfits.HDUList(hdus)
197         img_out.writeto(output,clobber=clobber)
198         return(cfht_img(output))
199
200     def nonlincor(adu,det):
201         #nonlinear corrections, !!specific to CFHT!!
202         allcoeffs = ([0.991276,1.72141e-6,7.57226e-12],[
                    0.993746,1.82717e-6,1.9395e-11],[0.994254,1.9277e-6,
                    1.69437e-11],[0.994799,1.49037e-6,2.85603e-11])
203         coeffs = allcoeffs[det]
204         return adu * (coeffs[0] + (coeffs[1]*adu) + (coeffs[
                    2]*adu*adu))
205
206     def row_correct(im):
207         med_x = numpy.nanmedian(im,axis=0)
208         im2=im.copy()
209         im2[:]=[im[i,:]/med_x for i in range(0,len(im[1]))]
210         im2=im2*numpy.nanmedian(med_x)
211         return im2
212
213     ############ MAIN ############
214     index_master = 0
215     output_dir = cmdir(output_dir,fp=True,makenew=newdir)
216     master_table = output_dir + master_table
217     columns=["file","exp","typ"]
218     try:
219         #check for saved progress
220         dataset = pandas.read_pickle(master_table)
```

```
221         print "\nReading data from saved table.."
222     except IOError:
223         raw_images = file_list_wext(direc,".fits")
224         if debug_short_test==True:
225             raw_im_sci = [i for i, v in enumerate(raw_images
                ) if "o.fits" in v]
226             raw_im_cal = [i for i, v in enumerate(raw_images
                ) if "o.fits" not in v]
227             raw_im_sci=nar(raw_images)[raw_im_sci]
228             raw_im_cal=nar(raw_images)[raw_im_cal]
229             imglen = int(math.floor(len(raw_im_sci)/10))
230             raw_im_sci=raw_im_sci[::imglen]
231             raw_images = raw_im_cal.tolist()+raw_im_sci.
                tolist()
232             print "WARNING: DEBUG MODE IS ON, NOT REDUCING
                ALL IMAGES"
233         dataset = pandas.DataFrame(columns=columns)
234         print "\nReading data from fits.."
235         bar = pbar(len(raw_images))
236         counter = 0
237         object_names=[]
238         for fl in raw_images:
239             data = pyfits.open(direc+fl)
240             dataset.loc[index_master] = [direc+fl,data[1].
                header["EXPTIME"],data[1].header["OBSTYPE"]]
241             if data[1].header["OBSTYPE"] != "DARK" and data[
                1].header["OBSTYPE"] != "FLAT":
242                 object_names.append(data[1].header["OBJECT"])
243             index_master += 1
244             bar.update(counter)
245             counter+=1
246         bar.finish()
247         object_names=numpy.unique(object_names)
248         if len(object_names) > 1:
249             print "Mutiple objects detected:"
250             c1=0;
251             for ob in object_names:
252                 c1+=1
253                 print str(c1)+" - "+ob
254             sci_ob = object_names[int(input("Please enter
                science object:"))-1]
255         else:
256             sci_ob = object_names[0]
257         print "Science Object:",sci_ob
258         dataset.to_pickle(master_table)
259
260     #dark correction
261     print "\nCreating master darks.."
262     masterdarks = dataset.loc[dataset['typ'] == "MASTERDARK"]
263     darks = dataset.loc[dataset['typ'] == "DARK"]
```

```
264 bar = pbar(len(darks.exp.unique()));cnt = 0;
265 for exp in darks.exp.unique():
266     bar.update(cnt); cnt += 1;
267     if exp in masterdarks.exp.unique():continue;
268     darklist = [cfht_img(x) for x in darks.loc[darks.exp
         == exp].file.tolist()]
269     md_out = cmdir(output_dir+"masterdarks/") +
        "master_dark_"+str(exp)+".fits"
270     darkcombine(darklist, md_out,clobber=True)
271     dataset.loc[index_master] = [md_out,exp,"MASTERDARK"]
272     index_master += 1
273 dataset.to_pickle(master_table)
274 bar.finish()
275 masterdarks = dataset.loc[dataset['typ'] == "MASTERDARK"]
276
277 #flat correction
278 masterflats = dataset.loc[dataset['typ'] == "MASTERFLAT"]
279 print "\nCreating master flats.."
280 flats = dataset.loc[dataset['typ'] == "FLAT"]
281 bar = pbar(len(flats.exp.unique()));cnt = 0;
282 for exp in flats.exp.unique():
283     bar.update(cnt); cnt += 1;
284     if exp in masterflats.exp.unique():continue;
285     flatlist = [cfht_img(x) for x in flats.loc[flats.exp
         == exp].file.tolist()]
286     mf_out = cmdir(output_dir+"masterflats/") +
        "master_flat_"+str(exp)+".fits"
287     md = cfht_img(masterdarks.loc[masterdarks['exp'] ==
        exp].file.tolist()[0])
288     flatcombine(flatlist, md, mf_out,clobber=True)
289     dataset.loc[index_master] = [mf_out,exp,"MASTERFLAT"]
290     index_master += 1
291 dataset.to_pickle(master_table)
292 bar.finish()
293 masterflats = dataset.loc[dataset['typ'] == "MASTERFLAT"]
294
295 #bad pixel map creation
296 masterbpmap = dataset.loc[dataset['typ'] == "BADPIXMAP"]
297 for i in masterflats.index:
298     fits = cfht_img(masterflats.loc[i].file)
299     for ext in range(1,fits.extensions):
300         fits_img = fits.imgs[ext]
301         cut_hi = median(fits_img) + (5 * med_abs_dev(
            fits_img))
302         cut_lo = median(fits_img) - (5 * med_abs_dev(
            fits_img))
303         fits_img[numpy.where(fits_img>cut_hi)] = numpy.
            nan
304         fits_img[numpy.where(fits_img<cut_lo)] = numpy.
            nan
```

```
305             fits_img[~numpy.isnan(fits_img)] = 0
306         bp_out = cmdir(output_dir+"badpixmap/") +
            "bad_pix_map_"+str(masterflats.loc[i].exp)+".fits"
307         fits.write(bp_out,clobber=True)
308         dataset.loc[index_master] = [bp_out,masterflats.loc[
            i].exp,"BADPIXMAP"]
309         index_master += 1
310     plt.show()
311     masterbpmap = dataset.loc[dataset['typ'] == "BADPIXMAP"]
312
313     if debug_short_test == True:
314         raw_input("Science Correction Starting - enter to
            continue")
315
316     #raw image correction
317     science = dataset.loc[dataset['typ'] == "SCIENCE"]
318     print "\nCorrecting Raw Images.."
319     raw = dataset.loc[dataset['typ'] == "OBJECT"]
320     if skipimcor==False:
321         bar = pbar(len(raw));cnt = 0;1
322         for exp in raw.exp.unique():
323             md = cfht_img(masterdarks.loc[masterdarks['exp']
                 == find_closest_exp(masterdarks,exp)].file.
                tolist()[0])
324             mf = cfht_img(masterflats.loc[masterflats['exp']
                 == find_closest_exp(masterflats,exp)].file.
                tolist()[0])
325             mbp = cfht_img(masterbpmap.loc[masterbpmap['exp'
                ] == find_closest_exp(masterbpmap,exp)].file.
                tolist()[0])
326             for i in raw.index:
327                 fits = cfht_img(raw.loc[i].file)
328                 for ext in range(1,fits.extensions):
329                     for frm in range(0,fits.frames):
330                         try:
331                             #set all saturated pixels to nans
332                             fits.imgs[ext][frm][numpy.where(
                                fits.imgs[ext][frm]==65536)] =
                                numpy.nan
333                             #chipbias correction
334                             fits.imgs[ext][frm] = fits.imgs[
                                ext][frm] - 7000
335                             #Flag all bad pixels (>36000ADU)
336                             fits.imgs[ext][frm][numpy.where(
                                fits.imgs[ext][frm]>36001)] =
                                numpy.nan
337                             #apply bad pixel mask
338                             fits.imgs[ext][frm] = fits.imgs[
                                ext][frm] * mbp.imgs[ext]
339                             # show_fits(fits.imgs[ext][frm])
```

```
340                             #Non-Linear Correction
341                             fits.imgs[ext][frm] = nonlincor(
                                fits.imgs[ext][frm],ext-1)
342                             #Dark Subtraction
343                             fits.imgs[ext][frm] = fits.imgs[
                                ext][frm] - md.imgs[ext] + 7000
                                - 1 #chipbias+dark+bzero_remnant
344                             #Flat Division
345                             fits.imgs[ext][frm] = fits.imgs[
                                ext][frm] / mf.imgs[ext]
346                             #Row correction
347                             if row_correction==True:
348                                 to_cor = fits.imgs[ext][frm
                                    ].copy()
349                                 to_cor=to_cor.T
350                                 corrected = row_correct(
                                    to_cor)
351                                 fits.imgs[ext][frm]=
                                    corrected.T
352                         except ValueError:
353                             print "ERROR FOR ", raw.loc[i].
                                file, ext, frm
354                 sci_out = cmdir(output_dir+"science/") + raw
                    .loc[i].file.split("/")[-1]
355                 fits.write_frames(sci_out,clobber=True)
356                 bar.update(cnt); cnt += 1;
357         bar.finish()
358
359         fits = get_files(output_dir+"science/",ext="fits")
360         print "Organising Images.."
361         bar = pbar(len(fits));cnt=0
362         for fl in fits:
363             bar.update(cnt);cnt+=1
364             i,h = fits_import(output_dir+"science/"+fl,dext=
                1,hext=1)
365             dr=cmdir(output_dir+"science/"+h["OBJECT"])
366             shutil.move(output_dir+"science/"+fl,dr+fl)
367         bar.finish()
368
369     # NAN fix for CFHT data
370     print "Correcting NaNs.."
371     #-- User Variables
        ------------------------------------------------------
        -------
372     sci_direc=slash(output_dir+"science/"+sci_ob)
373     print sci_direc
374     flist = get_files(sci_direc,ext="fits")
375     #-- Libraries
        ------------------------------------------------------
        ------------
```

```
376  from standard import *
377  import sep
378  import cv2
379  from lmfit import *
380  from scipy import ndimage, interpolate
381  from astropy.modeling import models, fitting
382
383  #-- Functions
     ------------------------------------------------------------
     ------------
384  def CircularMask(img, x,y, radius=10):
385      #create a circular mask around a given x,y image
386      #inputs image, x_center, y_center, mask radius
387      #returns numpy array of mask
388      h, w=numpy.shape(img)
389      center=[int(y),int(x)]
390      Y, X = np.ogrid[:h, :w]
391      dist_from_center = np.sqrt((X - center[0])**2 + (Y-
         center[1])**2)
392      mask = dist_from_center <= radius
393      return mask
394
395  def window(img,x,y,w,ret="i"):
396      #create a subimage around x,y with width y
397      #return window image
398      x,y,w=int(x),int(y),int(w)
399      x_lo = x-w
400      x_hi = x+w+1
401      y_lo = y-w
402      y_hi = y+w+1
403      if x_lo < 0: x_lo=0;
404      if x_hi > len(img): x_hi = len(img)
405      if y_lo < 0: y_lo=0;
406      if y_hi > len(img[0]): y_hi = len(img[0])
407      if ret=="i":
408          return (img[x_lo:x_hi,y_lo:y_hi].copy(),(x_lo,
             x_hi,y_lo,y_hi))
409      if ret=="v":
410          return(x_lo,x_hi,y_lo,y_hi)
411
412  def show_fitsc(img, clims="auto",show=True,newfig=False,
     bgsub=False,title=False):
413    #plot fits image with cut levels defined by clims
414    import matplotlib.pyplot as plt
415    if newfig == False:
416      fig = plt.figure()
417      cmap = plt.cm.hot
418      cmap.set_bad((0, 0.6, 1, 1))
419      ax = fig.add_subplot(111)
420    else:
```

```
421         fig,pos = newfig
422         ax = fig.add_subplot(pos)
423       if title != False:
424         ax.set_title(title)
425       if clims == "auto":
426         if bgsub == True:
427           from scipy.stats import mode
428           goodpix = img[~numpy.isnan(img)]
429           bad = mode(img[~numpy.isnan(img)])[0][0]
430           med = numpy.median(goodpix[numpy.where(goodpix!=
              bad)])
431           mad = med_abs_dev(goodpix[numpy.where(goodpix!=bad
              )])
432         else:
433           med = numpy.median(img[~numpy.isnan(img)])
434           mad = med_abs_dev(img[~numpy.isnan(img)])
435         thrh,thrl = med+(mad*10), med-(mad*10)
436         if thrl < min(flatten_list(img.tolist())): thrl =
          min(flatten_list(img.tolist()))
437         if thrh > max(flatten_list(img.tolist())): thrh =
          max(flatten_list(img.tolist()))
438       else:
439         thrh=clims[0]
440         thrl=clims[1]
441       cmap = plt.cm.hot
442       im1 = ax.imshow(img.T,clim=(thrl,thrh),origin='lower',
          interpolation="none",cmap=cmap)
443       fig.colorbar(im1)
444       numrows, numcols = img.shape
445       imFORMAT = img.T
446       def format_coord(x, y):
447         col = round(x)
448         row = round(y)
449         if col>=0 and col<numcols and row>=0 and row<numrows:
450             z = imFORMAT[int(row),int(col)]
451             return 'x=%1.4f, y=%1.4f, count=%1.4f'%(x, y, z)
452         else:
453             return 'x=%1.4f, y=%1.4f'%(x, y)
454       ax.format_coord = format_coord
455       plt.tight_layout()
456       if show == True:
457         plt.show()
458       else:
459         return ax,(thrl,thrh)
460
461   #-- PSF Fitting
          ------------------------------------------------------------
          ------------
462   def psf_compare(free_params,psf1,psf2,ret="lsq"):
463       # print
```

```
        free_params['x'].value,free_params['y'].value,free_pa
        rams['factor'].value#debug
464     shift = ndimage.interpolation.shift(psf1,(float(
        free_params['x'].value),float(free_params['y'].value
        )))
465     shift = numpy.asarray(shift)*free_params['factor'].
        value
466     shift[numpy.where(shift<0)]=0
467     try:
468         res=psf2-shift
469     except ValueError:
470         res=numpy.asarray([[9999,9999],[9999,9999]],
        dtype="float")
471     if ret == "lsq":
472         res = res[~numpy.isnan(res)]
473         return res.flatten()
474     elif ret == "psf":
475         return shift
476     else:
477         return res
478
479 def psf_fix(psf_tofit,psf_match,plot=False):
480     if numpy.shape(psf_tofit) != numpy.shape(psf_match):
481         psf_match = reshape_psf(psf_tofit,psf_match)
482     kx,ky=flux_weighted_centroid(psf_match)
483     wx,wy=flux_weighted_centroid(psf_tofit)
484     psf_match_gd = psf_match[~numpy.isnan(psf_match)]
485     psf_tofit_gd = psf_tofit[~numpy.isnan(psf_tofit)]
486     psf_match_gd = psf_match_gd[numpy.where(psf_match_gd
        !=0)]
487     psf_tofit_gd = psf_tofit_gd[numpy.where(psf_tofit_gd
        !=0)]
488     ratio=numpy.nanmean(numpy.asarray(psf_tofit_gd,dtype
        ="float"))/numpy.nanmean(numpy.asarray(psf_match_gd,
        dtype="float"))
489     free_params = Parameters()
490     free_params.add('x', value= wx-kx,min=wx-kx-5.01,max
        =wx-kx+5.01)
491     free_params.add('y', value= wy-ky,min=wy-ky-5.01,max
        =wy-ky+5.01)
492     free_params.add('factor', value=ratio,min=0.001,max=
        2.0)
493     if plot==True:
494         fig = plt.figure(figsize=(20,20))
495         cl,ch = -200,1000
496         show_fitsc(psf_tofit,newfig=(fig,231),show=False
            ,title="Original PSF",clims=(cl,ch))
497         show_fitsc(psf_match,newfig=(fig,232),show=False
            ,title="PSF Kernel",clims=(cl,ch))
498     result = minimize(psf_compare, free_params,args=(
```

```
        psf_match,psf_tofit),method="anneal")
499     psf_match = psf_compare(free_params,psf_match,
        psf_tofit,ret="psf")
500     try:
501         psf_res = psf_tofit- psf_match
502         psf_tofit[numpy.isnan(psf_tofit)] = psf_match[
            numpy.isnan(psf_tofit)]
503     except ValueError:
504         return psf_tofit
505     if plot == True:
506         show_fitsc(psf_match,newfig=(fig,233),show=False
            ,title="Matched kernel",clims=(cl,ch))
507         show_fitsc(psf_res,newfig=(fig,234),show=False,
            title="Residuals",clims=(cl,ch))
508         show_fitsc(psf_tofit,newfig=(fig,235),title=
            "Corrected Orig PSF",clims=(cl,ch))
509     return psf_tofit
510
511 def reshape_psf(psf,kern):
512     kern_resize = kern.copy()
513     xd = len(psf)-len(kern)
514     xl = int(abs(math.floor(xd/2)))
515     xh = int(abs(xd) - xl)
516     if xd <0:
517         kern_resize = kern_resize[xl:-xh,:]
518     elif xd >0:
519         kern_resize = numpy.insert(kern_resize,[0]*xl,0,
            axis=0)
520         kern_resize = numpy.insert(kern_resize,[len(
            kern_resize)]*xh,0,axis=0)
521     yd = len(psf[0])-len(kern[0])
522     yl = int(abs(math.floor(yd/2)))
523     yh = int(abs(yd) - yl)
524     if yd < 0:
525         kern_resize = kern_resize[:,yl:-yh]
526     elif yd >0:
527         kern_resize = numpy.insert(kern_resize,[0]*yl,0,
            axis=1)
528         kern_resize = numpy.insert(kern_resize,[len(
            kern_resize[0])]*yh,0,axis=1)
529     return kern_resize
530
531 def flux_weighted_centroid(img):
532     X,Y,flux = [],[],[]
533     for y in range(0,len(img)):
534         for x in range(0,len(img[0])):
535             X.append(x)
536             Y.append(y)
537             flux.append(img[y][x])
538     X,Y,flux = numpy.asarray(Y),numpy.asarray(X),numpy.
```

```
        asarray(flux)
539     flux[numpy.where(numpy.isnan(flux))] = 0
540     try:
541         return numpy.array((numpy.average(X,weights=flux
            ),numpy.average(Y,weights=flux)))
542     except ZeroDivisionError:
543         return (int(len(img)/2),int(len(img[0])/2))
544
545
546 #-- Main
    ------------------------------------------------------------
    -----------------
547 nan_out = cmdir(output_dir+"nanfix/")
548 if remove_bad==True:
549     ap_mult=1.
550 bar=pbar(len(flist));cnt=0
551 for fl in flist:
552     bar.update(cnt);cnt+=1
553     kernel="test"
554     for det in [1,2,3,4]:
555         det_out = cmdir(nan_out + "det"+str(det)+"/")
556         if os.path.exists(det_out+fl):
557             continue
558         img,hdr=fits_import(sci_direc+fl,dext=det,hext=
            det)
559         imgin=img.copy()
560
561         #Calculate and subtract background
562         img = img.copy(order='C')
563         img = img.byteswap().newbyteorder()
564         bkg = sep.Background(img)
565         img[numpy.isnan(img)] = nar(bkg)[numpy.isnan(img
            )]
566         data_sub = img - bkg
567
568         #PSFs -> gaussian
569         data_sub = cv2.GaussianBlur(data_sub,(15,15),0)
570
571         #Extract sources
572         objects = sep.extract(data_sub, 5, err=bkg.rms())
573
574         #filter false flags - objects too elliptical
575         bad = numpy.where(objects['a']/objects['b']>2)[0]
576         objects=numpy.delete(objects,bad)
577
578         #filter false flags - objects too small
579         bad = numpy.where(objects['npix']<ap_size_lim)[0]
580         objects=numpy.delete(objects,bad)
581
582         #Plot
```

```
583             if show_sources==True:
584                 from matplotlib.patches import Ellipse
585                 fig, ax = plt.subplots()
586                 m, s = np.nanmedian(imgin), med_abs_dev(
                    imgin)*10
587                 im = ax.imshow(imgin.T, interpolation='none'
                    , cmap='hot',
588                                vmin=m-s, vmax=m+s, origin=
                                   'lower')
589                 for i in range(len(objects)):
590                     e = Ellipse(xy=(objects['y'][i], objects
                        ['x'][i]),
591                                 width=6*objects['a'][i],
592                                 height=6*objects['b'][i],
593                                 angle=objects['theta'][i] *
                                    180. / np.pi)
594                     e.set_facecolor('none')
595                     e.set_edgecolor('cyan')
596                     ax.add_artist(e)
597                 plt.show()
598 
599             #get object positions and radii
600             x,y =objects['y'], objects['x']
601             good = numpy.where(~numpy.isnan(x))
602             x,y=x[good],y[good]
603             good = numpy.where(~numpy.isnan(y))
604             x,y=x[good],y[good]
605             apsize = numpy.sqrt(numpy.mean(objects['npix'])/
                numpy.pi) * ap_mult
606 
607             img_flagged = imgin.copy()
608             for i in range(0,len(x)):
609                 try:
610                     mask=CircularMask(img_flagged,x[i],y[i],
                        apsize)
611                 except ValueError:
612                     print x
613                     print y
614                     print "FATAL ERROR: Masking Failed [699]"
615                     sys.exit()
616                 img_flagged[mask]=987654
617 
618             #correct BG pixels
619             img_flagged[numpy.isnan(img_flagged)]=nar(bkg)[
                numpy.isnan(img_flagged)]
620 
621             #guider square fix
622             med=numpy.nanmedian(img_flagged)
623             dev=med_abs_dev(img_flagged)*5
624             img_flagged[numpy.where(img_flagged<med-dev)] =
```

```
            nar(bkg)[numpy.where(img_flagged<med-dev)]
625
626         #unmask image
627         img_unmask=img_flagged.copy()
628         img_unmask[numpy.where(img_unmask==987654)]=
            imgin[numpy.where(img_unmask==987654)]
629
630         #edge nan correction
631         img_unmask[:,:5]=nar(bkg)[:,:5]
632         img_unmask[:5,:]=nar(bkg)[:5,:]
633         img_unmask[-4:,:]=nar(bkg)[-4:,:]
634         img_unmask[:,-4:]=nar(bkg)[:,-4:]
635
636         #PSF nan correction:
637         if remove_bad == True:
638             img_nancor2=img_unmask.copy()
639             for i in range(0,len(x)):
640                 mask=CircularMask(img_nancor2,x[i],y[i],
                    apsize)
641                 if True in numpy.isnan(img_nancor2[mask
                    ]):
642                     img_nancor2[mask]=numpy.nan
643         else:
644             #    get kernel
645             img_nancor2=img_unmask.copy()
646             if kernel=="test":
647                 for i in range(0,len(x)):
648                     X,Y = x[i],y[i]
649                     win = window(img_unmask,X,Y,apsize*2
                        )[0]
650                     if len(numpy.where(numpy.isnan(win
                        ))[0])!=0:
651                         continue
652                     kernel=win-(numpy.nanmedian(win)+(
                        sigma_psf*med_abs_dev(win)))
653                     kernel[numpy.where(kernel<0)]=0
654                     break
655             if kernel=="test":
656                 print "ERROR: Could not find good PSF
                    in whole image!"
657                 sys.exit()
658
659             #    fix bad psf's
660             for i in range(0,len(x)):
661                 X,Y = x[i],y[i]
662                 win,pos = window(img_unmask,X,Y,apsize*2)
663                 if len(numpy.where(numpy.isnan(win))[0
                    ])==0:
664                     continue
665                 X,Y =numpy.array([pos[0],pos[2]],dtype=
```

```
                    "float")+flux_weighted_centroid(win)
666                 win,p2 = window(img_unmask,X,Y,apsize*2)
667                 win_check=win.copy()
668                 if len(numpy.where(numpy.isnan(win))[0
                    ])==0:
669                     continue
670                 bgsub=(numpy.nanmedian(win)+(sigma_psf*
                    med_abs_dev(win)))
671                 win=win-bgsub
672                 x_lo,x_hi,y_lo,y_hi=p2
673                 fixed=psf_fix(win,kernel,False)+bgsub
674                 img_nancor2[x_lo:x_hi,y_lo:y_hi] = fixed
675         output_fits(img_nancor2,hdr,det_out+fl,clobber=
          True)
676
677
678 bar.finish()
679
680 print "Calibration Complete"
```

A.2 Photometry Routine

```
#Photometry code
#b.j.clark@keele.ac.uk

# Libraries
############################################################
############
from standard import *
from uncertainties import ufloat,unumpy
import pandas
import datetime
import pyfits
import numpy
from photutils import CircularAperture,CircularAnnulus,
aperture_photometry
from photutils.utils import calc_total_error
import matplotlib.pyplot as plt
import sep
from uncertainties import ufloat
import pandas
import os
from lmfit import *
from astropy.modeling import models, fitting
from scipy import ndimage, interpolate
from astropy.convolution import convolve, convolve_fft
import signal
import sys
import numpy as np

# Variables
############################################################
############
#Detector 2
fits_directory=
"/data/1_imaging/cfht/w36/cal/w36_cal/nanfix/det1/"
output_dir = "w36_phot_out_test_man/" #output file
directory
target = (112,1016) #(X,Y) of target star
max_stars = 10#maxiumum number of stars to measure
ref_image="1674427o_04.fits" #image used for source
detection
star_number_add=0 #addition to star count for other
detectors i.e. start on star 8 instead of 1
#Aperture Setup
ap_min = 6 #Lowest aperture size
ap_max = 15 #Highest aperture size
ap_step=.5 #Gap between apertures
annulus_inner=1.5 #sky annulus size as a multiple of
aperutre size
annulus_size=10 #size of sky annulus in pixels
fwhm = 6.5 #approximate FWHM used as fallback
```

```
centering="fwc"#centering method: psf fitting (fit) or flux-weighted centroid (fwc)
#Source detection
source_list = "w36-d1.coords" #location of manual source list - False for autodetect
window_size = 18 #window size in pixels to use around PSFs for cetnroiding
#Detector Information
detector = 0 #detector within fits image for FITS that contain more than one image
key_gain="GAIN" #GAIN fits header keyword
key_time = "MJD-OBS" #TIME/DATE fits header keyword
key_airm="AIRMASS" #Airmass fits header keyword
key_exp="EXPTIME" #Exposure time fits header keyword
#Runtime
debug = False
rerun = True
bgsig=6
#FWHM Variation
# fwhm_cor = ["None","Linear","Squared"];
# fw_arr=[1,fwhm_dif,fwhm_dif*fwhm_dif]
fwhm_cor = ["None"];
fw_arr=[1]

# Functions
############################################################
############
def signal_handler(signal, frame):
        print('Exiting!')
        sys.exit(0)
signal.signal(signal.SIGINT, signal_handler)

def arrays_to_file(listofarrays,filename,append=False, sepchar="\t"):
  ltemp = []
  if len(listofarrays[0]) <2:
    print ("ERROR: Check array length")
  for arr in listofarrays:
    try:
      if arr == 0:
        arr = numpy.zeros(len(listofarrays[0]))
        arr = numpy.arr(arr,dtype="int")
        arr = numpy.arr(arr,dtype="str")
    except:
      normalarray=True
    ltemp.append(arr)
  listofarrays = ltemp
  if append == True:
    fout = open(filename,"a")
  else:
```

```
84        fout = open(filename,"w")
85      for i in range(0, len(listofarrays[0])):
86        for j in range(0,len(listofarrays)):
87          fout.write(str(listofarrays[j][i]))
88          if j == len(listofarrays)-1:
89            fout.write("\n")
90          else:
91            fout.write(sepchar)
92      fout.close()
93
94
95    def nar(array,typ="float"):
96      try:
97        return numpy.asarray(array,dtype=typ)
98      except:
99        print ("Using String array")
100       return numpy.asarray(array,dtype="str")
101
102   def fits_import(img_name,dext=0,hext=0,det=False):
103     import pyfits
104     if det != False:
105       dext,hext = det, det
106     o_img = pyfits.open(img_name)
107     img = o_img[dext].data
108     hdr = o_img[hext].header
109     img2 = img.T
110     return (img2,hdr)
111
112
113   def is_array(var):
114       return isinstance(var, (list, tuple))
115
116   def flatten_list(to_flatten,once=False):
117     values = []
118     for val in to_flatten:
119       if is_array(val) and once == False:
120         [values.append(v) for v in flatten_list(val)]
121       else:
122         values.append(val)
123     return values
124
125   def med_abs_dev(data):
126       return median(numpy.absolute(data -median(data)))
127
128   def median(array,**kwargs):
129     return median(array[~numpy.isnan(array)],**kwargs)
130
131   def show_fits(img, clims="auto",show=True,newfig=False,
      bgsub=False,title=False,ax=False):
132     img=img.T
```

```
    import matplotlib.pyplot as plt
    if newfig == False:
      fig = plt.figure()
      cmap = plt.cm.hot
      cmap.set_bad((0, 0.6, 1, 1))
      ax = fig.add_subplot(111)
    else:
        if ax == True:
            fig,ax = newfig
        else:
            fig,pos = newfig
            ax = fig.add_subplot(pos)
    if title != False:
      ax.set_title(title)
    if clims == "auto":
      if bgsub == True:
        from scipy.stats import mode
        goodpix = img[~numpy.isnan(img)]
        bad = mode(img[~numpy.isnan(img)])[0][0]
        med = median(goodpix[numpy.where(goodpix!=bad)])
        mad = med_abs_dev(goodpix[numpy.where(goodpix!=bad
        )])
      else:
        med = median(img[~numpy.isnan(img)])
        mad = med_abs_dev(img[~numpy.isnan(img)])
      thrh,thrl = med+(mad*10), med-(mad*10)
      if thrl < min(flatten_list(img.tolist())): thrl =
      min(flatten_list(img.tolist()))
      if thrh > max(flatten_list(img.tolist())): thrh =
      max(flatten_list(img.tolist()))
    else:
      thrh=clims[0]
      thrl=clims[1]
    cmap = plt.cm.hot
    im1 = ax.imshow(img,clim=(thrl,thrh),origin='lower',
    interpolation="none",cmap=cmap)
    fig.colorbar(im1)
    numrows, numcols = img.shape
    imFORMAT = img
    def format_coord(x, y):
      col = round(x)
      row = round(y)
      if col>=0 and col<numcols and row>=0 and row<numrows:
          z = imFORMAT[row,col]
          return 'x=%1.4f, y=%1.4f, count=%1.4f'%(x, y, z)
      else:
          return 'x=%1.4f, y=%1.4f'%(x, y)
    ax.format_coord = format_coord
    plt.tight_layout()
    if show == True:
```

```
      plt.show()
    else:
      return ax

def slash(flname):
    if not flname.endswith("/"):
        flname = flname+"/"
    return str(flname)

def cmdir(direc,makenew=False,fp=False):
  direc = slash(direc)
  if not os.path.exists(direc):
    os.makedirs(direc)
    if not direc.endswith("/"):
      direc +='/'
  else:
    if makenew == True:
      rerun = 0
      if direc.endswith("/"):
        direc = direc[:-1]
      directory_init = direc
      while os.path.exists(direc):
          rerun += 1
          direc = directory_init + "_"+str(rerun)
      direc +='/'
      os.makedirs(direc)
      print ("Created new directory at: ", direc)
  if not direc.startswith("/") and fp == True:
    direc = os.getcwd()+"/"+direc
  return direc


def alt_combine(list1,list2):
    result = [None]*(len(list1)+len(list2))
    result[::2] = list1
    result[1::2] = list2
    return result

def plot_ap(x,y,ax,star,clr="#62FF00"):
    circle1 = plt.Circle((x, y), 25, color=clr,alpha=0.6)
    plt.plot(x,y,"+",ms=25,color="k")
    plt.text(x+2.,y+2.,"star"+str(star),color="k")
    ax.add_artist(circle1)

def plot_sources(data,coords):
  ax = show_fits(data,show=False)
  for i in range(0,len(coords)):
    clrr = "#62FF00"
    x = coords[i][0]
    y = coords[i][1]
```

```
229       plot_ap(x,y,ax,i+1,clrr)
230     plt.axis(ymin=0,ymax=len(data[0]),xmin=0,xmax=len(data
        ))
231     plt.title("Sources")
232     plt.show()
233
234   def get_sources(data,kernel,targ,sigma=4,show=False,
      debug=False,stars=False):
235       data = data.copy(order='C')
236       data = data.byteswap().newbyteorder()
237       bkg = sep.Background(data)
238       bkg_subtraced_data = data - bkg
239       if show==True and debug == True:
240           show_fits(data,show=False)
241           show_fits(np.array(bkg),show=False)
242           show_fits(bkg_subtraced_data,show=False)
243       to_convolve = bkg_subtraced_data.copy()
244       to_convolve[numpy.where(numpy.isnan(to_convolve))] =
           median(to_convolve[numpy.where(~numpy.isnan(
        to_convolve))])
245       tcM, tcMAD = median(to_convolve),med_abs_dev(
        to_convolve)
246       result = convolve_fft(to_convolve, kernel)
247       result = (((result-median(result))/med_abs_dev(
        result) ) * tcMAD ) + tcM
248       res = result.copy(order='C')
249       if sigma == "bad":
250         thresh=1.
251       else:
252         thresh = median(res) + (sigma*med_abs_dev(res))

253       if debug==True:
254         print "CONVOLVED"
255         show_fits(res,show=False)
256         plt.clf()
257         r2 = res.copy()
258         r2[numpy.where(r2<thresh)] = 0
259         print "threshold:",thresh
260         print r2[:10]
261         show_fits(r2,show=True)
262       objects = sep.extract(res, thresh, filter_type=
        'conv')
263       if debug == True:print "OBJECTS:", (len(objects))
264       objects = sorted(zip(objects['flux'],objects['y'],
        objects['x']),reverse=True)
265       if stars != False:
266         objects=objects[:stars]
267       source_xy = [x[1:] for x in objects]
268       distances =  numpy.sum(numpy.abs(nar(source_xy) - [
        targ[0],targ[1]]),axis=1)
```

```
269         source_i = numpy.where(distances==numpy.amin(
            distances))[0][0]
270         t_x,t_y = source_xy[source_i][0],source_xy[source_i
            ][1]
271         skipi=False
272         coordlist=[0]
273         ax = show_fits(bkg_subtraced_data,show=False)
274         for i in range(0,len(objects)):
275             clrr = "#62FF00"
276             x = objects[i][1]
277             y = objects[i][2]
278             if skipi==True:i=i-1
279             if x == t_x and y == t_y:
280                 clrr="b"
281                 i=-1
282                 skipi=True
283                 coordlist[0]=(x,y)
284             else:
285                 coordlist.append((x,y))
286             if show == True:plot_ap(x,y,ax,i+2,clrr)
287         print ("Please check sources are correct and re-run
            if necessary (Target in BLUE)")
288         if show == True:
289             plt.axis(ymin=0,ymax=len(bkg_subtraced_data[0]),
                xmin=0,xmax=len(bkg_subtraced_data))
290             plt.title("Sources")
291             plt.show()
292         return coordlist
293
294     def sub_bg(data):
295         data = data.copy(order='C')
296         data = data.byteswap().newbyteorder()
297         bkg = sep.Background(data)
298         bkg_subtraced_data = data - bkg
299         return bkg_subtraced_data,bkg.rms()
300
301     def get_psf(img,sx,sy,w=17,rcord=False):
302         img,rms = sub_bg(img)
303         img[numpy.where(img<rms*3)] = 0
304         psf = img[int(sx-w):int(sx+w+1),int(sy-w):int(sy+w+1
            )]
305         if rcord==False:
306             return psf
307         else:
308             return (psf,sx-w,sy-w)
309
310     def median(array,**kwargs):
311         gdar = array[~numpy.isnan(array)]
312         return numpy.median(gdar[numpy.where(gdar!=0)],**
            kwargs)
```

```
313 def mean(array,**kwargs):
314     gdar = array[~numpy.isnan(array)]
315     return numpy.mean(gdar[numpy.where(gdar!=0)],**
        kwargs)
316
317
318 #----- PSF Profile Fitting ------
319 def profile(x, A1=1,A2=1, mu=0, fwg=1,fwl=1, width=10):
320     x = numpy.linspace(numpy.amin(x)-1,numpy.amax(x),
        1000)
321     gauss_model_l = models.Voigt1D(amplitude_L=A1, x_0=
        mu, fwhm_L=fwl, fwhm_G=fwg)
322     gauss_model_r = models.Voigt1D(amplitude_L=A2, x_0=
        mu, fwhm_L=fwl, fwhm_G=fwg)
323     gauss_left_x = x[numpy.where(x<=mu)]
324     gauss_left = gauss_model_l(gauss_left_x)
325     gauss_right_x = x[numpy.where(x>=mu)]
326     gauss_right = gauss_model_r(gauss_right_x)
327     gauss_left_x = gauss_left_x - (width/2)
328     gauss_right_x = gauss_right_x + (width/2)
329     X = numpy.append(gauss_left_x,gauss_right_x)
330     Y = numpy.append(gauss_left,gauss_right)
331     X = numpy.append(numpy.asarray([numpy.amin(x)]),X);X
         = numpy.append(X,numpy.asarray([numpy.amax(x)]));
332     Y = numpy.append(numpy.asarray([0]),Y);Y = numpy.
        append(Y,numpy.asarray([0]));
333     gauss_func = interpolate.interp1d(X,Y)
334     return gauss_func
335
336 def model(free_params,x):
337     func = profile(x,free_params['A1'].value,free_params
        ['A2'].value,free_params['mu'].value,free_params[
        'fw_g'].value,free_params['fw_l'].value,free_params[
        'width'].value)
338     return func(x)
339
340 def residuals(free_params,x,y):
341     return y - model(free_params,x)
342
343 def profile_center(profile,fw_min,window_size,plot=False
    ,rpar=False,params=False,ax=False):
344     xr = numpy.arange(0,len(profile))
345     if params==True:
346         free_params = params
347     else:
348         free_params = Parameters()
349         free_params.add('A1', value= max(profile))
350         free_params.add('A2', value= max(profile))
351         free_params.add('mu', value= len(profile)/2)
352         free_params.add('fw_g', value= 3,min=0,max=10)
```

```
353             free_params.add('fw_l', value= 3,min=0,max=10)
354             free_params.add('width', value= 10,min=fw_min,
                max=window_size)
355         result = minimize(residuals, free_params,args=(xr,
            profile),method="leastsq")
356         free_params = result.params
357         fwl = free_params["fw_l"].value
358         fwg = free_params["fw_g"].value
359         fwhm = free_params["width"].value + ( (0.5346*fwl) +
             numpy.sqrt( (0.2166*numpy.square(fwl)) + numpy.
            square(fwg)  ) )
360         if plot == True:
361             if ax == False:
362                 plt.figure()
363                 plt.plot(xr,profile,"k-")
364                 plt.plot(xr,model(free_params,xr),"r-")
365                 plt.axvline(free_params["mu"].value)
366             else:
367                 ax.plot(xr,profile,"k-")
368                 ax.plot(xr,model(free_params,xr),"r-")
369                 ax.axvline(free_params["mu"].value,color="k")
370                 ax.axvline(free_params["mu"].value+(fwhm/2))
371                 ax.axvline(free_params["mu"].value-(fwhm/2))
372         if rpar==False:
373             return (free_params["mu"].value,fwhm)
374         else:
375             return (free_params["mu"].value,fwhm,free_params)
376
377     def get_centre(img,x,y,fw_min=5,w=10,plot=False,rpar=
        False,params=False):
378         psf,xlr,ylr = window(img,x,y,w,ret="i")
379         psf = psf - median(psf)
380         psf[numpy.where(psf<0)]=0
381         if plot==True:
382             fig = plt.figure()
383             ax = fig.add_subplot(222)
384             ax3 = fig.add_subplot(221)
385             ax2 = fig.add_subplot(224)
386             ax3.set_title("PSF Kernel")
387             show_fits(psf,bgsub=True,show=False,newfig=(fig,
                ax),ax=ax)
388             # plt.show()
389         ypr = numpy.mean(psf,axis=0)
390         xpr = numpy.mean(psf.T,axis=0)
391         if params == True and plot==True:
392             cntr_x = profile_center(xpr,fw_min,w,plot,rpar,
                params[0],ax=ax2)
393             cntr_y = profile_center(ypr,fw_min,w,plot,rpar,
                params[1],ax=ax3)
394         elif params == True:
```

```
395             cntr_x = profile_center(xpr,fw_min,w,plot,rpar,
                params[0])
396             cntr_y = profile_center(ypr,fw_min,w,plot,rpar,
                params[1])
397         elif plot ==True:
398             cntr_x = profile_center(xpr,fw_min,w,plot,rpar,
                ax=ax2)
399             cntr_y = profile_center(ypr,fw_min,w,plot,rpar,
                ax=ax3)
400         else:
401             cntr_x = profile_center(xpr,fw_min,w,plot,rpar)
402             cntr_y = profile_center(ypr,fw_min,w,plot,rpar)
403         if plot == True: plt.show()
404         if rpar==True:
405             return (cntr_x[0]+xlr,cntr_y[0]+ylr,cntr_x[1],
                cntr_y[1],cntr_x[2],cntr_y[2])
406         else:
407             return (cntr_x[0]+xlr,cntr_y[0]+ylr,cntr_x[1],
                cntr_y[1])
408
409     def window(img,x,y,w,ret="i"):
410         x_lo = x-w
411         x_hi = x+w+1
412         y_lo = y-w
413         y_hi = y+w+1
414         if x_lo < 0: x_lo=0;
415         if x_hi > len(img): x_hi = len(img)
416         if y_lo < 0: y_lo=0;
417         if y_hi > len(img[0]): y_hi = len(img[0])
418         if ret=="i":
419             return img[int(x_lo):int(x_hi),int(y_lo):int(
                y_hi)].copy(),x_lo,y_lo
420         if ret=="v":
421             return(x_lo,x_hi,y_lo,y_hi)
422
423
424     def flux_weighted_centroid(img,x,y,fw_min=5,w=10,plot=
    False,rpar=False,params=False):
425       img,xlr,ylr = window(img,x,y,w,ret="i")
426       X,Y,flux = [],[],[]
427       for y in range(0,len(img)):
428           for x in range(0,len(img[0])):
429               X.append(x)
430               Y.append(y)
431               flux.append(img[y][x])
432       X,Y,flux = numpy.asarray(Y),numpy.asarray(X),numpy.
    asarray(flux)
433       flux[numpy.where(numpy.isnan(flux))] = 0
434
435       return numpy.array((numpy.average(X,weights=flux)+xlr,
```

```
      numpy.average(Y,weights=flux)+ylr,17,17))
436
437
438   # Main
      ############################################################
      ################
439   prihdr("Photometry Pipeline")
440   if rerun==True:
441       output_dir = cmdir(output_dir)
442   else:
443       output_dir = cmdir(output_dir,True)
444   #Find Sources
445   targ_x, targ_y = target
446   ref_fl = fits_directory+ref_image
447   ref_im, ref_hd = fits_import(ref_fl,det=detector)
448   ref_im_fx = ref_im.byteswap().newbyteorder()
449   #Find Background
450   data = ref_im_fx.copy(order='C')
451   bkg = sep.Background(data)
452   ref_im[numpy.isnan(ref_im)] = bkg.back()[numpy.isnan(
      ref_im)]
453   if centering=="fwc":targ_x,targ_y,fw_ref_x,fw_ref_y =
      flux_weighted_centroid(ref_im,targ_x,targ_y,fw_min=5,w=
      window_size,plot=True)
454   if centering=="fit":targ_x,targ_y,fw_ref_x,fw_ref_y =
      get_centre(ref_im,targ_x,targ_y,fw_min=5,w=window_size,
      plot=True)
455   fwhm_ref = numpy.mean([fw_ref_x,fw_ref_y])
456   psf_kernel = get_psf(ref_im,targ_x,targ_y,w=window_size)
457   if debug==True:
458       print "PSF KERNEL"
459       show_fits(psf_kernel)
460   if source_list == False:
461       print ("Finding Sources..")
462       stellar_coords = get_sources(ref_im,psf_kernel,(
          targ_x,targ_y),show=True,debug=debug,sigma=bgsig,
          stars=max_stars)
463       plt.savefig(output_dir+"sources.png",filetype="png",
          dpi=500)
464       arrays_to_file(zip(*stellar_coords),output_dir+
          "sources.coords")
465       # plt.show()
466   else:
467       print ("Reading sources from", source_list)
468       stellar_coords=zip(*readfile(source_list))
469       print stellar_coords
470       plot_sources(ref_im,stellar_coords)
471
472   if max_stars != False:
473       stellar_coords=stellar_coords[:max_stars]
```

```
474
475     #set up apertures
476     aper_range = numpy.arange(ap_min,ap_max+ap_step,ap_step)
477     annulus_inner = annulus_inner * aper_range
478
479     file_list = get_files(fits_directory,ext="fits")#[::10]
480     aper_out = numpy.asarray(aper_range)
481     #Photometry
482     print ("Performing Photometry")
483     phot_out = open(output_dir+"phot.df","w")
484     phot_out.write("#"+"\t".join(["time","star","x","y","ap"
        ,"an_in","an_out","counts","count_err","bg_mean",
        "bg_mean_err","flux","flux_err","fwhm_x","fwhm_y","fwhm"
        ,"fwhmd","fwhmcor","airmass","exptime","fwcorap"])+"\n")
485     bar = pbar(len(file_list));cnt=0;
486     for fl in file_list:
487         #Load Data
488         bar.update(cnt);cnt+=1
489         img,hdr = fits_import(fits_directory+fl,det=detector)
490         time=float(hdr[key_time])
491         airmass=float(hdr[key_airm])
492         exptime=float(hdr[key_exp])
493         gain = float(hdr[key_gain])
494         if not isinstance(aper_range, (list, np.ndarray)):
495             aper_range = [aper_range]
496         if not isinstance(annulus_inner, (list, np.ndarray)):
497             annulus_inner = [annulus_inner]
498         #Center Stars
499         this_coords,this_fwhm = [],[]
500         for st in stellar_coords:
501             if centering=="fwc":
502                 x,y,fw_x,fw_y = flux_weighted_centroid(img,
                    st[0],st[1],fw_min=5,w=window_size,plot=
                    False)
503             if centering=="fit":
504                 x,y,fw_x,fw_y = get_centre(img,st[0],st[1],
                    fw_min=5,w=window_size,plot=False)
505             this_coords.append((x,y))
506             this_fwhm.append((fw_x,fw_y))
507         fwhm_dif = numpy.mean(this_fwhm[0])/fwhm_ref
508         #Mask out bad pixels
509         mask = numpy.zeros_like(img, dtype=bool)
510         mask[numpy.isnan(img)] = True
511         #Calculate error
512         bkg = img.copy(order='C')
513         bkg = sep.Background(bkg.byteswap().newbyteorder())
514         bkg_err = bkg.rms()
515         error = calc_total_error(img, bkg_err, gain)
516         #setup aperture
517         if debug == True: print this_coords, "\n\n"
```

```
518         fwcnt = 0;
519         for fwcor in fw_arr:
520             this_aper = numpy.asarray(aper_range) * fwcor
521             this_ann = numpy.asarray(annulus_inner) * fwcor
522             aperture = [CircularAperture(this_coords, r=ap)
                for ap in this_aper]
523             sky_aperture=[CircularAnnulus(this_coords, r_in=
                an, r_out=an+annulus_size) for an in this_ann]
524             apers=aperture+sky_aperture
525             #Perform Photometry
526             phot_table = aperture_photometry(img.T, apers,
                mask=mask,error=error)
527             #Read Outputs
528             counts = [unumpy.uarray(numpy.asarray(phot_table
                ['aperture_sum_'+str(aa)].data,dtype="float"),
                numpy.asarray(phot_table['aperture_sum_err_'+str
                (aa)].data,dtype="float")) for aa in range(0,len
                (this_aper))]
529             bkgs = [unumpy.uarray(numpy.asarray(phot_table[
                'aperture_sum_'+str(aa)].data,dtype="float"),
                numpy.asarray(phot_table['aperture_sum_err_'+str
                (aa)].data,dtype="float")) for aa in range(len(
                this_aper),2*len(this_aper))]
530             for ST in range(0,len(this_coords)):
531                 fwx,fwy=this_fwhm[ST]
532                 fwhm = numpy.mean([fwx,fwy])
533                 for i in range(0,len(this_aper)):
534                     bmg = (bkgs[i][ST]/sky_aperture[i].area
                        ())*aperture[i].area()
535                     flx=counts[i][ST]-bmg
536                     phot_out.write("\t".join([str(col) for
                        col in [time,ST+1,this_coords[ST][0],
537                         this_coords[ST][1],aper_out[i],this_ann[
                        i],this_ann[i]+annulus_size,counts[i][ST
                        ].n,
538                         counts[i][ST].s,bmg.n,bmg.s,flx.n,flx.s,
                        fwx,fwy,fwhm,fwhm_dif,fwhm_cor[fwcnt],
                        airmass,exptime,this_aper[i]]])+"\n")
539             fwcnt += 1
540 phot_out.close()
541 bar.finish()
542
543 #Seperate outputs into star data files
544 dat = pandas.read_csv(output_dir+"phot.df",delimiter=
    "\t",header=0)
545 dat['ap'] = dat['ap'].map(lambda x: '%.2f' % x) #float
    fix
546 print "read"
547 bar = pbar(len(dat.fwhmcor.unique()) * len(dat.star.
    unique()) * len(dat.ap.unique()) ); cnt =0;
```

```
548 for fwc in dat.fwhmcor.unique():
549     out_top = output_dir+cmdir("fw_"+str(fwc))
550     this_fwc = dat.loc[dat["fwhmcor"]==fwc]
551     for st in dat.star.unique():
552         out_star = cmdir(out_top+"star"+str(st))
553         this_star = this_fwc.loc[this_fwc["star"]==st]
554         for ap in dat.ap.unique():
555             select=this_star.loc[this_star["ap"]==ap]
556             select.to_csv(out_star+"star"+str(st+
                star_number_add)+"_"+str(ap)+"px.dat",
                columns=['time','flux','flux_err'],header=
                False,sep="\t",index=False)
557             select.to_csv(out_star+"star"+str(st+
                star_number_add)+".dat",sep="\t")
558             bar.update(cnt);cnt+=1;
559 bar.finish()
560
561 #Plot Apertures
562 show_fits(data,show=False)
563 apertures.plot(color="k",fill="rgb(21, 82, 164, 0.59)",
    alpha=0.2)
564 annulus_apertures.plot(color="#21b5d5")
565 plt.show()
566
```

A.3 Comparison Star and Eclipse Depth Explorer

```
#*********************************************************************************
#                          Eclipse Explorer - v0.07 (CFHT VERSION!!) - b.j.clark@keele.ac.uk
#*********************************************************************************

# Libraries
------------------------------------------------------------
from standard import *
from uncertainties import unumpy
from numpy import linspace, meshgrid
from matplotlib.mlab import griddata
import matplotlib.colorbar
import scipy.signal
import scipy.stats
import commands
import subprocess
import time as tcon
import sys
import multiprocessing
import signal
import pandas
import astropysics.phot

debug = False

# User Variables
------------------------------------------------------------
star_dir = "/media/bjc/Processing/nu_w48/phots_4/pre_filt/fw_None/" #output folder from phot code
output_dir = "/media/bjc/Processing/nu_w48/phots_4/runs/run2_backup/" #output folder

target = 1 #star number of target (usually 1)
sig_cut = 6 #sigma cut level
phot_output = "pltsecl06_01.dat" #the photometry file output by the mcmc for the specific eclipse
phot_mod = "pltsmod06.dat"
channel_name = "ch6.csv" #output csv file containing eclipse depth
rms_cut = 15 #% above minimum rmsbeta for LCs
script_dir = "/home/bjc/desk/cfht/lcfit/main/mcmc_inputs/" #path with mcmc inputs
col_no = 1 #output csv eclipse depth channel
```

```
36  mcmc_name = "mcmc_2016_occ2" #mcmc input scipt name
37  mcmc_path = script_dir+mcmc_name
38  mcmc_inp = script_dir+"linT.inp" #base mcmc input file
39  transit = False #is this a transit(True) or
    occultation(False)
40  max_stars=15 #maximum number of stars included in the
    final lightcurve
41
42  # Functions
    ------------------------------------------------------------
    -----------
43  def getstar(x,ap):
44      #Get time,flux information from the aperture
        photometry file
45      #x - number of star ie. 1 for star1_12.0px.dat
46      #ap - aperture size ie. 12.0 for star1_12.0px.dat
47      ap = "%.2f"%float(ap)
48      star_dat = readfile(star_dir+"star"+str(x)+"/star"+
        str(x)+"_"+ap+"px.dat")
49      star_flux = unumpy.uarray(star_dat[1],star_dat[2])
50      star_time = star_dat[0]
51      return (star_time,star_flux)
52
53  def signal_handler(signal, frame):
54      print('WAIT: Clearing any MCMC runs..')
55      commands.getoutput("kill -9 `ps -ef | grep "+
        mcmc_name+" | grep -v grep | awk '{print $2}'`")
56      print "Done, exiting.."
57      sys.exit(0)
58
59  def sigma(x):
60      x = numpy.asarray(x,dtype="float")
61      return numpy.std(x[~numpy.isnan(x)])
62
63  def beta_red(sig_n,sig_1,N,M):
64      B_red = (float(sig_n)/float(sig_1)) * numpy.sqrt( (
        float(N)* (float(M) - 1) ) / float(M) )
65      return B_red
66
67  def time_bin(time,arr,binsize=5):
68      #time in days
69      #arr = y values to be binned
70      #binsize in minutes
71      twidth_days = numpy.amax(time) - numpy.amin(time)
72      twidth_mins = twidth_days * 24 *60
73      nbins = int(twidth_mins/binsize)
74      if nbins == 0:
75          return (numpy.nan,numpy.nan)
76      biny,binx,binloc = scipy.stats.binned_statistic(time
        , res, statistic='mean', bins=nbins)
```

```
77      nbins = numpy.amax(binloc)
78      Nbin = int(len(time)/nbins)
79      binx = 0.5*(binx[:-1] + binx[1:])
80      return (binx,biny,nbins,Nbin)
81
82  def lcbin(time,flux,binsize):
83      twidth_days = numpy.amax(time) - numpy.amin(time)
84      twidth_mins = twidth_days * 24 *60
85      nbins = int(twidth_mins/binsize)
86      tsplit = numpy.array_split(time,nbins)
87      bin_t = [numpy.mean(x) for x in tsplit ]
88      bin_f = [numpy.mean(x) for x in numpy.array_split(
        flux,nbins)]
89      bin_e = [numpy.std(x)*(1/numpy.sqrt(len(x))) for x
        in numpy.array_split(flux,nbins)]
90      return (bin_t,bin_f,bin_e)
91
92  def rms_beta(time,res,bs=10,be=30,br=20):
93      time,res = zip(*sorted(zip(time,res)))
94      sig_white = sigma(res)
95      beta_rs = []
96      for binsz in numpy.linspace(bs,be,br):
97          bt,br,nbins,Nbin = time_bin(time,res,binsz)
98          sig_red = sigma(br)
99          beta_rs.append(beta_red(sig_red,sig_white,Nbin,
            nbins))
100     B_red = numpy.amax(beta_rs)
101     return sig_white * B_red * B_red
102
103
104 def grid(x, y, z, resX=100, resY=100):
105     "Convert 3 column data to matplotlib grid"
106     from scipy.interpolate import griddata
107     grid_x, grid_y = np.mgrid[min(x): max(x):1j * resX,
108     min(y): max(y):1j * resY]
109     Z = griddata(np.array(zip(x, y)), np.array(z),
110     (grid_x, grid_y), method='linear')
111     return grid_x, grid_y, Z
112
113 def rectangle(axs,x,y,c="k"):
114     import matplotlib.patches as patches
115     axs.add_patch(
116     patches.Rectangle(
117         (x, y),  # (x,y)
118         0.25,       # width
119         1.,         # height
120         facecolor=c,
121         alpha=1.,
122         hatch=None,
123         edgecolor=c,
```

```
124             linewidth=1.,
125             linestyle='solid'
126         ))
127 
128     def plot_rms(y,x,flux,fig1=False):
129         x=nar(x)-.125
130         y=nar(y)-.5
131         if fig1==False:
132             fig1 = plt.figure(figsize=(18,5))
133         ax1 = fig1.add_axes([0.05, 0.575, 0.80, 0.375])
134                             # [x0    y0  w      h]
135         fl = nar(flux)
136         ma = median(fl)+(3*med_abs_dev(fl))
137         norm = plt.Normalize(vmax=ma,vmin=min(flux))
138         colors = plt.cm.hot(norm(flux))
139         for i in range(0,len(z)):
140             rectangle(ax1,x[i],y[i],colors[i])
141         plt.axis(xmin=min(x),xmax=max(x),ymin=min(y),ymax=
            max(y))
142         axis_ticks(ax1,xticks=(1,0.25),scale=0.2)
143         plt.ylabel("Number of Stars")
144         plt.xlabel("Aperture Size")
145         ax2 = fig1.add_axes([0.9, 0.575, 0.02, 0.375])
146         cb1 = matplotlib.colorbar.ColorbarBase(ax2, cmap=plt
            .cm.hot,
147                                        norm=norm,
148                                        orientation='vertical')
149         cb1.set_label("% above minimum "+ r'$rms \times
            {\beta}^2$',labelpad=-75)
150         return ax1,x,y,flux
151 
152 
153     def plot_ecl(y,x,flux,fig1=False):
154         x=nar(x)-.125
155         y=nar(y)-.5
156         if fig1==False:fig1 = plt.figure(figsize=(18,5))
157         ax1 = fig1.add_axes([0.05, 0.075, 0.80, 0.3750])
158                             # [x0    y0  w      h]
159         fl = nar(flux)
160         ma = median(fl)+(4*med_abs_dev(fl))
161         mi = median(fl)-(4*med_abs_dev(fl))
162         norm = plt.Normalize(vmax=ma,vmin=mi)
163         colors = plt.cm.hot(norm(flux))
164         for i in range(0,len(z)):
165             rectangle(ax1,x[i],y[i],colors[i])
166         plt.axis(xmin=min(x),xmax=max(x),ymin=min(y),ymax=
            max(y))
167         axis_ticks(ax1,xticks=(1,0.25),scale=0.2)
168         plt.ylabel("Number of Stars")
169         plt.xlabel("Aperture Size")
```

```
170         ax2 = fig1.add_axes([0.9, 0.075, 0.02, 0.375])
171         cb1 = matplotlib.colorbar.ColorbarBase(ax2, cmap=plt
            .cm.hot,
172                                                norm=norm,
173                                                orientation='vertical')
174         cb1.set_label("Eclipse Depth (%)",labelpad=-100)
175         return ax1,x,y,flux
176
177     def contour(ax1,x,y,flux):
178         flux_cntr = flux[:]
179         x_cntr = x.tolist()
180         y_cntr = y.tolist()
181
182         #Pad for contour plot to edge
183         x_pad_idx = numpy.where(x_cntr==min(numpy.unique(
            x_cntr)))[0]
184         x_lo_pad = nar(x_cntr)[x_pad_idx] -.5
185         yx_lo_pad = nar(y_cntr)[x_pad_idx]
186         zx_lo_pad = nar(flux_cntr)[x_pad_idx]
187         x_cntr = x_cntr+x_lo_pad.tolist()
188         y_cntr = y_cntr + yx_lo_pad.tolist()
189         flux_cntr = flux_cntr+ zx_lo_pad.tolist()
190
191         x_pad_idx = numpy.where(y_cntr==min(numpy.unique(
            y_cntr)))[0]
192         x_lo_pad = nar(x_cntr)[x_pad_idx]
193         yx_lo_pad = nar(y_cntr)[x_pad_idx]-.5
194         zx_lo_pad = nar(flux_cntr)[x_pad_idx]
195         x_cntr = x_cntr+x_lo_pad.tolist()
196         y_cntr = y_cntr + yx_lo_pad.tolist()
197         flux_cntr = flux_cntr+ zx_lo_pad.tolist()
198
199         flux_cntr= nar(flux_cntr)
200         flux_cntr[numpy.where(flux_cntr<=rms_cut)] = 0
201         flux_cntr[numpy.where(flux_cntr>rms_cut)] = 10
202         X, Y, Z = grid(x_cntr, y_cntr, flux_cntr)
203
204         CS = ax1.contour(X+.5, Y+.5, Z, 1,
205                          #[-1, -0.1, 0, 0.1],
206                          #alpha=0.5,
207                          colors="#00BCFA",
208                          linecolor="white",
209                          #cmap=plt.cm.hot,
210                          origin='lower')
211
212     def flux2mag(flux,flxerr):
213         med = numpy.median(flux[~numpy.isnan(flux)])
214         flux = flux/med
215         flxerr = flxerr/med
216         mag,merr = astropysics.phot.lum_to_mag(flux,0,1,
```

```
        flxerr)
217     return (mag,merr)
218
219
220 # Main
    ------------------------------------------------------------
    ----------------
221 script_dir =    slash(os.path.dirname(os.path.realpath(
    __file__)))
222 output_dir = cmdir(output_dir)
223 rms_dir = cmdir(output_dir+"rms/")
224
225 #get list of all stars and apertures
226 stars = [int(x.strip("/").split("star")[-1]) for x in
    get_files(star_dir,typ="d")]
227 comps = stars[:]
228 del comps[comps.index(target)]
229 apertures = [x.split("_")[-1].split("px")[0] for x in
    get_files(star_dir+"star"+str(target)+"/",contains=
    "star"+str(target)+"_")]
230 apertures = numpy.array(apertures,dtype="float")
231 apertures = apertures[numpy.where(apertures<30.01)]
232 apertures = ["%.2f"%ap for ap in apertures]
233
234 ngood = len(getstar(target,numpy.amax(nar(apertures)))[0
    ])
235
236 #create initial lighcurves for targ/comp for every
    individual star/ap
237 init_lc_dir = cmdir(output_dir+"init_lcs/")
238 print "\nCreating lighcurves for each star and
    aperture.."
239 bar = pbar(len(apertures));cnt=0;
240 for ap in apertures:
241     bar.update(cnt);cnt+=1;
242     try:
243         targt, targf = getstar(target,ap)
244     except:
245         continue
246     for c in comps:
247         this_path = init_lc_dir+"lc_st"+str(c)+"_ap"+str
            (ap)+"/"
248         if os.path.exists(this_path+"quadT.lc"):continue;
249         lcpath = cmdir(this_path)
250         compt, compf = getstar(c,ap)
251         compf[numpy.where(compf==0)]=numpy.nan
252         lc = targf/compf
253         t,f,e = targt, nar([x.n for x in lc]), nar([x.s
            for x in lc])
254         if debug==False:
```

```
255             if transit == False:
256                 if t[0] < 50000:
257                     t = t + 249999.5 #CFHT ONLY
258                 elif t[0] < 2400000:
259                     t = t + 2399999.5 #CFHT ONLY
260             else:
261                 if t[0] > 2450000:
262                     t = t - 2450000.5 #CFHT ONLY
263                 elif t[0] > 50000:
264                     t = t - 49999.5 #CFHT ONLY
265             filt = scipy.signal.medfilt(f,kernel_size=21)
266             res = f/filt
267             fme = numpy.median(res[~numpy.isnan(res)])
268             fsi = med_abs_dev(res[~numpy.isnan(res)])
269             if fsi == 0:
270                 os.rmdir(this_path)
271                 continue
272             t = t[numpy.where((res<(fme+(sig_cut*fsi)))
                & (res>(fme-(sig_cut*fsi))))]
273             e = e[numpy.where((res<(fme+(sig_cut*fsi)))
                & (res>(fme-(sig_cut*fsi))))]
274             f = f[numpy.where((res<(fme+(sig_cut*fsi)))
                & (res>(fme-(sig_cut*fsi))))]
275             e = e/median(f)
276             f = f/median(f)
277             if transit == True: f,e = flux2mag(f,e)
278             if len(f) < (ngood/100)*90:
279                 os.rmdir(lcpath)
280                 print "ONLY", len(f),"/",ngood, "Points
                    found - skipping"
281                 continue
282         else:
283             fme = numpy.median(f[~numpy.isnan(f)])
284             fsi = med_abs_dev(f[~numpy.isnan(f)])
285             t = t[numpy.where((f<(fme+(5*fsi))) & (f>(
                fme-(5*fsi))))]
286             t = t + 2400000.5 #CFHT ONLY
287             e = e[numpy.where((f<(fme+(5*fsi))) & (f>(
                fme-(5*fsi))))]
288             f = f[numpy.where((f<(fme+(5*fsi))) & (f>(
                fme-(5*fsi))))]
289             f = f/fme
290             e = e/fme
291         arrays_to_file([t,f,e,0,0],lcpath+"notr.lc")
292         arrays_to_file([t,f,e,t,0],lcpath+"linT.lc")
293         arrays_to_file([t,f,e,t,t*t],lcpath+"quadT.lc")
294 bar.finish()
295
296 #run mcmc's for initial lightcurves
297 signal.signal(signal.SIGINT, signal_handler)
```

```
298  print "\nRunning MCMC's for each lighcurve. This may
     take a while.."
299  main_dir = init_lc_dir
300  if main_dir.endswith("/"):main_dir=main_dir[:-1]
301  folds = get_files(init_lc_dir,typ="d")
302  bar = pbar(len(folds))
303  i = 0; nskip = 0;
304  nproc = multiprocessing.cpu_count()+2
305  if os.path.exists(rms_dir+"initial_lc_rms_beta.npy"):
306      print "- Skipping MCMC analysis due to saved RMS
     data"
307  else:
308      for i in range(0,len(folds)):
309          while True == True:
310              no_mcmcs = commands.getoutput("ps -ef |
                 grep "+mcmc_name+" | grep -v grep | awk
                 '{print $2}'")
311              no_mcmcs = len(no_mcmcs.split("\n"))
312              if no_mcmcs < nproc:
313                  break
314              tcon.sleep(5)
315          os.chdir(main_dir+"/"+folds[i])
316          bar.update(i)
317          if os.path.exists(main_dir+"/"+folds[i]+
             "mcmc.out"):
318              nskip += 1
319              continue
320          subprocess.Popen("nohup "+mcmc_path+" < "+
             mcmc_inp+" 2> Log &", shell=True)
321          i += 1
322      bar.finish()
323      if nskip != 0:
324          print "WARNING:", nskip, "folders skipped!"
325
326      while True == True:
327          no_mcmcs = commands.getoutput("ps -ef | grep "+
             mcmc_name+" | grep -v grep | awk '{print $2}'")
328          no_mcmcs = len(no_mcmcs.split("\n"))
329          if no_mcmcs == 1:
330              break
331          tcon.sleep(5)
332
333  #calculate RMS beta for initial runs
334  print "\nCalculating RMS Beta Squared for initial
     lightcurves.."
335  if os.path.exists(rms_dir+"initial_lc_rms_beta.npy"):
336      print "- Loading saved RMS data"
337      data = numpy.load(rms_dir+"initial_lc_rms_beta.npy")
338  else:
339      bar = pbar(len(folds)); cnt = 0;
```

```
340         stats = []
341         for f in folds:
342             bar.update(cnt); cnt +=1;
343             fl = slash(main_dir)+slash(f)+phot_output
344             try:
345                 time = readfile(fl)[1]
346                 if transit == True:
347                     res = readfile(fl)[3]
348                 else:
349                     res = readfile(fl)[5]
350                 stats.append((rms_beta(time,res),f))
351             except IndexError:
352                 print "ERROR: Cannot read output file in:", f
353             except IOError:
354                 stats.append((9999999.,f))
355                 # input("STOP")
356         bar.finish()
357         stats = sorted(stats)
358         stats = nar(stats)
359         sortd = []
360         for s in stats:
361             # print s
362             rms = s[0]
363             star = s[1].split("_st")[1].split("_")[0]
364             ap = s[1].split("_ap")[1].split("/")[0]
365             sortd.append((star,ap,rms))
366         data = nar(sortd)
367         numpy.save(rms_dir+"initial_lc_rms_beta.npy",data)
368
369
370     #Rank by median rmsbeta
371     print "\nRanking stars..",
372     cols = ["star","ap","rms"]
373     df = pandas.DataFrame(columns=cols,data=data)
374     sort = []
375     for star in df.star.unique():
376         star_dat = df.loc[df["star"]==star]
377         sort.append((median(star_dat.rms), med_abs_dev(
        star_dat.rms),star))
378     sort = sorted(sort)
379     stars_ranked = []
380     for s in sort:
381         stars_ranked.append("%d"%s[2])
382     stars_ranked = [int(x) for x in stars_ranked][:max_stars]
383     print "complete"
384
385     #create lightcurves with combined comparison stars
        based upon rmsbeta rank
386     print "\nCreating lightcurves with combined comparison
        stars.."
```

```
comb_lc_dir = cmdir(output_dir+"comb_lcs/")
bar = pbar(len(stars_ranked));cnt=0;
for no in range(1,len(stars_ranked)):
    bar.update(cnt); cnt += 1;
    comps = stars_ranked[:no]
    for ap in apertures:
        try:
            targt, targf = getstar(target,ap)
        except IndexError as e:
            # print target,ap
            # print e
            continue
        this_path = comb_lc_dir+"lc_"+str(len(comps))+
        "N_st"+str("+".join([str(x) for x in comps]))+
        "_ap"+str(ap)+"/"
        if os.path.exists(this_path+"quadT.lc"):continue
        lcpath = cmdir(this_path)
        comp_flux = []
        for c in comps:
            comp_flux.append(getstar(c,ap)[1])
        compf = numpy.mean(comp_flux,axis=0)
        compf[numpy.where(compf==0)]=numpy.nan
        lc = targf/compf
        t,f,e = targt, nar([x.n for x in lc]), nar([x.s
        for x in lc])
        if debug == False:
            if transit == False:
                if t[0] < 50000:
                    t = t + 2449999.5 #CFHT ONLY
                elif t[0] < 2400000:
                    t = t + 2399999.5 #CFHT ONLY
            else:
                if t[0] > 2450000:
                    t = t - 2450000.5 #CFHT ONLY
                elif t[0] > 50000:
                    t = t - 49999.5 #CFHT ONLY
            filt = scipy.signal.medfilt(f,kernel_size=21)
            res = f/filt
            fme = numpy.median(res[~numpy.isnan(res)])
            fsi = med_abs_dev(res[~numpy.isnan(res)])
            t = t[numpy.where((res<(fme+(sig_cut*fsi)))
            & (res>(fme-(sig_cut*fsi))))]
            e = e[numpy.where((res<(fme+(sig_cut*fsi)))
            & (res>(fme-(sig_cut*fsi))))]
            f = f[numpy.where((res<(fme+(sig_cut*fsi)))
            & (res>(fme-(sig_cut*fsi))))]
            e = e/median(f)
            f = f/median(f)
        else:
            fme = numpy.median(f[~numpy.isnan(f)])
```

```
431                 fsi = med_abs_dev(f[~numpy.isnan(f)])
432                 t = t[numpy.where((f<(fme+(5*fsi))) & (f>(
                    fme-(5*fsi))))]
433                 t = t + 2400000.5 #CFHT ONLY
434                 e = e[numpy.where((f<(fme+(5*fsi))) & (f>(
                    fme-(5*fsi))))]
435                 f = f[numpy.where((f<(fme+(5*fsi))) & (f>(
                    fme-(5*fsi))))]
436                 f = f/fme
437                 e = e/fme
438             if transit == True: f,e = flux2mag(f,e)
439             if len(f) < (ngood/100)*90:
440                 os.rmdir(lcpath)
441                 continue
442             arrays_to_file([t,f,e,0,0],lcpath+"notr.lc")
443             arrays_to_file([t,f,e,t,0],lcpath+"linT.lc")
444             arrays_to_file([t,f,e,t,t*t],lcpath+"quadT.lc")
445     bar.finish()
446
447     #Run mcmc's for combination lightcurves
448     print "\nRunning MCMC's for each best ranking
        combination lighcurve. This may take a while.."
449     main_dir = comb_lc_dir
450     folds = get_files(comb_lc_dir,typ="d")
451     bar = pbar(len(folds))
452     i = 0; nskip = 0;
453     nproc = multiprocessing.cpu_count()+2
454     if os.path.exists(rms_dir+"comb_lc_rms_beta.npy"):
455         print "- Skipping MCMC analysis due to saved RMS
            data"
456     else:
457         for i in range(0,len(folds)):
458             while True == True:
459                 no_mcmcs = commands.getoutput("ps -ef |
                    grep "+mcmc_name+" | grep -v grep | awk
                    '{print $2}'")
460                 no_mcmcs = len(no_mcmcs.split("\n"))
461                 if no_mcmcs < nproc:
462                     break
463                 tcon.sleep(5)
464             os.chdir(main_dir+"/"+folds[i])
465             bar.update(i)
466             if os.path.exists(main_dir+"/"+folds[i]+
                "mcmc.out"):
467                 nskip += 1
468                 continue
469             subprocess.Popen("nohup "+mcmc_path+" < "+
                mcmc_inp+" 2> Log &", shell=True)
470             i += 1
471         bar.finish()
```

```
472         if nskip != 0:
473             print "WARNING:", nskip, "folders skipped!"
474 
475         while True == True:
476             no_mcmcs = commands.getoutput("ps -ef | grep "+
                mcmc_name+" | grep -v grep | awk '{print $2}'")
477             no_mcmcs = len(no_mcmcs.split("\n"))
478             # print no_mcmcs
479             if no_mcmcs == 1:
480                 break
481             tcon.sleep(5)
482 
483     #calculate RMS beta for combination runs
484     lc_folds = get_files(comb_lc_dir,typ="d")
485     print "\nCalculating RMS Beta Squared for combined
        lightcurves.."
486     rms_dir = cmdir(output_dir+"rms/")
487     if os.path.exists(rms_dir+"comb_lc_rms_beta.npy"):
488         print "- Loading saved RMS data"
489         data = numpy.load(rms_dir+"comb_lc_rms_beta.npy")
490     else:
491         bar = pbar(len(lc_folds)); cnt = 0;
492         stats = []
493         for f in lc_folds:
494             bar.update(cnt); cnt +=1;
495             fl = comb_lc_dir+f+phot_output
496             try:
497                 time = readfile(fl)[1]
498             except IOError:
499                 stats.append((99999,f))
500                 continue
501             if transit == True:
502                 res = readfile(fl)[3]
503             else:
504                 res = readfile(fl)[5]
505             stats.append((rms_beta(time,res),f))
506         bar.finish()
507         stats = sorted(stats)
508         stats = nar(stats)
509         sortd = []
510         for s in stats:
511             # print s
512             rms = s[0]
513             star = s[1].split("_st")[1].split("_")[0]
514             ap = s[1].split("_ap")[1].split("/")[0]
515             sortd.append((star,ap,rms))
516         data = nar(sortd)
517         numpy.save(rms_dir+"comb_lc_rms_beta.npy",data)
518 
519 
```

```
#read in eclipse depths for combined runs
print "\nReading eclipse depths from combined lightcurve outputs"
rms_dir = cmdir(output_dir+"rms/")
if os.path.exists(rms_dir+"comb_lc_ecl_beta.npy"):
    print "- Loading saved RMS data"
    ecl_data = numpy.load(rms_dir+"comb_lc_ecl_beta.npy")
else:
    bar = pbar(len(lc_folds)); cnt = 0;
    stats = []
    for f in lc_folds:
        bar.update(cnt); cnt +=1;
        fl = comb_lc_dir+f+phot_mod
        try:
            time = readfile(fl)[3]
        except IOError:
            stats.append((99999,f))
            continue
        if transit == True:
            res = readfile(fl)[3]
            input("THIS IS WORNG - GRUJSH EHSAOI")
        else:
            res = readfile(fl)[3]
        stats.append((numpy.amax(res)-numpy.amin(res),f))
    bar.finish()
    stats = sorted(stats)
    stats = nar(stats)
    sortd = []
    for s in stats:
        # print s
        rms = s[0]
        star = s[1].split("_st")[1].split("_")[0]
        ap = s[1].split("_ap")[1].split("/")[0]
        sortd.append((star,ap,rms))
    ecl_data = nar(sortd)
    numpy.save(rms_dir+"comb_lc_ecl_beta.npy",ecl_data)


#Plot ap,nstar vs [rms,eclipse] and calculate new eclipse depth
rms = data
RMS = zip(*rms)
RMS_c = numpy.asarray(RMS[2],dtype="float")
RMS_c = ((RMS_c/numpy.amin(RMS_c))*100)-100
RMS[2] = RMS_c
rms = zip(*RMS)
rms_arr = []
for r in rms:
    nstar = len(r[0].split("+"))
    rms_arr.append((r[2],nstar,r[1],r[0]))
```

```
568
569 cols = ["rms","n","ap","comb"]
570 df = pandas.DataFrame(data=rms_arr,columns=cols)
571 aps = df.ap.unique()
572 nstars = df.n.unique()
573
574 best = df.loc[df["rms"]<=rms_cut]
575
576 x,y,z = [],[],[]
577 for ap in aps:
578     for N in nstars:
579         try:
580             z.append(df.loc[(df["ap"] == ap) & (df["n"]
                == N), "rms"].values[0])
581         except IndexError:
582             z.append(numpy.nan)
583         x.append(float(N))
584         y.append(float(ap))
585
586 arrays_to_file([x,y,z],output_dir+"rms.dat")
587 fig1 = plt.figure(figsize=(18,10))
588 rms_ax, rms_x,rms_y,rms_flux = plot_rms(x,y,z,fig1=fig1)
589 contour(rms_ax, rms_x,rms_y,rms_flux)
590
591 rms = ecl_data
592 RMS = zip(*rms)
593 RMS_c = numpy.asarray(RMS[2],dtype="float")
594 RMS[2] = RMS_c
595 rms = zip(*RMS)
596 rms_arr = []
597 for r in rms:
598     nstar = len(r[0].split("+"))
599     rms_arr.append((r[2],nstar,r[1],r[0]))
600
601 cols = ["rms","n","ap","comb"]
602 df = pandas.DataFrame(data=rms_arr,columns=cols)
603 aps = df.ap.unique()
604 nstars = df.n.unique()
605
606 x,y,z = [],[],[]
607 for ap in aps:
608     for N in nstars:
609         try:
610             z.append(df.loc[(df["ap"] == ap) & (df["n"]
                == N), "rms"].values[0])
611         except IndexError:
612             z.append(numpy.nan)
613         x.append(float(N))
614         y.append(float(ap))
615 arrays_to_file([x,y,z],output_dir+"eclipse_depth.dat")
```

```
rms_ax, n,n,n = plot_ecl(x,y,z,fig1=fig1)
contour(rms_ax, rms_x,rms_y,rms_flux)

plt.savefig(output_dir+"ap_vs_star.pdf",filetype="pdf")
plt.savefig(output_dir+"ap_vs_star.eps",filetype="eps")


fig,axs=plt.subplots(3,4,sharex=True,sharey=True,figsize
=(18,10))
ecl_depths = numpy.array([])
C1=0;C2=0;cnt=0;
for b in best.values:
    cnt+=1;
    if C1>=3:
        C1=0
        C2+=1
    ecl_col = readfile(comb_lc_dir+"lc_"+str(b[1])+
    "N_st"+str(b[3])+"_ap"+str(b[2])+"/"+channel_name)[
    col_no]
    ecl_depths = numpy.append(ecl_depths,ecl_col)
    if cnt<=12:
        pd = readfile(comb_lc_dir+"lc_"+str(b[1])+"N_st"
        +str(b[3])+"_ap"+str(b[2])+"/"+phot_output)
        md = readfile(comb_lc_dir+"lc_"+str(b[1])+"N_st"
        +str(b[3])+"_ap"+str(b[2])+"/"+phot_mod)
        mt = md[0]
        mf = md[3]
        ecld=numpy.amax(mf)-numpy.amin(mf)
        pt = pd[1]
        pflx = (pd[2]/pd[4])-ecld
        bt,bf,be = lcbin(pt,pflx,3)
        axs[C1][C2].plot(bt,bf,"o",color="k")
        errorbar(bt,bf,be,axs[C1][C2],cap=3)
        if C1!=0:
            axs[C1][C2].plot(mt,mf,"-",color="#FF5900",
            lw=5,alpha=.7)
            axs[C1][C2].axis(xmin=0.45,xmax=0.55,ymin=
            0.9971,ymax=1.0019)
        else:
            ax2 = axs[C1][C2].twiny()
            ax2.plot(mt,mf,"-",color="#FF5900",lw=5,
            alpha=.7)
            ax2.axis(xmin=0.45,xmax=0.55,ymin=0.9971,
            ymax=1.0019)
        if C2==3:
            ax3 = axs[C1][C2].twinx()
            ax3.plot(0.5,1,"+",alpha=0)
            ax3.axis(xmin=0.45,xmax=0.55,ymin=0.9971,
            ymax=1.0019)
        if C2 == 0 and C1==1:       axs[C1][C2].
```

```
            set_ylabel("Normalised Flux Ratios",fontsize=18)
656         C1+=1
657 fig.text(0.5, 0.04, 'Phases', ha='center',fontsize=18)
658 plt.tight_layout()
659 plt.subplots_adjust(bottom=0.1)
660
661 plt.savefig(output_dir+"best_eclipses.pdf",filetype=
    "pdf")
662 plt.savefig(output_dir+"best_eclipses.eps",filetype=
    "eps")
663
664 plt.figure()
665 plt.hist(ecl_depths,20)
666 ecl_dep=numpy.median(ecl_depths)
667 ecl_dep_err=numpy.std(ecl_depths)
668 priln("*")
669 print "Eclipse Depth:", ecl_dep*100,"+/-",ecl_dep_err*
    100, "%"
670 priln("*")
671 plt.axvline(ecl_dep)
672 plt.axvline(ecl_dep+ecl_dep_err)
673 plt.axvline(ecl_dep-ecl_dep_err)
674 print "Done!"
675 plt.show()
```

Bibliography

Abuter R., Schreiber J., Eisenhauer F., Ott T., Horrobin M., Gillesen S., 2006, New Astronomy Reviews, 50(4-5), 398

Agol E., Fabrycky D. C., Transit-Timing and Duration Variations for the Discovery and Characterization of Exoplanets, 7, 2017

Agol E., Steffen J., Sari R., Clarkson W., 2005, MNRAS, 359, 567

Agol E., Cowan N. B., Knutson H. A., Deming D., Steffen J. H., Henry G. W., Charbonneau D., 2010, ApJ, 721, 1861

Aigrain S., Parviainen H., Pope B. J. S., 2016, MNRAS, 459, 2408

Alsubai K., Mislis D., Tsvetanov Z. I., Latham D. W., Bieryla A., Buchhave L. A., Esquerdo G. A., Bramich D. M., Pyrzas S., Vilchez N. P. E., Mancini L., Southworth J., Evans D. F., Henning T., Ciceri S., 2017, AJ, 153, 200

Anderson D. R., Hellier C., Gillon M., Triaud A. H. M. J., Smalley B., Hebb L., Collier Cameron A., Maxted P. F. L., Queloz D., West R. G., Bentley S. J., Enoch B., Horne K., Lister T. A., Mayor M., Parley N. R., Pepe F., Pollacco D., Ségransan D., Udry S., Wilson D. M., 2010, ApJ, 709, 159

Anderson D. R., Collier Cameron A., Gillon M., Hellier C., Jehin E., Lendl M., Queloz D., Smalley B., Triaud A. H. M. J., Vanhuysse M., 2011, Astronomy and Astrophysics, 534, A16

Anderson D. R., Smith A. M. S., Madhusudhan N., Wheatley P. J., Collier Cameron A., Hellier C., Campo C., Gillon M., Harrington J., Maxted P. F. L., Pollacco D., Queloz D., Smalley B., Triaud A. H. M. J., West R. G., 2013, MNRAS, 430, 3422

Anderson D. R., Collier Cameron A., Hellier C., Lendl M., Lister T. A., Maxted P. F. L., Queloz D., Smalley B., Smith A. M. S., Triaud A. H. M. J., Brown D. J. A., Gillon M., Neveu-VanMalle M., Pepe F., Pollacco D., Ségransan D., Udry S., West R. G., Wheatley P. J., 2015a, A&A, 575, A61

Anderson D. R., Collier Cameron A., Hellier C., Lendl M., Lister T. A., Maxted P. F. L., Queloz D., Smalley B., Smith A. M. S., Triaud A. H. M. J., Brown D. J. A., Gillon M., Neveu-VanMalle M., Pepe F., Pollacco D., Ségransan D., Udry S., West R. G., Wheatley P. J., 2015b, A&A, 575, A61

Anderson D. R., Triaud A. H. M. J., Turner O. D., Brown D. J. A., Clark B. J. M., Smalley B., Collier Cameron A., Doyle A. P., Gillon M., Hellier C., Lovis C., Maxted P. F. L., Pollacco D., Queloz D., Smith A. M. S., 2015c, ApJL, 800, L9

Anglada-Escudé G., Amado P. J., Barnes J., Berdiñas Z. M., Butler R. P., Coleman G. A. L., de La Cueva I., Dreizler S., Endl M., Giesers B., Jeffers S. V., Jenkins J. S., Jones H. R. A., Kiraga M., Kürster M., López-González M. J., Marvin C. J., Morales N., Morin J., Nelson R. P., Ortiz J. L., Ofir A., Paardekooper S.-J., Reiners A., Rodríguez E., Rodríguez-López C., Sarmiento L. F., Strachan J. P., Tsapras Y., Tuomi M., Zechmeister M., 2016, Nature, 536, 437

Armstrong D. J., de Mooij E., Barstow J., Osborn H. P., Blake J., Saniee N. F., 2016, Nature Astronomy, 1, 0004

Bakos G., Noyes R. W., Kovács G., Stanek K. Z., Sasselov D. D., Domsa I., 2004, PASP, 116, 266

Bakos G. Á., Csubry Z., Penev K., Bayliss D., Jordán A., Afonso C., Hartman J. D., Henning T., Kovács G., Noyes R. W., Béky B., Suc V., Csák B., Rabus M., Lázár J., Papp I., Sári P., Conroy P., Zhou G., Sackett P. D., Schmidt B., Mancini L., Sasselov D. D., Ueltzhoeffer K., 2013, PASP, 125, 154

Ballard S., Fabrycky D., Fressin F., Charbonneau D., Desert J.-M., Torres G., Marcy G., Burke C. J., Isaacson H., Henze C., Steffen J. H., Ciardi D. R., Howell S. B., Cochran W. D., Endl M., Bryson S. T., Rowe J. F., Holman M. J., Lissauer J. J., Jenkins J. M., Still M., Ford E. B., Christiansen J. L., Middour C. K., Haas M. R., Li J., Hall J. R., McCauliff S., Batalha N. M., Koch D. G., Borucki W. J., 2011, ApJ, 743, 200

Baraffe I., Chabrier G., Barman T., 2008, A&A, 482, 315

Barbary K., 2016, The Journal of Open Source Software, 1(6)

Barnes S. A., 2007, ApJ, 669, 1167

Barrett P., Bridgman W., 1999, Astronomical Data Analysis Software and Systems VIII Vol. 172, p. 483

Batygin K., Stevenson D. J., 2010, ApJL, 714, L238

Bayliss D., Gillen E., Eigmüller P., McCormac J., Alexander R. D., Armstrong D. J., Booth R. S., Bouchy F., Burleigh M. R., Cabrera J., Casewell S. L., Chaushev A., Chazelas B., Csizmadia S., Erikson A., Faedi F., Foxell E., Gänsicke B. T., Goad M. R., Grange A., Günther M. N., Hodgkin S. T., Jackman J., Jenkins J. S.,

Lambert G., Louden T., Metrailler L., Moyano M., Pollacco D., Poppenhaeger K., Queloz D., Raddi R., Rauer H., Raynard L., Smith A. M. S., Soto M., Thompson A. P. G., Titz-Weider R., Udry S., Walker S. R., Watson C. A., West R. G., Wheatley P. J., 2018, MNRAS, 475, 4467

Bean J. L., Désert J.-M., Seifahrt A., Madhusudhan N., Chilingarian I., Homeier D., Szentgyorgyi A., 2013, ApJ, 771, 108

Bean J. L., Miller-Ricci Kempton E., Homeier D., 2010, Nature, 468, 669

Beaugé C., Nesvorný D., 2012, ApJ, 751, 119

Beaulieu J.-P., Bennett D. P., Fouqué P., Williams A., Dominik M., Jørgensen U. G., Kubas D., Cassan A., Coutures C., Greenhill J., Hill K., Menzies J., Sackett P. D., Albrow M., Brillant S., Caldwell J. A. R., Calitz J. J., Cook K. H., Corrales E., Desort M., Dieters S., Dominis D., Donatowicz J., Hoffman M., Kane S., Marquette J.-B., Martin R., Meintjes P., Pollard K., Sahu K., Vinter C., Wambsganss J., Woller K., Horne K., Steele I., Bramich D. M., Burgdorf M., Snodgrass C., Bode M., Udalski A., Szymański M. K., Kubiak M., Więckowski T., Pietrzyński G., Soszyński I., Szewczyk O., Wyrzykowski Ł., Paczyński B., Abe F., Bond I. A., Britton T. R., Gilmore A. C., Hearnshaw J. B., Itow Y., Kamiya K., Kilmartin P. M., Korpela A. V., Masuda K., Matsubara Y., Motomura M., Muraki Y., Nakamura S., Okada C., Ohnishi K., Rattenbury N. J., Sako T., Sato S., Sasaki M., Sekiguchi T., Sullivan D. J., Tristram P. J., Yock P. C. M., Yoshioka T., 2006, Nature, 439, 437

Becker J. C., Vanderburg A., Adams F. C., Rappaport S. A., Schwengeler H. M., 2015, ApJL, 812, L18

Bertin E., Arnouts S., 1996, Astronomy & Astrophysics, 117, 393

Boisse I., Pepe F., Perrier C., Queloz D., Bonfils X., Bouchy F., Santos N. C., Arnold L., Beuzit J.-L., Díaz R. F., Delfosse X., Eggenberger A., Ehrenreich D., Forveille T., Hébrard G., Lagrange A.-M., Lovis C., Mayor M., Moutou C., Naef D., Santerne A., Ségransan D., Sivan J.-P., Udry S., 2012, A&A, 545, A55

Bonfils X., Astudillo-Defru N., Díaz R., Almenara J.-M., Forveille T., Bouchy F., Delfosse X., Lovis C., Mayor M., Murgas F., Pepe F., Santos N. C., Ségransan D., Udry S., Wünsche A., 2017, ArXiv e-prints

Borucki W. J., Koch D., Basri G., Batalha N., Brown T., Caldwell D., Caldwell J., Christensen-Dalsgaard J., Cochran W. D., DeVore E., Dunham E. W., Dupree A. K., Gautier T. N., Geary J. C., Gilliland R., Gould A., Howell S. B., Jenkins

J. M., Kondo Y., Latham D. W., Marcy G. W., Meibom S., Kjeldsen H., Lissauer J. J., Monet D. G., Morrison D., Sasselov D., Tarter J., Boss A., Brownlee D., Owen T., Buzasi D., Charbonneau D., Doyle L., Fortney J., Ford E. B., Holman M. J., Seager S., Steffen J. H., Welsh W. F., Rowe J., Anderson H., Buchhave L., Ciardi D., Walkowicz L., Sherry W., Horch E., Isaacson H., Everett M. E., Fischer D., Torres G., Johnson J. A., Endl M., MacQueen P., Bryson S. T., Dotson J., Haas M., Kolodziejczak J., Van Cleve J., Chandrasekaran H., Twicken J. D., Quintana E. V., Clarke B. D., Allen C., Li J., Wu H., Tenenbaum P., Verner E., Bruhweiler F., Barnes J., Prsa A., 2010, Science, 327, 977

Borysow A., 2002, A&A, 390, 779

Bradley L., Sipocz B., Robitaille T., Vinícius Z., Tollerud E., Deil C., Barbary K., Günther H. M., Cara M., Busko I., Droettboom M., Bostroem A., Bray E., Bratholm L. A., Pickering T. E., Craig M., Barentsen G., Pascual S., Conseil S., adonath, Greco J., Kerzendorf W., de Val-Borro M., StuartLittlefair, Ogaz S., Lim P. L., Ferreira L., D'Eugenio F., Weaver B. A., 2017, *astropy/photutils: v0.4*

Brahm R., Espinoza N., Jordán A., Rojas F., Sarkis P., Díaz M. R., Rabus M., Drass H., Lachaume R., Soto M. G., Jenkins J. S., Jones M. I., Henning T., Pantoja B., Vučković M., 2018, MNRAS, 477, 2572

Brogi M., Snellen I. A. G., de Kok R. J., Albrecht S., Birkby J., de Mooij E. J. W., 2012, Nature, 486, 502

Brown D. J. A., Collier Cameron A., Hall C., Hebb L., Smalley B., 2011, MNRAS, 415, 605

Burrows A., Sharp C. M., 1999, ApJ, 512, 843

Burrows A., Budaj J., Hubeny I., 2008, ApJ, 678, 1436

Burrows A., Guillot T., Hubbard W. B., Marley M. S., Saumon D., Lunine J. I., Sudarsky D., 2000, ApJL, 534, L97

Burrows A., Hubeny I., Budaj J., Hubbard W. B., 2007a, ApJ, 661, 502

Burrows A., Hubeny I., Budaj J., Knutson H. A., Charbonneau D., 2007b, ApJL, 668, L171

Burton J. R., Watson C. A., Littlefair S. P., Dhillon V. S., Gibson N. P., Marsh T. R., Pollacco D., 2012, The Astrophysical Journal Supplement, 201, 36

Campante T. L., Lund M. N., Kuszlewicz J. S., Davies G. R., Chaplin W. J., Albrecht S., Winn J. N., Bedding T. R., Benomar O., Bossini D., Handberg R., Santos A. R. G., Van Eylen V., Basu S., Christensen-Dalsgaard J., Elsworth Y. P., Hekker S., Hirano T., Huber D., Karoff C., Kjeldsen H., Lundkvist M. S., North T. S. H., Silva Aguirre V., Stello D., White T. R., 2016, ApJ, 819, 85

Campbell B., Walker G. A. H., Yang S., 1988, ApJ, 331, 902

Castelli F., Kurucz R. L., 2004, ArXiv Astrophysics e-prints (astro-ph/0405087)

Catala C., 2009, Communications in Asteroseismology, 158, 330

Charbonneau D., Brown T. M., Latham D. W., Mayor M., 2000, ApJL, 529, L45

Charbonneau D., Brown T. M., Noyes R. W., Gilliland R. L., 2002, ApJ, 568, 377

Charbonneau D., Allen L. E., Megeath S. T., Torres G., Alonso R., Brown T. M., Gilliland R. L., Latham D. W., Mandushev G., O'Donovan F. T., Sozzetti A., 2005, ApJ, 626, 523

Charpinet S., Fontaine G., Brassard P., Green E. M., Van Grootel V., Randall S. K., Silvotti R., Baran A. S., Østensen R. H., Kawaler S. D., Telting J. H., 2011, Nature, 480, 496

Chatterjee S., Ford E. B., Matsumura S., Rasio F. A., 2008, ApJ, 686, 580

Christian D. J., Pollacco D. L., Skillen I., Street R. A., Keenan F. P., Clarkson W. I., Collier Cameron A., Kane S. R., Lister T. A., West R. G., Enoch B., Evans A., Fitzsimmons A., Haswell C. A., Hellier C., Hodgkin S. T., Horne K., Irwin J., Norton A. J., Osborne J., Ryans R., Wheatley P. J., Wilson D. M., 2006, MNRAS, 372, 1117

Christiansen J. L., Ballard S., Charbonneau D., Madhusudhan N., Seager S., Holman M. J., Wellnitz D. D., Deming D., A'Hearn M. F., EPOXI Team, 2010, Astrophysical Journal, 710, 97

Ciceri S., Mancini L., Southworth J., Bruni I., Nikolov N., D'Ago G., Schröder T., Bozza V., Tregloan-Reed J., Henning T., 2015, A&A, 577, A54

Claret A., 2000, A&A, 363, 1081

Claret A., 2004, A&A, 428, 1001

Cochran W. D., Hatzes A. P., Butler R. P., Marcy G. W., 1997, ApJ, 483, 457

Collier Cameron A., Pollacco D., Street R. A., Lister T. A., West R. G., Wilson D. M., Pont F., Christian D. J., Clarkson W. I., Enoch B., Evans A., Fitzsimmons A., Haswell C. A., Hellier C., Hodgkin S. T., Horne K., Irwin J., Kane S. R., Keenan F. P., Norton A. J., Parley N. R., Osborne J., Ryans R., Skillen I., Wheatley P. J., 2006, MNRAS, 373, 799

Collier Cameron A., Bouchy F., Hébrard G., Maxted P., Pollacco D., Pont F., Skillen I., Smalley B., Street R. A., West R. G., Wilson D. M., Aigrain S., Christian D. J., Clarkson W. I., Enoch B., Evans A., Fitzsimmons A., Fleenor M., Gillon M., Haswell C. A., Hebb L., Hellier C., Hodgkin S. T., Horne K., Irwin J., Kane S. R., Keenan F. P., Loeillet B., Lister T. A., Mayor M., Moutou C., Norton A. J., Osborne J., Parley N., Queloz D., Ryans R., Triaud A. H. M. J., Udry S., Wheatley P. J., 2007a, MNRAS, 375, 951

Collier Cameron A., Wilson D. M., West R. G., Hebb L., Wang X.-B., Aigrain S., Bouchy F., Christian D. J., Clarkson W. I., Enoch B., Esposito M., Guenther E., Haswell C. A., Hébrard G., Hellier C., Horne K., Irwin J., Kane S. R., Loeillet B., Lister T. A., Maxted P., Mayor M., Moutou C., Parley N., Pollacco D., Pont F., Queloz D., Ryans R., Skillen I., Street R. A., Udry S., Wheatley P. J., 2007b, MNRAS, 380, 1230

Collier Cameron A., Guenther E., Smalley B., McDonald I., Hebb L., Andersen J., Augusteijn T., Barros S. C. C., Brown D. J. A., Cochran W. D., Endl M., Fossey S. J., Hartmann M., Maxted P. F. L., Pollacco D., Skillen I., Telting J., Waldmann I. P., West R. G., 2010, MNRAS, 407, 507

Cowan N. B., Agol E., 2008, Astrophysical Journal, 678, L129

Croll B., Albert L., Lafreniere D., Jayawardhana R., Fortney J. J., 2010a, ApJ, 717, 1084

Croll B., Jayawardhana R., Fortney J. J., Lafrenière D., Albert L., 2010b, ApJ, 718, 920

Croll B., Albert L., Jayawardhana R., Cushing M., Moutou C., Lafreniere D., Johnson J. A., Bonomo A. S., Deleuil M., Fortney J., 2015, ApJ, 802, 28

Cumming A., Marcy G. W., Butler R. P., 1999, ApJ, 526, 890

Daemgen S., Hormuth F., Brandner W., Bergfors C., Janson M., Hippler S., Henning T., 2009, A&A, 498, 567

Dai X., Guerras E., 2018, ApJL, 853, L27

de Mooij E. J. W., Snellen I. A. G., 2009, A&A, 493, L35

de Wit J., Wakeford H. R., Lewis N. K., Delrez L., Gillon M., Selsis F., Leconte J., Demory B.-O., Bolmont E., Bourrier V., Burgasser A. J., Grimm S., Jehin E., Lederer S. M., Owen J. E., Stamenković V., Triaud A. H. M. J., 2018, Nature Astronomy, 2, 214

Deich A. N., Orlova O. N., 1977, Soviet Astronomy, 21, 182

Delfosse X., Forveille T., Ségransan D., Beuzit J.-L., Udry S., Perrier C., Mayor M., 2000, A&A, 364, 217

Delrez L., Santerne A., Almenara J.-M., Anderson D. R., Collier-Cameron A., Díaz R. F., Gillon M., Hellier C., Jehin E., Lendl M., Maxted P. F. L., Neveu-VanMalle M., Pepe F., Pollacco D., Queloz D., Ségransan D., Smalley B., Smith A. M. S., Triaud A. H. M. J., Udry S., Van Grootel V., West R. G., 2016, MNRAS, 458, 4025

Demianski M., Proszynski M., 1979, Nature, 282, 383

Deming D., Seager S., Richardson L. J., Harrington J., 2005, Nature, 434, 740

Deming D., Wilkins A., McCullough P., Burrows A., Fortney J. J., Agol E., Dobbs-Dixon I., Madhusudhan N., Crouzet N., Desert J.-M., Gilliland R. L., Haynes K., Knutson H. A., Line M., Magic Z., Mandell A. M., Ranjan S., Charbonneau D., Clampin M., Seager S., Showman A. P., 2013, ApJ, 774, 95

Deming D., Knutson H., Kammer J., Fulton B. J., Ingalls J., Carey S., Burrows A., Fortney J. J., Todorov K., Agol E., Cowan N., Desert J.-M., Fraine J., Langton J., Morley C., Showman A. P., 2015, ApJ, 805, 132

Demircan O., Kahraman G., 1991, Astrophysics and Space Science, 181, 313

Désert J.-M., Charbonneau D., Demory B.-O., Ballard S., Carter J. A., Fortney J. J., Cochran W. D., Endl M., Quinn S. N., Isaacson H. T., Fressin F., Buchhave L. A., Latham D. W., Knutson H. A., Bryson S. T., Torres G., Rowe J. F., Batalha N. M., Borucki W. J., Brown T. M., Caldwell D. A., Christiansen J. L., Deming D., Fabrycky D. C., Ford E. B., Gilliland R. L., Gillon M., Haas M. R., Jenkins J. M., Kinemuchi K., Koch D., Lissauer J. J., Lucas P., Mullally F., MacQueen P. J., Marcy G. W., Sasselov D. D., Seager S., Still M., Tenenbaum P., Uddin K., Winn J. N., 2011, The Astrophysical Journal Supplement, 197, 14

Diamond-Lowe H., Stevenson K. B., Bean J. L., Line M. R., Fortney J. J., 2014, ApJ, 796, 66

Dittmann J. A., Irwin J. M., Charbonneau D., Bonfils X., Astudillo-Defru N., Haywood R. D., Berta-Thompson Z. K., Newton E. R., Rodriguez J. E., Winters J. G., Tan T.-G., Almenara J.-M., Bouchy F., Delfosse X., Forveille T., Lovis C., Murgas F., Pepe F., Santos N. C., Udry S., Wünsche A., Esquerdo G. A., Latham D. W., Dressing C. D., 2017, Nature, 544, 333

Doyle A. P., Davies G. R., Smalley B., Chaplin W. J., Elsworth Y., 2014, MNRAS, 444, 3592

Dumusque X., 2016, A&A, 593, A5

Einstein A., 1936, Journal of The Franklin Institute, 221, 349

Enoch B., Collier Cameron A., Horne K., 2012, A&A, 540, A99

Enoch B., Collier Cameron A., Parley N. R., Hebb L., 2010a, Astronomy and Astrophysics, 516, A33

Enoch B., Collier Cameron A., Parley N. R., Hebb L., 2010b, A&A, 516, A33

Enoch B., Anderson D. R., Barros S. C. C., Brown D. J. A., Collier Cameron A., Faedi F., Gillon M., Hébrard G., Lister T. A., Queloz D., Santerne A., Smalley B., Street R. A., Triaud A. H. M. J., West R. G., Bouchy F., Bento J., Butters O., Fossati L., Haswell C. A., Hellier C., Holmes S., Jehin E., Lendl M., Maxted P. F. L., McCormac J., Miller G. R. M., Moulds V., Moutou C., Norton A. J., Parley N., Pepe F., Pollacco D., Segransan D., Simpson E., Skillen I., Smith A. M. S., Udry S., Wheatley P. J., 2011, Astrophysical Journal, 142, 86

Espinoza N., Jordán A., 2015, MNRAS, 450, 1879

Esposito M., Covino E., Mancini L., Harutyunyan A., Southworth J., Biazzo K., Gandolfi D., Lanza A. F., Barbieri M., Bonomo A. S., Borsa F., Claudi R., Cosentino R., Desidera S., Gratton R., Pagano I., Sozzetti A., Boccato C., Maggio A., Micela G., Molinari E., Nascimbeni V., Piotto G., Poretti E., Smareglia R., 2014, A&A, 564, L13

Esteves L. J., De Mooij E. J. W., Jayawardhana R., 2013, ApJ, 772, 51

Evans T. M., Aigrain S., Gibson N., Barstow J. K., Amundsen D. S., Tremblin P., Mourier P., 2015, MNRAS, 451, 680

Evans D. F., Southworth J., Maxted P. F. L., Skottfelt J., Hundertmark M., Jørgensen U. G., Dominik M., Alsubai K. A., Andersen M. I., Bozza V., Bramich D. M., Burgdorf M. J., Ciceri S., D'Ago G., Figuera Jaimes R., Gu S.-H., Haugbølle T.,

Hinse T. C., Juncher D., Kains N., Kerins E., Korhonen H., Kuffmeier M., Mancini L., Peixinho N., Popovas A., Rabus M., Rahvar S., Schmidt R. W., Snodgrass C., Starkey D., Surdej J., Tronsgaard R., von Essen C., Wang Y.-B., Wertz O., 2016, A&A, 589, A58

Fabrycky D., Tremaine S., 2007, ApJ, 669, 1298

Feng F., Tuomi M., Jones H. R. A., Barnes J., Anglada-Escudé G., Vogt S. S., Butler R. P., 2017, AJ, 154, 135

Fortney J. J., Hubbard W. B., 2004, ApJ, 608, 1039

Fortney J. J., Saumon D., Marley M. S., Lodders K., Freedman R. S., 2006, Astrophysical Journal, 642, 495

Fortney J. J., Lodders K., Marley M. S., Freedman R. S., 2008, ApJ, 678, 1419

Fressin F., Torres G., Charbonneau D., Bryson S. T., Christiansen J., Dressing C. D., Jenkins J. M., Walkowicz L. M., Batalha N. M., 2013, ApJ, 766, 81

Gardner J. P., Mather J. C., Clampin M., Doyon R., Greenhouse M. A., Hammel H. B., Hutchings J. B., Jakobsen P., Lilly S. J., Long K. S., Lunine J. I., Mccaughrean M. J., Mountain M., Nella J., Rieke G. H., Rieke M. J., Rix H.-W., Smith E. P., Sonneborn G., Stiavelli M., Stockman H. S., Windhorst R. A., Wright G. S., 2006, Space Science Reviews, 123(4), 485

Gaudi B. S., Stassun K. G., Collins K. A., Beatty T. G., Zhou G., Latham D. W., Bieryla A., Eastman J. D., Siverd R. J., Crepp J. R., Gonzales E. J., Stevens D. J., Buchhave L. A., Pepper J., Johnson M. C., Colon K. D., Jensen E. L. N., Rodriguez J. E., Bozza V., Novati S. C., D'Ago G., Dumont M. T., Ellis T., Gaillard C., Jang-Condell H., Kasper D. H., Fukui A., Gregorio J., Ito A., Kielkopf J. F., Manner M., Matt K., Narita N., Oberst T. E., Reed P. A., Scarpetta G., Stephens D. C., Yeigh R. R., Zambelli R., Fulton B. J., Howard A. W., James D. J., Penny M., Bayliss D., Curtis I. A., Depoy D. L., Esquerdo G. A., Gould A., Joner M. D., Kuhn R. B., Labadie-Bartz J., Lund M. B., Marshall J. L., McLeod K. K., Pogge R. W., Relles H., Stockdale C., Tan T. G., Trueblood M., Trueblood P., 2017, Nature, 546, 514

Gillon M., Demory B.-O., Barman T., Bonfils X., Mazeh T., Pont F., Udry S., Mayor M., Queloz D., 2007, Astronomy and Astrophysics, 471, L51

Gillon M., Demory B.-O., Triaud A. H. M. J., Barman T., Hebb L., Montalbán J., Maxted P. F. L., Queloz D., Deleuil M., Magain P., 2009a, A&A, 506, 359

Gillon M., Smalley B., Hebb L., Anderson D. R., Triaud A. H. M. J., Hellier C., Maxted P. F. L., Queloz D., Wilson D. M., 2009b, A&A, 496, 259

Gillon M., Jehin E., Lederer S. M., Delrez L., de Wit J., Burdanov A., Van Grootel V., Burgasser A. J., Triaud A. H. M. J., Opitom C., Demory B.-O., Sahu D. K., Bardalez Gagliuffi D., Magain P., Queloz D., 2016, Nature, 533, 221

Gilmozzi R., Spyromilio J., 2007, The Messenger, 127

Gómez Maqueo Chew Y., Faedi F., Pollacco D., Brown D. J. A., Doyle A. P., Collier Cameron A., Gillon M., Lendl M., Smalley B., Triaud A. H. M. J., West R. G., Wheatley P. J., Busuttil R., Liebig C., Anderson D. R., Armstrong D. J., Barros S. C. C., Bento J., Bochinski J., Burwitz V., Delrez L., Enoch B., Fumel A., Haswell C. A., Hébrard G., Hellier C., Holmes S., Jehin E., Kolb U., Maxted P. F. L., McCormac J., Miller G. R. M., Norton A. J., Pepe F., Queloz D., Rodríguez J., Ségransan D., Skillen I., Stassun K. G., Udry S., Watson C., 2013, A&A, 559, A36

Gould A., Udalski A., Shin I.-G., Porritt I., Skowron J., Han C., Yee J. C., Kozłowski S., Choi J.-Y., Poleski R., Wyrzykowski Ł., Ulaczyk K., Pietrukowicz P., Mróz P., Szymański M. K., Kubiak M., Soszyński I., Pietrzyński G., Gaudi B. S., Christie G. W., Drummond J., McCormick J., Natusch T., Ngan H., Tan T.-G., Albrow M., DePoy D. L., Hwang K.-H., Jung Y. K., Lee C.-U., Park H., Pogge R. W., Abe F., Bennett D. P., Bond I. A., Botzler C. S., Freeman M., Fukui A., Fukunaga D., Itow Y., Koshimoto N., Larsen P., Ling C. H., Masuda K., Matsubara Y., Muraki Y., Namba S., Ohnishi K., Philpott L., Rattenbury N. J., Saito T., Sullivan D. J., Sumi T., Suzuki D., Tristram P. J., Tsurumi N., Wada K., Yamai N., Yock P. C. M., Yonehara A., Shvartzvald Y., Maoz D., Kaspi S., Friedmann M., 2014, Science, 345, 46

Grimm S. L., Demory B.-O., Gillon M., Dorn C., Agol E., Burdanov A., Delrez L., Sestovic M., Triaud A. H. M. J., Turbet M., Bolmont É., Caldas A., de Wit J., Jehin E., Leconte J., Raymond S. N., Van Grootel V., Burgasser A. J., Carey S., Fabrycky D., Heng K., Hernandez D. M., Ingalls J. G., Lederer S., Selsis F., Queloz D., 2018, ArXiv e-prints

Groot P. J., 2012, ApJ, 745, 55

Gudkova T. V., Zharkov V. N., 1999, Planetary and Space Science, 47, 1201

Guillot T., 1999, Science, 286(5437), 72

Guillot T., 2005, Annual Review of Earth and Planetary Sciences, 33, 493

Günther M. N., Queloz D., Gillen E., Delrez L., Bouchy F., McCormac J., Smalley B., Almleaky Y., Armstrong D. J., Bayliss D., Burdanov A., Burleigh M., Cabrera J., Casewell S. L., Cooke B. F., Csizmadia S., Ducrot E., Eigmüller P., Erikson A., Gänsicke B. T., Gibson N. P., Gillon M., Goad M. R., Jehin E., Jenkins J. S., Louden T., Moyano M., Murray C., Pollacco D., Poppenhaeger K., Rauer H., Raynard L., Smith A. M. S., Sohy S., Thompson S. J., Udry S., Watson C. A., West R. G., Wheatley P. J., 2018, MNRAS

Hadden S., Lithwick Y., 2016, ApJ, 828, 44

Hardy R. A., Harrington J., Hardin M. R., Madhusudhan N., Loredo T. J., Challener R. C., Foster A. S. D., Cubillos P. E., Blecic J., 2017, ApJ, 836, 143

Hartman J. D., Bayliss D., Brahm R., Bakos G. Á., Mancini L., Jordán A., Penev K., Rabus M., Zhou G., Butler R. P., Espinoza N., de Val-Borro M., Bhatti W., Csubry Z., Ciceri S., Henning T., Schmidt B., Arriagada P., Shectman S., Crane J., Thompson I., Suc V., Csák B., Tan T. G., Noyes R. W., Lázár J., Papp I., Sári P., 2015, AJ, 149, 166

Hartman J. D., Bakos G. Á., Bhatti W., Penev K., Bieryla A., Latham D. W., Kovács G., Torres G., Csubry Z., de Val-Borro M., Buchhave L., Kovács T., Quinn S., Howard A. W., Isaacson H., Fulton B. J., Everett M. E., Esquerdo G., Béky B., Szklenar T., Falco E., Santerne A., Boisse I., Hébrard G., Burrows A., Lázár J., Papp I., Sári P., 2016, AJ, 152, 182

Hatzes A. P., Cochran W. D., Endl M., McArthur B., Paulson D. B., Walker G. A. H., Campbell B., Yang S., 2003, ApJ, 599, 1383

Haynes K., Mandell A. M., Madhusudhan N., Deming D., Knutson H., 2015, ApJ, 806, 146

Hearnshaw J. B., Abe F., Bond I. A., Gilmore A. C., Itow Y., Kamiya K., Masuda K., Matsubara Y., Muraki Y., Okada C., Rattenbury N. J., Sako T., Sasaki M., Sullivan D. J., Yock P. C. M., 2006, in Sutantyo W., Premadi P. W., Mahasena P., Hidayat T., Mineshige S., eds, The 9th Asian-Pacific Regional IAU Meeting, p. 272

Heintz W. D., 1988, Journal of the Royal Astronomical Society of Canada, 82, 140

Hellier C., Anderson D. R., Collier Cameron A., Gillon M., Hebb L., Maxted P. F. L., Queloz D., Smalley B., Triaud A. H. M. J., West R. G., Wilson D. M., Bentley S. J., Enoch B., Horne K., Irwin J., Lister T. A., Mayor M., Parley N., Pepe F., Pollacco D. L., Segransan D., Udry S., Wheatley P. J., 2009, Nature, 460, 1098

Hellier C., Anderson D. R., Collier Cameron A., Gillon M., Jehin E., Lendl M., Maxted P. F. L., Pepe F., Pollacco D., Queloz D., Ségransan D., Smalley B., Smith A. M. S., Southworth J., Triaud A. H. M. J., Udry S., West R. G., 2011a, A&A, 535, L7

Hellier C., Anderson D. R., Collier-Cameron A., Miller G. R. M., Queloz D., Smalley B., Southworth J., Triaud A. H. M. J., 2011b, ApJL, 730, L31

Hellier C., Anderson D. R., Collier Cameron A., Doyle A. P., Fumel A., Gillon M., Jehin E., Lendl M., Maxted P. F. L., Pepe F., Pollacco D., Queloz D., Ségransan D., Smalley B., Smith A. M. S., Southworth J., Triaud A. H. M. J., Udry S., West R. G., 2012, MNRAS, 426, 739

Hellier C., Anderson D. R., Collier Cameron A., Delrez L., Gillon M., Jehin E., Lendl M., Maxted P. F. L., Pepe F., Pollacco D., Queloz D., Ségransan D., Smalley B., Smith A. M. S., Southworth J., Triaud A. H. M. J., Turner O. D., Udry S., West R. G., 2015, AJ, 150, 18

Hellier C., Anderson D. R., Bouchy F., Burdanov A., Collier Cameron A., Delrez L., Gillon M., Jehin E., Lendl M., Nielsen L. D., Maxted P. F. L., Pepe F., Pollacco D., Queloz D., Segransan D., Smalley B., Triaud A. H. M. J., Udry S., West R. G., 2018, ArXiv e-prints

Holczer T., Mazeh T., Nachmani G., Jontof-Hutter D., Ford E. B., Fabrycky D., Ragozzine D., Kane M., Steffen J. H., 2016, ApJS, 225, 9

Holman M. J., Murray N. W., 2005, Science, 307, 1288

Howell S. B., 1989, PASP, 101, 616

Howell S. B., Sobeck C., Haas M., Still M., Barclay T., Mullally F., Troeltzsch J., Aigrain S., Bryson S. T., Caldwell D., Chaplin W. J., Cochran W. D., Huber D., Marcy G. W., Miglio A., Najita J. R., Smith M., Twicken J. D., Fortney J. J., 2014, PASP, 126, 398

Huang S.-S., 1959, American Scientist, 47, 397

Hubeny I., Burrows A., Sudarsky D., 2003, Astrophysical Journal, 594, 1011

Irwin J., Charbonneau D., Nutzman P., Falco E., 2009, in Stempels E., ed., 15th Cambridge Workshop on Cool Stars, Stellar Systems, and the Sun, American Institute of Physics Conference Series Vol. 1094, p. 445

Jackson B., Barnes R., Greenberg R., 2008, MNRAS, 391, 237

Jackson B. K., Lewis N. K., Barnes J. W., Drake Deming L., Showman A. P., Fortney J. J., 2012, ApJ, 751, 112

Jacob W. S., 1855, MNRAS, 15, 228

Jenkins J. M., Twicken J. D., Batalha N. M., Caldwell D. A., Cochran W. D., Endl M., Latham D. W., Esquerdo G. A., Seader S., Bieryla A., Petigura E., Ciardi D. R., Marcy G. W., Isaacson H., Huber D., Rowe J. F., Torres G., Bryson S. T., Buchhave L., Ramirez I., Wolfgang A., Li J., Campbell J. R., Tenenbaum P., Sanderfer D., Henze C. E., Catanzarite J. H., Gilliland R. L., Borucki W. J., 2015, AJ, 150, 56

Jensen O. G., Ulrych T., 1973, AJ, 78, 1104

Jones E., Oliphant T., Peterson P. et al. 2001–, *SciPy: Open source scientific tools for Python*, *[Online; accessed ¡today¿]*

Kalas P., Graham J. R., Chiang E., Fitzgerald M. P., Clampin M., Kite E. S., Stapelfeldt K., Marois C., Krist J., 2008, Science, 322, 1345

Kammer J. A., Knutson H. A., Line M. R., Fortney J. J., Deming D., Burrows A., Cowan N. B., Triaud A. H., Agol E., Desert J.-M. et al. 2015, The Astrophysical Journal, 810(2), 118

Karttunen H., Kröger P., Oja H., Poutanen M., Donner K. J., Binary Stars and Stellar Masses, p. 231, Springer New York, New York, NY, 1987

Kataria T., Evans T. M., Sing D., Goyal J., Nikolov N., Wakeford H. R., Deming D., Marley M. S., PanCET Team, 2018, American Astronomical Society Meeting Abstracts 231, American Astronomical Society Meeting Abstracts Vol. 231, p. 211.01

Kipping D. M., 2009, Monthly Notices of the Royal Astronomical Society, 396(3), 1797

Kitchin C., In: *Exoplanets*, p. 15, Springer, 2012

Knutson H. A., Charbonneau D., Allen L. E., Burrows A., Megeath S. T., 2008, ApJ, 673, 526

Knutson H. A., Lewis N., Fortney J. J., Burrows A., Showman A. P., Cowan N. B., Agol E., Aigrain S., Charbonneau D., Deming D., Désert J.-M., Henry G. W., Langton J., Laughlin G., 2012, ApJ, 754, 22

Koch D. G., Borucki W. J., Basri G., Batalha N. M., Brown T. M., Caldwell D., Christensen-Dalsgaard J., Cochran W. D., DeVore E., Dunham E. W., Gautier, III T. N., Geary J. C., Gilliland R. L., Gould A., Jenkins J., Kondo Y., Latham D. W., Lissauer J. J., Marcy G., Monet D., Sasselov D., Boss A., Brownlee D., Caldwell J., Dupree A. K., Howell S. B., Kjeldsen H., Meibom S., Morrison D., Owen T., Reitsema H., Tarter J., Bryson S. T., Dotson J. L., Gazis P., Haas M. R., Kolodziejczak J., Rowe J. F., Van Cleve J. E., Allen C., Chandrasekaran H., Clarke B. D., Li J., Quintana E. V., Tenenbaum P., Twicken J. D., Wu H., 2010a, ApJL, 713, L79

Koch D. G., Borucki W. J., Basri G., Batalha N. M., Brown T. M., Caldwell D., Christensen-Dalsgaard J., Cochran W. D., DeVore E., Dunham E. W. et al. 2010b, The Astrophysical Journal Letters, 713(2), L79

Konstan D., In: in Zalta E. N., ed., *The Stanford Encyclopedia of Philosophy*, Metaphysics Research Lab, Stanford University, 2016

Kopparapu R. K., Ramirez R., Kasting J. F., Eymet V., Robinson T. D., Mahadevan S., Terrien R. C., Domagal-Goldman S., Meadows V., Deshpande R., 2013, ApJ, 765, 131

Kozai Y., 1962, AJ, 67, 591

Kuijken K., Rich R. M., 2002, The Astronomical Journal, 124(4), 2054

Kuzuhara M., Tamura M., Kudo T., Janson M., Kandori R., Brandt T. D., Thalmann C., Spiegel D., Biller B., Carson J., Hori Y., Suzuki R., Burrows A., Henning T., Turner E. L., McElwain M. W., Moro-Martín A., Suenaga T., Takahashi Y. H., Kwon J., Lucas P., Abe L., Brandner W., Egner S., Feldt M., Fujiwara H., Goto M., Grady C. A., Guyon O., Hashimoto J., Hayano Y., Hayashi M., Hayashi S. S., Hodapp K. W., Ishii M., Iye M., Knapp G. R., Matsuo T., Mayama S., Miyama S., Morino J.-I., Nishikawa J., Nishimura T., Kotani T., Kusakabe N., Pyo T.-S., Serabyn E., Suto H., Takami M., Takato N., Terada H., Tomono D., Watanabe M., Wisniewski J. P., Yamada T., Takami H., Usuda T., 2013, ApJ, 774, 11

Laughlin G., Wolf A., Vanmunster T., Bodenheimer P., Fischer D., Marcy G., Butler P., Vogt S., 2005, ApJ, 621, 1072

Leconte J., Chabrier G., Baraffe I., Levrard B., 2010, A&A, 516, A64

Lederberg J., 1965, Nature, 207, 9

Lendl M., Gillon M., Queloz D., Alonso R., Fumel A., Jehin E., Naef D., 2013, Astronomy and Astrophysics, 552, A2

Lidov M. L., 1962, Planetary and Space Science, 9, 719

Lin D. N. C., Papaloizou J., 1986, ApJ, 309, 846

Lin D. N. C., Bodenheimer P., Richardson D. C., 1996, Nature, 380, 606

Line M. R., Knutson H., Wolf A. S., Yung Y. L., 2014, ApJ, 783, 70

Line M. R., Stevenson K. B., Bean J., Desert J.-M., Fortney J. J., Kreidberg L., Madhusudhan N., Showman A. P., Diamond-Lowe H., 2016, AJ, 152, 203

Machalek P., McCullough P. R., Burke C. J., Valenti J. A., Burrows A., Hora J. L., 2008, ApJ, 684, 1427

Madhusudhan N., Burrows A., 2012, ApJ, 747, 25

Madhusudhan N., Seager S., 2009, ApJ, 707, 24

Madhusudhan N., Seager S., 2010, ApJ, 725, 261

Madhusudhan N., 2012, ApJ, 758, 36

Madhusudhan N., Amin M. A., Kennedy G. M., 2014, ApJL, 794, L12

Madhusudhan N., Harrington J., Stevenson K. B., Nymeyer S., Campo C. J., Wheatley P. J., Deming D., Blecic J., Hardy R. A., Lust N. B., Anderson D. R., Collier-Cameron A., Britt C. B. T., Bowman W. C., Hebb L., Hellier C., Maxted P. F. L., Pollacco D., West R. G., 2011, Nature, 469, 64

Madhusudhan N., Knutson H., Fortney J., Barman T., 2014, arXiv:1402.1169

Madhusudhan N., Lee K. K. M., Mousis O., 2012, ApJL, 759, L40

Malavolta L., Borsato L., Granata V., Piotto G., Lopez E., Vanderburg A., Figueira P., Mortier A., Nascimbeni V., Affer L., Bonomo A. S., Bouchy F., Buchhave L. A., Charbonneau D., Collier Cameron A., Cosentino R., Dressing C. D., Dumusque X., Fiorenzano A. F. M., Harutyunyan A., Haywood R. D., Johnson J. A., Latham D. W., Lopez-Morales M., Lovis C., Mayor M., Micela G., Molinari E., Motalebi F., Pepe F., Phillips D. F., Pollacco D., Queloz D., Rice K., Sasselov D., Ségransan D., Sozzetti A., Udry S., Watson C., 2017, AJ, 153, 224

Males J. R., Close L. M., Guyon O., Morzinski K., Puglisi A., Hinz P., Follette K. B., Monnier J. D., Tolls V., Rodigas T. J., Weinberger A., Boss A., Kopon D., Wu Y.-l., Esposito S., Riccardi A., Xompero M., Briguglio R., Pinna E., 2014, Adaptive Optics Systems IV, Proceedings of the SPIE Vol. 9148, p. 914820

Mallama A., Krobusek B., Pavlov H., 2017, Icarus, 282, 19

Mamajek E. E., Hillenbrand L. A., 2008, ApJ, 687, 1264

Mandel K., Agol E., 2002, ApJL, 580, L171

Mao S., Paczynski B., 1991, ApJL, 374, L37

Marcy G., Butler R. P., Fischer D., Vogt S., Wright J. T., Tinney C. G., Jones H. R. A., 2005, Progress of Theoretical Physics Supplement, 158, 24

Markus E. Kasper, Jean-Luc Beuzit C. V. N. Y. P. B. A. B. R. G. G. N. H. F. K. R. R. H. M. S. N. A. T. K. D. M. F. L. V. S. W., 2008, 2008, EPICS: the exoplanet imager for the E-ELT

Masset F. S., Papaloizou J. C. B., 2003, ApJ, 588, 494

Maxted P. F. L., Serenelli A. M., Southworth J., 2015a, A&A, 575, A36

Maxted P. F. L., Serenelli A. M., Southworth J., 2015b, A&A, 575, A36

Mayor M., Queloz D., 1995, Nature, 378, 355

Mayor M., Marmier M., Lovis C., Udry S., Ségransan D., Pepe F., Benz W., Bertaux J. ., Bouchy F., Dumusque X., Lo Curto G., Mordasini C., Queloz D., Santos N. C., 2011, ArXiv e-prints

Mazeh T., Faigler S., 2010, A&A, 521, L59

McLaughlin D. B., 1924, ApJ, 60

McLean A., Mitchell C., Swanston D., 1994, Journal of Electron Spectroscopy and Related Phenomena, 69(2), 125

McQuillan A., Aigrain S., Mazeh T., 2013, MNRAS, 432, 1203

Meibom S., Mathieu R. D., Stassun K. G., 2009, ApJ, 695, 679

Militzer B., Hubbard W. B., Vorberger J., Tamblyn I., Bonev S. A., 2008, ApJL, 688, L45

Miller-Ricci Kempton E., Rauscher E., 2012, ApJ, 751, 117

Mordasini C., Alibert Y., Benz W., Naef D., 2008, in Fischer D., Rasio F. A., Thorsett S. E., Wolszczan A., eds, Extreme Solar Systems, Astronomical Society of the Pacific Conference Series Vol. 398, p. 235

Mortier A., Santos N. C., Sousa S. G., Fernandes J. M., Adibekyan V. Z., Delgado Mena E., Montalto M., Israelian G., 2013, A&A, 558, A106

Moses J. I., Line M. R., Visscher C., Richardson M. R., Nettelmann N., Fortney J. J., Barman T. S., Stevenson K. B., Madhusudhan N., 2013, ApJ, 777, 34

Moulton F. R., 1899, AJ, 20, 33

Močnik T., Clark B. J. M., Anderson D. R., Hellier C., Brown D. J. A., 2016, AJ, 151, 150

Močnik T., Southworth J., Hellier C., 2017, MNRAS, 471, 394

Mullally F., Thompson S. E., Coughlin J. L., Burke C. J., Rowe J. F., 2018, ArXiv e-prints

Munitz M. K., 1951, Journal of the History of Ideas, , 231

Murgas F., Pallé E., Parviainen H., Chen G., Nortmann L., Nowak G., Cabrera-Lavers A., Iro N., 2017, A&A, 605, A114

Neveu-VanMalle M., Queloz D., Anderson D. R., Brown D. J. A., Collier Cameron A., Delrez L., Díaz R. F., Gillon M., Hellier C., Jehin E., Lister T., Pepe F., Rojo P., Ségransan D., Triaud A. H. M. J., Turner O. D., Udry S., 2016, A&A, 586, A93

Nikolov N., Chen G., Fortney J. J., Mancini L., Southworth J., van Boekel R., Henning T., 2013, A&A, 553, A26

Olivero J., 1977, Journal of Quantitiative Spectroscopy and Radiative Transfer, 17, 233

Ollivier M., Roques F., Casoli F., Encrenaz T., Selsis F., 2009, Planetary Systems

O'Rourke J. G., Knutson H. A., Zhao M., Fortney J. J., Burrows A., Agol E., Deming D., Désert J.-M., Howard A. W., Lewis N. K., Showman A. P., Todorov K. O., 2014, ApJ, 781, 109

Ortiz M., Reffert S., Trifonov T., Quirrenbach A., Mitchell D. S., Nowak G., Buenzli E., Zimmerman N., Bonnefoy M., Skemer A., Defrère D., Lee M. H., Fischer D. A., Hinz P. M., 2016, A&A, 595, A55

Parviainen H., Aigrain S., Thatte N., Barstow J. K., Evans T. M., Gibson N., 2015, MNRAS, 453, 3875

Pasquini L., Cristiani S., Garcia-Lopez R., Haehnelt M., Mayor M., 2010, The Messenger, 140, 20

Patience J., White R. J., Ghez A. M., McCabe C., McLean I. S., Larkin J. E., Prato L., Kim S. S., Lloyd J. P., Liu M. C., Graham J. R., Macintosh B. A., Gavel D. T., Max C. E., Bauman B. J., Olivier S. S., Wizinowich P., Acton D. S., 2002, ApJ, 581, 654

Paul Butler R., Marcy G., Fischer D., W. Brown T., R. Contos A., G. Korzennik S., Nisenson P., W. Noyes R., 1999

Penev K., Hartman J. D., Bakos G. Á., Ciceri S., Brahm R., Bayliss D., Bento J., Jordán A., Csubry Z., Bhatti W., de Val-Borro M., Espinoza N., Zhou G., Mancini L., Rabus M., Suc V., Henning T., Schmidt B., Noyes R. W., Lázár J., Papp I., Sári P., 2016, AJ, 152, 127

Pepe F., Molaro P., Cristiani S., Rebolo R., Santos N. C., Dekker H., Mégevand D., Zerbi F. M., Cabral A., Di Marcantonio P., Abreu M., Affolter M., Aliverti M., Allende Prieto C., Amate M., Avila G., Baldini V., Bristow P., Broeg C., Cirami R., Coelho J., Conconi P., Coretti I., Cupani G., D'Odorico V., De Caprio V., Delabre B., Dorn R., Figueira P., Fragoso A., Galeotta S., Genolet L., Gomes R., González Hernández J. I., Hughes I., Iwert O., Kerber F., Landoni M., Lizon J.-L., Lovis C., Maire C., Mannetta M., Martins C., Monteiro M., Oliveira A., Poretti E., Rasilla J. L., Riva M., Santana Tschudi S., Santos P., Sosnowska D., Sousa S., Spanó P., Tenegi F., Toso G., Vanzella E., Viel M., Zapatero Osorio M. R., 2014, Astronomische Nachrichten, 335, 8

Pepper J., Pogge R. W., DePoy D. L., Marshall J. L., Stanek K. Z., Stutz A. M., Poindexter S., Siverd R., O'Brien T. P., Trueblood M., Trueblood P., 2007, PASP, 119, 923

Perri F., Cameron A. G. W., 1974, Icarus, 22, 416

Perryman M., 2011, The Exoplanet Handbook

Perryman M., Hartman J., Bakos G. Á., Lindegren L., 2014, ApJ, 797, 14

Petigura E. A., Marcy G. W., Howard A. W., 2013, ApJ, 770, 69

Pierrehumbert R., Gaidos E., 2011, ApJ, 734, L13

Poddaný S., Brát L., Pejcha O., 2010, New Astronomy, 15, 297

Pollacco D. L., Skillen I., Cameron A. C., Christian D. J., Hellier C., Irwin J., Lister T., Street R., West R. G., Anderson D. et al. 2006, Publications of the Astronomical Society of the Pacific, 118(848), 1407

Pollacco D., Skillen I., Collier Cameron A., Loeillet B., Stempels H. C., Bouchy F., Gibson N. P., Hebb L., Hébrard G., Joshi Y. C., McDonald I., Smalley B., Smith A. M. S., Street R. A., Udry S., West R. G., Wilson D. M., Wheatley P. J., Aigrain S., Alsubai K., Benn C. R., Bruce V. A., Christian D. J., Clarkson W. I., Enoch B., Evans A., Fitzsimmons A., Haswell C. A., Hellier C., Hickey S., Hodgkin S. T., Horne K., Hrudková M., Irwin J., Kane S. R., Keenan F. P., Lister T. A., Maxted P., Mayor M., Moutou C., Norton A. J., Osborne J. P., Parley N., Pont F., Queloz D., Ryans R., Simpson E., 2008, MNRAS, 385, 1576

Pollack J. B., Hubickyj O., Bodenheimer P., Lissauer J. J., Podolak M., Greenzweig Y., 1996, Icarus, 124, 62

Pont F., Gilliland R. L., Moutou C., Charbonneau D., Bouchy F., Brown T. M., Mayor M., Queloz D., Santos N., Udry S., 2007, A&A, 476, 1347

Pont F., Knutson H., Gilliland R. L., Moutou C., Charbonneau D., 2008, MNRAS, 385, 109

Press W. H., Teukolsky S. A., Vetterling W. T., Flannery B. P., 1992, Numerical recipes in FORTRAN. The art of scientific computing

Puget P., Stadler E., Doyon R., Gigan P., Thibault S., Luppino G., Barrick G., Benedict T., Forveille T., Rambold W., Thomas J., Vermeulen T., Ward J., Beuzit J.-L., Feautrier P., Magnard Y., Mella G., Preis O., Vallee P., Wang S.-y., Lin C.-J., Hall D. N., Hodapp K. W., 2004, in Moorwood A. F. M., Iye M., eds, Ground-based Instrumentation for Astronomy, Society of Photo-Optical Instrumentation Engineers (SPIE) Conference Series Vol. 5492, p. 978

Queloz D., Eggenberger A., Mayor M., Perrier C., Beuzit J. L., Naef D., Sivan J. P., Udry S., 2000, A&A, 359, L13

Quintana E. V., Barclay T., Raymond S. N., Rowe J. F., Bolmont E., Caldwell D. A., Howell S. B., Kane S. R., Huber D., Crepp J. R., Lissauer J. J., Ciardi D. R., Coughlin J. L., Everett M. E., Henze C. E., Horch E., Isaacson H., Ford E. B., Adams F. C., Still M., Hunter R. C., Quarles B., Selsis F., 2014, Science, 344, 277

Rabus M., Alonso R., Belmonte J. A., Deeg H. J., Gilliland R. L., Almenara J. M., Brown T. M., Charbonneau D., Mandushev G., 2009, A&A, 494, 391

Rasio F. A., Ford E. B., 1996, Science, 274, 954

Rauer H., Catala C., 2010, Proceedings of the International Astronomical Union, 6(S276), 354–358

Rauer H., Catala C., Aerts C., Appourchaux T., Benz W., Brandeker A., Christensen-Dalsgaard J., Deleuil M., Gizon L., Goupil M.-J., Güdel M., Janot-Pacheco E., Mas-Hesse M., Pagano I., Piotto G., Pollacco D., Santos Ċ., Smith A., Suárez J.-C., Szabó R., Udry S., Adibekyan V., Alibert Y., Almenara J.-M., Amaro-Seoane P., Eiff M. A.-v., Asplund M., Antonello E., Barnes S., Baudin F., Belkacem K., Bergemann M., Bihain G., Birch A. C., Bonfils X., Boisse I., Bonomo A. S., Borsa F., Brandão I. M., Brocato E., Brun S., Burleigh M., Burston R., Cabrera J., Cassisi S., Chaplin W., Charpinet S., Chiappini C., Church R. P., Csizmadia S., Cunha M., Damasso M., Davies M. B., Deeg H. J., Díaz R. F., Dreizler S., Dreyer C., Eggenberger P., Ehrenreich D., Eigmüller P., Erikson A., Farmer R., Feltzing S., de Oliveira Fialho F., Figueira P., Forveille T., Fridlund M., García R. A., Giommi P., Giuffrida G., Godolt M., Gomes da Silva J., Granzer T., Grenfell J. L., Grotsch-Noels A., Günther E., Haswell C. A., Hatzes A. P., Hébrard G., Hekker S., Helled R., Heng K., Jenkins J. M., Johansen A., Khodachenko M. L., Kislyakova K. G., Kley W., Kolb U., Krivova N., Kupka F., Lammer H., Lanza A. F., Lebreton Y., Magrin D., Marcos-Arenal P., Marrese P. M., Marques J. P., Martins J., Mathis S., Mathur S., Messina S., Miglio A., Montalban J., Montalto M., Monteiro M. J. P. F. G., Moradi H., Moravveji E., Mordasini C., Morel T., Mortier A., Nascimbeni V., Nelson R. P., Nielsen M. B., Noack L., Norton A. J., Ofir A., Oshagh M., Ouazzani R.-M., Pápics P., Parro V. C., Petit P., Plez B., Poretti E., Quirrenbach A., Ragazzoni R., Raimondo G., Rainer M., Reese D. R., Redmer R., Reffert S., Rojas-Ayala B., Roxburgh I. W., Salmon S., Santerne A., Schneider J., Schou J., Schuh S., Schunker H., Silva-Valio A., Silvotti R., Skillen I., Snellen I., Sohl F., Sousa S. G., Sozzetti A., Stello D., Strassmeier K. G., Švanda M., Szabó G. M., Tkachenko A., Valencia D., Van Grootel V., Vauclair S. D., Ventura P., Wagner F. W., Walton N. A., Weingrill J., Werner S. C., Wheatley P. J., Zwintz K., 2014, Experimental Astronomy, 38, 249

Rauscher E., Menou K., Cho J. Y.-K., Seager S., Hansen B. M. S., 2007, ApJL, 662, L115

Raymond S. N., Armitage P. J., Gorelick N., 2009, ApJL, 699, L88

Ribas I., Bolmont E., Selsis F., Reiners A., Leconte J., Raymond S. N., Engle S. G., Guinan E. F., Morin J., Turbet M., Forget F., Anglada-Escudé G., 2016, A&A, 596, A111

Ricker G. R., Winn J. N., Vanderspek R., Latham D. W., Bakos G. Á., Bean J. L., Berta-Thompson Z. K., Brown T. M., Buchhave L., Butler N. R., Butler R. P., Chaplin W. J., Charbonneau D., Christensen-Dalsgaard J., Clampin M., Deming D., Doty J., De Lee N., Dressing C., Dunham E. W., Endl M., Fressin F., Ge J., Henning T., Holman M. J., Howard A. W., Ida S., Jenkins J., Jernigan G.,

Johnson J. A., Kaltenegger L., Kawai N., Kjeldsen H., Laughlin G., Levine A. M., Lin D., Lissauer J. J., MacQueen P., Marcy G., McCullough P. R., Morton T. D., Narita N., Paegert M., Palle E., Pepe F., Pepper J., Quirrenbach A., Rinehart S. A., Sasselov D., Sato B., Seager S., Sozzetti A., Stassun K. G., Sullivan P., Szentgyorgyi A., Torres G., Udry S., Villasenor J., 2014, Space Telescopes and Instrumentation 2014: Optical, Infrared, and Millimeter Wave, Proceedings of the SPIE Vol. 9143, p. 914320

Rodríguez A., Ferraz-Mello S., 2010, in Gożdziewski K., Niedzielski A., Schneider J., eds, EAS Publications Series, EAS Publications Series Vol. 42, p. 411

Rossiter R. A., 1924, ApJ, 60

Rowe J. F., Matthews J. M., Seager S., Miller-Ricci E., Sasselov D., Kuschnig R., Guenther D. B., Moffat A. F. J., Rucinski S. M., Walker G. A. H., Weiss W. W., 2008, Astrophysical Journal, 689, 1345

Ryden B., Peterson B. M., Demianski M., 2010, American Journal of Physics, 78, 127

Sada P. V., Deming D., Jennings D. E., Jackson B. K., Hamilton C. M., Fraine J., Peterson S. W., Haase F., Bays K., Lunsford A., O'Gorman E., 2012, PASP, 124, 212

Schwarz G., 1978, Annals of Statistics, 6, 461

Schwarz H., Brogi M., de Kok R., Birkby J., Snellen I., 2015, A&A, 576, A111

Seager S., Deming D., 2010a, Annu. Rev. Astron. Astrophys., 48, 631

Seager S., Deming D., 2010b, Annu. Rev. Astron. Astrophys., 48, 631

Seager S., Mallén-Ornelas G., 2003, ApJ, 585, 1038

Seager S., In: in Binzel R. P., ed., *Oxford Handbook of Innovation*, Exoplanets, 2010

Sedaghati E., Boffin H. M. J., MacDonald R. J., Gandhi S., Madhusudhan N., Gibson N. P., Oshagh M., Claret A., Rauer H., 2017, Nature, 549, 238

See T. J. J., 1896, AJ, 16, 17

Showman A. P., Guillot T., 2002, A&A, 385, 166

Showman A. P., Fortney J. J., Lian Y., Marley M. S., Freedman R. S., Knutson H. A., Charbonneau D., 2009, ApJ, 699, 564

Shporer A., O'Rourke J. G., Knutson H. A., Szabó G. M., Zhao M., Burrows A., Fortney J., Agol E., Cowan N. B., Desert J.-M., Howard A. W., Isaacson H., Lewis N. K., Showman A. P., Todorov K. O., 2014a, ApJ, 788, 92

Shporer A., O'Rourke J. G., Knutson H. A., Szabó G. M., Zhao M., Burrows A., Fortney J., Agol E., Cowan N. B., Desert J.-M., Howard A. W., Isaacson H., Lewis N. K., Showman A. P., Todorov K. O., 2014b, ApJ, 788, 92

Sing D. K., López-Morales M., 2009, Astronomy and Astrophysics, 493, L31

Sing D. K., 2010, A&A, 510, A21

Sing D. K., Pont F., Aigrain S., Charbonneau D., Désert J.-M., Gibson N., Gilliland R., Hayek W., Henry G., Knutson H., Lecavelier Des Etangs A., Mazeh T., Shporer A., 2011, MNRAS, 416, 1443

Smart W. M., 1933, MNRAS, 94, 115

Smith A. M. S., Anderson D. R., Madhusudhan N., Southworth J., Collier Cameron A., Blecic J., Harrington J., Hellier C., Maxted P. F. L., Pollacco D., Queloz D., Smalley B., Triaud A. H. M. J., Wheatley P. J., 2012, A&A, 545, A93

Snellen I. A. G., de Kok R. J., de Mooij E. J. W., Albrecht S., 2010, Nature, 465, 1049

Southworth J., Hinse T. C., Jørgensen U. G., Dominik M., Ricci D., Burgdorf M. J., Hornstrup A., Wheatley P. J., Anguita T., Bozza V., Novati S. C., Harpsøe K., Kjærgaard P., Liebig C., Mancini L., Masi G., Mathiasen M., Rahvar S., Scarpetta G., Snodgrass C., Surdej J., Thöne C. C., Zub M., 2009, Monthly Notices of the Royal Astronomical Society, 396, 1023

Southworth J., Tregloan-Reed J., Andersen M. I., Calchi Novati S., Ciceri S., Colque J. P., D'Ago G., Dominik M., Evans D. F., Gu S.-H., Herrera-Cordova A., Hinse T. C., Jørgensen U. G., Juncher D., Kuffmeier M., Mancini L., Peixinho N., Popovas A., Rabus M., Skottfelt J., Tronsgaard R., Unda-Sanzana E., Wang X.-B., Wertz O., Alsubai K. A., Andersen J. M., Bozza V., Bramich D. M., Burgdorf M., Damerdji Y., Diehl C., Elyiv A., Figuera Jaimes R., Haugbølle T., Hundertmark M., Kains N., Kerins E., Korhonen H., Liebig C., Mathiasen M., Penny M. T., Rahvar S., Scarpetta G., Schmidt R. W., Snodgrass C., Starkey D., Surdej J., Vilela C., Essen C. v., Wang Y., 2016, MNRAS, 457, 4205

Spiegel D. S., Burrows A., Milsom J. A., 2011, ApJ, 727, 57

Stassun K. G., Collins K. A., Gaudi B. S., 2017, AJ, 153, 136

Stevenson K. B., Désert J.-M., Line M. R., Bean J. L., Fortney J. J., Showman A. P., Kataria T., Kreidberg L., McCullough P. R., Henry G. W., Charbonneau D., Burrows A., Seager S., Madhusudhan N., Williamson M. H., Homeier D., 2014, Science, 346, 838

Still M., Barclay T., 2012, *PyKE: Reduction and analysis of Kepler Simple Aperture Photometry data*, Astrophysics Source Code Library

Strand K. A., 1942, Sky and Telescope, 1

Strand K. A., 1957, AJ, 62, 35

Street R. A., Pollaco D. L., Fitzsimmons A., Keenan F. P., Horne K., Kane S., Collier Cameron A., Lister T. A., Haswell C., Norton A. J., Jones B. W., Skillen I., Hodgkin S., Wheatley P., West R., Brett D., 2003, in Deming D., Seager S., eds, Scientific Frontiers in Research on Extrasolar Planets, Astronomical Society of the Pacific Conference Series Vol. 294, p. 405

Streicher O., 2016, *Python-CPL: Python interface for the ESO Common Pipeline Library*, Astrophysics Source Code Library

Talens G. J. J., Albrecht S., Spronck J. F. P., Lesage A.-L., Otten G. P. P. L., Stuik R., Van Eylen V., Van Winckel H., Pollacco D., McCormac J., Grundahl F., Fredslund Andersen M., Antoci V., Snellen I. A. G., 2017a, A&A, 606, A73

Talens G. J. J., Spronck J. F. P., Lesage A.-L., Otten G. P. P. L., Stuik R., Pollacco D., Snellen I. A. G., 2017b, A&A, 601, A11

Tanaka H., Ward W. R., 2004, ApJ, 602, 388

Thanjavur K., Teeple D., Yan C.-H., 2011, in Gajadhar S., Walawender J., Genet R., Veillet C., Adamson A., Martinez J., Melnik J., Jenness T., Manset N., eds, Telescopes from Afar

The Astropy Collaboration, Robitaille, Thomas P., Tollerud, Erik J., Greenfield, Perry, Droettboom, Michael, Bray, Erik, Aldcroft, Tom, Davis, Matt, Ginsburg, Adam, Price-Whelan, Adrian M., Kerzendorf, Wolfgang E., Conley, Alexander, Crighton, Neil, Barbary, Kyle, Muna, Demitri, Ferguson, Henry, Grollier, Frédéric, Parikh, Madhura M., Nair, Prasanth H., Günther, Hans M., Deil, Christoph, Woillez, Julien, Conseil, Simon, Kramer, Roban, Turner, James E. H., Singer, Leo, Fox, Ryan, Weaver, Benjamin A., Zabalza, Victor, Edwards, Zachary I., Azalee Bostroem, K., Burke, D. J., Casey, Andrew R., Crawford, Steven M., Dencheva, Nadia, Ely, Justin, Jenness, Tim, Labrie, Kathleen, Lim, Pey Lian, Pierfederici, Francesco, Pontzen, Andrew, Ptak, Andy, Refsdal, Brian, Servillat, Mathieu, Streicher, Ole, 2013, A&A, 558, A33

Todorov K. O., Deming D., Knutson H. A., Burrows A., Fortney J. J., Lewis N. K., Cowan N. B., Agol E., Desert J.-M., Sada P. V., Charbonneau D., Laughlin G., Langton J., Showman A. P., 2013, The Astrophysical Journal, 770, 102

Tregloan-Reed J., Southworth J., Tappert C., 2013, MNRAS, 428, 3671

Triaud A. H. M. J., 2017a, ArXiv e-prints

Triaud A. H. M. J., The Rossiter-McLaughlin Effect in Exoplanet Research, 2, 2017b

Udalski A., Szymanski M., Kaluzny J., Kubiak M., Mateo M., 1992, Acta Astronomica, 42, 253

Udry S., Mayor M., Naef D., Pepe F., Queloz D., Santos N. C., Burnet M., 2002, A&A, 390, 267

Udry S., Lovis C., Bouchy F., Collier Cameron A., Henning T., Mayor M., Pepe F., Piskunov N., Pollacco D., Queloz D., Quirrenbach A., Rauer H., Rebolo R., Santos N. C., Snellen I., Zerbi F., 2014, ArXiv e-prints

Van Cleve J. E., Howell S. B., Smith J. C., Clarke B. D., Thompson S. E., Bryson S. T., Lund M. N., Handberg R., Chaplin W. J., 2016, PASP, 128(7), 075002

van de Kamp P., Lippincott S. L., 1951, AJ, 56, 49

van de Kamp P., 1963, AJ, 68, 295

van Maanen A., 1917, PASP, 29, 258

Vanderburg A., Johnson J. A., 2014, PASP, 126, 948

Vanderburg A., Johnson J. A., Rappaport S., Bieryla A., Irwin J., Lewis J. A., Kipping D., Brown W. R., Dufour P., Ciardi D. R., Angus R., Schaefer L., Latham D. W., Charbonneau D., Beichman C., Eastman J., McCrady N., Wittenmyer R. A., Wright J. T., 2015, Nature, 526, 546

Vida K., Kővári Z., Pál A., Oláh K., Kriskovics L., 2017, ApJ, 841, 124

Walker G. A. H., Bohlender D. A., Walker A. R., Irwin A. W., Yang S. L. S., Larson A., 1992, ApJL, 396, L91

Ward W. R., 1996, in Rettig T., Hahn J. M., eds, Completing the Inventory of the Solar System, Astronomical Society of the Pacific Conference Series Vol. 107, p. 337

Ward W. R., 1997, Icarus, 126, 261

Welsh W. F., Orosz J. A., Seager S., Fortney J. J., Jenkins J., Rowe J. F., Koch D., Borucki W. J., 2010, ApJL, 713, L145

Wheatley P. J., Collier Cameron A., Harrington J., Fortney J. J., Simpson J. M., Anderson D. R., Smith A. M. S., Aigrain S., Clarkson W. I., Gillon M., Haswell C. A., Hebb L., Hébrard G., Hellier C., Hodgkin S. T., Horne K. D., Kane S. R., Maxted P. F. L., Norton A. J., Pollacco D. L., Pont F., Skillen I., Smalley B., Street R. A., Udry S., West R. G., Wilson D. M., 2010, ArXiv e-prints

Wheatley P. J., West R. G., Goad M. R., Jenkins J. S., Pollacco D. L., Queloz D., Rauer H., Udry S., Watson C. A., Chazelas B., Eigmüller P., Lambert G., Genolet L., McCormac J., Walker S., Armstrong D. J., Bayliss D., Bento J., Bouchy F., Burleigh M. R., Cabrera J., Casewell S. L., Chaushev A., Chote P., Csizmadia S., Erikson A., Faedi F., Foxell E., Gänsicke B. T., Gillen E., Grange A., Günther M. N., Hodgkin S. T., Jackman J., Jordán A., Louden T., Metrailler L., Moyano M., Nielsen L. D., Osborn H. P., Poppenhaeger K., Raddi R., Raynard L., Smith A. M. S., Soto M., Titz-Weider R., 2018, MNRAS, 475, 4476

Winn J. N., 2010, ArXiv e-prints

Winn J. N., Holman M. J., Torres G., McCullough P., Johns-Krull C., Latham D. W., Shporer A., Mazeh T., Garcia-Melendo E., Foote C., Esquerdo G., Everett M., 2008, ApJ, 683, 1076

Winn J. N., Holman M. J., Henry G. W., Torres G., Fischer D., Johnson J. A., Marcy G. W., Shporer A., Mazeh T., 2009, ApJ, 693, 794

Wolszczan A., Frail D. A., 1992, Nature, 355, 145

Wright J. T., Marcy G. W., Howard A. W., Johnson J. A., Morton T. D., Fischer D. A., 2012, ApJ, 753, 160

Zellem R., Griffith C. A., Lewis N. K., Swain M. R., Knutson H. A., 2014, AAS/Division for Planetary Sciences Meeting Abstracts, AAS/Division for Planetary Sciences Meeting Abstracts Vol. 46, p. 104.04

Zhou G., Bayliss D. D. R., Kedziora-Chudczer L., Salter G., Tinney C. G., Bailey J., 2014, MNRAS, 445, 2746

Zhou G., Bayliss D. D. R., Kedziora-Chudczer L., Tinney C. G., Bailey J., Salter G., Rodriguez J., 2015, MNRAS, 454, 3002

Zhou G., Bakos G. Á., Hartman J. D., Latham D. W., Torres G., Bhatti W., Penev K., Buchhave L., Kovács G., Bieryla A., Quinn S., Isaacson H., Fulton B. J., Falco

E., Csubry Z., Everett M., Szklenar T., Esquerdo G., Berlind P., Calkins M. L., Béky B., Knox R. P., Hinz P., Horch E. P., Hirsch L., Howell S. B., Noyes R. W., Marcy G., de Val-Borro M., Lázár J., Papp I., Sári P., 2017, AJ, 153, 211